STRUCTURE-PROPERTY RELATIONSHIPS IN TWO-COMPONENT LIQUIDS

SHEPHARD, JACOB,JAMES,ELDRED

STRUCTURE-PROPERTY RELATIONSHIPS IN TWO-COMPONENT LIQUIDS

By JACOB SHEPHARD

This thesis tackles several two-component liquids where we currently have a poor understanding of their fundamental structures and influence on properties. A novel approach was taken to investigate hydrophobic interactions.[1] Rather than studying the aqueous liquid, for which only very low hydrophobe concentrations are possible, the metastable glassy state formed by thermally annealing a H_2O/C_{60} fullerene vapour deposit was examined. These 'trapped solutions' of fullerene in an amorphous solid water (ASW) matrix were prepared in newly built apparatus **(Chapter 3)** using deposition rates of ~5 H_2O monolayers per second to give a total mass > 1 g without crystalline ice contamination. H_2O desorption rate analysis indicated that the limits of ASW growth are associated with the influence of deposition rate on porosity and consequent decreases in deposit to cooling plate heat transfer with increasing deposit thickness. Characterisations by FT-IR, Raman, optical absorbance and photoluminescence spectroscopies, as well as by X-ray and neutron diffraction showed unexpected continual structural relaxation until their crystallisation to ice I at 150–160 K **(Chapter 4)**.[2] Contrary to Frank and Evans's description of 'iceberg' hydration structures,[3] for C_{60} in ASW there is a weakening of the average hydrogen bonding interaction and increases in dynamics of the first hydration layer. The present work tentatively supports theories of hydrophobic hydration forces involving a disconnection of water in the hydration shell from the extended hydrogen bonding network **(Chapter 5)**.[4-5]

The intermolecular interactions in the chloroform–acetone (negative) and benzene–methanol (positive) azeotropes were investigated by Raman spectroscopy and neutron diffraction. Structural models of pure liquid chloroform and the chloroform-acetone azeotrope were prepared by Empirical Potential Structural Refinement[6] of experimental data and described using radial distribution functions, spatial density functions, orientation correlation functions and Kirkwood correlation factors. These analyses revealed that 'super dipole' $Cl_3H\cdots Cl_3H\cdots Cl_3H$ self-associations in pure liquid chloroform (29 % molecules) may contribute to its good solvent quality and anaesthetic properties **(Chapter 6)**,[7] and that $C_2H_6O\cdots HCCl_3$ hydrogen bonding interactions are present in the chloroform-acetone azeotrope **(Chapter 7)**. Through comparisons of radial distribution functions between 'like' and 'unlike' species in the azeotropes it is revealed that the azeotropic vapour pressure condition is not only characterised by the non-ideality of intermolecular interaction but also by significant deviations in mixing character from that of a regular mixture; the benzene-methanol azeotrope exhibit microscopic statistical demixing and the chloroform-acetone azeotrope exhibits transient complexation.

STRUCTURE-PROPERTY RELATIONSHIPS IN TWO-COMPONENT LIQUIDS:

HYDROPHOBIC EFFECTS AND AZEOTROPY

Jacob James Shephard

Supervised by Dr Christoph G. Salzmann
and by Professor John S. O. Evans

Submitted for the partial fulfilment of the degree:
Doctor of Philosophy

Department of Chemistry
Durham University, 2014

Table Of Contents

Abbreviations

ASW – amorphous solid water

COM – centre of mass

CSD – Cambridge Structural Database

DSC – differential scanning calorimetry

DCS – differential cross section

FT – Fourier transform

FT-IR – Fourier transform infrared

FWHM – full width at half maximum

HDA – high density amorphous ice

uHDA – unannealed high density amorphous ice

eHDA – expanded high density amorphous ice

vHDA – very high density amorphous ice

HS – Hard Sphere

LDA – low density amorphous ice

LJ – Lennard-Jones

LN_2 – liquid nitrogen

LJ + C – Lennard-Jones plus Coulomb

OCF – orientational correlation function

RDF – radial distribution function

SDF – spatial density function

SFG – Sum Frequency Generation

SSNMR – solid-state nuclear magnetic resonance

XRD – X-ray diffraction

Declaration

The work herein described is entirely my own, expect for that acknowledged below or where I have provided a published source. The copyright of this thesis rests with the author. No quotation from it should be published without the author's *prior* written consent and information derived from it should be acknowledged.

Acknowledgements

I acknowledge the workshop staff at the Chemistry Department of Durham University and the MAPS workshop of University College London for fabricating the practical parts required to obtain the data presented in this report; Neil Holmes and Scott Ramsey created the deposition stage; Kelvin Appleby and Barry Barker assembled the C_{60} sublimation power supply; Peter Coyne prepared the glass vials for storing substrates upright in liquid nitrogen; Aaron Brown created the triple H_2O flask inlet system; Harpal Sandu adapted the baseplate for water cooling and rebuilt the Raman cryostat for transmission FT-IR; John Benbo adapted the deposition plate for better thermal contact and constructed the aluminium sample containers. Several services of Durham University Chemistry were also employed: Solid state NMR was carried out at the EPSRC UK National Solid-state NMR Service by David Apperley and Fraser Markwell; DFT calculation were carried out by Mark Fox.

My supervisors, Professor John Evans and Dr Christoph Salzmann, provided me with a large amount of direction and support, without which this project would not have been possible.

1 Introduction

1.1.1 MOLECULAR LIQUIDS

The liquid state is commonly defined by its tendency to flow freely but maintain a constant volume.[8] Despite the obvious importance of liquids their intermolecular structures are generally much less well characterised than those of crystalline solids and some of their properties are not fully understood. This thesis focusses on mixtures containing molecular liquids, which display significantly more complex behaviour than atomic liquids.[9-10] The structure of molecular liquids depends closely upon the balance of intermolecular interactions and the available thermal energy, with structural order typically increasing as the temperature decreases. The average structure of liquids may be viewed as the time or space averaged sum of the most likely 'inherent' structural arrangements. The fluid property of liquids arise due to the 'inherent' structures, which correspond to shallow potential energy minima on an energy landscape, being interconverted by dynamic rotation and translation motions.[11] To uncover the complex behaviours of liquids a deeper understanding of the physical nature of the energy landscape is commonly sought. *i.e* the interactions which give rise to the inherent structural arrangements (structure) and the origin of the transition state barriers to dynamic rearrangements (dynamics).

In this thesis, the structure of several different two-component liquids are investigated experimentally. Firstly, the structure of aqueous solutions containing a model hydrophobe (C_{60}, fullerene) are explored. These mixtures are of significant interest because of the presently unexplained attractive interaction that occurs between solvated hydrophobes in water.[1] These 'hydrophobic effects' are thought to support molecular self-assembly processes, such as protein folding and micelle formation.[12] A novel approach was taken to investigate the nature of hydrophobic interactions. Rather than studying aqueous solutions, for which only very low hydrophobe concentrations are possible, the metastable glassy state formed by thermally annealing a H_2O/C_{60} fullerene vapour deposit was examined. Secondly, this thesis investigates the structure of highly non-ideal liquid mixtures containing small polar molecules (chloroform and acetone; and benzene and methanol). In addition to spectroscopic techniques, a powerful data analysis tool called Empirical Potential Structural Refinement was used in this section to create 3D structural

models consistent with neutron scattering data. The aim of this modelling is to uncover the structural characteristics of negative and positive pressure azeotropy[13] in these systems.

1.1.2 ORDER AND DISORDER IN CONDENSED FORMS OF H_2O

Liquid water (H_2O) is intricately linked to, or indeed responsible for, the evolution of life on Earth. Despite an extensive body of research carried out to understand its structural and dynamical properties, there is still no, universally accepted, structural model and there remain several poorly understood, 'anomalous', properties.[14-15] These include a density maximum at ~4 °C,[16-20] and the aforementioned attractive forces which form between non-polar surfaces immersed in the liquid, termed hydrophobic effects.[1,12] To date, experimental measurements of liquid water have been unable to categorically explain these 'anomalous' properties. Diffraction data indicates that liquid water, under ambient pressure-temperature conditions, has an average first neighbour coordination number of 4.67 ± 0.01, short intermolecular distance correlations at ~1.85 Å (O–H) and ~2.82 Å (O–O), and a loss of spatial correlations in the second and third molecular shells.[21-23] These imply, respectively, a tendency for four coordinate structures as in ice but with coordination defects,[24] hydrogen bond formation, and dynamic disordering due to thermal motions. Experimental investigations into water's dynamical character have shown its modes of motion to be energetically coupled, molecular reorientation to be a cooperative phenomenon and defect migration and hydrogen bond switching mechanisms to contribute significantly.[11,25-27] These observations and the large heat capacity of 4.18 J g^{-1} K^{-1},[28] have led to water being described as a 'random network of hydrogen bonds, with frequent strained and broken bonds, that is continually undergoing topological reformation.[29]

To explain the more complicated 'anomalous' properties a more exact description of the structural and dynamic character of the hydrogen bonding network is needed. The large range of different structural arrangements with potential to contribute to the hydrogen bonding network can be demonstrated by the structurally diverse range of crystalline phases in the temperature–pressure phase diagram of H_2O. The up to date phase diagram of water and ice is shown in Figure 1.1 (taken

from a work by Salzmann *et al.*[30]). Thermodynamically stable phases are indicated in bold and metastable crystalline phases are shown in a non-bold smaller font size. The phases are named in Roman numerals in order of discovery and all adhere to the Bernal-Fowler ice rules which state: (1) one hydrogen atom is found along each of the hydrogen bonds and (2) the stoichiometry of the H_2O molecule is preserved.[31] This effectively means that the crystalline phases of ice, unlike liquid water, all have a four coordinate near neighbour environment giving structures comprised of tetrahedra with interlinked vertices. The structures of the different phases, described by Salzmann *et al.*[30] will not be repeated here. Instead, we will illustrate the many different structural permutations available to the hydrogen-bonding network by describing the structural changes which occur as the phase diagram is crossed from low to high pressures and from high to low temperatures.

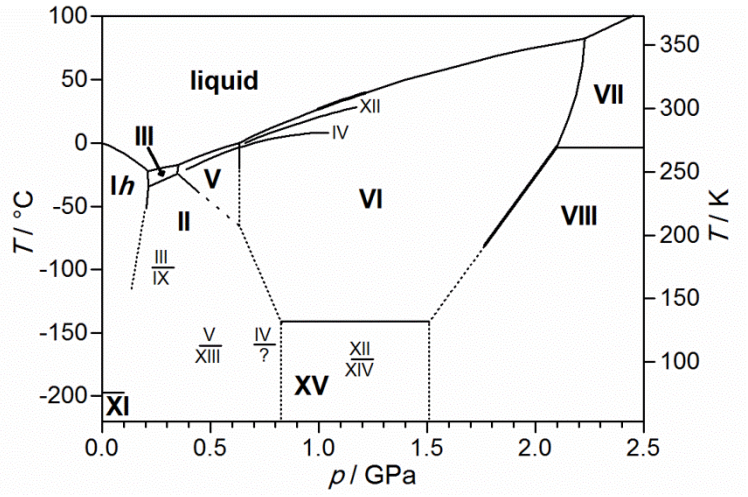

Figure 1.1 Phase diagram of water and ice, taken from Salzmann *et al.*[30] Thermodynamically stable phases are indicated in bold. Metastable phases and stable phases outside their boundaries of stability are indicated in a smaller font size. Solid lines correspond to experimentally accessible phase transitions and dashed lines correspond to extrapolations based on ΔV and ΔS.

As the phase diagram is crossed from low to high pressure at –30 °C the density of the most thermodynamically stable crystalline phases increases ($I_h \rightarrow$ III$\rightarrow$ II$\rightarrow$ V$\rightarrow$ VI$\rightarrow$ VIII). The increase is mostly associated with changes in the interconnectivity of the water molecules, bending the hydrogen bonds (in I_h the hydrogen bonds are linear), and (for ices VI and VIII) the interpenetration of hydrogen bonding networks. These structures each have unique distributions of oxygen-oxygen distances and specific ring statistics, characterising their different

interconnectivities. Another metastable ice, termed cubic ice, I_c,[32-34] is not included in the phase diagram because it has not yet been prepared as a pure phase, only as 'structural motifs' which cause stacking faults in I_h.[35-39] As shown in Figure 1.2, the structural differences between ice I_c and I_h involve a subtle change in the relative arrangement of the 6 membered rings giving identical oxygen-oxygen distances in the first and second molecular shells. The ability of the hydrogen bonding networks to form with a range of different interconnectivities is further illustrated by clathrate hydrates,[40] in which non-polar species are enclosed in the crystalline H_2O network rather than being expelled. Despite having very different interconnectivity,[30] these structures accommodate the non-polar molecules without a prohibitory energetic demand.

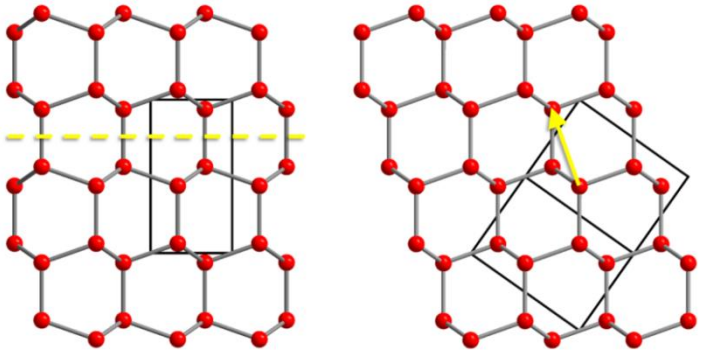

Figure 1.2 Stacking arrangements in I_h (left) and I_c (right). The solid lines correspond to the position of the unit cell. The yellow dashed line shows the mirror plane between two layers in I_h and the yellow arrow shows the corresponding glide plane. Image used with the permission of its author, C. Salzmann.

The structural changes which occur as the phase diagram is crossed from high to low temperatures at a constant pressure may not involve changes in molecular interconnectivity. Instead, the transition may solely involve changes in the orientational ordering of the water molecules, termed hydrogen ordering. These extra degrees of freedom (and the residual entropy of ice I_h) arise because of the 6 different ways to orientate the water molecules without changing their interconnectivity (a tetrahedron has 6 edges, *c.f.* Figure 2 by Salzmann[30]). Whilst for the majority of the higher temperatures phases (I_h, III, V, VI, VII) diffraction analysis indicates no long range bond orientational ordering, for ice II and the lower temperature phases (XI, XV and XIII) the hydrogen atoms display low enthalpy ordering patterns which extend over the dimensions of the

crystallites. As the interconnectivity is essentially unperturbed upon bond orientational ordering, phases may be grouped into pairs associated with the order-disorder transition (I_h/XI, III/IX, ?/II, V/XIII, IV/?, XII/XIV,VI/XV, VII/VIII) (Figure 1.1). It is also important to consider that whilst the long range structure of the crystalline phases are, in the main, either orientationally ordered or disordered, over intermediate length scales, the orientational ordering conditions may not be so easily categorised.

This range of different interconnectivities and bond orientational orderings means that a huge number of structural permutations are consistent with the Bernal-Fowler ice rules over intermediate distances. Whilst for local first neighbour distances the structure of condensed phases of H_2O may overwhelming be described as having a tendency to be 4 coordinate, over slightly larger length scales and for the 'broken' networks found in liquid water there are a very large number of different ways to arrange the molecules.[41] This was recognised by Stillinger who referred to the hydrogen bonding network as a 'continuum of architectural possibilities'.[29] It is not presently clear to what extent specific structural arrangements with different oxygen–oxygen positioning (interconnectivity) or bond orientational ordering contribute to the average structure of the liquid state. The lower density of liquid water than ice I_h at ambient pressures does suggest that liquid water has a significant proportion of bent or broken hydrogen bonds, but the specific structural arrangements which persist over intermediate length scales are unknown.[42] It may be that different arrangements become more or less prevalent as the temperature or pressure are changed in an analogous way to the ices but with ordering only over much shorter length scales. It is of particular interest to test experimentally if arrangements with a distinctly different 4 coordinate structure grow in liquid water with decreasing temperature, as predicted by computer simulation.[43] The presence of two liquids with different structural characteristics and an associated hidden critical point in the supercooled region of the temperature-pressure phase diagram would seemingly explain many of liquid water's anomalous properties.[20,44-55]

In addition to liquid water and the thermodynamically stable and metastable crystalline phases indicated on the phase diagram there are also several metastable non-crystalline

(amorphous) phases of particular relevance to this study. A supercooled liquid may be formed when liquid water is cooled to temperatures below its melting point (homogeneous nucleation temperature = 235 K)[56] and several solid metastable amorphous forms may also be prepared and recovered into liquid nitrogen at 77 K. The solid metastable amorphous forms have been named according to their method of preparation. Hyperquenched glassy water (HGW) is prepared by quickly cooling small droplets of the liquid.[57-58] Amorphous solid water (ASW) is produced by vapour deposition at temperature < 150 K.[59-61] High density amorphous (HDA) ice is formed by compressing I_h to 1.2 GPa at 77 K.[62-63] Low density amorphous ice (LDA) may be formed by heating HDA > 120 K,[63] but is also the term most generally used to describe any of the amorphous forms after their annealing to 120 K at ambient pressures. The structural states of these materials are thought to be between the disordered and dynamic state of liquid water and the more ordered and less dynamic structure of the crystalline solids. Interestingly, the pressures required for the transition between I_h and HDA correspond approximately to an extension of the hypothetical melting line in the metastable phase diagram, suggesting that the structure of HDA may be the glassy analogue of a high density liquid phase (HDL),[64-67] proposed to exist as part of the hidden critical point scenario of liquid water.[44] HDA is thought to have a greater number of broken or bent hydrogen bonds than LDA.[68] The structure of ASW is often porous and highly dependent on the deposition conditions.[60,69-70] HGW and LDA are presumed to have structures representative of the ambient pressure supercooled liquid at the glass transition temperature. The thermodynamic states of the different amorphous ices are discussed further by Johari *et al*.[71-73] and by Loerting *et al*..[74]

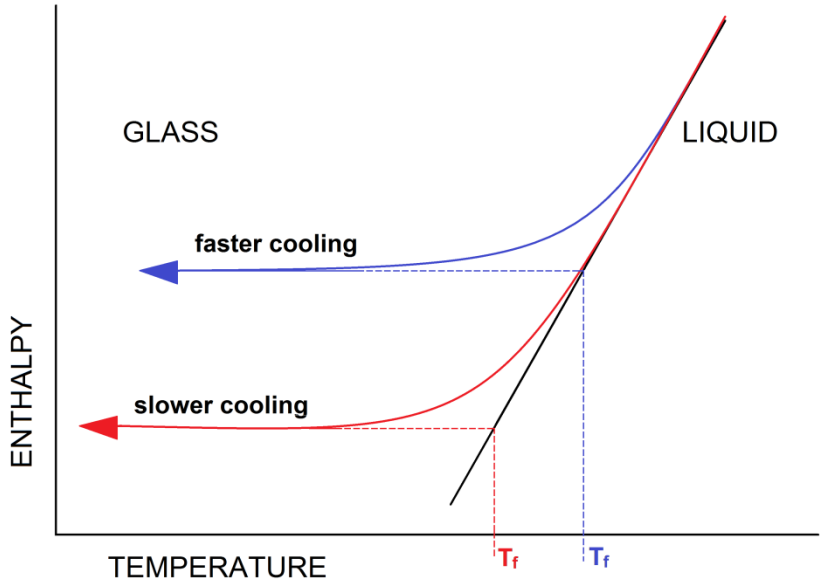

Figure 1.3 Schematic illustration of the enthalpy change which occurs during glass formation. The black line indicates the trend for a hypothetical liquid. The blue and red lines show the changes which occur as liquids are cooled below the glass transition temperature quickly and more slowly. The fictive temperature, T_f, indicates the temperature at which the hypothetical liquid state would have a similar structure to that of the glass.

At 77 K, the modes of motion which would allow the solid amorphous metastable forms to transform into more energetically favoured crystalline phases are inactive. Unlike liquids, which may be described as having ergodicity (a time averaged structural state which is equal to ensemble average of the accessible phase space) these metastable amorphous solids are 'kinetically trapped' and thus experience only extremely slow structural relaxation at 77 K. The temperature required to activate the translational and rotational modes of motion, transforming the solids into liquids, is called the glass transition temperature, T_g.[75] It is typically characterised by a marked change in viscosity. The kinetic trapping of the amorphous ices causes their structures to depend upon their thermal history. For example, the structural state of the glassy solid, HGW, will depend on the cooling rate at which it was prepared.[76-77] The influence of cooling rate on structure may be understood by considering its fictive temperature, T_f.[75] The T_f relates the structure of the glass to the corresponding temperature of a liquid with identical structure and indicates the extent of the structural changes which occurred upon cooling before the glassy structure was 'frozen in'. This is shown schematically in Figure 1.3. If a liquid is cooled more slowly to temperatures below its T_g

then its structure will be able to become more relaxed, giving a glass with lower enthalpy and lower T_f.

Despite ASW, HDA and LDA having less obvious connections with liquid water than HGW, it is thought that upon heating these materials toward T_g their structural state should approach that of HGW and therefore also that of the supercooled liquid.[50,78] The postulate that a unified structural state can be reached from HGW, ASW and HDA depends upon the temperature required to enable the local and intermediate range structural rearrangements of the amorphous phases relative to those required for the longer range periodic reconstructions of crystallisation. In other words the dynamics must be activated, to an extent, but crystallisation must be avoided. The low temperature dynamics of ASW are of particular significance because ASW in the icy mantel of comets in space may provide an ideal matrix for the irradiation catalysed reactions needed to produce the small organic molecules required for the evolution of life on earth.[79] The prevalence of ASW in space is supported by spectroscopic analysis of light reaching earth,[80-82] and also more directly by the spectroscopic data collected by the 'deep impact' spacecraft in the aura produced after penetrating comet *9P/Tempel*. [83 84]

The temperature required to unify the structural states of the amorphous phases or enable the diffusion and reaction of molecules trapped in an ASW matrix is thought to be between 124 and 136 K. This hypothesis is mostly based upon reversible increases in heat capacity observed for ASW and HGW by differential scanning calorimetry (DSC),[85-87] seemingly indicating the glass to liquid transition.[88] However, it has recently been pointed out that for hydrogen bonding networks, other dynamic modes of motion not involving free rotational and translational motion of molecules may also give reversible increases in heat capacity.[2,30] The feature observed calorimetrically, which is unexpectedly weak for a H_2O T_g, may instead be associated with activation of defect-mediated reorientation dynamics, either that corresponding to hydroxyl and oxonium ion migration, (the Grotthuss mechanism[89]) or the rotations which occur with lower activation energy about 'broken bonds' (O···O and H···H), termed Bjerrum point defects.[90-91] The Grotthuss mechanism involves the migration of H_3O^+ and OH^- defects through the structure with only a minimum change in the

position of the oxygen or hydrogen atoms. Essentially, for an adjacent pair of molecules the hydrogen bonding and covalent bonding pairs switch over ($H_2O\cdots H–OH_2+ \rightarrow +H_2O–H\cdots OH_2$) moving the hydrogen atom and the physical charge from one molecule to the next in a linked chain. Similarly, Bjerrum point defects also move along a linked chain by rotation, moving O···O and H···H defects until the two defect types converge. These defect-mediated dynamics are fundamental in enabling the low-temperature elevated pressure hydrogen-disorder to hydrogen-order phase transitions. [30,92] These processes are known to occur in the crystalline phases of ice V, XII and IV[30] at similar temperatures to the proposed T_g of ASW.

In this work, the controlled way in which the structural state of ASW may be changed towards that of the supercooled liquid by incremental increases in temperature and its route of preparation from the vapour phase have been exploited to study the 'anomolous' properties of liquid water related to hydrophobic hydration. Specifically, water vapour has been codeposited with a model hydrophobe (C_{60}, fullerene) to give C_{60} dispersed in an ASW matrix. These mixtures are referred to as 'trapped solutions' since their structural state may be similar to that of unstable solutions before they precipitate. The apparatus used to prepare the ASW/C_{60} 'trapped solutions' is described in Chapter 3. The changes in the structural state of pure ASW upon thermal annealing are investigated in Chapter 4. The structures of the thermally annealed ASW/C_{60} 'trapped solutions' are examined in Chapter 5.

1.1.3 STRUCTURE-PROPERTY RELATIONSHIPS OF SOLVENT MIXTURES

Despite the large number of different solvents available for chemical and industrial processes, relatively few are in common usage,[93] and solvent mixtures which offer the possibility for properties to be specifically tailored to applications are rarely employed. The most relevant properties in terms of chemical and industrial applications are the solvent's vapour pressure, solubility and dielectric behaviour. As examples, (1) volatile solvents are desired for industrial separation application as they allow the solvent to be removed from the product quickly using only moderate increases in temperatures or decreases in pressures; and (2) the most effective solvents

for cleaning applications are often those which are miscible with or able to polarise the substance to be removed. The difficulty in designing solvent mixtures for particular purposes is that we cannot, at present, accurately predict their properties, which depend upon the temperature and the exact nature of the intermolecular interactions. The structural analysis of azeotropes carried out in this study explores the power of a newly developed data analysis technique, termed Empirical Potential Structural Refinement (EPSR),[6] to elucidate the inherent structural arrangements which occur in the liquid state, revealing the nature of the intermolecular interactions.

Azeotropes are two-component liquids with the interesting property that they produce a vapour composition equal to the liquid composition.[94] They are most commonly encountered upon distillation as purification beyond the azeotropic composition cannot be achieved directly. Unlike most liquid mixtures, azeotropes have found several applications for which they have better properties than the single component liquids. Prominent examples include cleaning solvents in the electronics industry,[95] and safe low-cost anaesthetics.[96] Azeotropes are formed in highly non-ideal systems where the vapour pressure varies strongly with composition giving either a minimum or maximum in vapour pressure-composition plots. These are termed negative and positive pressure azeotropes, respectively.[13] Absolute azeotropes are those which display azeotropic behaviour over the whole of the liquid range and limited azeotropes are those which display a return to normal behaviour under certain conditions of temperature and pressure. Limited azeotropes showing azeotropic behaviour only at a single specific temperature are said to be at a Bancroft point.[13]

The variation in vapour pressure with composition for binary mixtures of acetone and chloroform (a negative pressure azeotrope),[97] and for benzene and methanol (a positive pressure azeotrope),[98-100] are shown in Figure 2.4. The dashed line indicates the vapour pressure which would be obtained for an ideal mixture obeying Raoult's law. Pressure-composition isotherms (PXY plots) showing the variations in both liquid and vapour composition with pressure are given as Appendix 1. The freezing point diagram for acetone–chloroform mixtures is given by Campbell *et al.*.[101]

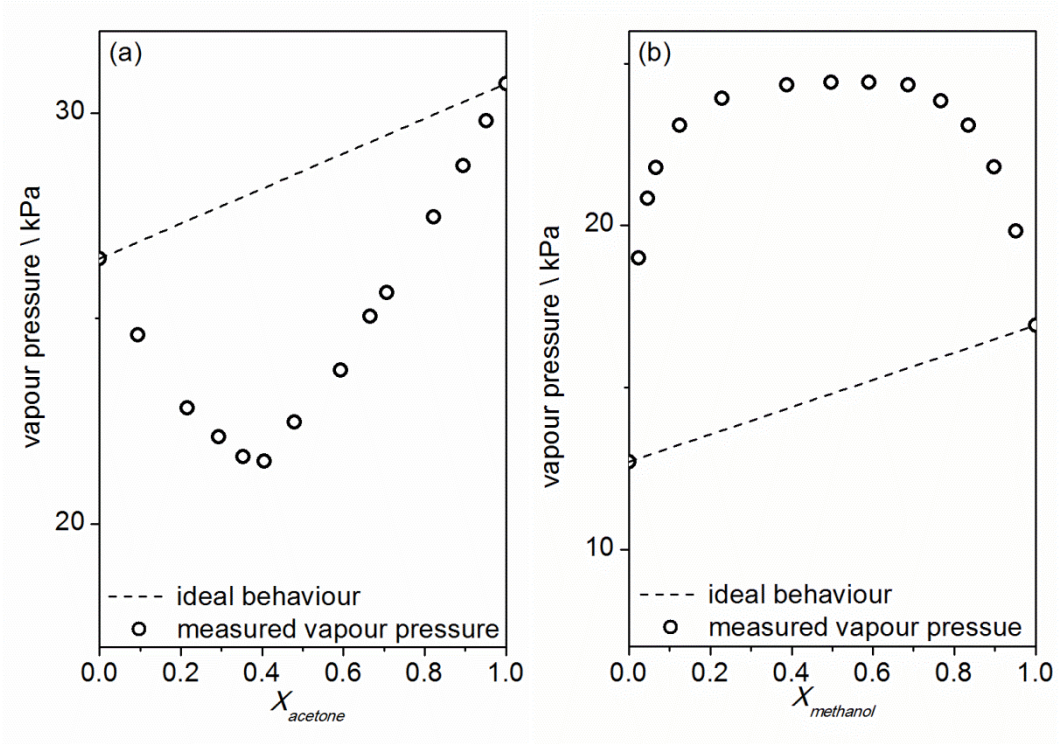

Figure 1.4 Variation of vapour pressure with composition at room temperature for binary mixtures of (a) acetone and chloroform[97,102] and (b) methanol and benzene.[99] The azeotropic composition corresponds to the minimum and maximum in vapour pressure, respectively.

The presence or absence of minima or maxima in the vapour pressure composition plots depends on the structure and intermolecular interactions of the liquid mixture. They are most likely to occur in systems for which the pure components have similar vapour pressure and for mixtures which are highly non-ideal with a large positive or negative enthalpy of mixing. The binary heterogeneous equilibrium behaviour can be shown more formally using by the Gibbs-Konowalow laws.[13] The series of deductions given by Rowlinson *et al.*[13] show that binary mixtures with an equality of phase composition must either display critical or azeotropic behaviour. If the enthalpy difference is zero then the phase boundary vanishes to give critical behaviour but if the enthalpy difference remains then the variation in vapour pressure with composition must be either at a maximum or minimum, giving azeotropic behaviour. Rowlinson *et al*. also pointed out that azeotropes have fewer degrees of freedom than expected for a binary mixture and display some of the thermodynamic properties of single component liquids, such as a vapour pressure (at the azeotropic composition), which varies with temperature according to the Clausius-Clapeyron relationship.

In this work, the structural origin of the non-ideality in the chloroform-acetone and benzene-methanol azeotropes are explored. The current extent of our understanding of these systems is mostly based upon their negative or positive enthalpy of mixing, (Figure 1.4) which indicate stronger interactions between the 'unlike' species for the chloroform-acetone azeotrope and stronger interactions between 'like' species in the benzene-methanol azeotrope. Although this energetic description has allowed some hypotheses about the inherent structural arrangements which may be forming,[97,103-104] direct experimental structural evidence is not available. In this work structural hypotheses are tested by comparing 3D structural models of the azeotropes and the pure liquids prepared using EPSR and consistent with neutron diffraction data. Structural models of pure liquid chloroform are described in Chapter 6. The EPSR structural model of pure liquid acetone has recently been reported by McLain *et al*..[105] Structural models of the chloroform-acetone azeotrope are described in Chapter 7. Structural models of the benzene-methanol system have not yet been prepared but analysis of the neutron diffraction data is given in section 7.18. The use of neutron diffraction for structural analysis of liquids and amorphous solids and the EPSR data analysis technique are described in the following sections.

1.1.4 Structural Modelling by Computer Simulation

The structural characterisation of amorphous materials, such as liquids, can be much more challenging than for crystalline materials. For crystalline materials, the least squares fit to the position of atoms in a repeating unit cell to diffracted intensities provides an effective route to structure determination of even very complex materials. Amorphous materials, however, do not produce Bragg peaks in diffraction experiments and without 3D long-range ordering, the concept of a small repeating unit cell is not applicable. Structural characterisation of molecular liquids is particularly challenging because of orientational correlations which arise due to directional aspects of specific interactions and their more complicated packing arrangements. [9,106]

For molecular liquids, where the intermolecular interactions can be accurately described by a series of intermolecular pair potentials (molecular force fields), very accurate structural models may be prepared by computer simulation. For these simulations the unit cell is replaced with a

large (usually cubic) box, typically containing several thousand molecules. The simulation box is like a unit cell in that it represents a periodic repeatable unit of the liquid's structure. However, to account for the dynamic nature of liquids the walls must also be permeable, allowing molecules to leave the box through the wall on one side, immediately reentering through the opposite wall. By fixing the box dimensions and composition the simulation density is constrained. The size of box determines the range over which structure may be modelled. It is typically prepared such that the distances over which the intermolecular potentials operate are less than half the box dimension.

There are two main algorithms commonly used to study liquids: molecular dynamics and Metropolis Monte Carlo.[107] The EPSR software employed in this study uses the Metropolis Monte Carlo algorithm and is designed specifically for molecular liquids. Molecular dynamics simulations, which model the movement of atoms/molecules in the simulation box and examine the time dependence of structure are not discussed further.

Metropolis Monte Carlo Simulations,[107-108] are predominantly used to prepare structural models of the equilibrium state. In this approach, the starting condition is that the molecules contained within the simulation box are randomly arranged. The molecules are then moved individually in steps which are either accepted or discarded according to the Metropolis condition. In the Metropolis condition, moves which decrease the potential energy, U, of the system ($\Delta U < 0$) are accepted and moves which increase the potential energy ($\Delta U > 0$) are accepted with an acceptance probability, P_a, related to the temperature, T and the Boltzmann constant, k, as shown by Equation 1.1.

$$p_a = \exp\left[-\frac{\Delta U}{kT}\right].$$

Equation 1.1

The dependence of the move acceptance rate on temperature and potential energy enables Monte Carlo simulations to reproduce the balance of intermolecular interactions and thermal energy present in liquids. The accuracy of the structural models produced are limited by the accuracy of the pairwise potentials between the molecules for describing the intermolecular

interactions. Several different intermolecular interactions are typically considered in the force fields used for Monte Carlo simulations of liquids. The 'reference' potential for the EPSR Monte Carlo simulation program is given as Equation 1.2.[21] The discussion below defines the parameters and describes how the terms in the 'reference' potential are related to intermolecular interactions.[10] Figure 1.5 shows how each of the three terms in the EPSR potential vary with atom pair separation. The values shown are for the interaction of two chlorine atoms using the empirically derived force field of Barlette *et al.* and a van der Waals distance of 1.75 Å.[109] The additional truncation terms used by EPSR to reduce the potentials to zero for distances greater than half the box dimensions are given by Soper *et al*.[6]

Short range repulsive potentials are included in EPSR Monte Carlo simulations to reproduce the repulsions between molecules with closely overlapping electron clouds. Term 1 in Equation 1.2 is an optional repulsive potential available in EPSR. It is an exponential decay function giving a 'soft' repulsive boundary. The variation in the potential with separation of two chlorine atoms is shown in Figure 1.5(a). In some of our work, simulations were carried out using solely these 'soft' repulsive potentials. This approximates a 'hard sphere' model for which separations less than a specified distance contributes a distance independent infinite repulsive potential. By setting the $r_{\alpha\beta}$ parameters to the van der Waals radius, representing the average separation of the atoms in a 'non-interacting' crystal, [109-110] a model representing the most efficient packing of the molecules may be produced.

$$U_{\alpha\beta}(r) = C_{\alpha\beta}\exp\left[\frac{1}{0.3}\ \left(r_{\alpha\beta} - r\right)\right] + 4\varepsilon_{\alpha\beta}\left[\left(\frac{\sigma_{\alpha\beta}}{r}\right)^{12} - \left(\frac{\sigma_{\alpha\beta}}{r}\right)^{6}\right] + \frac{q_\beta q_\beta}{4\pi\varepsilon_0 r}.$$

Equation 1.2

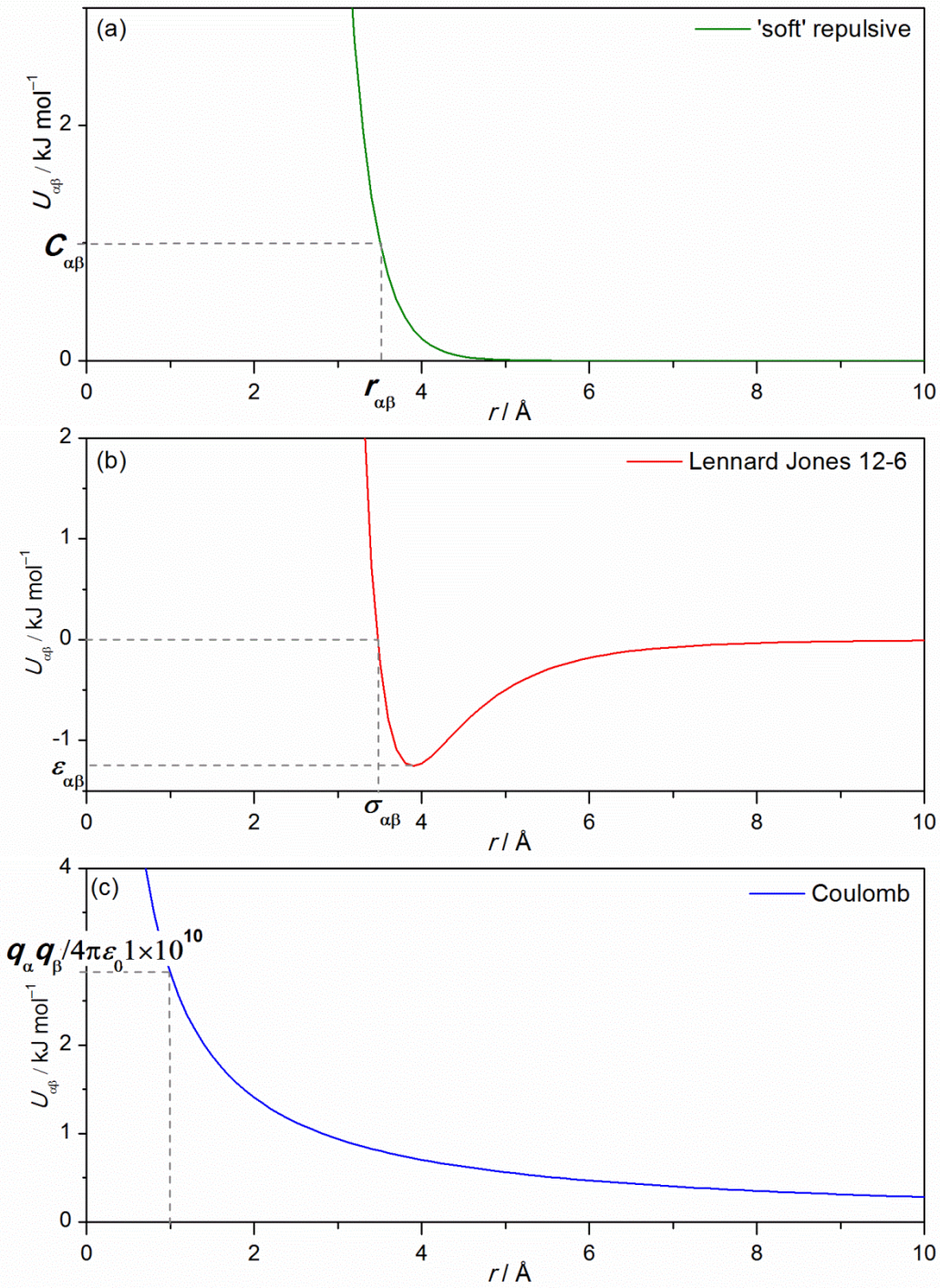

Figure 1.5 Variation in the potential energy, $U_{\alpha\beta}$ for two chlorine atoms (α and β) with separation, r, as a result of (a) 'soft' repulsive potentials, (b) Lennard-Jones 12-6 potentials and (c) Coulomb monopole partial charge interactions. The potentials have been drawn using the parameters used by Barlette *et al*. to study liquid chloroform.[111] The main distance and energy inputs to equation 1.2 are indicated in bold and the relationships to r or U *are* shown by the dashed lines.

For non-polar liquids, the attractive forces holding the liquid together arise due to instantaneous dipole–induced dipole interactions, termed dispersive or London forces.[10] In EPSR, these attractive dispersion forces are described together with repulsive overlap potentials using

Lennard-Jones (LJ) 12-6 potentials (term 2). The variation in the LJ potential with separation for two chlorine atoms is shown in Figure 1.5(b). The LJ distance, $\sigma_{\alpha\beta}$, and energy parameters, $\varepsilon_{\alpha\beta}$, describe the depth of the potential energy well and the separation at which the repulsive core potential crosses zero. For liquids containing polar molecules there are also attractive and repulsive interactions between regions of positive and negative charge termed Coulomb charge interactions (term 3). The variation in Coulomb charge potential for two chlorine molecules assigned a partial charge of –0.045,[111] is shown in Figure 1.5(c). The Coulomb charge interaction is much longer range than the dispersion force or the overlap potential.

This description of the intermolecular pair potentials may not entirely be sufficient in order to describe the actual interactions in some liquids. Unfortunately, more detailed force fields presently require prohibitively larger amounts of computational time in order to produce a structural model. The main inadequacies of the reference potential described above are: (1) The monopole Coulomb partial charges centred on nuclei may not describe the true charge distribution of a molecule and thus cannot accurately describe directional permanent dipole-permanent dipole interactions (*e.g.* hydrogen bonds[112]); (2) The Coulomb charge interactions are truncated at distance less than half the dimension of the simulation box but the interaction may in fact be much longer ranged, especially for non-isotropic arrangements of polar molecules; (3) The dispersion interaction is likely to be much greater in mixtures containing polar molecules due to permanent dipole-induced dipole, polarisation interactions; (4) Dispersion and polarisation interactions are not strictly pairwise additive as the induced dipole effect may depend on the specific arrangement of molecules in the near vicinity.[10]

The combination of inaccurate force fields and the inadequacies described above can lead to significant differences between structural information obtained by experiment and that from computer simulation. The experimental data most often employed for comparison are calorimetry, dielectric, and diffraction measurements. For liquids, the enthalpy of vaporisation from calorimetric measurements is commonly used to improve the accuracy of the force field in a process called parameterisation. However, caution is required as this enthalpy is dependent on both the liquid

structure and the potentials, with neither being independently accessible from the calorimetric data. For polar liquids experimental dielectric properties,[113] are related to the structural arrangements present in the liquid and the molecule's dipole moments (charge separation) by the Kirkwood-Fröhlich equation. This relationship has been used in Chapter 6 to compare the dielectric constant of liquid chloroform predicted from model structures with that measured experimentally.

Diffraction is, perhaps, the most powerful of the experimental methods to determine liquid structure, providing information about the distribution of atom pair distances in the liquid, commonly shown as radial distribution functions (RDFs), g(r).[114] Equation 1.3 shows how the radial distribution function of a one-component (A) monoatomic system, $g_{AA}(r)$, may be found from the number of atoms, $Z_{AA}\,dr$, in a radial distance range, *r to r + dr*, normalised by the number density, ρ_A, multiplied by the volume of a shell at that radial distance, $4\pi r^2$. The similar relationship between the $g_{AA}(r)$ and coordination number, $Z_{A\leftarrow A}$, for a distance range, r_1–r_2, is given as Equation 1.4. For polyatomic systems several partial radial distribution functions are needed to describe the structure, each indicating the distance distributions of different pairs of atom types.

$$g_{\mathrm{AA}}(r) = \frac{Z_{AA}(r)}{4\pi r^2 \rho_A}.$$

Equation 1.3

$$Z_{\mathrm{A}\leftarrow\mathrm{A}} = 4\pi\rho \int_{r_1}^{r_2} r^2\, g_{\mathrm{AA}}(r)\mathrm{d}r.$$

Equation 1.4

Characteristic $g(r)$ data for a monoatomic crystalline solid, liquid and gas are shown in Figure 1.6. In crystalline materials the distances corresponding to the first, second and third molecular shell are well defined giving sharp peaks in the $g(r)$. For a liquid, the distances within the molecular shells are less well defined and the peaks in $g(r)$ are much broader. At large r the $g(r)$ for liquids oscillates about unity reflecting the influence of thermal motions which cause there to be an almost equal probability of finding an atom at any distance. The $g(r)$ for gases increases from zero at distances below a minimum intermolecular separation to unity at distances above this value.

This profile reflects the absence of structural ordering other than that imposed by the atoms not overlapping.

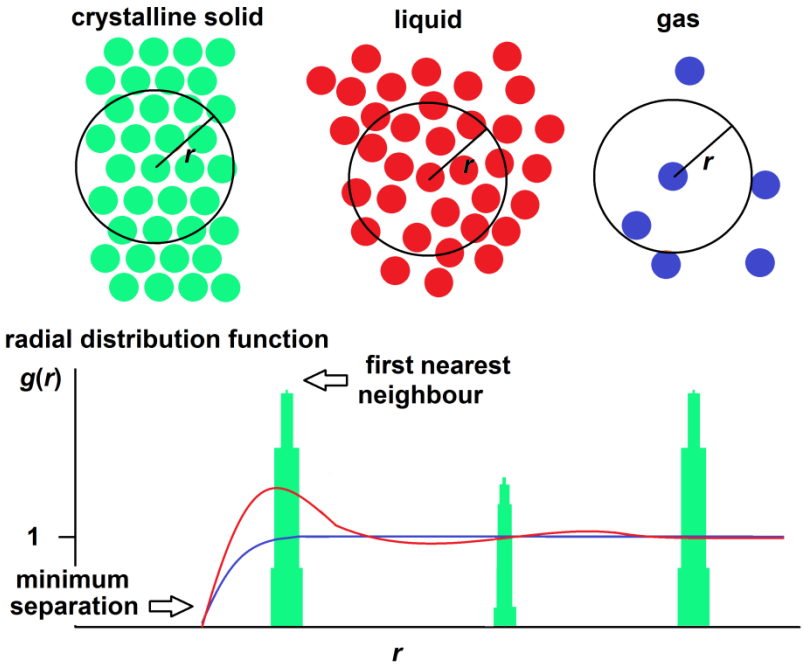

Figure 1.6 Schematic illustration of the radial distribution function, $g(r)$, for a monoatomic crystalline solid (green), liquid (red) and gas (blue).

1.1.5 NEUTRON DIFFRACTION FOR STRUCTURAL ANALYSIS OF LIQUIDS

The $g(r)$ of amorphous material such as liquids can be obtained from total scattering measurements using either X-rays or neutrons. This study has primarily used neutron diffraction and a brief introduction to the technique is provided here. More thorough treatment of the subject is given elsewhere.[115-117] The interaction between a neutron and nucleus, α, is described by a scattering length, b_α. Due to their small size, nuclei act as isotropic point scatterers. Positive scattering lengths correspond to repulsive nuclei potentials and negative scattering lengths correspond to attractive nuclei potentials. b^2, referred to as a cross section, corresponds to the effective area presented by a nucleus to an incident neutron. The overall scattering from an arrangement of atoms with different scattering lengths may be described by a scattering law, first proposed by van Hove. The equation given as equation 1.5, shows how the variation in scattered intensity, I, with

wavevector transfer, Q, and energy transfer, ϵ, is related to the scattering-length-weighted sum of the space and time Fourier transform of the time-dependent radial distribution functions for the constituent atoms pairs, $g_{\alpha\beta}(r, t)$. N is the number of atoms, h is Planck's constant and k and k' are the wave vectors of the incident and scattered neutrons, respectively. For zero energy transfer, Q the wavevector transfer, is a function of the scattering angle θ and the neutron wavelength, λ, *via* $Q = 4\pi\sin\theta/\lambda$. The $g_{\alpha\beta}(r, t)$ functions shown here are equivalent to Dirac delta functions with a probability of 1 at the interatomic distance (and time) and zero at other distances (and times); when summed over the many atom pairs present in the material they describes a time dependent-pair correlation function. For diffraction, equation 1.5 is evaluated at $t = 0$.

$$I(Q,\epsilon) = \frac{1}{h}\frac{k\prime}{k}\sum_{\alpha,\beta,i} b_\alpha b_\beta \int_{-\infty}^{\infty} g_{\alpha\beta}(r,t)\, e^{-iQr} e^{-i\epsilon t}\, d^3r\, dt.$$

Equation 1.5

In addition to the general form of the equation whereby the $g(r)$ and $I(Q)$ are related by a Fourier transform (FT), it is also significant that the scattering lengths are outside of the integral and that the sum is over all atom pairs including self-pairs ($\alpha\alpha$ and $\beta\beta$). The scattering length of a nucleus is determined by the element, the isotope and also its nuclear spin state. To dissect a scattering pattern into contributions from the different atom types contained within the sample it is necessary to consider two different spin/isotope averages. In addition to the average scattering length, $\langle b\rangle$, which allows $b_\alpha b_\beta$ combinations to be described, the average of the scattering length squared, $\langle b^2\rangle$, is also needed to account for $b_\alpha b_\alpha$ atom pair combinations, the so called self-scattering of the sample. This leads to two different scattering lengths of an element or isotope: the coherent scattering length, $b_{coh} = \langle b\rangle$, and the incoherent scattering length, $b_{inc} = \sqrt{(\langle b^2\rangle - \langle b\rangle^2)}$. Due to the dependence of these on the average of the spin states of the individual nuclei, b_{coh} and b_{inc} do not vary consistently across the periodic table. Most significantly for this report for hydrogen, b_{coh} is negative (–3.74 fm) and b_{inc} is relatively large (25.18 fm); and for deuterium, b_{coh} is relatively large and positive (+6.67 fm) and b_{inc} is relatively small (3.99 fm). A complete list of scattering cross sections has been given most recently by Sears.[118]

A characteristic scattering pattern for a hypothetical diffraction experiment (t=0) is given in Figure 1.7. The *I(Q)* is shown in units corresponding to the differential scattering cross section (DCS) which indicates the variation in cross section (barns, b) normalised by the solid angle ($1/4\pi$, steradians^{-1}) and the number of atoms in the neutron beam (atom^{-1}). The average DCS level obtained is $\langle b^2 \rangle$. It can be separated into contributions from incoherent, $\langle b^2 \rangle - \langle b \rangle^2$, and coherent scattering $\langle b \rangle^2$. The interference features are superimposed on the coherent scattering part. The total structure factor, *S*, is defined here as the DCS normalised by $\langle b \rangle^2$ after subtraction of $\langle b^2 \rangle - \langle b \rangle^2$. The total structure factor is also commonly defined[114] as the DCS after subtraction of the average scattering level, $I(Q) - \langle b^2 \rangle$, which is available more directly for materials with unknown composition. In the present study, this function is called the total interference function, $F(Q) = I(Q) - \langle b^2 \rangle$.

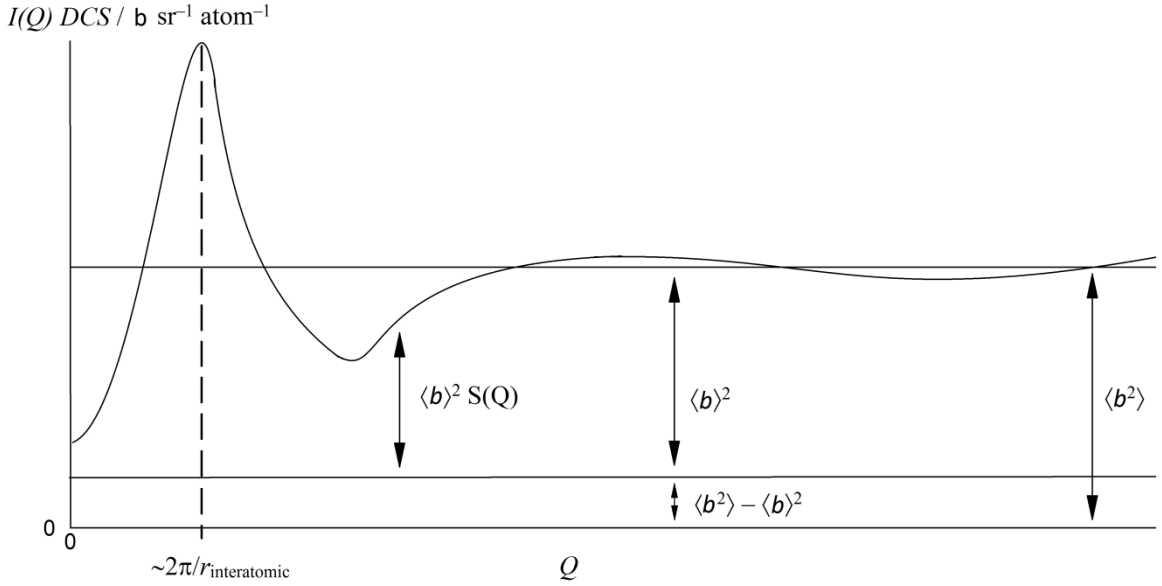

Figure 1.7 Schematic illustration of a characteristic differential scattering cross section (DCS) of a hypothetical liquid. The separation of the DCS into a total structure factor, $S(Q)$, coherent, $\langle b \rangle^2$, and incoherent, $\langle b^2 \rangle - \langle b \rangle^2$ cross sections are indicated by the arrows. Reoccurring peaks in the DCS may loosely be related to interatomic distances by ~$2\pi/r$. Image adapted from Fischer et al..[117]

The $F(Q)$ obtained by neutron diffraction is the sum of the interferences produced by different atom pairs present in the material weighted by their scattering lengths, and may be separated into the interference features produced by different pairs of atom types according to Equation 1.6.[114] *A* and *B* correspond to the different atom types, c_A and c_B are their atomic mole

fractions, $b_{\text{coh-A}}$ and $b_{\text{coh-B}}$ are their coherent scattering lengths and $s_{AB}(Q)$ are the Faber-Ziman partial structure factors. As indicated by equation 1.7 the $F(Q)$ is related to a total radial distribution function, $G(r)$, by an FT. Equation 1.8 shows that the $G(r)$ is comprised of the weighted sum of individual partial radial distribution functions, $g_{AB}(r)$. The same FT relationship (equation 1.7) may be used to interconvert partial structure factors ($S_{AB}(Q)$–1) and partial radial distribution functions, ($g_{AB}(r)$–1).

$$F(Q) = \sum_{A,B}^{n} c_A\, c_B b_{coh\,A} b_{coh\,B} [S_{AB}(Q) - 1]$$

Equation 1.6

$$G(r) = \frac{1}{(2\pi)^3 \rho} \int_0^{\infty} 4\pi Q^2\, [F(Q)] \frac{\sin Qr}{Qr}\, dQ$$

Equation 1.7

$$G(r) = \sum_{A,B}^{n} c_A\, c_B b_{coh\,A} b_{coh\,B} [g_{AB}(r) - 1]$$

Equation 1.8

The summative way in which interference produced from different pairs of atom types may be combined is experimentally significant as it allows significant simplifications to be sought by isotopic substitution. This approach, called the isotopic difference technique,[119-120] involves substituting atoms within a material with isotopes of different scattering length. Assuming the isotopic composition has no impact on structure,[121] and that the scattering lengths are sufficiently different, the interference is perturbed by the substitution and by subtracting several datasets the number of atom types contributing to the interference may be reduced. With sufficient scattering length contrast the $S_{AB}(Q)$, and hence also the $g_{AB}(r)$, for the different atom pairs may be extracted. For a material comprised of n atom types there are $m = n(n+1)/2$ distinct atom pairs. To extract all the $g_{AB}(r)$ using the isotopic difference technique m datasets with scattering length contrast on each atom type are required.[122] Although this would appear to be a very powerful approach for the

structural analysis of amorphous materials, the signal to noise ratio decreases when many data sets are combined and the range of available isotopes with significantly different scattering lengths is limited. This causes many of the systems of interest to fail to meet these scattering length contrast criteria (*i.e.* the problem remains somewhat under-determined).

In addition to the use of neutron scattering to study the pairwise distance distribution of materials, as suggested by equation 1.5, the technique may also be used to carry out spectroscopic analysis of energy transfer. The instruments used for these spectroscopic measurements typically select a range of neutron energies. By examination of coherent inelastic data ($\varepsilon \neq 0$) information about the collective motions of the atoms may be obtained and by examination of incoherent inelastic data the diffusion of single species in the liquid matrix may be studied. Unfortunately, for some systems, it is very difficult to entirely uncouple the energy and momentum transfers which are associated with spectroscopic and diffraction measurements, respectively. The extent of the perturbation to diffraction data caused by unavoidable inelasticity can be understood by considering how effectively equation 1.5 may be evaluated at $t=0$ using neutrons of a particular energy (for totally elastic $t=\infty$). For $t=0$ diffraction corresponds to the 'static approximation' whereby the diffraction pattern obtained is the average of many instantaneous 'snapshots', each seemingly recorded from an independent quanta of neutron radiation. The $t=0$ static approximation applies, and the data is essentially unperturbed, when the energy transfer for the scattering process is much smaller that the energy of the incident photon. Whilst short wavelength neutrons and X-rays typically employed travel quickly and therefore allow diffraction at close to $t=0$, slower long wavelength neutrons allow a greater t interval between scattering centres and inelasticity may give rise to data perturbations. The static approximation also becomes increasingly invalid for more dynamic (less static) materials, such as solids containing very light atoms, as a greater degree of structural change occurs during the t interval. A useful analogy is 'blurring' in photographic images which may be reduced by a faster shutter speed (fast short wavelength neutrons) and static subjects (heavy atoms). The incomplete validity of the static approximation in total scattering neutron measurements of materials containing hydrogen erroneously affects the calculated values of Q,

causing a perturbation to the diffraction data which needs to be subtracted before EPSR structural modelling can carried out.

The measurements reported in the present study were carried out on the Small Angle Neutron Diffractometer for Liquids and Amorphous Solids at the pulsed spallation source at ISIS (Didcot, UK). This time of flight spectrometer was designed to reduce the influence of 'inelastic perturbations' by having detectors only over low scattering angles between 3.9 and 39°. Furthermore as the inelastic perturbation solely affects the background scattering levels and not the interference features, it is possible to estimate and subtract the 'inelastic perturbations' to SANDALS data using the *GudrunN* software. For this procedure, the perturbation is estimated by 'binning' the scattered intensity as a function of neutron wavelength (averaged over the trajectory before and after impinging on the sample) to obtain a general form of the perturbation (interference features only appear when merged on a *Q* scale) and then refining this estimate iteratively by subtracting estimates of the interference features. The inelasticy corrections applied to SANDALS data are described more fully by Soper.[123]

1.1.6 Empirical Potential Structural Refinement

Empirical potential structural refinement (EPSR) software is a Metropolis Monte Carlo based technique used to produce 3D structural models of molecular systems consistent with neutron diffraction data collected using the isotropic difference technique. A brief discussion of its merits is given below; and more thorough descriptions are given by Soper.[6] EPSR has been used to prepare structural models of liquid water,[21,124] THF,[125], methanol,[119], DMSO water mixtures,[126] DMSO,[105] acetone,[105] concentrated hydroxide solutions,[127-128] and to study the crystallisation of benzoic acid.[129] In the present study, it has been used to produce structural models of liquid chloroform and the chloroform-acetone azeotrope.

In many ways, EPSR can be viewed as a combination of the Metropolis Monte Carlo simulation technique and the isotopic difference neutron diffraction technique. Essentially, EPSR derives a perturbation to the force field from the difference between the measured diffraction data

and data simulated from a Monte Carlo simulation (using the reference potential given as Equation 1.2). These additional empirical potentials (EPs) then drive the Monte Carlo simulation toward structural convergence with the diffraction data. Impressively, by combining the two different approaches, specific difficulties associated with each are largely avoided. The inadequacies and inaccuracies of the force field used in classical Monte Carlo simulation described in section 1.1.4 are corrected by the additional EPs and for undetermined systems (lack of scattering length contrast) the ability to isolate partial structural factors from a series of total structure factors (or partial radial distribution functions from total radial distribution functions) is dramatically improved. This mutual symbiotic relationship is facilitated by the way in which the diffraction data are separated into partial structure factors and the way in which the EPs are derived.

EPSR isolates partial structure factors in underdetermined systems using pair distances from the simulated model structure to substitute for those not available from the experimental datasets. This estimate of the unknown partial structure factors then allows estimates of the complete set of partial structure factors to be obtained. During iterations of the model under the Metropolis condition the accuracy of the structure, and thus also the estimates of the partial structure factors, improves. EPSR produces the EPs by considering the difference between simulated and estimated partial structure factors. The EPs have the form of power exponential functions (given by Soper[6]). These provide a good representation of an intermolecular potential whilst smoothing the statistical noise and artefacts of the measurement which otherwise would be transferred into the structural model. Importantly the EPs may be negative or positive and at low r can vary rapidly with distance. This allows the inadequacies of the reference force fields to be overcome, enabling the model structure to better fit experimental data than for classical Monte Carlo simulations.

Although, structural models may be produced by EPSR which are consistent with diffraction data, it is difficult to quantify the certainty with which the simulated structure represents the materials true ‘correct’ structure. The diffraction data essentially constrains the structural model, with more datasets and greater scattering length contrast providing more constraining

influence. Unlike many techniques, where convergence is indicative of success, in EPSR the simulation is much more likely to converge if the number of neutron data sets constraining the structural model is reduced. Assessing the quality of diffraction data as constraints to a structural model of molecular liquids is a complex problem. Although, it is true that the pairwise data may be reproduced by many different arrangements within the simulation box and thus that no unique solution is truly possible, it can be argued that, from a statistical thermodynamics viewpoint, for models containing a large number of molecules the probability of any particular solution being greatly different from the most likely or 'correct' solution is small. [130-131]

For under-determined systems, the certainty in the 'correctness' of the structural model will be less than for fully determined systems. In designing an experiment for EPSR analysis it is important to recognize that EPSR can provide no measurement derived 'push' to molecules containing no substituted atom positions. Conversely, for partially under-determined systems, for which every molecule type has at least one atom with scattering length contrast, the constraining influence of the data may be much greater than expected. This is because the radial distribution functions, and hence also the partial structure factors, of atoms pairs not isotropically substituted are constrained in EPSR indirectly by their covalent connection to substituted atom types. Considering this, the operations which should be most constrained are dependent on the shape and symmetry of the molecules. For the EPSR simulations of pure liquid chloroform and the chloroform-acetone azeotrope carried out in this study H/D substitution has been carried out. The weightings for the differently substituted liquids measured are given in Appendices 10 (chloroform), 11 (chloroform-acetone azeotrope) and 12 (benzene-methanol azeotrope).

2 Materials and Methods

2.1.1 Materials

Ultrapure H_2O (Milli-Q, Millipore) was used throughout. D_2O was purchased from Sigma Aldrich who report a D/H isotopic purity > 99.9 atom %. H_2O and D_2O used to prepare ASW were degassed by three freeze, evacuate (1×10^{-2} mbar), thaw cycles. C_{60} with purity > 99.9 % was obtained from MERcorp (Tuscon, Arizona, USA) and used without further purification. Liquid nitrogen (LN_2), nitrogen and argon gases were provided by BOC. The protiated chloroform ($CHCl_3$), acetone (C_3H_7O), benzene (C_6H_6) and methanol (CH_3COH) solvents were HPLC grade (CHROMOSOLV, Sigma-Aldrich) with reported purity > 99.9 %. The deuterated chloroform ($CDCl_3$), acetone (C_3D_7O), benzene (C_6D_6) and methanol (CH_3COD and CD_3COH) were also purchased from Sigma Aldrich who report a D/H isotopic ratio > 99.5 atom %. The chloroform liquids contained small amounts (200 ppm) of amylenes (C_5H_{10}) as a chemical stabiliser. Absolute ethanol was used for the optical absorbance measurements. Indium metal (99.99 %) used to line the pressure dies was purchased from Alfa Aesar and rolled into thin sheets (~0.5 mm) using a steel rod.

2.1.2 Pumping-Rate Calibration of Chamber Pressure

The apparatus for the preparation of ASW/C_{60} trapped solutions is described in detail in Chapter 3. Here, I detail experimental procedures for its use. The variation in pumping rate with chamber pressure, *pmp*(*p*), was estimated by measuring changes in chamber pressure which occurred whilst inletting N_2 gas into the vapour deposition chamber through a graduated needle valve (EV 016 DOS AB, Oerlikon Leybold Vacuum) at different rates. The chamber pressure was first reduced to a base pressure of $<1\times10^{-6}$ mbar using the same procedure used to prepare the chamber for deposition described below, and the N_2 leak rate was then increased by changing the position of the graduated needle valve from 0 to 300 in steps of 10. Interpolation (Labview, version 6) was used to relate the chamber pressures to leak rate data supplied with the needle valve (Figure 3.3a).[132]

2.1.3 Deposition of Water Vapour and C_{60}

To prepare the deposition apparatus the copper deposition plate was first cleaned with water, 'sandpaper' (aluminium oxide, 80 μm grit) and ethanol solvent, to remove the copper oxide layer. The plate was then installed in the vapour deposition apparatus by attaching it to the deposition stage. The arrangement is shown in Figure 3.4 and as a scale drawing in Appendix 3. The inlet flask was then weighed on a balance to 0.01 g precision. The crucible was filled with C_{60} and weighed on a balance to 1 mg precision. The pressure in the chamber was then reduced in several sequential stages. Data showing the decrease in chamber pressure together with decreases in the temperature of the deposition stage are given as Appendix 2. First, the chamber pressure was reduced to ~1×10^{-2} mbar using a rotary vane pump (model 12, BOC Edwards). A two way tap was then adjusted to switch from actively evacuating the chamber to evacuation of the diffusion pump (Diffstack 63, BOC Edwards, Crawley, UK). A LN_2 baffle was then filled reducing the pressure within the chamber to ~5×10^{-4} mbar. After ~20 min a butterfly valve above the diffusion pump was then opened, reducing the chamber pressure to ~1×10^{-6} mbar. The LN_2 cooling was then initiated by activating a second rotary vane pump (Sogevac SV16, Oelikon Leybold Vacuum) and opening its choking tap. The temperature of the deposition plate decreased to 80 K in ~30 min further reducing the pressure to < 1×10^{-6} mbar. The deposition of water vapour was started by opening the graduated needle valve to give a desired inlet pressure and the C_{60} deposition was started by adjusting the variable transformer to give a desired filament current. The approximate variation in crucible temperature with transformer voltage and the variation in C_{60} vapour pressure with temperature from the measurements of Mathews *et al.*[133] are provided as Appendix 4. The stability of C_{60} to the deposition conditions was confirmed by solid state NMR. The spectra are given in Appendix 5.

2.1.4 Measurements of H_2O, D_2O and C_{60} Chamber Dose Rates

The variation in H_2O, D_2O and C_{60} chamber dose rate with inlet pressure and filament current were measured by monitoring decreases in the weight of the water flasks and C_{60} crucible after depositions carried out for inlet pressures (Pirani sensor calibrated for air) between 0.02 and 0.20 mbar and filament currents between 17.0 and 24.0 A. To obtain data for low inlet pressures and filament currents the deposition time was extended to give a total H_2O chamber dose > 0.1g and total C_{60} chamber dose > 0.001 g giving an uncertainty < 10 %. The dose rate data for H_2O and D_2O were fitted to quadratic functions ($y = 0.15x + 1.32x^2$ for H_2O and $y = 0.13x + 1.30x^2$ for D_2O) and the data for C_{60} were fit to an exponential function ($y = 2\times10^{-12}\exp(0.7x)$. The dose rates were also measured for each deposition carried out and the C_{60} concentration of the ASW/C_{60} 'trapped solutions' reported throughout the thesis correspond to the molar ratio of H_2O and C_{60} chamber dose.

2.1.5 Measurements of H_2O and C_{60} Dosing Trajectory

A series of optical absorbance measurements were carried out to investigate the angular dependence of H_2O and C_{60} flux (dosing trajectory). In order to sample different trajectories 7 copper discs with a diameter of 1 cm and thickness of 6 mm were fitted to the deposition plate with internal grub screws. Five repeat deposition experiments were carried out using the co-deposition base plate (shown as Appendix 5), a 5 h deposition time and an aperture–deposition plate distance of 9.4 cm to give an average H_2O dose rate of 0.196 g h^{-1} and an average C_{60} dose rate of 0.0054 g h^{-1}. For each deposition, the copper discs were recovered under LN_2 and placed into small volumes (5 ml) of absolute ethanol. The concentration of C_{60} and water in the ethanol were then determined by comparing the absorbance of UV (C_{60} at 330 nm) and NIR (H_2O at 1950 nm) peaks for a dilution series prepared from the ethanol-water-C_{60} mixture with the absorbance of standards, prepared with known concentrations of H_2O and C_{60}. A Perkin Elmer Lambda 900 spectrometer and quartz cuvettes were used to record the spectra. To model the variation in H_2O and C_{60} flux, y, with trajectory, x, the data were fitted to Gaussian amplitude functions [$y = a\exp(x/2b)$] (OriginPro

8.0). To estimate the yield and the average composition for different aperture-deposition plate distances and dosing rates the fitted functions were integrated over limits corresponding to material impinging on the plate. The error estimates quoted were calculated by combining the individual errors for *a* and *b* fitted parameters.

2.1.6 H_2O Desorption Rate analysis of ASW Growth

To probe factors affecting ASW's growth, the chamber pressure and deposition plate temperature were recorded as ASW samples prepared using different deposition conditions were heated in the deposition apparatus from 80 K to 180 K. ASW was either deposited at 0.40 g h^{-1} to different thickness by adjusting the deposition time to give total chamber dose between 0.1 and 2.3 g, or deposited at different rates between 0.2 and 5.8 g h^{-1} and for different times to give total chamber dose of 1.0 g. These experiments employed the ASW baseplate, in which the H_2O inlet is centrally placed, and an aperture deposition plate distance of 20 cm. After each deposition had completed the LN_2 flow cooling the deposition plate was stopped causing the deposition plate to warm. After the temperature had reached 180 K the deposition plate was recooled to 80 K and allowed to warm to 180 K a second time. The H_2O desorption rate (adjusted for readsorption) was calculated from the measured chamber pressure by its interpolation with *pmp*(*p*) (Labview, version 6).

2.1.7 Solid State NMR Analysis of C_{60} Stability

The stability of C_{60} towards oxidation during its co-deposition with H_2O was investigated by solid-state nuclear magnetic resonance (SSNMR) carried out at the EPSRC UK National Solid-State NMR Service at Durham. A 100.56 MHz Varian VNMRS spectrometer was used to record ^{13}C spectra of the raw C_{60} material as obtained from MERcorp and the C_{60} material recovered after evaporation of the H_2O from a co-deposited ASW/C_{60} sample (H_2O dose rate = 0.2 g h^{-1}, C_{60} dose rate = 0.015 g h^{-1}, deposition time = 5 h, aperture deposition plate distance = 9.4 cm). The spectrometer employed a magic-angle spinning probe with rotor outer diameter of 4 mm and spectral referencing was with respect to an external sample of neat tetramethylsilane, carried out by

setting the high-frequency signal from adamantane to 38.5 ppm. Spectra were obtained using direct excitation with a 30 s recycle delay, an ambient probe temperature and a sample spin-rate of 8 kHz. The reported spectra (Appendix 5) are for ~100 accumulations.

2.1.8 X-ray Diffraction of ASW/C_{60} 'Trapped Solutions'

The ASW/C_{60} 'trapped solutions' produced for structural analysis by X-Ray diffraction (XRD) were deposited onto circular single crystal silicon discs with a diameter of 16 mm and a thickness of 2 mm which were cut in the (511) plane and gave no background reflections. The apparatus used to secure the substrates to the deposition plate is shown in Figure 3.9. A H_2O deposition rate of 0.2 g h^{-1}, a total deposition time of 5 hours and an aperture to deposition plate distance of 9.4 cm were used. The filament current was varied to give 'trapped solutions' with X_{C60} = 0.0006, 0.0014 and 0.0028 (X_{C60} is assumed to be equal to the molar ratio of H_2O and C_{60} chamber dose). To record XRD patterns the coated silicon discs were placed into a purpose built copper sample holder under liquid nitrogen, which was then quickly transferred to a cold (90 K) XRD cryostat (TTK 450, Anton Paar, Graz, Austria). A membrane pump (Jun-Air/GAST, Norresundby, Denmark) able to provide a ~5 L h^{-1} LN_2 flow rate and a flow controller (Oxford Instruments, Abingdon, UK) were used to cool the cryostat.

The temperature of the cryostat was measured by a temperature probe positioned inside the copper sample holder directly below the coated substrates. The accuracy of the probe to determine the temperature at the surface of the substrates was determined to be to ± 5 K from the cell parameters of a mixed sample containing crystalline aluminium found by Rietveld refinement (TOPAS-Academic version 4.1, Alan Coelho).[134-135] After loading the coated substrates the internal pressure in the cryostat was immediately reduced by evacuating the cryostat to 1 mbar using a rotary vane pump (model 5, BOC Edwards). The diffractometer (D8 Advance, Bruker AXS, Karlsruhe, Germany) was equipped with a copper tube, nickel filter and semiconductor strip detector (LynxEye, Bruker AXS) and operated in Bragg-Brentano (reflection) geometry. Patterns were first recorded at 90 K over a 2θ range of 10–60° using a step size of 0.02055° and a counting

time of 1.17 s per step. The samples were then heated in the cryostat by stopping the LN_2 cooling. This gave a non-linear heating rate which was ~2.4 K min^{-1} at 160 K. As the crysostat warmed patterns were recorded over a 2θ range of 12–52°, using a step size of 0.02055° and a counting time of 0.036 s (~70 s per scan).

2.1.9 FT-IR Spectroscopy of ASW and ASW/C_{60} 'Trapped Solutions'

To collect Fourier transform infrared (FT-IR) spectra of ASW and ASW/C_{60} 'trapped solutions' thin films were deposited onto circular MgF_2 substrates with a diameter of 15 mm and a thickness of 2 mm using a H_2O/D_2O dose rate of 0.4 g h^{-1}, a total chamber dose of 0.4 g and an aperture–deposition plate distance of 20 cm. For the 'trapped solutions' the filament current was varied to give samples with X_{C60} = 0.0040 and 0.0208. The water used to prepare these samples was substituted with 5 mol% D_2O giving ASW samples comprised of ~91.0 mol% H_2O and ~9.0 mol% HDO. This approach enabled uncoupled OD-stretching-related absorptions to be recorded. After deposition, the coated substrates were recovered into LN_2 and transferred into an Oxford Microstat^N cryostat fitted with two MgF_2 windows and cooled to 78 K by a flow of LN_2. A sprung clip ensured good thermal contact between the substrate and the cryostat body. The apparatus used to reduce the temperature and pressure of the cryostat was the same as used for the XRD measurements described above although a lower flow rate of 1 L h^{-1} was required to maintain the temperature at 78 K.

The temperature of the cryostat was measured using a resistance probe internal to the housing of the cryostat. Spectra were recorded in transmission using an ATI Mattson Research Series 1 spectrometer with a spectral resolution of 4 cm^{-1}. The spectra recorded at 78 K were produced from 512 summed scans (~5 min), and spectra recorded as the cryostat warmed from 78 K to 180 K were each produced from 32 summed scans giving a time interval between scans of ~30 s. To thermally anneal the samples the cryostat was heated to a specified temperature using the internal heating element, maintained at that temperature for a given time (0 s, 4 min or 2 hours) and then recooled to 78 K. To record spectra as the cryostat warmed from 78 to 180 K the LN_2 cooling

was stopped and the temperature of the cryostat allowed to increase. This approach gave a non-linear heating rate which was ~5 K min^{-1} at 160 K. In addition to these spectra of ASW and ASW 'trapped solutions', FT-IR spectra were also recorded of room temperature liquid water (91.0 mol% H_2O and 9.0 mol% HDO) trapped between two MgF_2 discs and ice I_h which formed upon cooling the water trapped between the discs from room temperature to 78 K.

To convert the raw spectral data onto an absorbance scale a background spectrum was recorded at 78 K after evaporating the ice at 260 K. To account for the attenuation caused by the ASW films the intensity of the background spectrum was scaled to give zero absorbance at 2700 cm^{-1}. Peak fitting (OriginPro 8.0) was used to follow changes in the position and width of the OD related absorption. This involved subtracting a linear baseline between 2280 cm^{-1} and 2600 cm^{-1}, and then fitting the spectral range between 2385 and 2550 cm^{-1} with either 1 or 2 (indicated in text) pseudo-Voigt peaks.

2.1.10 Raman Spectroscopy of ASW and LDAs Formed from HDA

Raman spectra of ASW, unannealed high density amorphous ice (uHDA), very high density amorphous ice (vHDA),[136-137] expanded high density amorphous ice (eHDA) and the LDAs formed from the HDA samples were recorded on a Renishaw Ramascope spectrometer (632.8 nm) using the same cryostat employed for FT-IR but equipped with a single fused silica window and a solid cryostat body without a sprung clip. To ensure a good thermal contact between the ice samples the cryostat body was pre prepared with a thin indium plate which was pressed (Hypress 30 tonne shop press equipped with a powerteam P59B 700 bar hydraulic pump) onto the copper cryostat body with a moderate force. The ice samples were then transferred into the cryostat under LN_2 and pushed into this soft substrate using a 'hand-held' cooled steel piston.

The ASW used for this analysis was formed from a H_2O deposition rate of 0.4 g h^{-1}, a 1 h deposition time and an aperture deposition plate distance of 20 cm. It was recovered from the surface of the deposition plate into LN_2 and stored in an aluminium sample container. uHDA was prepared by compressing 0.6 g of ice I_h at 77 K to ~1.7 GPa (11 tonnes or 93100 N) in an indium

lined pressure die (Specac 9 mm). The I_h to HDA transition was indicated by sudden decreases in pressure at ~1.46 GPa which is slightly greater than the pressure of 1.2 GPa reported by Mishima.[62-63] To ensure homogenous HDA samples the pressure was increased gradually to the maximum pressure over 10 min and maintained under pressure for a further 10 min. To recover uHDA the pressure was released gradually to ambient and the material recovered under LN_2. To prepare eHDA the pressure of the uHDA was reduced to 0.3 GPa and the material was then heated from 77 to 130 K. To prepare vHDA the pressure of the uHDA was reduced to 1.4 GPa and the material was then heated from 77 to 155 K (at 1.4 GPa crystallisation was found to occur at ~173 K[138-139]). Once the target temperatures had been reached the eHDA and vHDA samples were quenched and recovered at ambient pressure under LN_2.

The different HDA samples were converted to LDA in the cryostat by slowly heating the samples whilst monitoring the spectral changes associated with the transition. The samples were held at the transition temperature (~110 K for HDA, ~118 K for vHDA, and ~122 K for eHDA)[140-141] for 2 minutes and then recooled to 80 K. For annealing, the cryostat was heated at ~5 K min^{-1} from 78 K to a given annealing temperature and then immediately cooled back to 78 K. The spectra shown are for 4 accumulations collected from a variable grating scan between 3800 and 2900 cm^{-1} for a time period of 60 s. The Raman shift was calibrated using the emissions of a neon lamp, a linear background was subtracted and the spectra were normalised by the maximum intensity at ~3100 cm^{-1}.

2.1.11 Raman Spectroscopy of Chloroform and Acetone Liquids

Raman spectra of acetone and chloroform liquids as well as the azeotropic liquid mixture ($X_{acetone}$ = 0.405) were recorded on samples contained in 2 mm quartz capillaries using a Renishaw Ramascope spectrometer (632.8 nm). In addition to the protiated liquids, several liquid mixtures containing deuterium were measured. This procedure enabled changes in the shape of overlapping acetone and chloroform C-H related absorptions which occurred upon mixing the pure liquids to be investigated independently. The liquid compositions measured were: (1) 38.5 mol% of

CD_3COCD_3, 2.0 mol% of CH_3COCH_3 and 59.5 mol% of $CDCl_3$ (2) 95.0 mol% of CD_3COCD_3 and 5 mol% of CH_3COCH_3, (3) 40.5 mol% of CD_3COCD_3, 56.5 mol% $CDCl_3$ and 3.0 mol % $CHCl_3$, (4) 95.0 mol% $CDCl_3$ and 5 mol% $CHCl_3$. Spectra of the protiated liquids were produced from 4 accumulations of variable grating scans between 4000 and 50 cm^{-1} using a time interval of 10 s. Spectra of the deuterated liquid mixtures were produced from 4 fixed grating scans centred at 3000 cm^{-1} and accumulated for 100 s. The Raman shift was again calibrated using the emissions of a neon lamp.

2.1.12 Optical absorbance and Photoluminescence of ASW/C_{60} 'Trapped Solutions'

The ASW/C_{60} 'trapped solutions' used to record optical absorbance and photoluminescence spectra were deposited onto the same circular MgF_2 substrates used for FT-IR. A H_2O dose rate of 0.4 g h^{-1}, a 1 h deposition time and an aperture to deposition plate distance of 20 cm were used. Two different C_{60} dose rates were investigated giving 'trapped solutions' with X_{C60} = 0.0010 and 0.0029. For each deposition two substrates were fitted to the deposition plate and coated with sample. The first was used to record optical absorbance and the second was used to record photoluminescence. As for FT-IR, the substrates were recovered into liquid nitrogen, transferred into the cold cryostat (78 K) fitted with two MgF_2 windows and held in place with a sprung clip. Optical absorbance spectra were recorded between 180 and 800 nm using an integration time of 0.32 s on a Lambda 950 spectrometer. Photoluminescence spectra were recorded using the same Renishaw Ramanscope spectrometer used to record Raman spectra which provided a fixed 632.8 nm excitation. Spectra were recorded over a Raman shift range between 50 and 6000 cm^{-1} (635.82–1020.1 nm) using a variable grating scan with a 20 s time interval. Optical absorbance and photoluminescence spectra were recorded at 78 K after being heated to sequentially higher temperatures and also at the elevated annealing temperature. The heating and cooling rate was ~5 K min^{-1} and the time spent at the annealing temperature during spectral acquisition was ~5 min.

2.1.13 Neutron Diffraction of ASW and ASW/C_{60} 'Trapped Solutions'

The ASW and ASW/C_{60} 'trapped solutions' prepared for structural analysis by neutron diffraction were deposited using the codeposition baseplate, an aperture deposition plate distance of 20 cm, a H_2O, D_2O or H_2O:D_2O (1:1) dose rate of 0.4 g h^{-1} and a ~5 h deposition time giving a total chamber dose of ~2 g. For trapped solutions the current passed through the crucible filament was varied to give X_{C60} between 0.0065 and 0.0034. The compositions of the 9 samples (estimated using the measured chamber doses) are given in Appendix 7. Before recovering the samples into LN_2 they were thermally annealed *in situ* by allowing the temperature of the deposition plate to increase to 105 K and then immediately cooling it back to 80 K. For a deposition stage temperature of 105 K the surface of these thick deposits is estimated to be ~115 K. This procedure was expected to be sufficient to fully anneal and relax the ASW structure.[142] For the diffraction measurements the samples were transferred under liquid nitrogen into $Ti_{0.68}Zr_{0.32}$ sample containers with dimensions of 2.0 × 3.8 × 3.8 mm (2.88 cm^3). The sample containers were then attached to an aluminium rod under liquid nitrogen and transferred into the measurement cryostat of the diffractometer at 77 K. The packing fractions calculated from the average DCS using an atom number density of 0.094067 atom A^{-3} are given in Appendix 7.

The Small Angle Neutron Diffractometer for Liquids and Amorphous Solids (SANDALS) at the pulsed neutron facility of the Rutherford Appleton Laboratory in the UK (Didcot, UK) was employed for these measurements. This instrument has detectors at angles between 3.9 and 39° and an available *Q*-range between 0.1 and 50 $Å^{-1}$. For each of the 9 samples, time-of-flight scattering data was collected for > 1000 μA h of proton current. In addition to data recorded at 77 K the ASW/C_{60} 'trapped solution' containing a D_2O ASW matrix and a X_{C60} of 0.0034 was heated from 77 to 180 K at 0.4 K min^{-1}. For this variable temperature experiment scattering data were accumulated over 10 min time intervals (~25 μA h). Background subtractions and corrections for absorption and multiple scattering were carried out using the *GudrunN* software package (*GudrunN*, version 4) and background data for the empty cryostat and empty sample containers in

the cryostat at 77 K. The absolute DCS levels were calculated using a vanadium calibration and were adjusted for microporosity and the incomplete packing of the materials in the sample containers assuming an atom number density unchanged from that of ASW, 0.094067 atom $Å^{-3}$. The *iterate Gudrun* subroutine with minimum intermolecular separation of 0.75 Å and smoothing parameter of 0.5 was used to estimate and subtract the perturbation to the data caused by inelastic collisions (correction not applied to variable temperature data). The 77 K DCS data corrected for attenuation and multiple scattering are given in Appendix 8. The 77 K DCS data corrected for attenuation, multiple scattering and inelasticity are given in Appendix 9. The $G(r)$ data of H_2O samples found to be free of crystalline ice contamination were calculated by Gudrun as the Fourier transform (FT) of the interference function, $F(Q)$, formed by subtracting the average scattering level. Termination ripples were removed using Lorch smoothing ($g(r)$ broadening of 0.1Å at r = 1 Å and a broadening power of 0.5) and the $G(r)$ data shown were normalised by their negative intensity at 0.95 Å.

2.1.14 Neutron Diffraction of Chloroform, Chloroform-Acetone, Benzene-Methanol Azeotropes

The structure of chloroform liquid, and the room temperature chloroform-acetone ($X_{acetone}$ = 0.405)[97,102] and benzene-methanol ($X_{methanol}$ = 0.550)[98-100] azeotropes were investigated in a series of neutron diffraction measurements carried out on SANDALS. These measurements employed $Ti_{0.68}Zr_{0.32}$ sample containers with smaller internal dimensions of 1.0 × 3.8 × 3.8 mm (1.44 cm^3). A water bath was used to maintain the temperature of the evacuated measurement chamber at 25 °C and an automated sample changer was used to switch between different sample containers. For each system, liquids with different H/D isotopic composition were measured: three for chloroform liquid, 7 for the chloroform-acetone azeotrope, and 9 for the benzene-methanol azeotrope. The isotopic compositions and corresponding neutron weights are given in Appendix 10, 11 and 12, respectively. The liquid mixtures were prepared by mass measurement giving mole fraction accuracy of >0.005. The neutron weights given in the Appendices were calculated using the mass measured compositions. *GudrunN* was again used to subtract backgrounds and correct the data for

absorption, multiple scattering and the inelastic perturbation. The absolute DCS levels were calculated using a vanadium calibration, assuming a packing fraction of 1 and for liquid densities: 0.037405 atom $Å^{-3}$ for chloroform, 0.05462 atom $Å^{-3}$ for the chloroform–acetone azeotrope and 0.08379 atom $Å^{-3}$ for the benzene–methanol azeotrope.

2.1.15 EPSR Structural Modelling of Chloroform and the Chloroform-Acetone Azeotrope

Empirical Potential Structural Refinement software (EPSR, version 18),[122] was used to prepare structural models of chloroform liquid and the chloroform-acetone azeotrope. EPSR performs Monte Carlo simulations selecting molecule translations and molecule rotations which reduce the system's potential energy for a given set of potentials corresponding to the Metropolis condition (see sections 1.14–1.16). This study employed a temperature of 298 K, a moves:acceptance ratio of 0.25, cubic simulation boxes and a harmonic intramolecular potential ($C/2 = 65/Å\ amu^{1/2}$). The intermolecular potentials used by EPSR have several different components. The reference potential, given as Equation 1.2, describes repulsive overlap interactions, dispersion and permanent electrostatic interactions using exponential decay potentials, Lennard-Jones 12-6 potentials and monopole Coulomb charges, respectively. In addition to these standard potentials, EPSR enables empirical potentials (EPs) to be derived from the difference between the measured interference functions of the differently isotropically substituted liquids and those simulated from the simulation box. These EPs direct the Monte Carlo simulation to produce a structural model consistent with the measured diffraction data. Further details of the EPSR program are described in Section 1.16.

For chloroform liquid and the chloroform-acetone azeotrope three different models with different intermolecular potential information were produced using EPSR. A model representing the most efficient packing of the molecules, termed the hard sphere model (HS), was prepared using the liquids densities (given above), average bond lengths and average intramolecular angles (Tables 2.1 and 2.2) and van der Waals distances as inputs to the program. The van der Waals radii of Bondi *et al.*[109] were used in this study. In order to obtain the most efficiently packed arrangement, the amplitude of the 'soft' repulsive potentials (term 1 in Equation 1.2) were varied to

reduce overlap of the molecules' van der Waals shells. For the second model, termed LJ + C, the repulsive potentials were removed and replaced with Lennard-Jones 12-6 potentials and monopole Coulomb charges, *q*. For the third model EPSR was allowed to develop empirical potentials (EPs) between the atom pairs improving the fit between the simulated and measured interference functions. For chloroform the EPs were truncated at 9 Å and extended to 12 Å and were estimated using a confidence factor of 0.9. For the chloroform–acetone azeotrope the EPs were truncated at 15 Å and extended to 20 Å and were estimated using a confidence factor of 0.95. The EPSR simulations with EPs were carried out until no further improvement in fit could be obtained. The EPs were then reset to 0, allowed to build once more and then fixed to give the best possible fit between simulation and experiment. Tables 2.2 and 2.3 give the average bond distances, average bond angles, energy and distance parameters of the Lennard-Jones 12-6 potentials and the magnitudes of the monopole Coulomb charges for molecules used in the models of pure liquid chloroform and the chloroform-acetone azeotrope. The composition and dimension of the cubic simulation box and the values of *ecore* and *dcore* which are used by EPSR to constrain the shape of the molecules are also given.

Table 2.1 Bond lengths and angles, Lennard-Jones parameters and partial charges for chloroform in the models of pure chloroform liquid, taken from Barlette *et al*.[111]

bond / Å		angle / °	
r(C–Cl)	1.758	∠ClCCl	111.3
r(C–H)	1.085*	∠ClCH	107.5
	σ / Å	ε / kJ mol^{-1}	*q* / e
C	3.800	0.3138	-0.050
H	0	0	0.185
Cl	3.470	1.2552	-0.045
other parameters			
composition	1500 $CDCl_3$	*ecore*	3
dimension	58.5298 Å	*dcore*	1

* Changed from 1.1 Å to provide a better fit to the diffraction data

Table 2.2 Average bond lengths and angles, Lennard-Jones parameters and partial charges used for the chloroform and acetone molecules in the models of the chloroform acetone azeotrope, based on those from Barlette *et al.*[111] and McLain *et al.*[105] Atom labels are given in Figure 6.1.

bond / Å		angle / °	
r(C_c–Cl)	1.765	∠ClCCl	111.0
r(C_C–H)	1.085	∠ClCH	107.9
r(C_o–O)	1.210	∠$C_mC_OC_m$	118.0
r(C_m–C_o)	1.500	∠OC_OC_m	121.0
r(C_m–H_a)	1.085	∠C_OC_mHa	113.0
		∠$H_aC_mH_a$	110.0
	σ / Å	ε / kJ mol^{-1}	*q* / e
C_c	3.800	0.3138	–0.050
H_C	0.000	0.0000	0.185
Cl	3.470	1.2552	–0.045
C_o	3.750	0.4390	0.566
C_m	3.880	0.7605	–0.032
O	2.960	0.8780	–0.502
H_a	0.000	0.0000	0.000
other parameters			
composition	902+614 $CDCl_3$+C_3D_6O	*ecore*	1
dimensions	57.9873 Å	*dcore*	1

2.1.16 Extracting Structural Data from the Simulation Models

Two different approaches were used to extract structural information from the EPSR models. The first involved collecting pairwise information about the distances between specific atom types after each step of molecular moves and accumulating (>200) the data into histograms by averaging the results. Several different EPSR subroutines were used to select the specific pairwise information and apply the correct constraints: *bonds* was used to extract the average bond length; *triangles* was used to extract the bond angle information; *partials* was used to obtain the radial distribution functions, $g_{AB}(r)$; *coord* gave the average coordination number data. For the EPSR model of liquid chloroform the self-associations of chloroform into dipole aligned stacks, $[Cl_3CH]_n$, was calculated using *chains* by counting molecules with a C–H distance range of 2.0–4.2 Å and H···C–H angle range of 150–180°. *chains* was also used to investigate the number of acetone–chloroform and chloroform–chloroform associations in the EPSR model of the chloroform–acetone azeotrope. Chloroform–chloroform associations, CC, were calculated using the same conditions as used for the pure chloroform liquid. Acetone-chloroform associations, AC and CAC, were calculated by

counting molecules with O···$H_{chloroform}$ distances < 2.72 Å. Acetone-chloroform-chloroform associations, ACC, were calculated by applying both conditions. The number of specific types of association [C_N, AC_N and $A(C_N)_2$] in the model were found using the differences in the chain length distributions produced using the three different sets of conditions.

The second approach used to extract information from the structural models involved calculating the Clebsch-Gordan coefficients, *C*, for the spherical harmonic expansion of the model's spatial and orientational quantities using *SHARM* and *SDF* EPSR subroutines. This procedure effectively maps the structure around each of the molecules in the box and averages information about the spatial position and relative orientation of the other molecules around them. These routines are able to represent the model's structures as a series of radial functions showing the variation in the Clebsch-Gordan coefficients with intermolecular separation, *r*, with different combinations of the generalised spherical harmonic functions: $h(l_1\ l_2\ l;\ n_1\ n_2;\ r)$. The spatial distribution of an atom, β about another atom, α may be described in 3D by the separation distance and polar angles, ϕ_1 and θ_1, as shown for the C–H contacts of two chloroform molecule in Figure 2.1(a). The corresponding correlation function with the form $g(r,\ \phi_1,\ \theta_1)$ is called a 3D spatial density function (3D SDF). To visualize 3D SDFs fractional isosurface levels showing the smallest volume containing a specified fraction of the atoms over a specified radial distance range have been used. To plot $g(r,\ \phi_1,\ \theta_1)$ the inputs to the EPSR *plot3d* subroutine are l_1 = 0, 1, 2, 3, 4; l_2 = 0; n_1 = 0, 1, 2, 3, 4; n_2 = 0. 2D SDFs displayed as contour plots have also been used in this work. These take the form $g(r,\ \theta_1)$ or $g(r,\ \phi_{1\text{-fixed}},\ \theta_1)$. For chloroform, $g(r,\ \theta_1)$ plots are shown whereby the spatial data are averaged over all possible ϕ_1 angles. For acetone $g(r,\ \phi_{1\text{-fixed}},\ \theta_1)$ plots are shown where ϕ_1 has been specified as 90 and 180° in order to plot the *zx*- and *zy*-planes, respectively (in and perpendicular to the molecular plane). To plot $g(r,\ \theta_1)$ the inputs into the EPSR *plot 2d* subroutine are: l_1 = 0, 1, 2, 3, 4; l_2 = 0; n_1 = 0; n_2 = 0. To plot $g(r,\ \phi_{1\text{-fixed}},\ \theta_1)$ the inputs to the EPSR *plot 2d* subroutine are the same as for the 3D SDF plots: l_1 = 0, 1, 2, 3, 4; l_2 = 0; n_1 = 0, 1, 2, 3, 4; n_2 = 0.

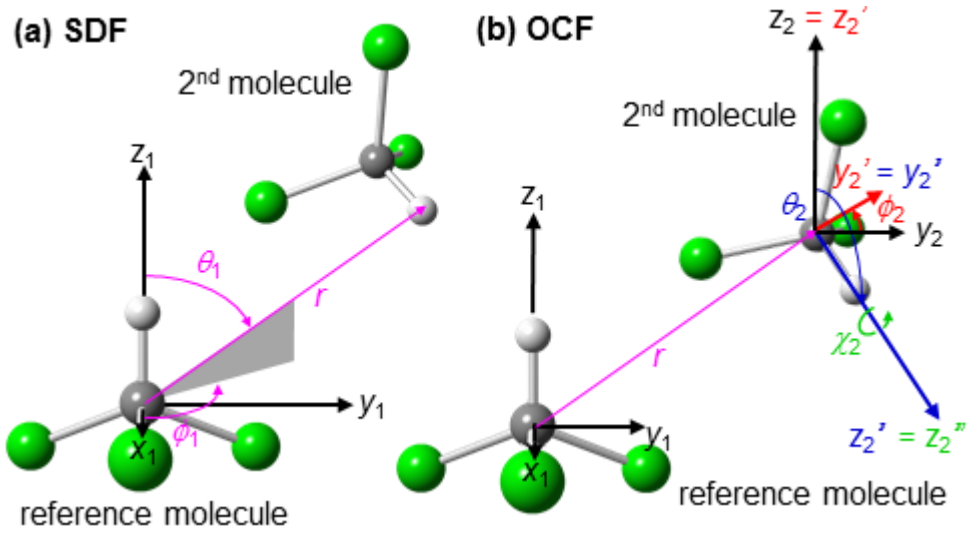

Figure 2.1 Schematic drawings showing (a) the spherical coordinates ϕ_1, θ_1 and r, which describe the position of atoms on the 2nd molecule with respect to a reference molecule and (b) the Euler angles ϕ_2, θ_2 and χ_2 which describe sequential clockwise rotations about the z_2, y_2' and z_2'' axes of the 2nd molecule and therefore specify its relative orientation with respect to the reference molecule. The reference molecule is fixed by aligning the C-H bond with the z_1-axis and placing one of the atoms in the x_1z_1-plane.

The orientational information extracted from the models describes how the alignment of the second molecule relative to a reference molecule changes with intermolecular separation. These are called orientation correlation functions (OCFs).[122,124] The relative orientation may be described by three Euler angles (describing sequential clockwise *zyz* rotations) as shown for two chloroform molecules in Figure 2.1(b). In this instance the intermolecular separation is shown between the C atom of the reference molecule and the C atom of the second molecule. However, in the Kirkwood analysis of Section 6.2.8 the arithmetic mean of the chlorine positions was used to define the centre of the chloroform molecules because it is much closer to the molecule's centre of mass (COM) and enabled a more direct comparison between the model structure and measured dielectric behaviour. Several different orientation correlation functions may be plotted from this combination of angles. For chloroform the 2D OCFs plotted in Chapter 6 show $g(r, \theta_{1\text{-fixed}}, \phi_2 = 90° \text{ or } 270°, \theta_2)$. These functions show how the relative alignment, θ_2, of molecules with $\phi_2 = 90°$ or 270° vary with intermolecular separation at different angles around the reference ($\theta_1 = 0$, 45, 90, 135 and 180°). The data are averaged for molecules located at any ϕ_1 angle and with any χ_2 rotation. For these plots the input to the EPSR *plot2d* subroutine are $l_1 = 0, 1, 2, 3, 4$; $l_2 = 1, 2, 3, 4$; $n_1 = 0$; $n_2 = 0$. For

acetone in Chapter 7, orientational correlations functions are shown for $g(r, \phi_{1\text{-fixed}}, \theta_{1\text{-fixed}}, \phi_2 = 90°$ or 270°, $\theta_2)$ and for $g(r, \phi_{1\text{-fixed}}, \theta_{1\text{-fixed}}, \phi_2 = 90°$ or 270°, $\theta_2, \chi_{2\text{-fixed}})$. The first OCF shows how the relative alignment, θ_2, of molecules in either the *zx*- ($\phi_1 = 90°$) or *zy*-planes ($\phi_1 = 180°$), and with specified θ_1 (0, 45, 90 , 135, 180) and with $\phi_2 = 90°$ or 270° vary with intermolecular separation *r*. For this OCF the orientational data for molecules with different χ rotations are averaged. For the second type of OCF, the χ rotation has also been specified as either 90° or 180° separating those molecules with parallel and perpendicular alignments of their *zy*-planes. To plot $g(r, \phi_{1\text{-fixed}}, \theta_{1\text{-fixed}}, \phi_2 = 90°$ or 270°, $\theta_2)$ the inputs to the EPSR *plot2d* subroutine are l_1 = 0, 1, 2, 3, 4; l_2 = 1, 2, 3, 4; n_1 = 0, 1, 2, 3, 4; n_2 =0. To plot $g(r, \phi_{1\text{-fixed}}, \theta_{1\text{-fixed}}, \phi_2 = 0°$ or 180°, $\theta_2, \chi_{2\text{-fixed}})$ the inputs to the EPSR *plot2d* subroutine are l_1 = 0, 1, 2, 3, 4; l_2 = 1, 2, 3, 4; n_1 = 0, 1, 2, 3, 4; n_2 =0, 1, 2, 3 ,4.

3 Preparation of ASW/C_{60}, 'Trapped Solutions'

3.1 INTRODUCTION

In 1935 Burton and Oliver showed that water vapour condenses into an amorphous 'liquid-like' material in a vacuum at temperatures < 150 K.[143] The material formed, called amorphous solid water (ASW), is metastable, transforming into crystalline ice or water vapour over time. The three stages involved in its preparation are summarised by the arrows in Figure 3.1(a). (1), the vapour formed above liquid water is introduced into a low pressure environment, (2) its temperature is reduced at a rate sufficiently high to prevent crystallisation and (3), the pressure is increased to ambient in order to recover the material into liquid nitrogen (LN_2) in which it is kinetically stable. A simplified diagram of the apparatus designed to enable these transitions whilst maximising the amount of material that can be prepared is shown in Figure 3.1(b). Water vapour is introduced into a vacuum chamber (base pressure < 1×10^{-6} mbar) through an aperture which directs the flux onto a detachable deposition plate cooled to ~80 K. A large door and gate valve allow the rapid evacuation of the chamber and recovery of the material under LN_2. In addition to the H_2O inlet, our apparatus is equipped with a crucible filament capable of subliming solids to form co-deposits of water with insoluble substances or those with very low vapour pressures. C_{60} fullerene was used in this study in order to investigate its hydrophobic hydration structures, not stable if formed at room temperature as the solutions quickly precipitate. The different aspects and operation of the apparatus are described in more detail in the following sections. The remainder of the introduction considers how the deposition conditions influence ASW structure.

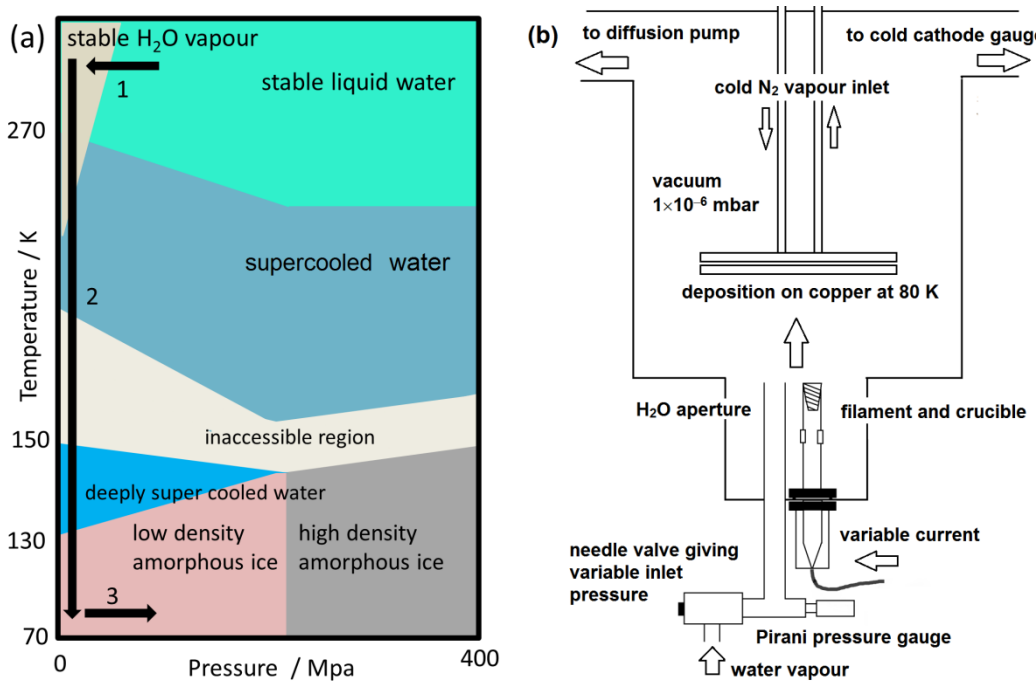

Figure 3.1 Schematic representation of the ASW preparation process. (a) Temperature-pressure diagram indicating the most thermodynamically stable of the non-crystalline forms of H_2O (The transitions from liquid water to ASW are indicated by the numbered arrows) and (b) a simplified diagram of the apparatus.

Figure 3.1(a) shows the pressure-temperature boundaries indicating the most stable amorphous forms of H_2O, adapted from the review of Loerting *et al*.[74] These boundaries reflect our current understanding of the potential energy landscape which, at low temperatures, contains shallow minima in free energy preventing transformations to more thermodynamically stable crystalline phases. At 77 K and ambient pressures, where our ASW is recovered, the most stable amorphous form is postulated to have a density of ~0.94 g cm^{-3}, whilst at higher pressures, a material with different structure and higher density is more stable. These forms are termed low density amorphous ice (LDA) and high density amorphous ice (HDA), respectively. At higher temperatures, liquid states are the most thermodynamically stable of the amorphous forms. In addition to the supercooled region, which can be reached by cold-quenching of the ambient liquid, there is also evidence suggesting at ambient pressures a liquid state is the most stable amorphous form at temperatures above ~130 K.[85-88,144-147] This material has been called deeply supercooled water, reflecting its separation from supercooled water by a region of phase space in which no amorphous form is stable due to rapid ice crystallisation. However, it has also been argued that the

true glass to liquid transition of LDA should be at temperatures higher than 130 K,[77,148-149] implying that this material may not be a liquid in its true form with active translational diffusion character. In Chapter 4, the existence of deeply supercooled water is investigated in a spectroscopic study of LDA's structural relaxations.

One of the main obstacles to understanding the ASW potential energy landscape is that the preparatory routes into metastability do not typically give the most relaxed of the metastable forms but instead materials, on the edge of energy basins, with higher potential energy. For example, the material formed by quickly quench-cooling small droplets of liquid water, termed hyperquenched glassy water (HGW), is kinetically trapped in a structural state near its glass transition temperature, T_g. As shown in Figure 1.3 its structural state may then be described by a fictive temperature, T_f, reflecting the influence of cooling rate on its state of relaxation. However, the situation for vapour-deposited materials is more complex as the structural state depends upon the physical aspects of the deposition process and the relaxation pathways available to the molecules as they cool upon deposition. From this view point, the structure of ASW may only be expected to resemble that of HGW or the supercooled liquid if related routes of relaxation are available either during deposition or subsequent annealing.

It is also known that the layer by layer vapour deposition process can give materials with far greater thermal stability than those formed by quench cooling.[150] These materials have an 'unusually high density' and have been called 'ultrastable'.[151] The authors suggest that at certain substrate temperatures the relaxation during deposition is predominantly local, giving structures lower in enthalpy (more relaxed) than those formed by quench-cooling, where increases in viscosity 'lock in' medium range disorder. From their computer simulation of a binary Lennard-Jones model, a temperature around 50 K below T_g has been predicted to give the greatest degree of relaxation, kinetically stabilising the deposits and giving the greatest increases in thermally stability.[151] These theoretical insights into the deposition process suggest that in the absence of active relaxation processes, explored in Chapter 4, the structure of ASW may be highly dependent on deposition conditions such as the temperature and the rate of deposition. Furthermore the

structure of ASW may also be expected to differ significantly from HGW, especially over medium range length scales.

The influence of the deposition conditions on ASW structure may be explored by considering the structural difference between materials prepared using different instruments. These have been reviewed by Blackman and Lisgarten in 1956,[32] and Angell in 2004.[152] Unlike the apparatus used in the present study, optimised for large sample volumes, the vast majority of experiments have been designed for *in situ* studies of thin ASW films. Some have enabled variations in the deposition conditions, revealing much about their impact on the material structure, and particularly, its porosity.[69] An exception to these is the apparatus of Hallbrucker *et al*.[153] which was used to prepare gram-sized quantities needed for neutron scattering studies.[154] The influences on ASW structure may be split into two main groups: those which predetermine some form of structure during deposition, typically manifesting as increases in porosity; and those which influence the deposition cooling rate and hence the amount of structural relaxation.

The importance of both factors was illustrated nicely in the N_2 adsorption measurements of Stevenson *et al*. which showed that a significant porosity achieved at obtuse deposition angles was diminished at higher deposition temperatures as the ASW was able to relax.[155] From a theoretical perspective, an impinging molecule will cool and slow down as it approaches a cold object, transmitting its thermal energy to the substrate. Thus the temperature of the substrate determines the rate at which the molecule cools and hence its potential to relax into a favourable structural position within the newly deposited material. Stevenson *et al*. showed that at sufficiently high temperatures of deposition ASW's porosity is actively removed in a relaxation process termed sintering.[156] Differences in the local structure and density in ASW deposited at 20 K, relative to ASW deposited at 80 K, have also been identified by X-ray,[157] and electron,[158] diffraction. Although, it has been speculated that the densification is due to the radiation experienced during the measurements,[159-160] it is intriguing to consider that the limited relaxation available at 20 K would be expected to give a less thermodynamically stable material, perhaps structurally equivalent to HDA. To more fully understand the influences of deposition temperature on structure it will be

necessary to understand the temperature at which the various forms of structural relaxation become available to the hydrogen bonded H_2O network. These relaxations are considered more closely in Chapter 4.

In addition to the N_2 adsorption studies of Stevenson *et al.*, [155,161] the porosity of ASW has been investigated using the intensity of features related to 'dangling' O-H bonds present in vibrational spectra[70,162-165] and by optical-interference measurements.[166-167] Porosity is also demonstrated in ASW by exothermic signals upon heating associated with sintering.[87,168] Optical interference measurements of thin ASW films, prepared at low deposition rates of 1×10^{13} molecules cm^{-2} s^{-1} on a substrate at 77 K found an effective density of 0.82 g cm^{-3}.[166] However, two experimental effects increasing ASW porosity and decreasing the effective density have also been identified: deposition at non-incident angles and supersonic flow conditions in the H_2O inlet aperture. Laser interferometry measurements suggest that at deposition angles > 80° the effective density of ASW may be as low as 0.1 g cm^{-3}.[167] The influence of deposition angle on porosity has also been modelled using a ballistic deposition modelling technique.[161 69,167] This investigation suggests a 'network' porosity, which is 'filamentous' and 'columnar' and caused by 'random height differences that block incoming flux'. The influence of aperture flow conditions is postulated to be related to the Joule-Thompson effect which may cause H_2O clusters to form in the impinging H_2O flux upon cooling.[60,153] Although, not observed directly under the conditions of the deposition, small clusters have been observed in molecular beams,[169] and three levels of differential pumping are described in the procedures of Smith *et al.*,[170] presumably to allow temperature equilibration between reductions in pressure which cause the cooling effect. Unlike the structural perturbation caused by non-incident deposition angles, which are predicted to remain locally relaxed,[167] the presence of gas phase H_2O clusters may influence the local intermolecular structure in the absence of subsequent relaxation.

Due to the potential impact of deposition conditions on the structure of ASW described above, this chapter explores the range of deposition conditions available with our new ASW preparation apparatus: specifically, the deposition rate, deposition angle and the temperatures

experienced by the deposited material. As the instrument has been designed to maximise sample quantity, particular attention has been given to understanding the limiting deposition rate and film thickness giving ASW without crystalline ice contamination. This chapter comprises of two parts: In the first, the different aspects of the apparatus are explored in detail and in the second a series of *in situ* variable-temperature measurements of chamber pressure are presented, revealing the main factors influencing the growth of ASW.

3.2 APPARATUS

3.2.1 THE VACUUM CHAMBER

Photographic images of the apparatus used to deposit ASW are shown in Figure 3.2. Images on the left and right show the apparatus viewed from the front and from the side. The main body of the apparatus is a purpose built vacuum chamber, **1**, (Kurt J. Lesker, Hastings, UK) with internal dimensions of 24×12×12 inches. The chamber has several large KF40 and LF100 flanges and a full-sized door with a glass viewing window, **2**. The total volume of the chamber and its connections is estimated to be ~0.080 m^3 and its total internal surface area to be ~1 m^2. A base pressure $< 1\times10^{-6}$ mbar was reliably achieved using a diffusion pump, **3**, (Diffstack 63, BOC Edwards, Crawley, UK) containing polyphenol ether oil (Santovac 5, BOC Edwards) backed with a two-stage rotary vane pump (model 12, BOC Edwards). A liquid nitrogen baffle, **4**, positioned directly above the diffusion pump was employed to trap oil residues. The chamber pressure was measured using a dual Pirani/cold cathode ionisation pressure gauge, **5**, (PenningVac PTR 90, Oelikon Leybold Vacuum, Cologne, Germany) and recorded (Labview) using RS232 connections to a computer. The procedure for evacuating the chamber is given in Appendix 2 with a plot showing the stages involved in the pump down. Also shown in the front view image (left) is the linear z-positioner used to adjust the distance between the aperture and the deposition stage, **6**, the display used to monitor chamber pressures and temperatures, **7**, the needle valve used to control H_2O chamber dose rates, **8**, the power supply used to control C_{60} sublimation rates, **9**, and the pump used to pump cold nitrogen vapour through the deposition stage, **10**. Shown in the side view

image (right) are the liquid nitrogen Dewar used to cool the deposition stage, **11**, the hand held liquid nitrogen Dewar, **12**, and gate valve, **13,** used to vent the chamber. These parts of the apparatus, associated with cooling the deposition stage, controlling H_2O and C_{60} dosing rates and collecting the deposited material, are discussed in separate sections to follow.

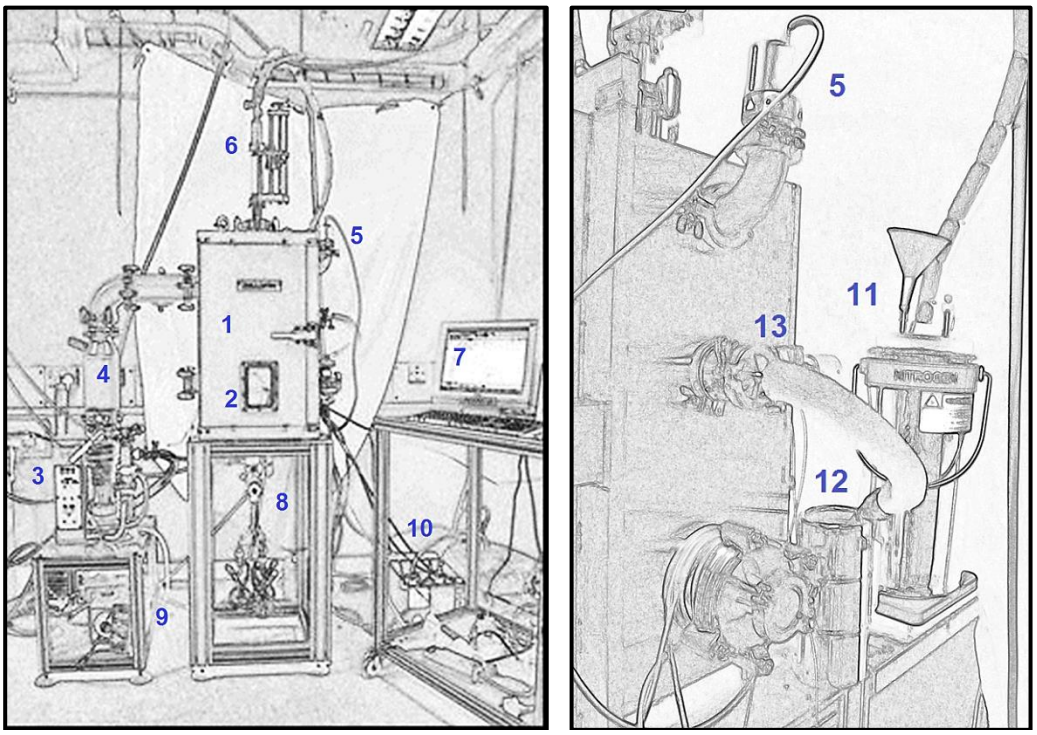

Figure 3.2 Photographic image of the deposition apparatus, viewed from the front (left) and from the side (right).

The pumping performance of the chamber was characterised by measuring the response of the chamber pressure to different rates of dosed N_2 gas. The N_2 dose rate was controlled using the graduated needle valve (EV 016 DOS AB, Oerlikon Leybold Vacuum) for which position-flow rate calibration data are available (air, Δp = 1 bar).[132] Figure 3.3 shows the calibration data (a) and the measured response in chamber pressure (b). Figure 3.3(c) shows the corresponding relationship between the chamber pressure and the N_2 flow, found by interpolation. As the chamber equilibrates to a steady state, the data in (c) also indicate the variation in pumping performance with chamber pressure. This relationship is in close agreement with the published data for Edwards diffusion pumps of similar size,[171] which show a 'drop off' in pumping performance at pressures > 1×10^{-3} mbar.

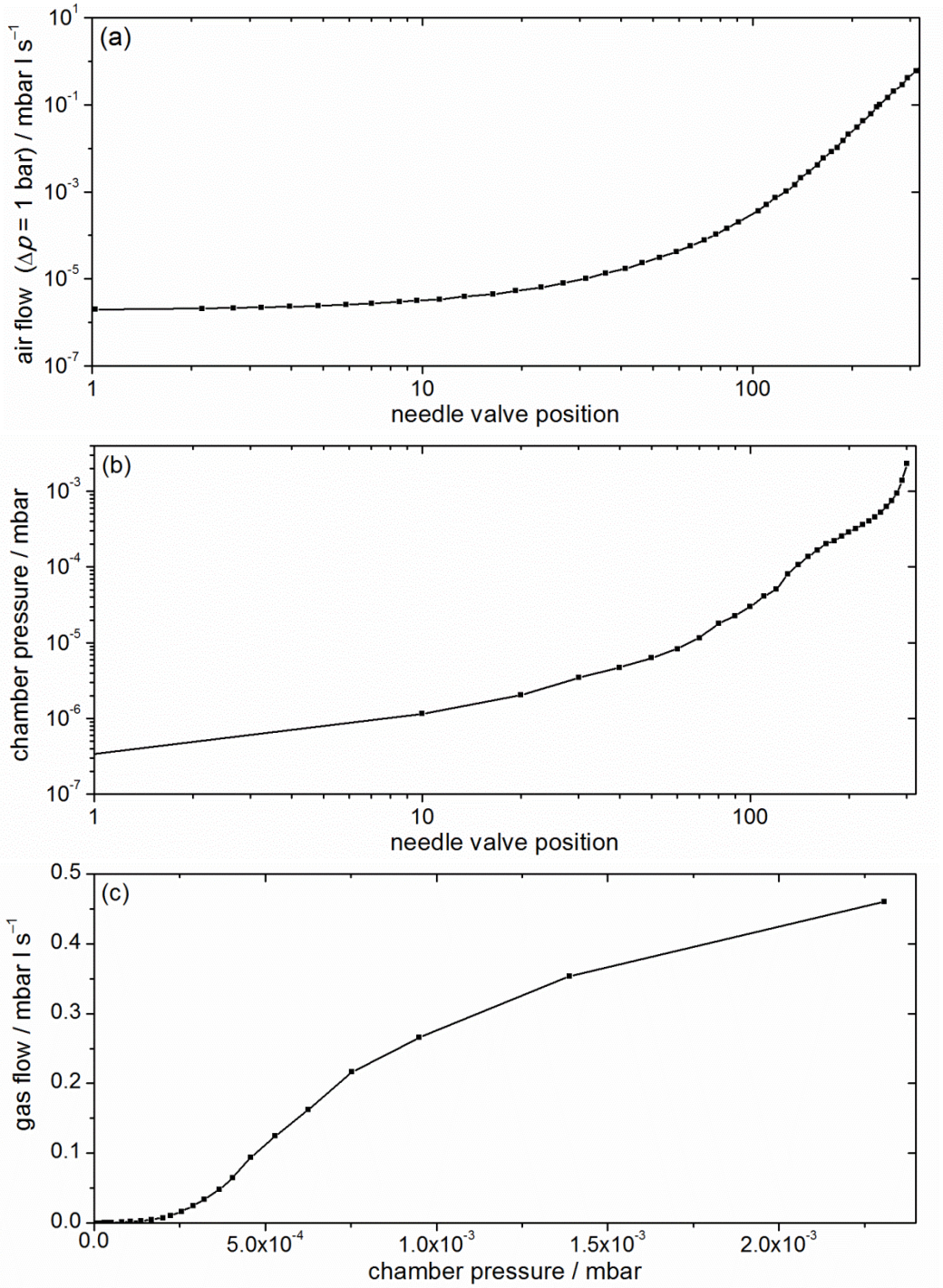

Figure 3.3 (a) calibration data supplied in the manual of the needle valve showing the variation in air flow (Δp = 1 bar) with position, (b) the measured variation in chamber pressure with needle valve position for dosed N_2 gas and (c) the interpolation of the calibration data shown in (a) for the pressure values of (b) indicating the variation in gas flow with chamber pressure.

3.2.2 THE COOLED DEPOSITION STAGE

Figure 3.4 shows images of the deposition stage, viewed through the open door of the vacuum chamber. The zoomed image (right) shows the deposition plate, **1**, and deposition stage, **2,** to which it is attached. This two piece arrangement allowed the plate to be detached and hence the deposited material to be removed from the chamber under liquid nitrogen. The stage is comprised of a circular piece of copper with a thickness of 6 mm and a diameter of 20.3 cm (324 cm^2). It is cooled by a flow of cold nitrogen vapour through an embedded spiral of copper tubing, (¼ inch diameter), **3**, and a purpose built stainless steel feed through, **4** (¼ inch diameter) (Kurt J. Lesker, Hastings, UK) from which it is suspended. This arrangement is also shown as a scale drawing in Appendix 3. Copper to steel tube connections, **5**, were made using hard silver solder (Silverflow 55, Johnson Matthey). The vertical position of the deposition stage within the chamber could be adjusted (5–25 cm from H_2O inlet aperture) by changing the height of the feedthrough using a z-positioner (Kurt J. Lesker, Hastings, UK) (**6** in Figure 3.2). The nitrogen flow was achieved by connecting the feedthrough to a 5 L liquid nitrogen Dewar by ~2 m of insulated tubing, and to a rotary vane pump, (Sogevac SV16, Oelikon Leybold Vacuum), by ~5 meters of tubing. A water bath was positioned between the feedthrough and the rotary vane pump to increase the temperature of the N_2 vapour. The temperature variations of the deposition stage were monitored and recorded using a K-type thermocouple bolted to the centre of the deposition stage, **6**, a temperature controller (331, Lakeshore cryotronics, Ohio, USA) and a computer equipped with Labview. Thermal paste was used to ensure good contact between the thermocouple and the deposition stage. A K-type thermocouple feedthrough, **7,** was used to connect the internal and external parts of the thermocouple wire. Also shown in the photographic images are the H_2O vapour inlet, **8** and the basket filament as well as crucible used to sublime C_{60}, **9,** which are described more fully in the following section.

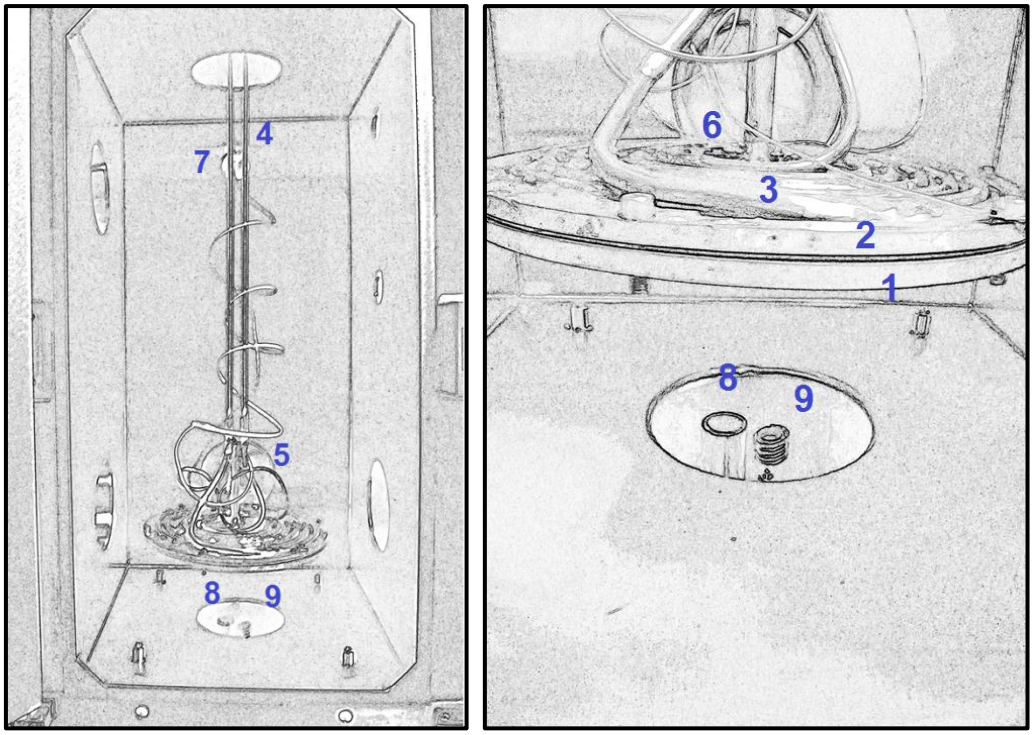

Figure 3.4 Photographic images of the deposition stage viewed through the open door of the vacuum chamber.

A tap positioned between the water bath and the rotary vane pump was used to adjust the flow of cold nitrogen vapour though the deposition stage allowing its temperature to be controlled. To cool the deposition stage from room temperature to < 80 K the tap was opened fully giving a liquid nitrogen evaporation rate of 5 L h^{-1}. To maintain the temperature of the deposition stage at < 80 K a minimum evaporation rate of ~1 L h^{-1} was required. This minimum flow was necessary to counteract four independent heating processes typically experienced during deposition: (1) conductive heat transfer through the metal tubes of the feedthrough, (2) energy transferred during deposition, (3) convective transfer due to the movement of gas molecules across the vacuum, and (4) radiative heating from the room temperature walls of the vacuum chamber and the hot (~700 K) crucible which glowed during C_{60} sublimation.

The heating resulting from the processes active at base pressure for a clean deposition stage have been investigated by reducing the temperature of the stage to 80 K and then stopping the LN_2 cooling. The rate at which the stage warmed is shown in Figure 3.5. Initially the heating rate was ~1.1 K min^{-1} but decreased smoothly with increasing temperature to ~0.58 K min^{-1} at 180 K. The

variation in heating rate with temperature reflects changes in the heat capacity and thermal conductivity of the copper, and the decreasing temperature difference between the deposition stage and the external walls of the chamber, which are unaffected by the LN_2 cooling. The heat capacity of the copper has a pronounced influence over this temperature range, as the constant volume heat capacity (C_V) of copper increases from 12.8 J K^{-1} mol^{-1} at 80 K to 21.59 J K^{-1} mol^{-1} at 180 K.[172-173] Given the total volume of the deposition stage (~195 cm^3), the density of copper (8.96 g cm^{-3}),[174] and the values of C_V given above, a heating rate of 1.0 K min^{-1} at 80 K corresponds to 5.9 J s^{-1} and a heating rate of 0.58 K min^{-1} at 180 K corresponds to 5.7 J s^{-1}.

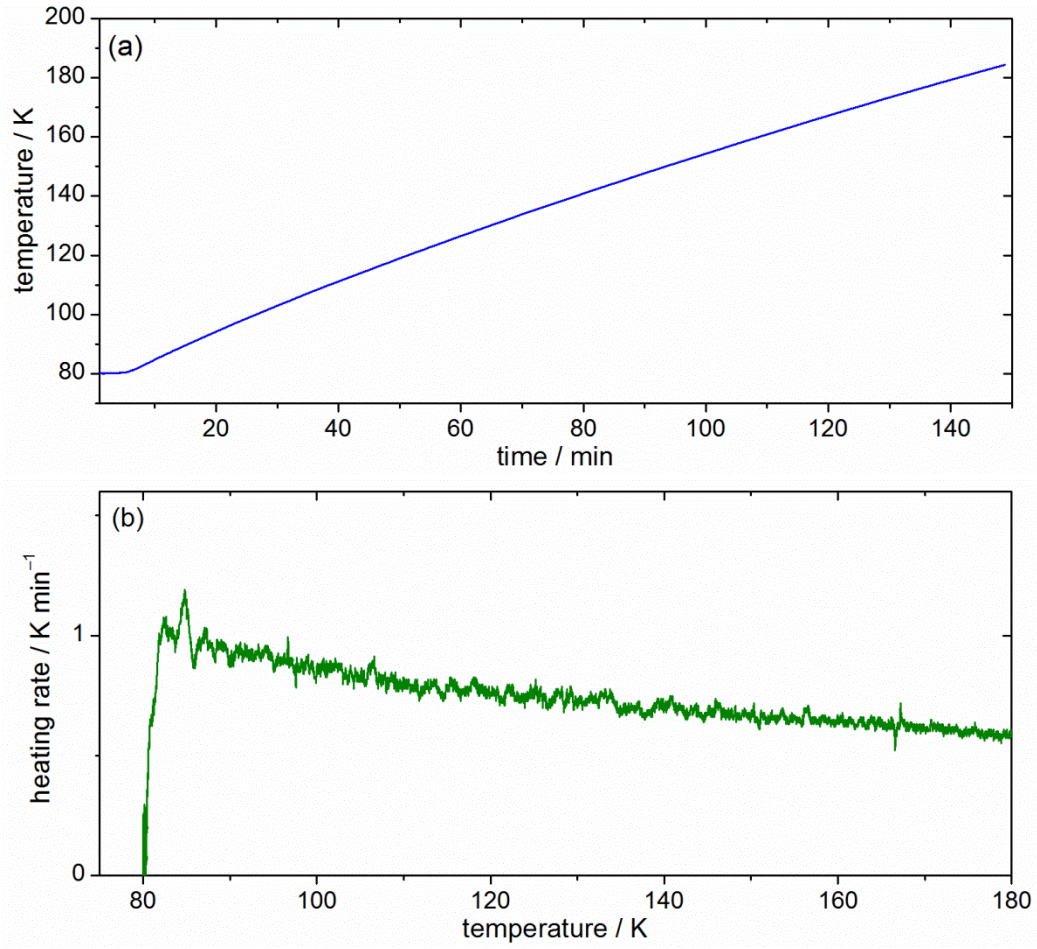

Figure 3.5 (a) Variations in the temperature of the deposition stage warming from 80 K and (b) corresponding heating rate data smoothed over 1 minute intervals.

3.2.3 H_2O AND C_{60} DOSING APPARATUS

Figure 3.6 shows images of the H_2O and C_{60} dosing apparatus. Images (a) and (b), respectively, show the external parts of the H_2O apparatus and the electrical feedthrough to the filament used to sublime C_{60}, (c) shows the positions of the internal part of the H_2O inlet and filament, and (d) shows the power supply used to control the C_{60} sublimation rate. The 200 mm long stainless steel tube with an internal diameter of 16 mm used to inlet H_2O, **1,** is fitted into a base plate flange positioned in a recess directly below the deposition stage. The recess is visible in image (c). Two different base plates with slightly different positioning of the H_2O inlet were used in this study. In the first, termed the ASW base plate, the H_2O inlet was centrally placed with respect to the deposition stage. In the second, termed the co-deposition base plate, the H_2O inlet, was offset from the centre of the base plate by 1.11 cm to allow the filament to be installed at a symmetrically offset position, **2**. The images of Figure 3.6 and the drawing given as Appendix 6 show this co-deposition base plate. The H_2O dosing apparatus connected to the H_2O inlet described below is the same for both. The H_2O vapour is transmitted to the H_2O inlet *via* a graduated needle valve, **3**, (EV 016 DOS AB, Oerlikon Leybold Vacuum) and T-piece housing a Pirani pressure sensor, **4**, (Thermovac TTR91, Oerlikon Leybold Vacuum). The needle valve is connected *via* a threaded Radley's fitting to a short glass manifold, **5**, and three detachable round bottomed flasks, **6**, each sealed from the chamber with a Young's tap, **7**. This arrangement of three flasks enabled liquids with different H_2O/D_2O compositions to be degassed and stored for separate depositions.

The C_{60} sublimation apparatus consists of an Al_2O_3 crucible, (EVC1A0, Kurt J. Lesker), tungsten filament, **2**, (6.3 V, 43 A, 271 W, 1800°C) (EVB8B3025W+, Kurt J. Lesker), high current (20 A, 1.3 mm diameter copper conductors) electrical base plate feed-through, **8**, (264-13Cu1K-2-BP, Allectra, Sussex, UK) and a purpose built power supply, **9**, containing transformers (MPI-400-12, SignalTransformer, New York, USA) able to regulate the electric potential across the filament to between 0 and 6 V. A 3 V potential gave a measured crucible temperature of ~900 K (data given as Appendix 4); extrapolation indicating that temperatures in excess of 1500 K may be achieved with this arrangement, far greater than required to sublime C_{60}.[133,175-178] The stability of C_{60} to

oxidation,[179-182] under typical deposition conditions was confirmed by solid state NMR of recovered material. These spectra are included as Appendix 5. The current flowing through the filament is monitored with a current sense resistor, **10**, by measuring the voltage across two 20 mΩ/50 W resistors in parallel (1 A = 10 mV) with a multimeter, **11**, (IDM 72, ISO-TECH, Gyeonggi-do, Korea). A water-cooled brass plate, **12,** was fitted to the co-deposition base plate to reduce the heating impact of the filament used to sublime C_{60} on the water inlet.

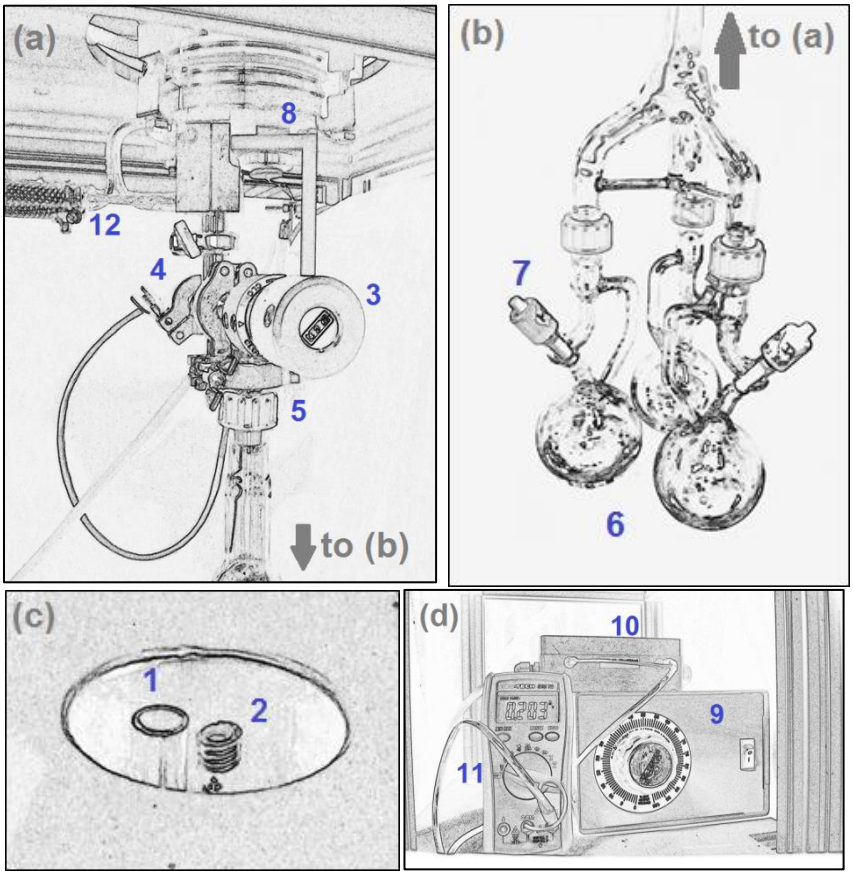

Figure 3.6 Photographic images of the H_2O and C_{60} dosing apparatus. (a) and (b) show the external parts of co-deposition base plate and the liquid flasks suspended below, (c) shows the positions of the internal part of the H_2O inlet and filament and (d) shows the power supply used to control the C_{60} sublimation rate.

The H_2O dosing rate was controlled by adjustments to the graduated needle valve. Opening (closing) the valve, **3**, increased (decreased) the flow of H_2O vapour, increasing (decreasing) the inlet pressure and changing the pressure gradient across the tubular aperture. To achieve very high dose rates (> ~2 g h^{-1}) a water bath was positioned around the flasks to counteract the effects of evaporative cooling. The C_{60} sublimation rate was controlled by adjusting the current flowing

through the filament. The relationships between inlet pressure/H_2O dose rate and filament current/C_{60} sublimation rate were determined by measuring the decrease in weight of the H_2O flask and C_{60} crucible for depositions experiments carried out over a range of inlet pressures and filament currents. These data are shown in Figure 3.7 with their fit to quadratic ($y = 0.15x + 1.32x^2$ for H_2O and $y = 0.13x + 1.30x^2$ for D_2O) and exponential functions ($y = 2\times10^{-12}\exp(0.7x)$ for C_{60}). The good fit to quadratic equations for H_2O and D_2O demonstrate the transitional nature of the flow through the aperture, which was neither purely molecular nor fully viscous (these are characterised by linear and quadratic relationships between flux and pressure, respectively.[183] The slightly lower molar dose rate for equivalent Pirani measured inlet pressures of D_2O relative to H_2O reveals the small isotopic differences between these molecules which affect their flow dynamics in the aperture.[121] As the Pirani sensor used was calibrated for air, which has a much lower heat capacity than H_2O or D_2O, the curves presented overestimate the true inlet pressure by a factor of ~2.[184]

The exponential increase in C_{60} sublimation rate with filament current reflects the exponential form of the Clausius-Clapeyron equation relating C_{60} vapour pressure to temperature.[133] This in turn also implies that the temperature of the crucible increased linearly with current. Independent measurements of crucible temperature confirmed the essentially linear relationship over this range of filament currents (Appendix 4). The poor precision of the C_{60} sublimation rate data, which deviate from the fitted function by amounts greater than the uncertainty associated with the mass measurement, suggest an additional source of variation between different experiments. Two potential sources were identified, variations in the packing of C_{60} within the crucible and in the physical contact between the crucible and the basket filament. The variations in packing may be reduced by using pellets of C_{60} material as opposed to powder. The problems associated with a poor contact were resolved using a filament and crucible combined into a single unit (alumina coated basket filament, AC-36, Midwest Tungsten service). An additional advantage of this single unit approach is the lower filament temperature, and hence less radiative heating for a specific dosing rate. Although difficulties in removing the crucible in order

to measure the C_{60} dose have prevented its use in this study, it is now paired with a quartz crystal microbalance capable of accurately measuring the desorption rates *in situ*.

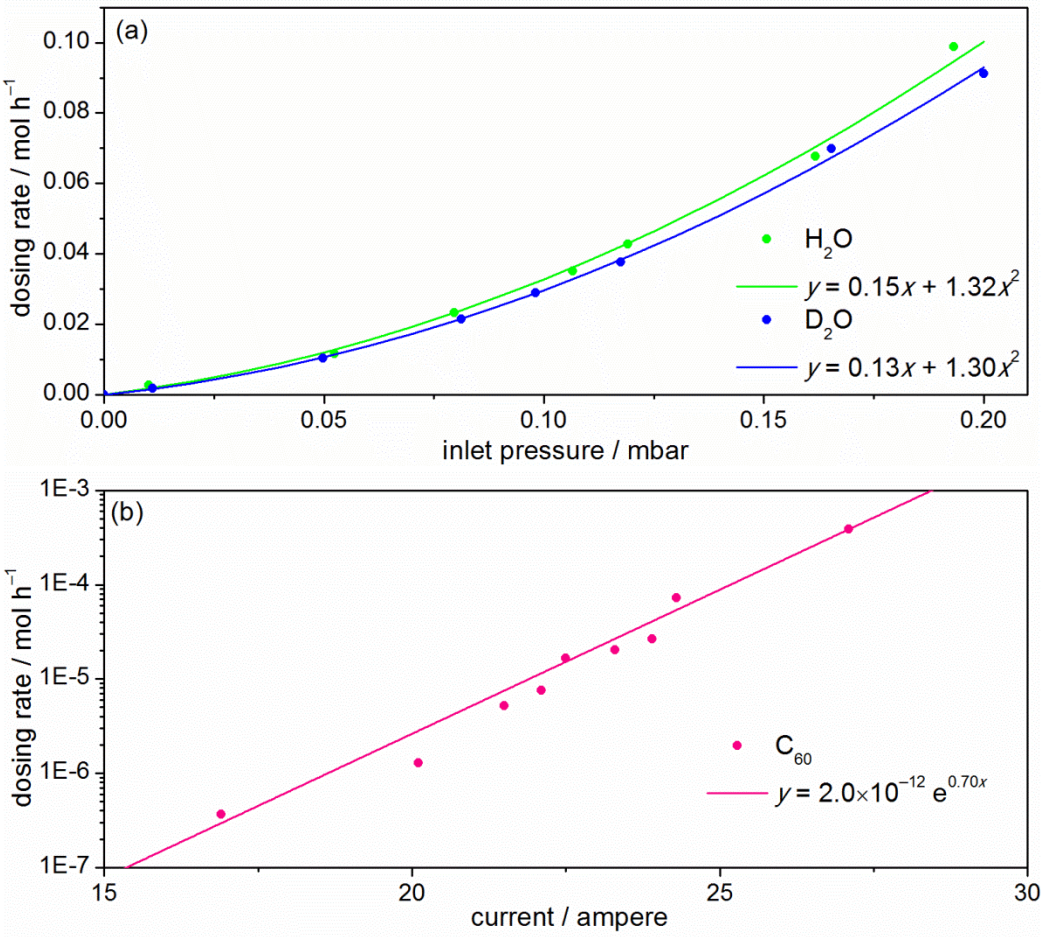

Figure 3.7 Variation in H_2O, D_2O (a) and C_{60} (b) dosing rates with inlet pressure (Pirani calibrated for air, calibration factor for H_2O is ~0.5[184]) and filament current. The error in dosing rate associated with the mass measurements is < 10 %. Values of inlet pressure and filament current were found by averaging measurements recorded during the deposition period.

The flux of H_2O and C_{60} from these apertures varies with the angular offset (deposition angle) of its trajectory from that of the apertures, being greatest for deposition angles, $\theta = 0$, corresponding to a normal incidence of deposition. For thin-walled effusive sources this effect is caused by the random direction of molecules entering the aperture and the greater area probed by molecules leaving the aperture at higher deposition angles.[183] This gives the flux a $\cos\theta$ relationship with deposition angle, θ. For differently shaped apertures and high pressures, the beam profile changes with tubular apertures further increasing flux for deposition angles close to 0. However, as molecular interactions cannot be neglected in the transitional flow regime used, a theoretical

analysis of the flow geometry based on the aperture dimensions has not been possible for our apparatus. Instead, the flow geometries have been investigated experimentally using optical absorbance spectroscopy to measure the amount of H_2O and C_{60} deposited onto copper probe discs (diameter = 1.5 cm) attached to the deposition plate at different deposition angles. The intensity of absorbance peaks at ~330 and ~1950 nm, respectively, were then used to determine C_{60} and H_2O concentrations from an ethanol dilution series and calibrations of the molar absorption coefficients. The offset between the H_2O inlet and C_{60} crucible was 2.22 cm and the aperture-deposition plate distance was 9.4 cm. As the disks were positioned in a line across the deposition plate, the data have an additional directional component, indicated by the positive and negative angles for disks on the left and right sides of the deposition stage.

The variations in H_2O and C_{60} flux with deposition angle calculated using this approach are shown in Figure 3.8. The data presented are for several separate H_2O/C_{60} co-depositions experiments, carried out with similar dosing rates (av. H_2O = 0.196 g h^{-1}, av. C_{60} = 0.0054 g h^{-1}).The spread in the data reflects the experimental difficulty transferring the copper discs into the ethanol solvent without ice contamination and due to a spectral background caused by the partial aggregation of C_{60}. To improve the accuracy of this approach, separate solvents could be used to measure the concentration of H_2O and C_{60} independently.

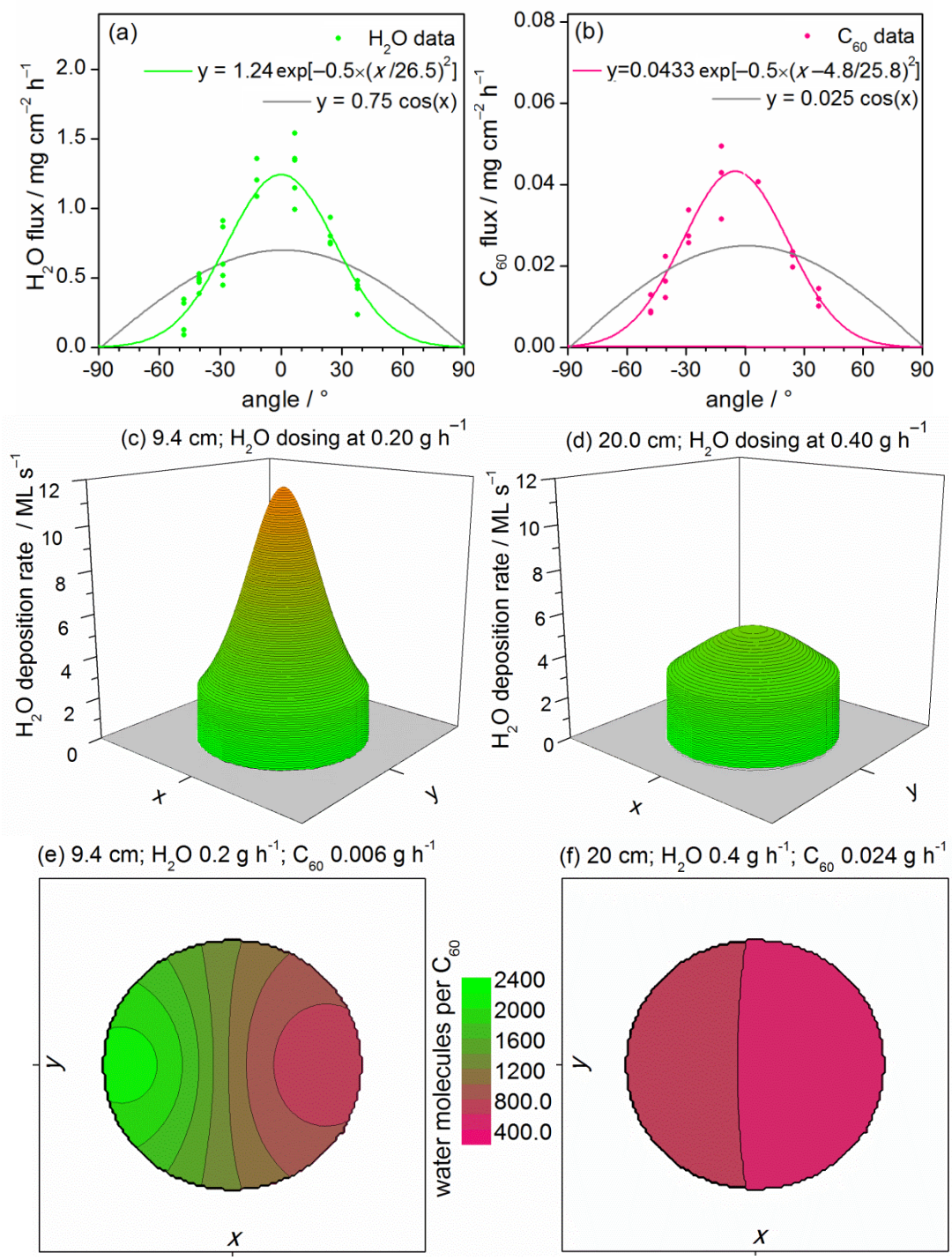

Figure 3.8 Measuring and modelling the H_2O and C_{60} dosing geometry. The measured angular variation in (a) H_2O and (b) C_{60} flux, (c and d) the modelled variation in deposition rate for pure ASW formed from a centrally placed aperture and (e and f) the composition of ASW/C_{60} mixtures co-deposited with a 2.22 cm offset between H_2O dosing inlet and C_{60} crucible. The *x* and *y* axis of (c,d,e and f) correspond to the cross sectional width (30.5 cm) and depth (30.5 cm) dimensions of the vacuum chamber. (c and e) show data for an aperture-deposition stage distance of 9.4 cm, H_2O dose rate of 0.4 g h^{-1} and C_{60} dosing rate of 0.006 g h^{-1} and (d and f) show extrapolated data for a distance of 20.0 cm, 0.4 g h^{-1} (H_2O) and 0.024 g h^{-1} (C_{60}).

Figure 3.8 also includes the best fit to cosine and Gaussian amplitude functions. The significant deviations from a cosine relationship, appropriate for an effusive source,[183] indicate that both the H_2O inlet and the C_{60} crucible directed the flux. This directing influence has been captured by the Gaussian functions, which, when integrated over 3D (2π solid angle) closely reproduce the average measured chamber dose (H_2O = 0.176 ± 0.022 g h^{-1} and C_{60} = 0.0059 ± 0.0008 g h^{-1}). Integration between the limits of 43.5 and 50.0°, corresponding to materials incident on the centrally placed deposition plate at 9.4 cm, indicates that 83 ± 3 % of dosed material was captured on the plate with an average C_{60} mole fraction, 1.0×10^{-3} ± 0.2 $\times10^{-3}$ (~1000:1 H_2O:C_{60}). Interestingly, the best fitting Gaussian function for C_{60} is offset from the plate centre by 4.8° indicating a slight misalignment of the crucible, which leaned towards the water inlet increasing the average C_{60} concentration and reducing the variation in composition across the deposition plate. Conversely, the maximum H_2O flux of 1.26 mg h^{-1} occurred at normal deposition angles. This flux corresponds to a deposition rate of 1.2×10^{16} molecules cm^{-2} s^{-1} or using the monolayer (ML) terminology of Smith *et al.*,[170] ~11 ML s^{-1} of crystalline ice (1 ML = 1.1×10^{15} molecules).[170]

These Gaussian functions have been used to predict the spatial variations in deposition rate and composition on the deposition stage for different conditions of water inlet position (centrally placed or offset by 1.11 cm), aperture-deposition stage distance and H_2O and C_{60} dosing rates. Figure 3.8(c) and (e) show the spatial variation in H_2O deposition rate (centrally placed H_2O inlet) and H_2O/C_{60} composition (H_2O inlet and C_{60} crucible offset by 1.11 cm) for the measurement conditions used to obtain the data in (a and b) (9.4 cm, av. H_2O = 0.2 g h^{-1}, av. C_{60} = 0.006 g h^{-1}) and Figure 3.8(d) and (f) show corresponding deposition rate and composition data for an extrapolation to more favourable conditions for producing uniform samples (20 cm, av. H_2O = 0.4 g h^{-1}, av. C_{60} = 0.0024 g h^{-1}). In these plots the *x* and *y*-axis describe horizontal *x* and *y* positions within the chamber (30.5×30.5 cm). The position of the deposition stage in this cross sectional area is indicated by the non-zero values of deposition rate and composition. The shape of the feature in Figure 3.8(c) and the wide range of colours from green (dilute C_{60}) to pink (concentrated C_{60}) in Figure 3.8(e) indicate that for an aperture-deposition stage distance of 9.4 cm, the deposition rate

and composition varies significantly with position on the deposition stage. The red tip of the peak in (c) and the green area in (d) show the locations of the unfavourably high deposition rates (11 ML s^{-1}) and dilute C_{60} solutions (1:2500), respectively. The flatter feature, shown in Figure 3.8(e) and smaller colour variation in Figure 3.8(f) indicates that a much smaller variation in deposition rate and composition is achieved by increasing the distance between the apertures and the deposition stage to 20 cm. The model also indicates the decreased deposition yield (55 ± 4 %) expected at 20 cm and the associated increases in dosing rate required to maintain a given deposition rate. Dosing rates of 0.4 g h^{-1} for H_2O and 0.024 g h^{-1} for $C_{60,}$ are predicted to give an average H_2O deposition rate of 5.1 ± 0.4 ML s^{-1} and an average C_{60} mole fraction of 1.8 $\times 10^{-3}$ ± 0.2 $\times 10^{-3}$ (~520:1 H_2O:C_{60}). This H_2O deposition rate is about an order of magnitude greater than typically used by Smith *et al*. (0.2 - 0.87 ML) 'outputting ~20 Torr of H_2O through a 0.1 μm orifice'.[70,170] The deposition conditions employed in the present study are more similar to those used by Mayer *et al.*[60] who used inlet pressures between 0.05 and 0.2 mbar (Pirani calibrated for air), and a tubular aperture with a diameter of 13 mm positioned 150 mm from the deposition stage. Interestingly, they report growth rates of 0.1 - 0.3 mm h^{-1} which for a structural density of 0.938 g cm^{-3},[185] and assuming similar dose rates to ours, would imply a large porosity and low effective density of ~0.06 g cm^{-3}.

3.2.4 COLLECTION AND STORAGE OF DEPOSITED MATERIALS

To recover material from the chamber, deposition was carried out onto the deposition plate (identical dimensions to the deposition stage) which was then detached and removed. This arrangement is visible in Figure 3.4 and also shown in Appendix 3. At the start of a typical deposition experiment the deposition plate was carefully cleaned with sandpaper and ethanol, and fastened to the stage from above with six bolts. It was also designed with six protruding copper contacts allowing the connection between the deposition plate and stage to be visibly checked. The temperature of the plate was monitored by a second thermocouple. This two piece apparatus allowed the material deposited on the plate to be removed from the chamber in a procedure designed to minimise heating and exposure to air. The procedure involved opening a high capacity

gate valve (series 012 mini gate valve, VATvalve, Haag, Switzerland) venting the chamber with cold N_2 vapour, opening the door and quickly lifting an insulated container of LN_2 over the deposition stage before unscrewing the bolts and removing the plate. The gate valve and hand held liquid nitrogen Dewar used to vent the chamber are visible in the images of Figure 3.2.

Two different deposition plates were produced. The first was designed to hold Si and MgF_2 substrates which were coated with ASW and then recovered. Figure 3.9(a) shows the apparatus used to fix the substrates to the surface of the plate, comprising of a copper ring, **1**, Teflon spacer, **2**, and three stainless steel bolts, **3**. The substrates coated with deposited material were then moved into specially prepared storage vessels in a LN_2 bath. A substrate resting vertically in the storage vessel is shown in Figure 3.9(b). It comprises of a glass vial, 'pinched' inwards to prevent the substrates from laying horizontally, **4**, a folded piece of tissue paper, **5**, allowing liquid nitrogen to flow into the container, **6**, and a wire enabling its extraction from the storage Dewar.

A second deposition plate was designed with a bevelled hole to enable the efficient recovery of material from its entire surface. This modification allowed ASW material, which was slightly denser than liquid nitrogen at 77 K (0.808 g cm^{-1}),[185] to be scraped from the surface of the plate into an aluminium sample container positioned below the hole. The yield of this approach is estimated to be > 90 %. Figure 3.10 shows the three stages involved in the ASW collection procedure. The deposition plate was first flipped onto a copper trivit in a polystyrene container of LN_2 with internal dimensions of 50 × 30 × 30 cm. To protect the LN_2 from ice contamination, argon gas was flowed into the container forming a protective 'blanket' which displaced any humid air. An aluminium sample container was then fastened directly underneath the hole using a small bolt. The sides of a spring form pan (cake form) were then secured around the deposition plate isolating the ASW from the LN_2 bath. After the material had been scraped from the surface of the deposition plate into the sample container, the sprung pan, deposition plate and copper trivit were removed, and the sample container sealed and moved to a storage Dewar.

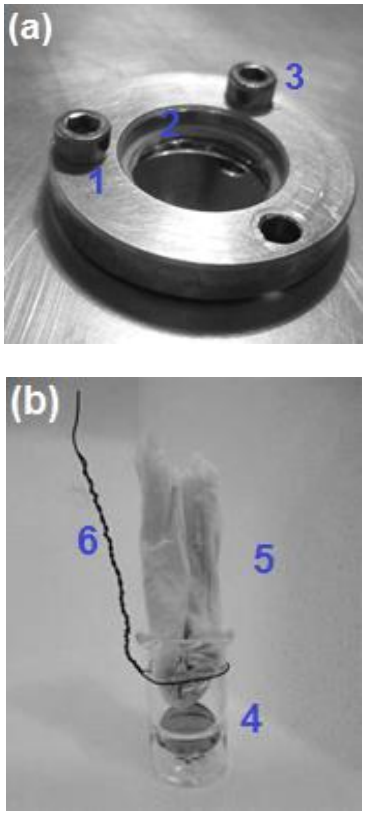

Figure 3.9 (left) Photographic images of the apparatus used to recover and store coated Si and MgF_2 substrates

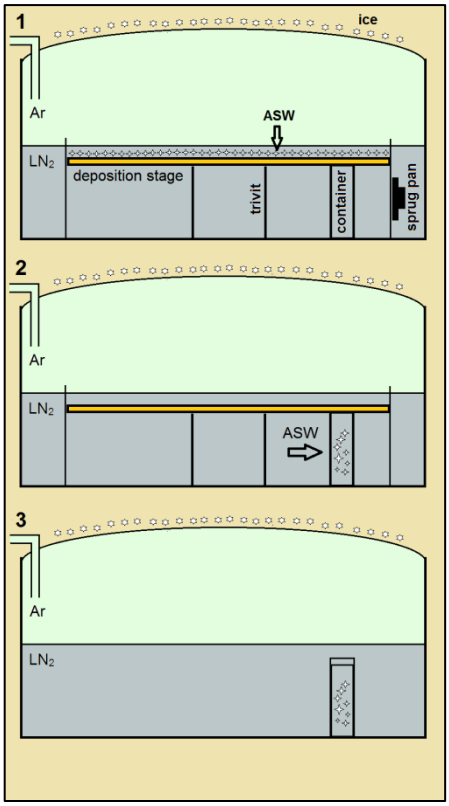

Figure 3.10 Schematic showing the three-stage procedure for collecting deposited material in a liquid nitrogen (LN_2) bath. Ice contamination was prevented using an argon blanket.

The successful deposition and recovery of ASW onto substrates and as bulk material scraped from the surface of the deposition plate, was confirmed by X-ray and neutron diffraction. X-ray data for a 'trapped solution' of ASW/C_{60} (X_{C60} =0.0028) is shown in Figure 3.11. Neutron diffraction data are presented in Chapter 5. Figure 3.11(a) shows the pattern obtained from a 40 min scan of a coated Si substrate (single crystal cut parallel to the 510 plane and thus having a 'zero background') after its recovery into liquid nitrogen, storage, and transfer into the cryostat at ~90 K. Figure 3.11(b) shows a contour plot formed from ~50 shorter scans (74 s) recorded as the substrate warmed to room temperature at ~2.4 K min^{-1}. The smooth profile of the 80 K pattern (a) comprised two features with broad maxima at 24° and 43°, is similar to that previously reported for pure ASW and indicates the amorphous nature of the ASW/C_{60} 'trapped solution'.[59,143,156] Tick marks at 43.2 and 50.2° (orange) indicate the 2θ position of reflections due to the copper metal of the X-ray cryostat body and those at 22.8° (100), 24.3° (002), 25.9 (101), 33.6° (102), 40.1° (110),

and 46.6° (200), show the position of reflections expected for ice I_h.[32,156] These ice I reflections are absent from the 90 K data (a) but visible in the patterns recorded at higher temperatures (b). Two sets of reflections (blue and pink tick marks) are required to explain the relaxation of ASW with increasing temperature. This is due to the presence of cubic and hexagonal H_2O stacking in the crystallites initially formed at ~160 K but not in the most relaxed form which has a purely hexagonal stacking.[35,37,186] The transformation of ASW into the stacking disordered ice (ice I_{sd}) at ~160 K is indicated by reflections at 22.9, 24.3, 40.1 and 46.6° (blue). The transition to purely hexagonal ice (ice I_h) at ~210 K is indicated by the additional reflections at 25.9 and 33.6° (pink).

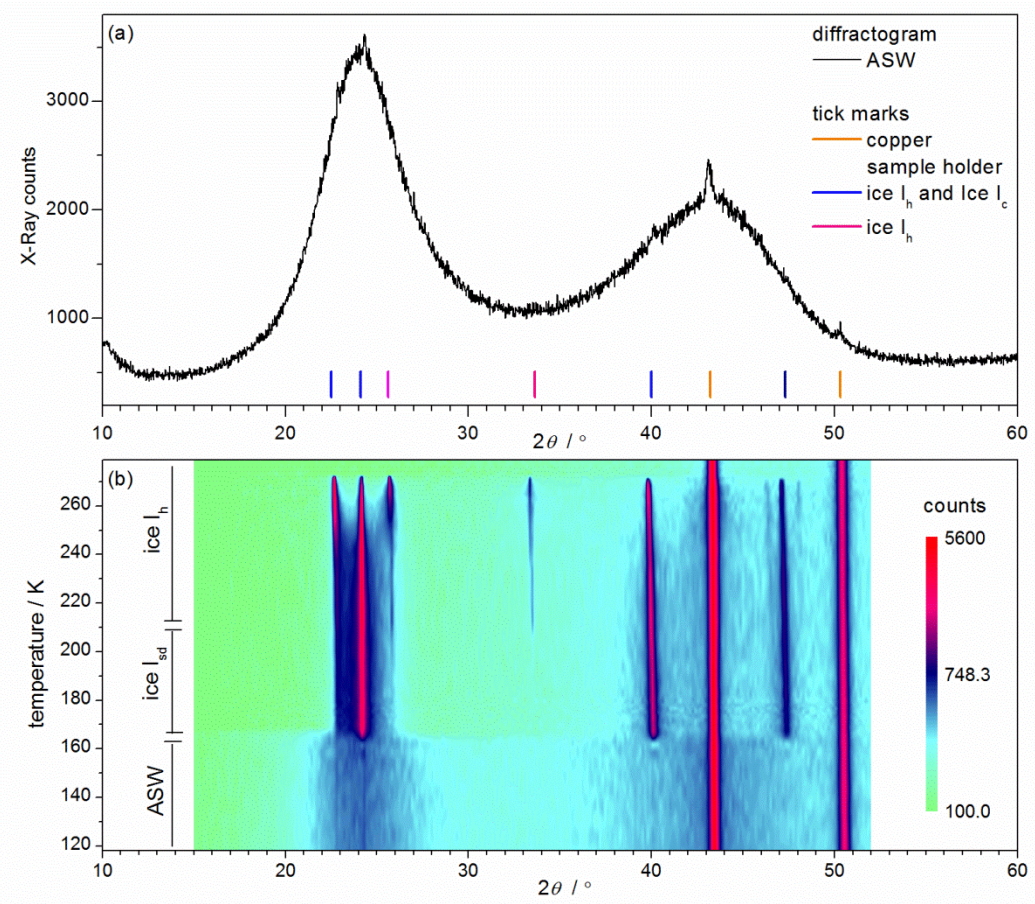

Figure 3.11 (a) X-ray diffractogram of the amorphous ASW/C_{60} 'trapped solution' (X_{C60} =0.0028) deposited onto a Si substrate, recovered, stored and transferred to a cryostat at 90 K (0.02055°, 1.17 s, 10-60°). (b) a contour plot with log scale showing the changing diffraction of the material as the temperature was allowed to increase at ~2.4 K min^{-1} (comprised from ~ 50 scans 0.02055°, 0.036 s, 10–52°). Tick marks in (a) show the expected position of reflections due to ice I_{sd} (blue) and ice I_h (blue and pink) and reflections due to the copper sample holder. These reflections are more intense in (b) than in (a) due to an increase in the width of the X-ray beam for these 'short scan' measurements.

Upon closer inspection of the diffraction pattern of the ASW/C_{60} trapped solution in (a), a small feature above the noise at 25° can be observed corresponding to a weak reflection of ice I. As the intensity of diffraction at this 2θ position is an order of magnitude greater in ice I than ASW (measured in the 150 and 160 K patterns) and the weak feature is only ~3 % of the total intensity, the ice contamination is estimated to be $0.1 \times 0.03 = 0.3$ %. Similar features were present for all of the measured ASW samples and in patterns of clean Si substrates cold loaded from liquid nitrogen, indicating that contamination most likely occurred due to the humidity from the air during transfer into the X-ray cryostat rather than during ASW preparation or recovery.

3.3 DESORPTION RATE ANALYSIS OF ASW GROWTH

3.3.1 RELATION OF H_2O DESORPTION RATE TO CHAMBER PRESSURE

In this section, changes in chamber pressure, reflecting changes in H_2O desorption rate, recorded as ASW deposited on the deposition stage warmed from 80 to 180 K have been used to probe the structure and morphology (surface area and porosity) of ASW. This is a similar technique to temperature programmed desorption (TPD) commonly used to study ASW.[69-70,146,155,161,167,170,187-195] The H_2O desorption rate is a good *in situ* probe of ASW's structure because it depends upon ASW's free energy (vapour pressure) and surface area.[155] The most pronounced change typically observed for ASW upon heating is a decrease in H_2O desorption rate upon crystallisation due to the much lower free energy of ice I relative to ASW. As the heating rate of these variable temperature measurements depended upon the amount of H_2O readsorption transport, which provided an additional mode of heat transfer to those discussed in section 3.2.2, a comparison of the heating rate data has allowed more information about the environment within the vacuum chamber to be extracted. This information is not usually available from temperature programmed desorption (TPD) measurements which typically employ fast linear heating rates and much thinner ASW films.[170]

The ASW films analysed in this section were all prepared using a centrally placed H_2O aperture positioned 20 cm from the deposition stage. In these measurements the chamber pressure

reflects the H_2O desorption rate because the steady state pressure monitored depends upon the balance of negative/outwards transfer due to pumping and the positive/inwards transfer caused by H_2O desorption. The subsequent readsorption of H_2O provided an additional negative/outwards transfer. An additional positive transfer due to chamber leaks will not significantly have affected the gas composition within the chamber which was consistently purged by H_2O desorption and pumping. The relationship between the chamber pressure, *p*, the pumping rate, *pmp,* desorption, *des,* and readsorption rates, *ads,* at steady state is given as Equation 3.1.

$$des = pmp(p) + ads.$$

Equation 3.1

As the variation in pumping rate with chamber pressure, *pmp(p),* is known from the response of the chamber pressure to different N_2 dose rates (Figure 3.3c) Equation 3.1 may be rearranged to Equation 3.2 giving the relationship between the chamber pressure and the H_2O desorption rates adjusted for readsorption, *des-ads*. For the data of this section an interpolation of the Figure 3.3c data was used to estimate the pumping rates and hence *des-ads,* from the measured chamber pressures. From a slightly different perspective; as *pmp(p)* for H_2O and N_2 may be assumed to be equivalent at these low pressures, the measured response of chamber pressure to different N_2 dose presented in Figure 3.3(c) can be viewed as a simulated H_2O desorption experiment with known H_2O desorption rates.

$$pmp(p) = des - ads.$$

Equation 3.2

3.3.2 A TYPICAL H_2O DESORPTION EXPERIMENT

This section discusses data for ASW deposited at a dose rate of 0.4 g h^{-1} for 2.5 hours (total chamber dose = 1.0 g) and introduces the conversions necessary to interpret the chamber measurements in terms of H_2O desorption rate. In sections 3.3.3 and 3.3.4 data are presented for different total chamber doses and different deposition rates. Figure 3.12(a) shows how the temperature of the deposition stage and chamber pressure varied as a function of time after the LN_2

cooling had been stopped, (b) and (c) shows the temperature variations in the effective desorption rate, *des-ads*, and the heating rate, respectively. Data are presented for an initial heating run (red line) and a subsequent, second, heating run (blue line), carried out after re-cooling the deposition stage from 180 to 80 K at ~5 K min^{-1}. The variation in chamber pressure with time (black line in a) and *des-ads* with temperature (red line in b) on the first heating run have a similar profile characterised by two regions of increasing pressure/*des-ads* separated by a region between ~140 and ~165 K in which they decrease. This produces a peak with maximum pressure/*des-ads* at ~140 K after ~ 25 minutes. In general the increases in chamber pressure and *des-ads* upon heating reflect the normal exponential increases in vapour pressure of ASW and crystalline ice as temperature increases.[170] The 'peak' is caused by the marked decrease in chamber pressure/*ads-des* as the irreversible transformation of ASW into crystalline ice occurs; ice has a much lower free energy and hence also a lower H_2O desorption rate than ASW. The shape and position of the 'peak' which reflects the size of the energetic barriers to desorption and crystallisation are in good agreement with the ultrahigh vacuum H_2O desorption rate measurements of Smith *et al.* carried out at similar heating rates.[170] The absence of 'peaks' in the data for the second warming run confirms that the ASW material had all crystallised on the first heating run.

The variation in the temperature of the deposition stage with time (green line in a) and the variation in heating rate with temperature (blue line in (c) shows a subtle decrease in heating rate as the temperature of the stage increased. In (c), the heating rate experienced for a clean deposition stage without any H_2O deposition is also shown for comparison (green line). This control primarily reflects the heat transferred through the tubes of the feedthrough and the convective heating processes that occur without any H_2O deposit on the Cu plate. The much greater heating rates experienced by the deposition stage with sample present indicates the extent of additional heating processes associated with ASW (first run) and crystalline ice (second run). Several possible causes for this additional heating have been considered. It has been postulated that exothermic relaxation of the ASW may be contributing to the heating, as observed by Ghormley *et al.*[168] However, the similar heating rate for ASW (first run) and ice (second run) indicates that the primary heating

process was not due to exothermic relaxations of ASW, which would have completed during first heating run. Instead it is believed that the additional heating is associated with the readsorptions of H_2O molecules after being heated by contact with the walls of the vacuum chamber. This hypothesis, although initially rejected because the heating rate does not closely follow changes in chamber pressure, may be true if the readsorption rate has a complex relationship to chamber pressure. A series of measurements is planned to confirm this hypothesis by measuring the rate of readsorption directly using a Quartz Crystal Microbalance.

Based on estimates of the deposition stage's heat capacity (~350 J K^{-1} at 80 K as described in section 3.2.2) and the difference between the heating rate with and without deposited H_2O at 80 K (~2 K min^{-1}), the readsorption can be calculated to contribute ~12 J s^{-1}. As the molar energy of water transferred by 80 K desorption and subsequent room temperature readsorption is about $3R\Delta T$ = 5.4 kJ mol^{-1} this implies a very large amount of H_2O readsorption, 2.2×10^{-3} mol s^{-1}. This is perhaps not surprising given the small flange area permitting flux to the diffusion pump (48 cm^2) relative to the total surface area inside the chamber (~1 m^2). This large amount of readsorption would also imply that the desorption rate, *des*, is much larger than *des-ads* and would bring the estimates of H_2O desorption rates more into line with those determined in mass spectrometry measurements by Smith *et al.*[170]. These are around two orders of magnitude greater than our *ads-des* values and for much thinner ASW films (100 ML *vs* ~27000 ML of crystalline ice). Despite the significant H_2O readsorption seemingly occurring in these experiments, the features in *des-ads* appear to retain their dependence on the excess free energy and surface area, and are thus representative of ASW's morphology.

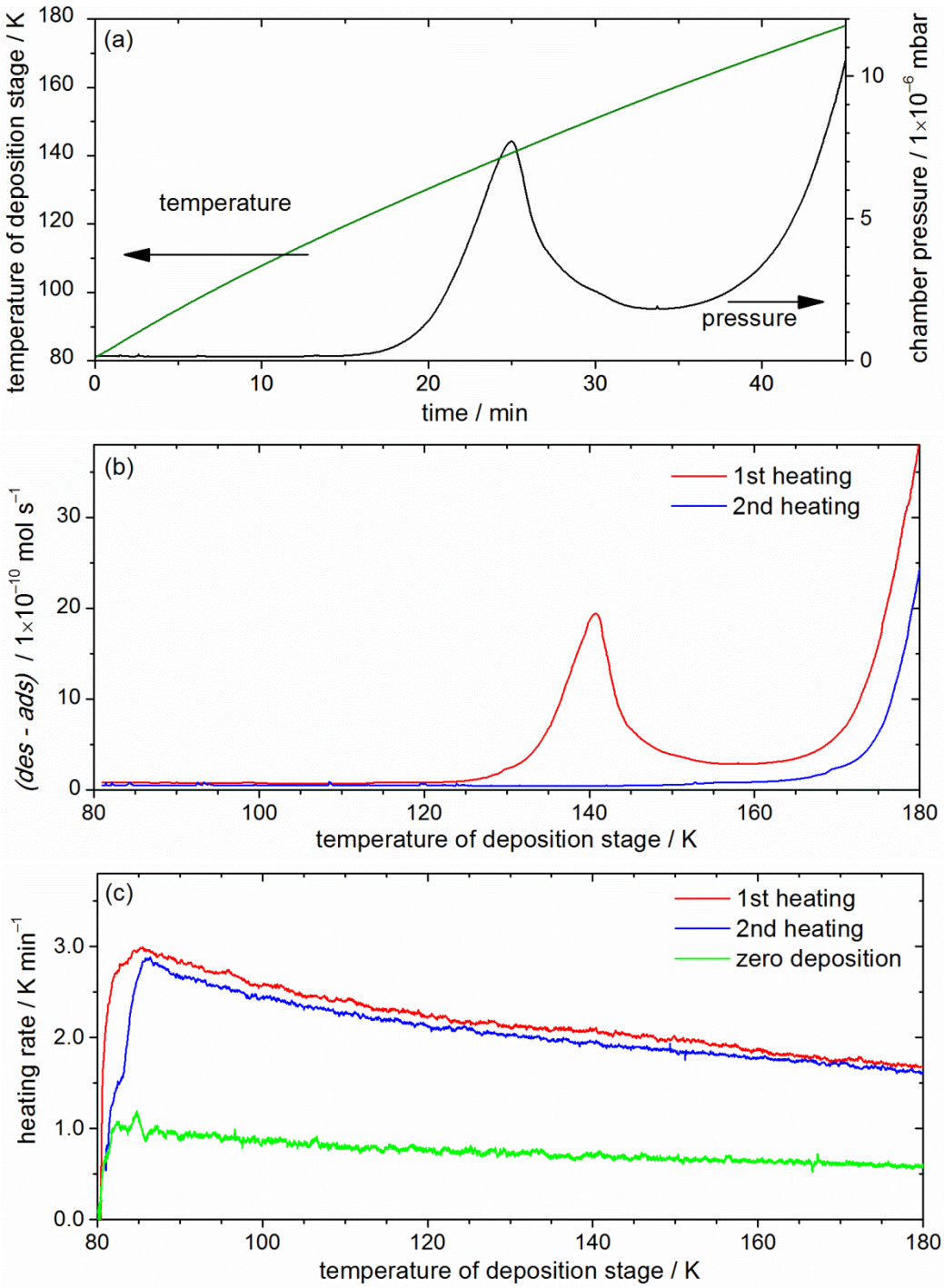

Figure 3.12 (a) Variations in chamber pressure (black line) and temperature (dark green line) with time whilst heating an ASW deposit formed at an aperture-deposition plate distance of 20 cm from a total H_2O chamber dose of 1.0 g introduced to the chamber at a rate of 0.40 g h^{-1}. (b) Variations in *des-ads* with temperature for this 1st (red line) and also a 2nd (blue line) heating cycle (c) Variations in heating rate for 1st and 2nd heating cycles and the variation in heating rate with temperature for the deposition stage without any ASW (green line).

3.3.3 Exploring the Changes in ASW Morphology during Growth

The visual appearance of the deposited material changed during ASW's growth indicating changes in the materials morphology. The first visible signs of the deposition were concentric circles of colour centred on the umbra of the deposit. These are caused by the constructive interference of visible light through the sample sometimes referred to as Newton's rings. The coloured rings were followed by the appearance of a white opaque frosting which grows from the centre. After approximately 0.5 g of chamber dose, the frosting completely covers the plate and small 'stalactites' start to become visible, hanging from the main body of ASW. After approximately 1.5 g of deposition, these stalactites can be seen to fall from the deposition plate and vaporise upon contact with the floor of the vacuum chamber. Some variation in the morphology of the samples was also observed after recovery into LN_2. Whilst thick samples were typically opaque with a white milky appearance, brittle and easy to remove, thinner samples (and the bottom layers of thicker samples), were translucent and more strongly connected to the copper deposition plate. For deposits formed from > 2 g of total chamber dose, regions of loose material, which we presume to be crystalline, were also sometimes found on the deposition plate. Interestingly, the loosest region typically formed in a ring around the centre of the plate with a radius of 2–5 cm. This observation, discussed further in Section 3.3.5 is somewhat counterintuitive as the highest deposition rates and hence the thickest deposits are expected to be in the centre at deposition angles in line with the H_2O aperture.

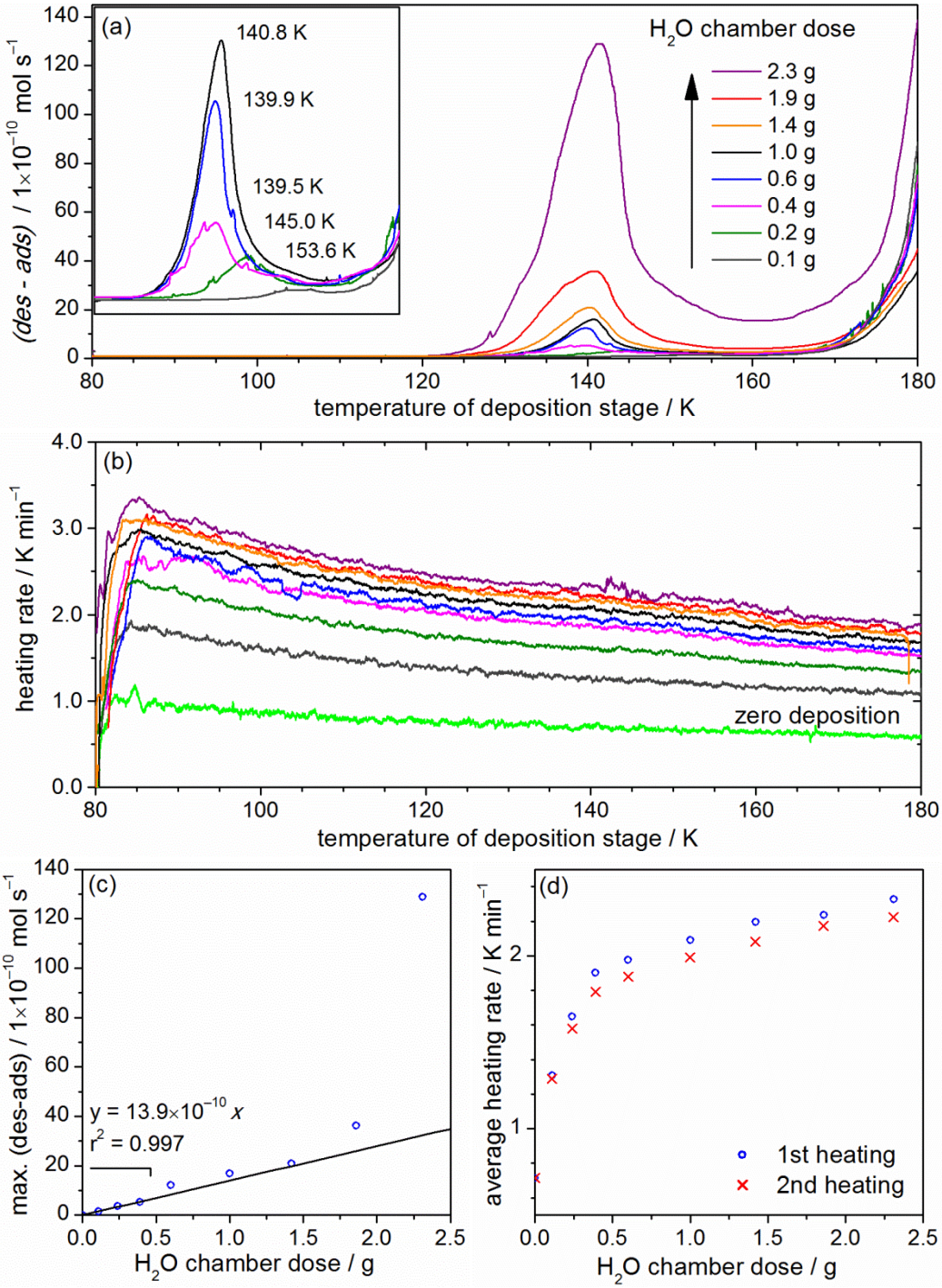

Figure 3.13 Desorption (a and c) and heating rate (b and d) data for ASW formed from different amounts of total H_2O chamber dose. For this series of measurements, a constant dosing rate of 0.4 g h^{-1} was used and the deposition time was varied between 10 minutes and 7 hours. The variations with temperature are indicated in (a) and (b). The inset in (a) shows the change in shape and maximum of the 140 K 'peak'. The 'peak' maximum is shown in (c) and the average heating rate between 90 and 180 K is shown in (d)

To better understand these changes in morphology and the factors allowing ASW formation without crystalline ice contamination, H_2O desorption (*des-ads*) and heating rate data were recorded for ASW films of different thicknesses. To vary the thickness, ASW films were prepared with a 0.4 g h^{-1} H_2O chamber dose rate for different periods of time, corresponding to different amounts of total H_2O chamber dose. Figure 3.13(a) and (b) show the variation in *des-ads*, and heating rate with temperature for the first heating run of ASW films prepared with total chamber doses between 0.1 and 2.3 g. The green line in (b) gives the heating rate for a clean deposition plate free of ASW (zero dose). The *des-ads* and heating rate data show significant differences with increasing chamber dose. The most pronounced effect is the increases in heating rate and *des–ads* in the temperature range between 80 and 145 K with ASW thickness. The dependence of these quantities on ASW thickness are shown most clearly in Figure 3.13(c) and (d) which give the variations in the maximum value of *des-ads* at ~140 K and the average heating rate between 90 and 180 K for the first and second warming runs, respectively. In addition to these variations, the inset in (a) gives an enlargement of the *des-ads* data for the thinnest films, showing a change in slope of *des-ads*, and decrease in ASW crystallisation temperature with increasing ASW thickness.

Figure 3.13 shows a linear relationship between maximum *des-ads* and total chamber dose for thin ASW films. A non-porous film would be expected to display a constant surface area, and hence desorption rate, for films of varying thickness. The data therefore suggests that the ASW formed is highly porous, giving a surface area, and hence desorption rate, which is proportional to the amount of H_2O deposited. Based on this understanding of ASW's porosity, the other trends in the data such as the increasing heating rate and shift in crystallisation temperature can be explained more easily. The most important concept is that as the ASW deposit grows there is a decrease in its ability to conduct heat from its surface to the deposition stage below. This is due to both an increase in thickness and also an increases in porosity which reduces the cross sectional area available for the heat to be transferred. Fourier's law relating the rate of heat transfer, *q*, to the

cross sectional area, *A*, the temperature gradient, ΔT, the material's thermal conductivity, *k*, and thickness, *x*, is given in Equation 3.3.

$$q = -kA\frac{\Delta T}{x}.$$

Equation 3.3

This heat transfer effect is most clearly demonstrated in the inset of Figure 3.13(a) which shows a decrease in crystallisation temperature from 154 to 140 K with increases in total chamber dose from 0.1 to 0.4 g. This decrease is associated with a growing temperature gradient across the film caused by H_2O readsorption mediated surface heating and an inability to transfer this heat to the deposition stage. The crystallisation temperatures approach the DSC-measured crystallisation temperature (~156 K),[86] for zero chamber dose. Furthermore, for these thin films the average heating rate shown in (d) increases almost linearly with total chamber dose reflecting an increasing amount of H_2O readsorption heating the surface. The morphology of the ASW over this range of film thicknesses, although porous, was consistent, giving translucent films which adhered strongly to the deposition stage.

The change in morphology during the growth of thicker films, which became increasingly opaque, is also reflected in the *des-ads* and heating rate data. For total chamber doses > 0.4 g, the maximum *des-ads* and heating rate begin to change differently with increases in films thickness. Increases in heating rate become less pronounced and increases in *des-ads* become more pronounced. A change in the morphology, characterised by the appearance of stalactites with a poor thermal connection to the deposition stage, may be expected to cause a local heating of the stalactites rather than heating the deposition stage. This effect would then account for the decrease in heating rate and increase in pressure as thickness increased because the local heating would increase the rate of H_2O desorption. This local heating would also be expected to lead to its premature crystallisation at the surface and limit the thickness to which ASW can be grown without ice contamination. This process affected the shape of the *des-ads* profiles giving low temperature shoulders most visible for total chamber doses of 1.9 and 2.3 g. Such premature crystallisation

would also cause the maximum in *des-ads* at ~140 K to be an underestimate of the maximum which would be obtained if the entire ASW film were to transform at a single temperature. The local heating may also be expected to cause some sintering of the stalactite material at the surface, increasing effective density stimulating them to fall from the main body of the deposit, as observed through the viewing window during growth.

The stages of ASW's growth discussed above are shown schematically in Figure 3.14. Figure 3.15 shows the relationship between maximum *des-ads* and average heating rate, highlighting the chamber dose at which increases in thickness cause disproportionately large increases in pressure indicative of stalactite formation, and only small increases in heating rate, implying a significant reduction in thermal contact between the surface and base of the ASW films.

3.3.4 Influence of Deposition Rate on ASW Porosity

To determine if ASW's porosity was influenced by changes in deposition rate a similar series of H_2O desorption experiments were carried out on ASW formed from a total chamber dose of 1 g deposited at rates between 0.2 and 5.8 g h^{-1}. As discussed in the previous section, the thermal contact of ASW with the cooled deposition stage begins to break down at a chamber dose of 1 g. This chamber dose is therefore a good choice for probing the influence of deposition rate on ASW porosity. Figure 3.16 shows a similar set of data to those discussed in Sections 3.3.2 and 3.3.3: (a) shows the temperature variation in *des-ads*, (b) the temperature variation in heating rate, (c) the variation in maximum *des-ads* with deposition rate and (d) the variation in average heating rate with deposition rate.

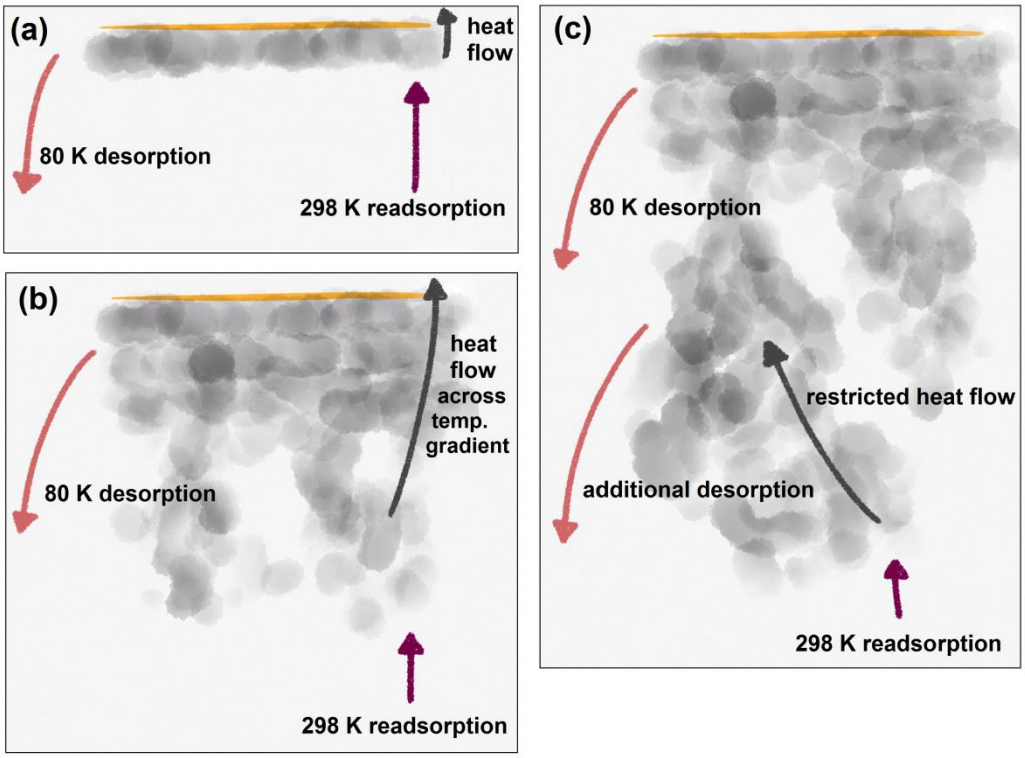

Figure 3.14 Schematic illustration of the different heating regimes occurring during ASW deposition: (a) During the initial stages (thin ASW films) H_2O desorption and subsequent readsorption processes produce a flow of heat towards the deposition stage which is roughly proportional to the thickness of the deposit, (b) As the thickness of the ASW film increases its ability to transfer heat from the surface to the deposition stage decreases, creating a temperature gradient, (c) as the thickness increases further and the heat transfer continues to decrease the thermal energy from readsorption stimulates additional desorption processes increasing the chamber pressure.

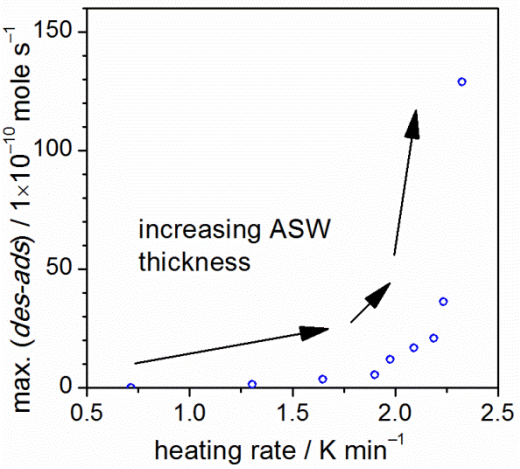

Figure 3.15 The relationship between the maximum H_2O desorption rate and average heating rate. Points from left to right are for 0, 0.2, 0.4, 0.6, 1.0, 1.4, 1.9 and 2.3 g total chamber dose.

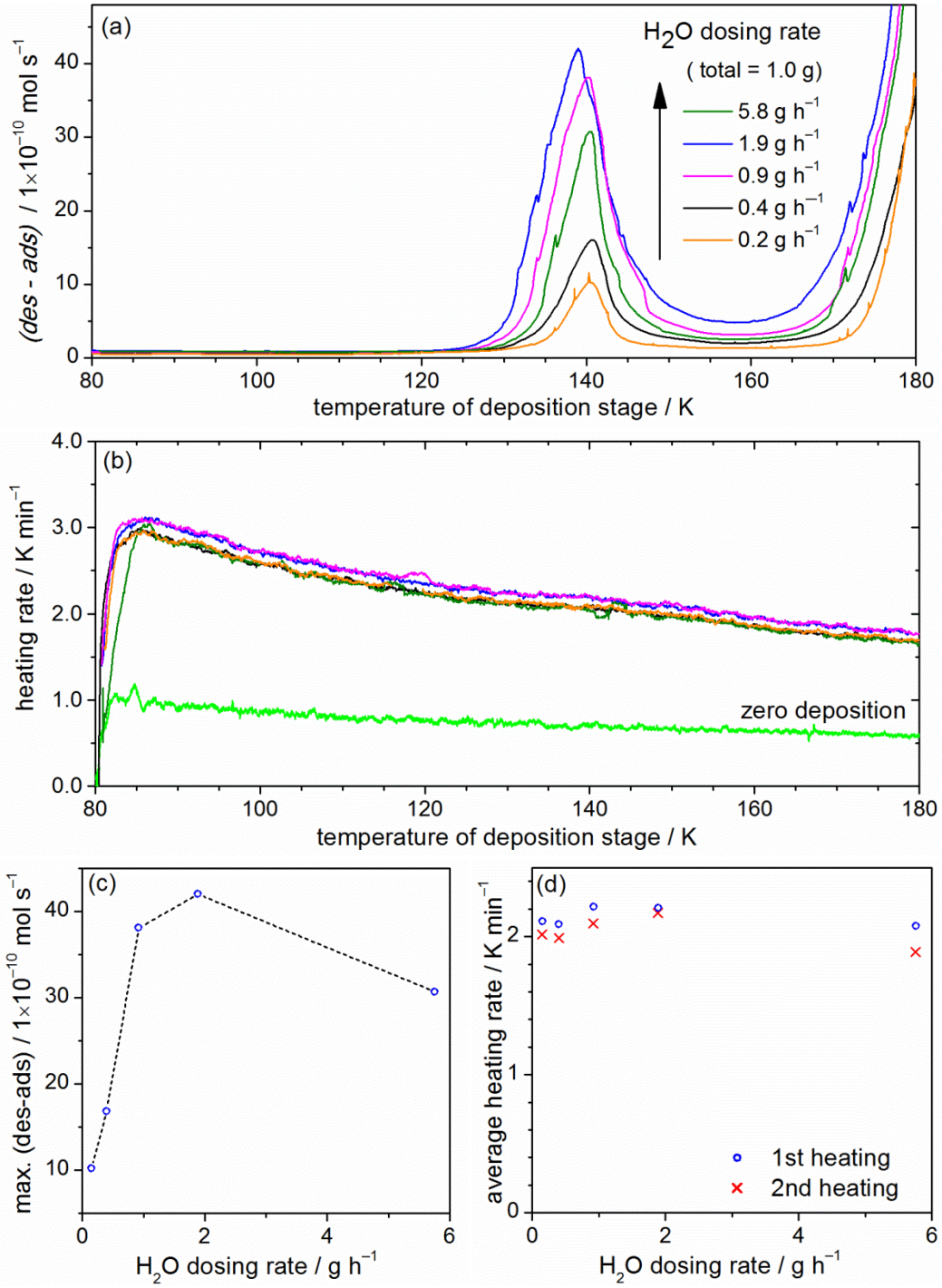

Figure 3.16 Desorption (a and c) and heating rate (b and d) data for ASW deposited at different dose rates. For this series of measurements the deposition time was varied to give a constant total H_2O chamber dose of 1.0 g. The variation with temperature are indicated in (a) and (b), the maximum ASW desorption rate is shown in (c), with dashed line to guide the eye, and the average heating rate between 90 and 180 K is shown in (d).

The temperature variations in *des-ads* and heating rate shown in Figure 3.16(a) and (b), look similar to those described in section 3.3.3, again showing a maximum in *des-ads* relating to

the surface area of ASW and a heating rate reflecting the heat transfer to the deposition stage *via* H_2O readsorption. However the changes with increasing deposition rate, shown in Figure 3.16(c) and (d) do not follow the changes for variations in ASW's thickness. Whilst the deposition rate has little influence on the average heating rate for these deposits, the maximum in *des-ads* varies between ~10×10^{-10} mol s^{-1} for 0.2 g h^{-1} to 40×10^{-10} mol s^{-1} for 1.9 g h^{-1}. This suggests that deposition at higher rates gave more porous deposits with poorer thermal contact and hence greater *ads-des*. This in turn implies that the maximum thickness of ASW deposit which can be formed without ice contamination may be extended by reducing the deposition rate. Interestingly, for ASW deposited at 5.8 g h^{-1} (green line in a), the maximum *des-ads* was found to be lower than for deposition at 1.9 g h^{-1}. This suggests that some of this deposit had crystallised, *prior* to the warming run.

3.3.5 THE SPATIAL DISTRIBUTION OF H_2O READSORPTION

Interestingly, the crystalline material sometimes recovered on the deposition plate for depositions with large total chamber dose or at high deposition rates, was not positioned in the centre of the plate, as might be expected from the angular dependence of H_2O flux, but was in a small ring around the centre of the plate. The approximate spatial distribution of the crystalline ice (which was clearly visible as it adhered poorly to the deposition plate), is shown in Figure 3.17(a). The crystalline region is indicated by the light blue ring surrounding the central dark blue circle, corresponding to ASW. As the size of the ring matches the dimensions of the recess in the walls of the chamber housing the H_2O inlet, directly below the deposition stage, I believe this volume causes a focussing in the H_2O readsorption on the deposition plate, heating the ASW. This is shown in Figure 3.17(b). This theory is supported by the understanding of gas movement within vacuum systems which cause small or restricted volumes to pump down much more slowly than the main body of the chamber.[183,196] This effect becomes most pronounced at low pressures because the fluid like flow properties of gases depend upon collisions, which are only available at higher pressures.

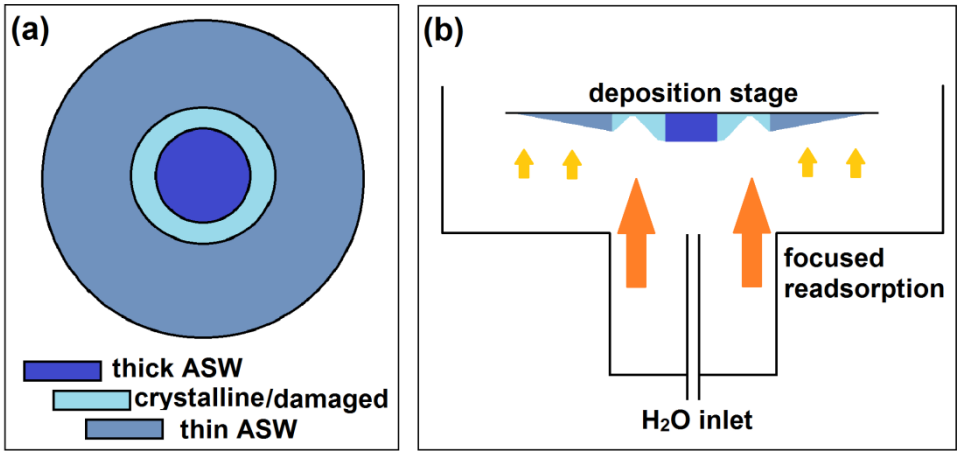

Figure 3.17 schematic illustrations showing (a) the uneven distribution of crystallisation on the deposition stage observed for thick deposits (> 2 g) and (b) a focusing of the H_2O readsorption caused by free volume within the vacuum chamber, thought to be the most likely cause of the spatial inhomogeneity.

3.4 CONCLUSIONS

In conclusion, careful study of the chamber properties has shown that the highest yields of ASW can be obtained using slow deposition rates and long deposition times. The lower porosity and greater heat transfer for deposits formed at lower deposition rates enable the growth of thick samples. As increasing the deposition time beyond 6-8 hours was impractical, the material analysed in this study was typically produced using a 0.4 g h^{-1} H_2O dose rate, which for a 5 hour deposition and an aperture to deposition plate distance of 20 cm reproducibly gave >1 g of ASW free of crystalline ice contamination. These thickness and rate limits may possibly be extended by removing or covering the recess around the water inlet to limit the focussing of H_2O readsorption or through a better understanding of the expansion characteristics of the H_2O beam. The incoming flux should be checked for the self-association of H_2O into clusters using spectroscopic methods,[169,197] and the H_2O inlet may need to be redesigned to give thermal equilibration between several sequential decreases in pressure. Overall, however, the chamber works very effectively in producing ASW and ASW/C_{60} 'trapped solutions' which are the focus of the structural investigations presented in Chapter 4 and 5.

4 The Structural Relaxations of ASW

4.1 Introduction

The structural changes which occur when metastable materials such as ASW become more thermodynamically stable are called relaxations. The rates at which relaxations proceed depend upon the potential energy barriers limiting the movements or reorganisations required for the structure to become more stable.[76] Upon heating ASW, several different relaxations have been found to occur: a macroscopic densification and pore collapse active from ~40 K, termed sintering; increases in the structural ordering of the oxygen-oxygen distance observed at ~130 K, termed structural annealing; and a long range periodic positional ordering at ~160 K, crystallisation. The main evidence for sintering, structural relaxation and crystallisation are, respectively, large exothermic heat signals,[69,144,168] the sharpening of ASW's X-ray diffraction pattern,[87] and the emergence of Bragg peaks (Figure 3.11). The relaxations of ASW are driven by increases in hydrogen bonding interactions which increase as the structural state evolves towards the periodic tetrahedral hydrogen bonding coordination of ice I. Sintering stabilises ASW by reducing the number of under-coordinated surface molecules and it may also be assumed that the subtle local ordering of oxygen-oxygen positions (indicated by the sharpening of the diffraction pattern) also gives rise to increases in the net hydrogen bonding interaction.[87] These observations of ASW's relaxation suggest that the structure of 'as-prepared' ASW will be 'unrelaxed' on local and on more extended length scales.

In order to understand the structural changes occurring during sintering, annealing and crystallisation, it is useful to have an understanding of the mechanisms preventing the relaxations of the metastable supercooled liquid upon cooling. This is because the mechanisms influencing the rate of relaxations upon cooling liquid water may be assumed to be reversed upon warming ASW. The most thermodynamically stable state in the supercooled regime at ambient pressures is ice I. The metastability of supercooled water at temperatures above the homogenous nucleation temperature is thought to be mostly entropic as the thermal motions and random reorganisations of the dynamic liquid prevent a crystal nucleus of sufficient size from forming. However, at lower temperatures, as the glass transition temperature (T_g) is approached, the rate of structural relaxation

becomes increasingly limited by slowing of molecule movements. At T_g the translational motions (α-relaxations) of the molecules are believed to become inactive on the experimental time scale, causing the system to become kinetically arrested or vitrified. The mechanisms slowing down dynamic motions as glass transitions are approached is still an active area of liquids research,[198] but there is growing evidence, reviewed by Malins[199] suggesting that the dynamics are strongly dependent on the intermolecular structure and that the distance of the correlation increases with decreasing temperature. In other words, the vitrification process and the eventual 'jamming' of the dynamics at temperatures around the T_g may be related to increases in the structural cooperativity with decreasing temperature. The increasing correlation length can be understood to originate from the impact of multi-body interactions on the potential energy of the transition states between local minima encountered during motion of the molecules.[198] This concept suggests that relaxation over different length scales will be favoured at different temperatures, predicting that as liquids are cooled mesoscale structural ordering occurring may become increasingly in competition with long range structural ordering, further frustrating crystallisation.[200] The impact of this structural inhomogeneity on the dynamic heterogeneity in supercooled glycerol has also recently been measured experimentally.[201]

On heating ASW, the opposite changes in dynamics and structural correlation may be expected to govern the rates of the relaxations occurring. *i.e.* with increasing temperature the correlation length should decrease 'unjamming' the kinetics.[76] For ASW, which will be 'unrelaxed' on different length scales, the link between structural inhomogeneity and dynamic heterogeneity may be particularly important in explaining certain unusual characteristics of its relaxation. For example, structure-dependent heterogeneous dynamics would explain the much greater temperature required for crystallisation (~155 K) than sintering (~40 K). If the dynamics were independent of structure these relaxations would be expected to occur at a similar temperature. On the other hand, a correlation between the dynamics and the mesoscale structure would provide a reason for the increased mobility of surface molecules relative to those in the bulk at a given temperature. Similar increases in surface mobility are also integral to understanding the premelting and sintering

behaviour commonly observed for crystalline materials below their melting point.[202] In ASW, a significant structural heterogeneity introduced by the deposition process may also be expected to occur in the bulk. Based on this concept, nano- or mesoscale-sized regions in ASW with particularly favourable positional or orientational ordering would have slower relaxation dynamics than less strongly bound regions. It is particularly interesting to consider that the specific length scale of the coupling between dynamics and structure may mean that structurally more ordered regions formed during the relaxation can have faster dynamics than the regions which remain unrelaxed. The complexity of the situation upon cooling liquids and upon warming amorphous solids, are discussed by Debenedetti *et al*.[198] and Angell *et al.*[76], respectively.

Changes in the dynamics of ASW upon heating have been investigated using differential scanning calorimetry (DSC)[203] and reversible increases in heat capacity have been observed between 124 and 136 K in both ASW and hyperquenched glassy water (HGW).[85-87,144] This increase has been assigned by some to the glass-liquid transition and mechanical indentation,[145] isotope exchange,[146] dilatometric,[147] neutron scattering[204] and deuteron NMR[88] measurements have been presented in support of this conclusion. The assignment of the feature to the T_g may appear to be fairly intuitive because ASW and HGW begin to crystallise much more rapidly at temperatures above 136 K. However, these studies have not, in the main, considered the considerable structural and dynamic heterogeneity predicted to occur in ASW and HGW. Angell and co-workers have pointed out that dynamic heterogeneity can give rise to very similar DSC signals, termed a shadow T_g, in a range of glass-forming systems and it has been suggested that the true glass-liquid transition should be at much higher temperatures.[77,148-149] It is also not clear which forms of dynamic motion are contributing to the DSC signal. Although it is presumed to be translational diffusion, defect migration, which causes reorientation of the H_2O molecules,[205] becomes active in crystalline phases of ice at around 130 K.[30,92,206-207]

An indirect approach to assess the changes in the dynamics of ASW with temperature is to look for indicators of ergodicity at temperatures above the proposed T_g. Conceptually, ergodicty would be expected above T_g because the motions would enable many different structural states to

be explored on the experimental timescale. It would be indicated if the average structure of materials heated above T_g were to reflect the temperature rather than the extent to which irreversible relaxations had been possible. An examination of metastable ergodicity has been possible by comparing the structure of the materials formed upon heating different low density amorphous ices (LDA) above the proposed T_g. In addition to ASW, formed by vapour deposition,[59,143,158] LDA and HGW formed by hyper quenching small droplets of liquid water (HGW),[57-58,86,208] LDA may also be formed by the relaxation of high-density amorphous ice (HDA), itself formed by compressing crystalline ice I_h.[55,62] Unfortunately, however, the structural evidence is conflicting and spectroscopy,[68,209] thermal conductivity,[210] and diffraction techniques[154,211] may be insufficiently sensitive over the correct length scales to differentiate between different structural states. Neutron diffraction with isotopic substitution has shown that LDA from HDA, ASW and HGW have identical structures.[154] On the basis of spectroscopic,[68,209] and thermal conductivity measurements,[210] as well as free-energy considerations,[72] it has been argued that LDA obtained from HDA is structurally different from ASW and HGW,[68,72,209-210] which were found to have similar structures.[87,209] In a later study using neutron diffraction sensitive to structural differences over a wide range of different length scales, two states of LDA with subtle structural differences were identified.[211] LDA-I was obtained by annealing HDA, and LDA-II was obtained by converting HDA to very high-density amorphous ice (vHDA) by heating at pressures greater than 0.8 GPa,[136,139] and then by isothermally decompressing this material at 140 K. This process is thought to proceed *via* the expanded high-density amorphous ice (eHDA) state.[55,212] LDA-I is proposed to have a more ordered first-neighbour environment and LDA-II was found to be more structurally ordered between 3.5 and 7.5 Å.

In this chapter, Raman and transmission FT-IR spectroscopies are used to follow the structural relaxations of ASW prepared as thin films in our vapour deposition apparatus. The Raman data for ASW have also been compared with similar data for LDA formed from HDA, eHDA and vHDA allowing a spectroscopic comparison of the recently discovered LDA-I and LDA-II states.[154] The main findings of this chapter are reported by Shephard *et al*..[2]

4.2 Results and Discussion

4.2.1 FT-IR Spectroscopy of Isolated O-D Oscillators in ASW

The ASW samples used for these transmission FT-IR measurements were prepared with deuterium as an isotopic impurity (91.0 mol% H_2O + 9.0 mol% HDO) and deposited as thin films (0.4 g total chamber dose) on MgF_2 substrates. The ASW-coated MgF_2 substrates were then transferred under liquid nitrogen into an 78 K cryostat. Owing to the low concentration of deuterium and the substantial frequency mismatch between the O–H and O–D oscillators, decoupled μ(O–D) modes can be observed.[213] Because these modes show very little inter- or intramolecular coupling, the position and width of the μ(O–D) absorption reflects the strength of the O–D bonds (hydrogen bonding weakens the covalent bonds) and the diversity of hydrogen bonding environments, respectively. As the structural relaxations of ASW are driven by increases in hydrogen bonding, μ(O–D) absorptions are an ideal probe to study the processes occurring during sintering, thermal annealing and crystallisation.

Two different approaches were used. The first involved recording spectra at 30 s time intervals as 'as-prepared' and 'preannealed' (122 K for 2 h) ASW films were heated from 78 to 180 K at ~4 K min^{-1}. The second approach involved heating an ASW film to successively higher temperatures, waiting for 5 minutes at each annealing temperature then recooling to 78 K for spectral acquisition. The first approach enabled the spectral changes occurring up to and during crystallisation to be observed; the second approach allowed the structural changes caused by the thermal annealing steps to be examined independently of the reversible influences of temperature. Peak fitting (pseudo-Voigt) was used to follow the subtle changes in peak position and width. Variable temperature, (T) data are shown in Figure 4.1 and 4.2 and variable annealing temperature (T_A) data, recorded at 78 K, are shown in Figure 4.3.

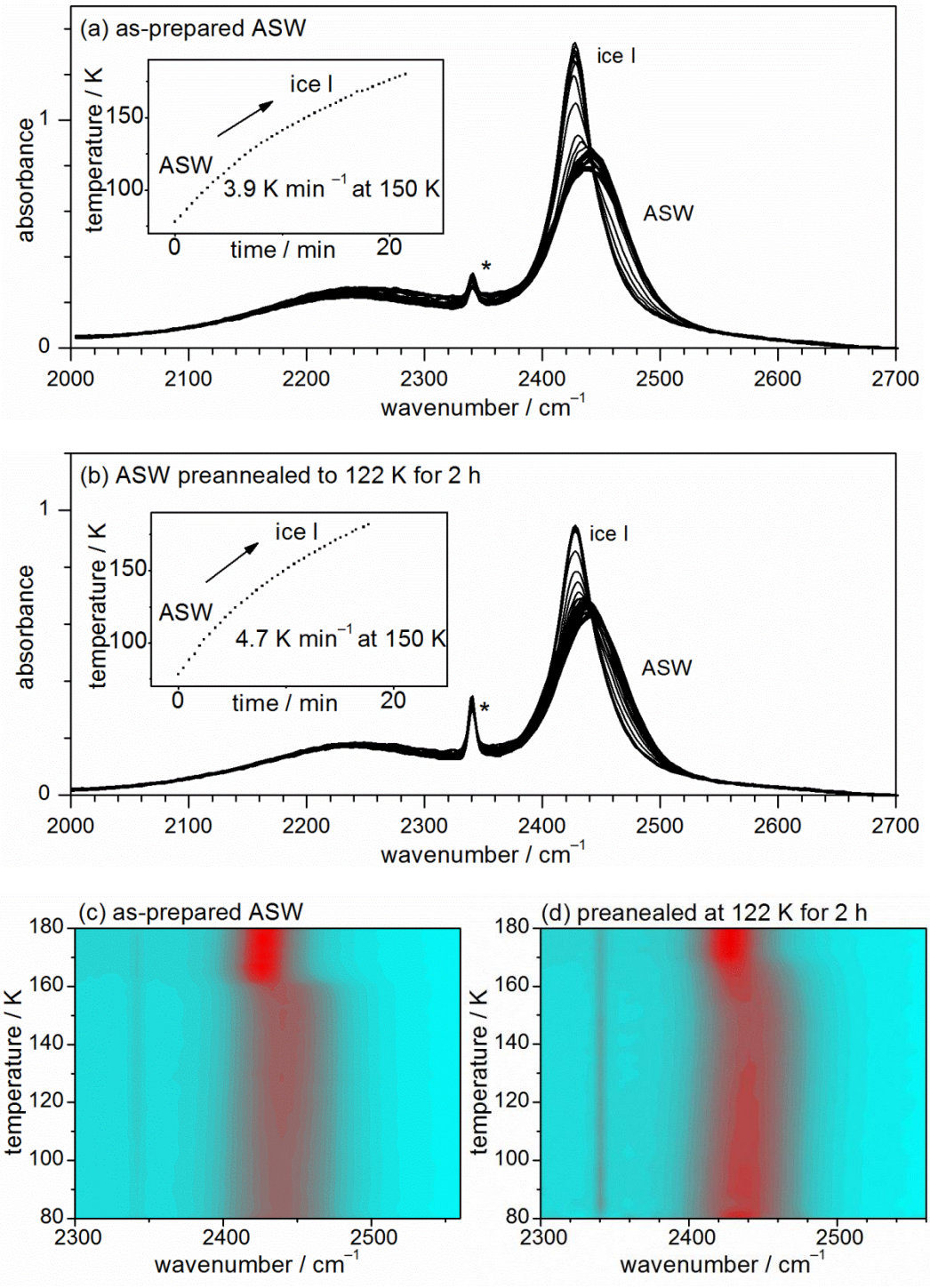

Figure 4.1 Variable temperature FT-IR absorbance spectra of μ(O–D) vibrations in ASW (91.0 mol% H_2O + 9.0 mol% HDO) deposited onto MgF_2 substrates from 0.4 g of total chamber dose. Data are presented for an 'as-prepared' ASW film (a and c) and an ASW film which had been annealed in the cryostat at 122 K for 2 hours *prior* to the heating run (b and d). The spectra are shown overlaid with corresponding heating rate data in (a and b). The spectral variations with temperature are indicated more clearly in the contour plots (c and d). * The peak at 2430 cm^{-1} is an absorption due to the CO_2 present in the spectrometer housing.[214]

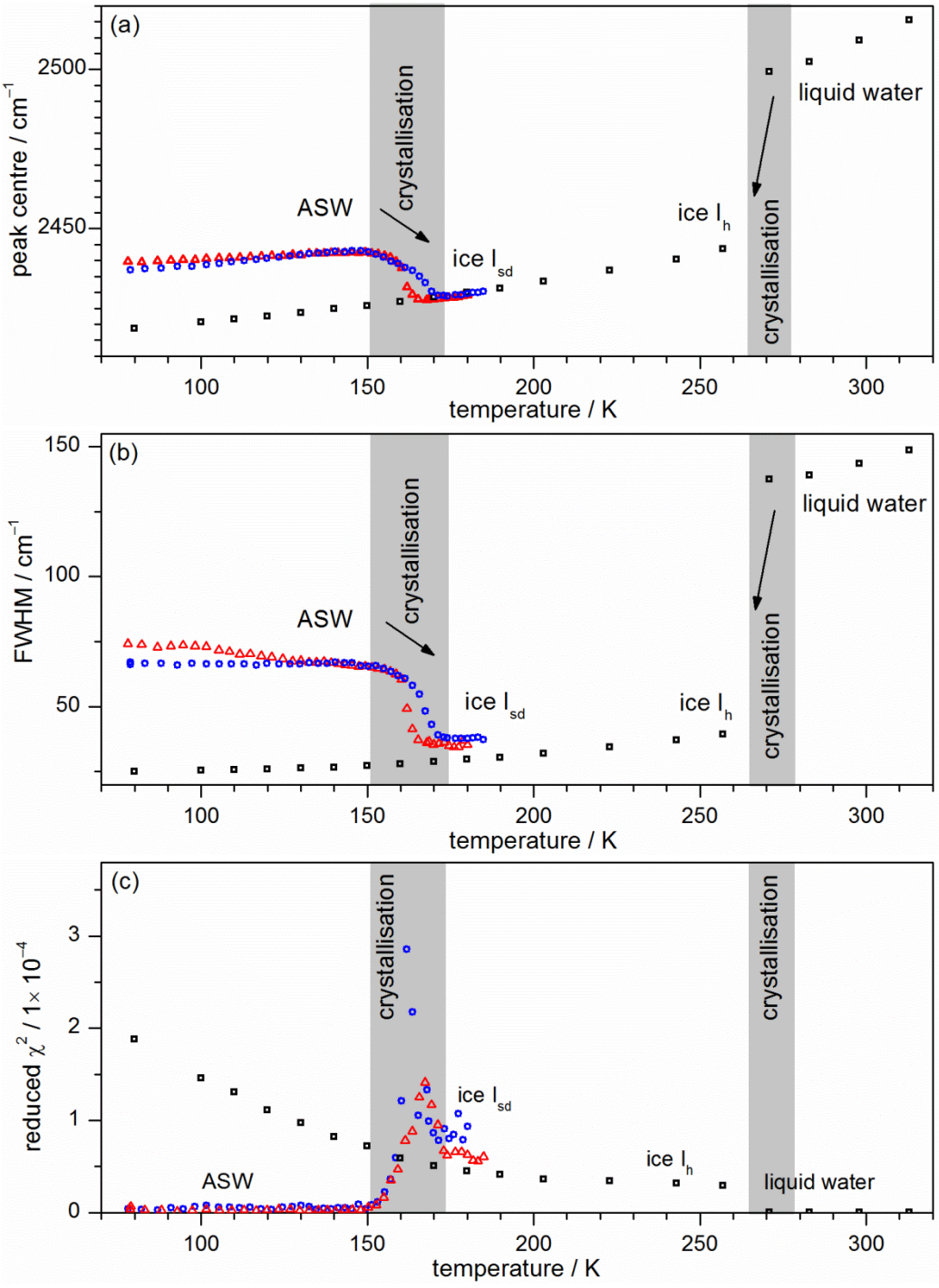

Figure 4.2 A comparison of position (a), FWHM (b) and goodness of fit obtained by peak fitting the μ(O–D) absorptions of 'as-prepared' ASW (red triangles), preannealed' ASW (blue circles), liquid water and ice I_h (black squares) with a single pseudo-Voigt peak.

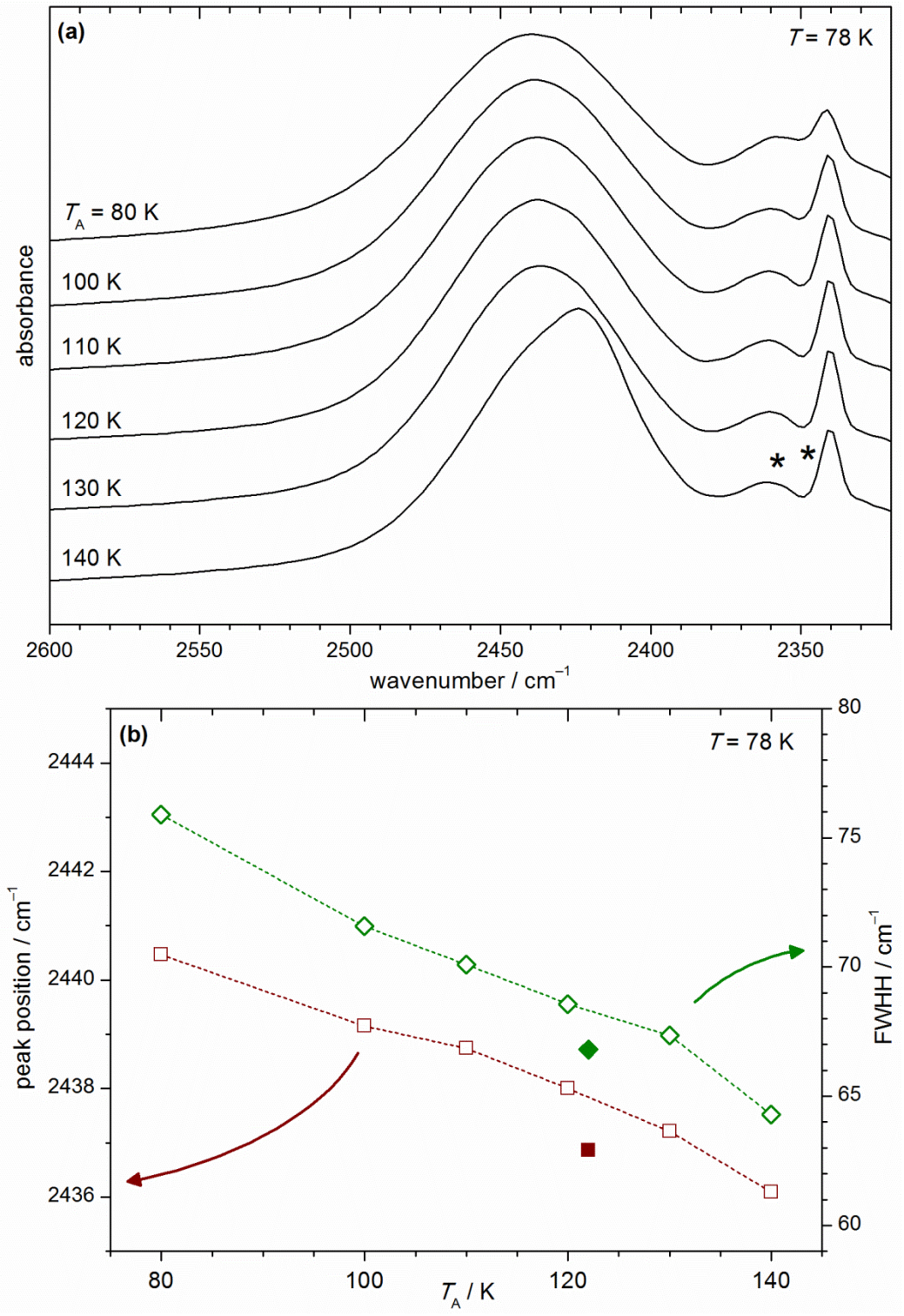

Figure 4.3 (a) FT-IR spectra of the μ(O–D) absorption of ASW (91.0 mol% H_2O + 9.0 mol% HDO) deposited onto MgF_2 substrates from 0.4 g of total chamber dose and annealed for 5 minutes at successively higher temperatures. (b) A comparison of the fitted position (brown squares) and width (FWHM) (green diamonds) pseudo-Voigt peak parameters. For the 140 K spectra a second pseudo-Voigt peak was used to fit absorptions due to crystalline ice. The position and FWHM obtained for ASW held at 122 K for 2 h and already presented in Figure 4.2 are also given (filled symbols). *an absorption due to the CO_2 present in the spectrometer housing.

Figure 4.1 shows FT-IR absorbance spectra in the region of the μ(O-D) mode recorded during heating between 78 and 180 K for 'as-prepared' ASW (a) and an ASW film which had been preannealed at 122 K for 2 hours (b). The spectra are comprised of a main absorption feature at ~2440 cm^{-1} due to μ(O–D),[209] and a broad secondary absorption centred at ~2230 cm^{-1} due to a combination of libration and bending of the H_2O molecules. The changes in the shape of the main absorption feature with temperature and those caused by 122 K preannealing can be more clearly observed in the contour plots (Figure 4.1 (c) and (d) and as changes in the fitted peak parameters (Figure 4.2). Figure 4.2 also shows peak position and FWHM parameters extracted from the μ(O-D) spectra of liquid water and crystalline ice I_h obtained upon cooling a small amount of liquid (91.0 mol% H_2O + 9.0 mol% HDO) trapped between two MgF substrates. Figure 4.2(c) shows the goodness of fit which decreases at temperatures near the ASW–ice I phase transition (150–160 K) and as crystalline ice I_h is cooled. The poor fit to a single pseudo-Voigt peak at temperatures near the ASW-ice I_{sd} phase transition is due to the contribution of two overlapping absorptions to the absorption band and indicates the partial transformation of ASW into ice I_{sd}. The increasingly poor fit of the ice I_h spectra to a single pseudo-Voigt peak with decreasing temperature is due to the more ordered structure of ice I_h which gives rise to some mode couplings. The equivalent spectra and peak fit data of Figure 4.3 are for an ASW film recorded at 78 K after being annealed for 5 minutes at sequentially higher temperatures.

The most pronounced change in the position and width of the μ(O-D) absorption was observed at ~155 K in the variable temperature data and after annealing at 145 K in the variable annealing temperature data. The decrease in width and position of the absorption is indicative of ASW's crystallisation into ice I_{sd}.[61,213] However, the spectra also show some changes at lower temperatures, thought to be associated with a combination of irreversible precrystallisation relaxations (sintering and thermal annealing) and the reversible impacts of temperature on structure. The spectral extent of the structural relaxations are most clear in Figure 4.3(b) data showing the fitted peak parameters of the spectra recorded at 78 K, which are therefore independent of reversible temperature effects. In this plot the *x*-axis corresponds to the annealing

temperature, the empty symbols correspond to the 5 minute annealing periods and the solid symbols correspond to a 2 hour annealing period. The data indicate that the position and width of the μ(O–D) absorption, and hence also the extent of structural relaxation, depends on the temperature and time period of thermal annealing. The significant time dependence of the structural relaxation is indicated by the much lower position and width found for ASW annealed at 122 K for 2 hours than at 130 K for 5 minutes. For these μ(O–D) modes the changes in the shape of the absorption correspond to changes in the distribution of H_2O first-neighbour hydrogen bonding environments, which may be characterised by different O–O distances and O–O–O angles. It is possible to estimate the changes in average O–O distance from the peak position using the reported correlations observed for crystalline ice.[186] Applying the relationship used by Tulk *et al.*[209] gives an average O–O distance of 2.783 Å for as-made ASW and 2.779 Å after annealing at 130 K. For comparison, a peak frequency of 2419.4 cm^{-1} for the μ(O-D) absorption of crystalline ice I_h at 78 K gives an average O–O distance of 2.757 Å. Furthermore, the decrease in FWHM observed during annealing indicates that the distribution of O–O distances narrows suggesting that the range of different hydrogen bonding environments decreases. It also seems intuitive to suggest that annealing ASW may lead to a decrease of the average O–O–O angle from 111° as measured in LDA,[154] towards the tetrahedral angle (109.5°) in ice I.[215]

The variable temperature data of Figure 4.1 and 4.2 provide further insights into the structural relaxation processes. Interestingly, differences in band-shape caused by the 2 h preannealing at 122 K are only visible at temperature between 78 and ~125 K and above ~150 K. At temperatures between 78 and 125 K the fitted peak parameters (Figure 4.2) indicate that the position of the absorption for the ‘as-prepared’ ASW film remained fairly constant with increasing temperature whilst the peak width decreased. Conversely, for the ‘preannealed’ ASW film the peak width remained constant and the position increased. These trends suggest that whilst the peak position depends upon both the temperature and the extent of structural relaxation, the peak width primarily depends on the structure and is not greatly influenced by changes in temperature between 78 and 125 K. The fairly constant peak centre with increasing temperature for ‘as-prepared’ ASW

may also imply that any increases in hydrogen bonding due to the structural relaxations occurring as the film was heated were almost equally offset by the reversible temperature effects. Furthermore, the absence of steps or features in the data suggests that the relaxation of ASW is not enabled by sudden increases in dynamic mobility but is instead limited more broadly by the available thermal energy. The smooth relaxation profile may imply a wide distribution of dynamic heterogeneity enabling sintering relaxations at lower temperatures and more local relaxations as the temperature increases. Although the spectra do not show any sharp features at 3700 cm^{-1}, sometimes observed in porous ASW and thought to indicate dangling OH bonds at the surface of the pores,[70,162-165,216] it would seem logical to assume that the change in position and width of the μ(O–D) absorption reflects sintering as well as more local ordering effects, reducing the structural heterogeneity and increasing the net hydrogen bonding interaction.

The similarity between the spectra of 'as-prepared' and 'preannealed' ASW between ~125 and ~150 K indicated by the overlap of their fitted position and width parameters could be taken to indicate that thermal annealing available during the heating run had enabled the relaxation state of the 'as-prepared' ASW to 'catch up' with that of the 'preannealed' ASW. However, the situation appears to be more complex than this. At temperatures > 150 K the data diverge, indicating different crystallisation rates and differences in the hydrogen bonding structure of the crystalline ice formed. Figure 4.1(d) shows a much less abrupt transition for the preannealed ASW than for the 'as-prepared' ASW (Fig. 4.1c). Although there is a small difference in heating rate between the two experiments this difference is not large enough to cause these effects. The differences in thermal stability of the two films, indicated by their different crystallisation profiles, and structural differences of the crystallites, indicated by the different widths of the features at temperatures > 160 K is an exciting result. It suggests that structural differences introduced by preannealing affected ASW's route over the potential energy landscape during the subsequent heating run. Potentially, the structure motifs formed during thermal annealing at 122 K were conserved during heating, even above the proposed T_g and after its eventual crystallisation. Alternatively, the preannealing could also conceivably have altered the samples thermal conductivity causing it to

become more thermally stable toward a surface activated crystallisation mechanism.[217] However, a similar increase in thermal stability due to structural annealing has also been observed for the LDA prepared from HDA. The LDA formed from pressure annealed HDA, vHDA, being more thermally stable than that formed from unannealed HDA, uHDA.[218] In this study, the lower thermal stability of uHDA was attributed to the presence of nanocrystalline remnants of I_h, not present for vHDA. Whilst nanoscale domains of crystalline material may reasonably be expected to occur during the pressure-induced amorphisation of ice I_h, no such structures would be expected for ASW.

Instead, the increased thermal stability of annealed forms of LDA, either ASW or LDA from vHDA, may be due to the correlation between dynamics and structure in condensed phases of H_2O near the T_g.[76,198] In essence, the structural motifs introduced by annealing may require higher temperatures to unjam their kinetics than would have been required if the structures were not introduced. Using an energy landscape formalism the route to ice I taken by the 'as-prepared' ASW could be viewed as skirting around the sides or rim of an energy basin, whilst 'preannealed' ASW was lower in the energy basin, increasing the effective barrier to crystallisation and ultimately also the temperature required. As discussed in Section 1.1.2 there are two potential sources of structural order in condensed phases of H_2O, the relative positioning of the oxygen atoms and bond orientational ordering. Although, there are likely to be many different perturbations with similar local free energy available to the relaxing ASW, a structural feature which may contribute to the increased thermal stability is the frustration caused by the presence of cubic and hexagonal stacking arrangements (changes in positional order or interconnectivity).[35-37] The presence of cubic stacking sequences in ASW would be supported by the mixed hexagonal/cubic stacking in the material initially formed upon crystallisation, termed stacking disordered ice I_{sd},[35-37] and the 'crystal-like' nature of LDA identified by thermal/acoustic conductivity and neutron scattering.[219-225]

A preferential relaxation into cubic rather than hexagonal stacking arrangements at 122 K would also, more generally, be supported by Ostwald's step rule of metastable states, an observation that metastable materials typically relax into other metastable forms more rapidly than they relax into the most thermodynamically stable form.[226-227] The mixed nature of I_{sd} would then

imply that the rates of cubic and hexagonal crystallisation are very similar and thus low temperatures and long periods of time would increase the proportion of cubic stacking sequences in ASW and then in ice I_{sd} upon crystallisation. As the first-neighbour environments of cubic and hexagonal stacks are essentially identical with structural differences only manifesting in the third coordination shell a quantification of their proportions in the amorphous state is understandably difficult. Yet the different widths of the μ(O–D) absorption of ice I_{sd} formed from 'preannealed' and 'as-prepared' ASW indicated in Figure 4.2(b) suggests that FT-IR spectroscopy of the μ(O–D) absorption may be sensitive to these subtle changes in the positional order. A systematic XRD study of the cubic/hexagonal stacking in ice I_{sd} formed from differently annealed ASW may prove a successful approach in revealing the contribution of different types of short range positional ordering to ASWs structural diversity.

4.2.2 Raman Spectroscopy of Coupled O-H Modes in ASW

The OH stretching modes, ν(OH), of H_2O ASW give a slightly different perspective on ASW's structural relaxations. Unlike the decoupled μ(O–D) modes of dilute HOD-ASW, the ν(OH) modes are coupled with the other O-H bonds of H_2O giving symmetric and antisymetric vibrations which then also couple with the surrounding molecules to give 'in phase' and 'out of phase' vibrations.[228] This coupling causes the shape of ν(OH) absorptions to reflect the structure of the hydrogen-bonded network over a longer length scale than for the μ(O–D) absorption. The distance of the coupling is thought to depend upon the positional order/disorder, the orientational order/disorder and the activity of the dynamics. Whalley has concluded that at least 25 molecules take part in the coupled symmetric ν(OH) stretching of ice I_h,[229] and Bakker *et. al.* has proposed that for liquid water the coupling is over ten or more molecules.[230] In this section, Raman spectra of the ν(OH) vibrations of ASW are investigated as transmission IR spectra have 'total absorption' in this spectral region. It was not possible to record absolute intensities with our Raman setup so the spectra have been normalised with respect to the maximum intensity of the main feature at ~3100 cm^{-1}. As for the spectra of μ(O–D) shown in Figure 4.3, the Raman spectra shown in Figure 4.4(a) were recorded at 78 K after the sample was annealed to sequentially higher temperatures. However,

for these measurements the heating cycle involved raising the temperature of the cryostat to the annealing temperature and then immediately recooling to 78 K (~5 K min^{-1}).

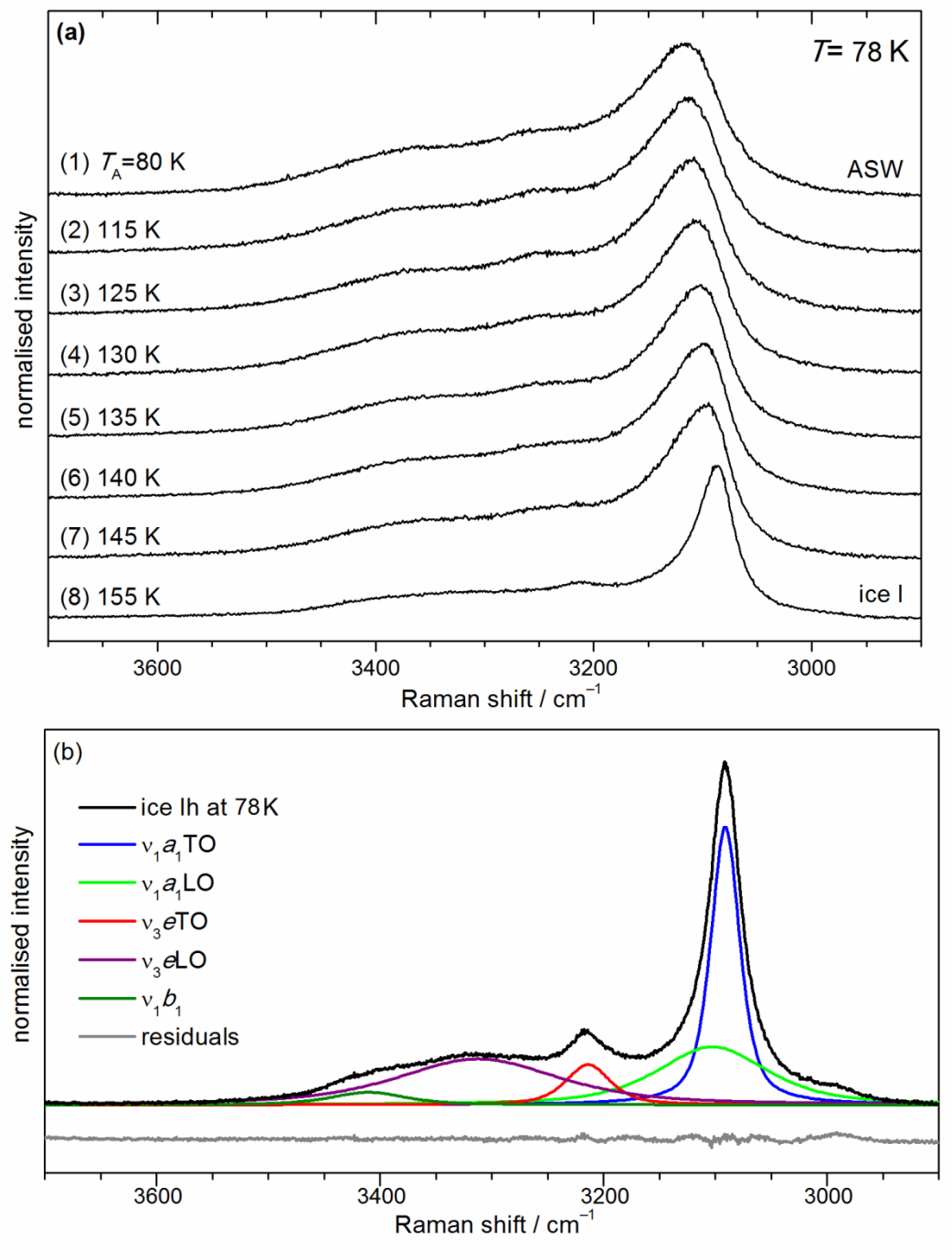

Figure 4.4 (a) 78 K Raman spectra of H_2O ASW recovered from the surface of the deposition plate and annealed to sequentially higher temperatures. (b) Raman spectrum of ice I_h at 78 K (black line) and decomposed into 5 component peaks according to Whalley.[229,231]

The overall shape of the absorptions for unanealed ASW, as well as the peak position of the most intense feature at ~3116 cm^{-1} are in good agreement with previously reported Raman

spectra of ASW.[232-236] As for the μ(O–D) absorption, thermal annealing at successively higher temperatures leads to gradual changes in band shape towards that of ice I. The position of the most intense feature shifts from 3116 cm^{-1} in 'as-prepared' ASW to 3098 cm^{-1} after annealing at 145 K and the intensities of the shoulders at ~3265 and ~3380 cm^{-1} decrease relative to the intensity of the main feature. The sample crystallised after annealing at 155 K. In Figure 4.4(b) the Raman spectrum of ice I_h at 78 K is shown for comparison. Interestingly, the spectra of ASW and ice I_h at 78 K have a similar profile, and hence also similar modes of intermolecular coupling, and are a much more closely matched than the spectra of ASW at 78 K and liquid water at room temperature (RT).[229] Despite there being conflicting views about the assignments of the features contributing to the spectrum of ice I, [228,234-235,237-239] the spectrum has been decomposed into five peaks as suggested by Whalley.[229,231] The assignments of Whalley include symmetric (ν_1) and antisymmetric (ν_3e) vibrations and in-phase ($\nu_1 a_1$) and out-of-phase ($\nu_1 b_1$) symmetric vibrations. A further two peaks required to provide a satisfactory fit were assigned by Whalley to longitudinal optical (LO) vibrations (LO), raised in energy relative to the transverse optical (TO) vibrations due to an anisotropy in the electric field environment during the IR active $\nu_1 a_1$ and ν_3e vibrations.[229,231]

Despite the controversy in assigning the individual features, the obvious similarity between the ice I and ASW spectra has motivated an attempt to extract some further information about structural changes taking place during the structural relaxation using peak fitting. The spectra of ASW shown in Figure 4.4 have each been decomposed into 5 peaks using the refined ice values as starting positions. However, the out of phase symmetric vibration ($\nu_1 b_1$) predicted to occur at 3483 cm^{-1},[229] was too broad/weak to give consistent results and was fixed with zero integrated intensity for the ASW spectra. The peak position (a), FWHM (b) and proportional area parameters (c) obtained relative to those obtained for 'as-prepared' ASW are shown in Figure 4.5. Also shown is the goodness of fit (d) and the wavenumber difference in position (splitting) between symmetric and antisymmetric peaks (e) and between TO and LO peaks (f) relative to that obtained for the 'as-prepared' ASW.

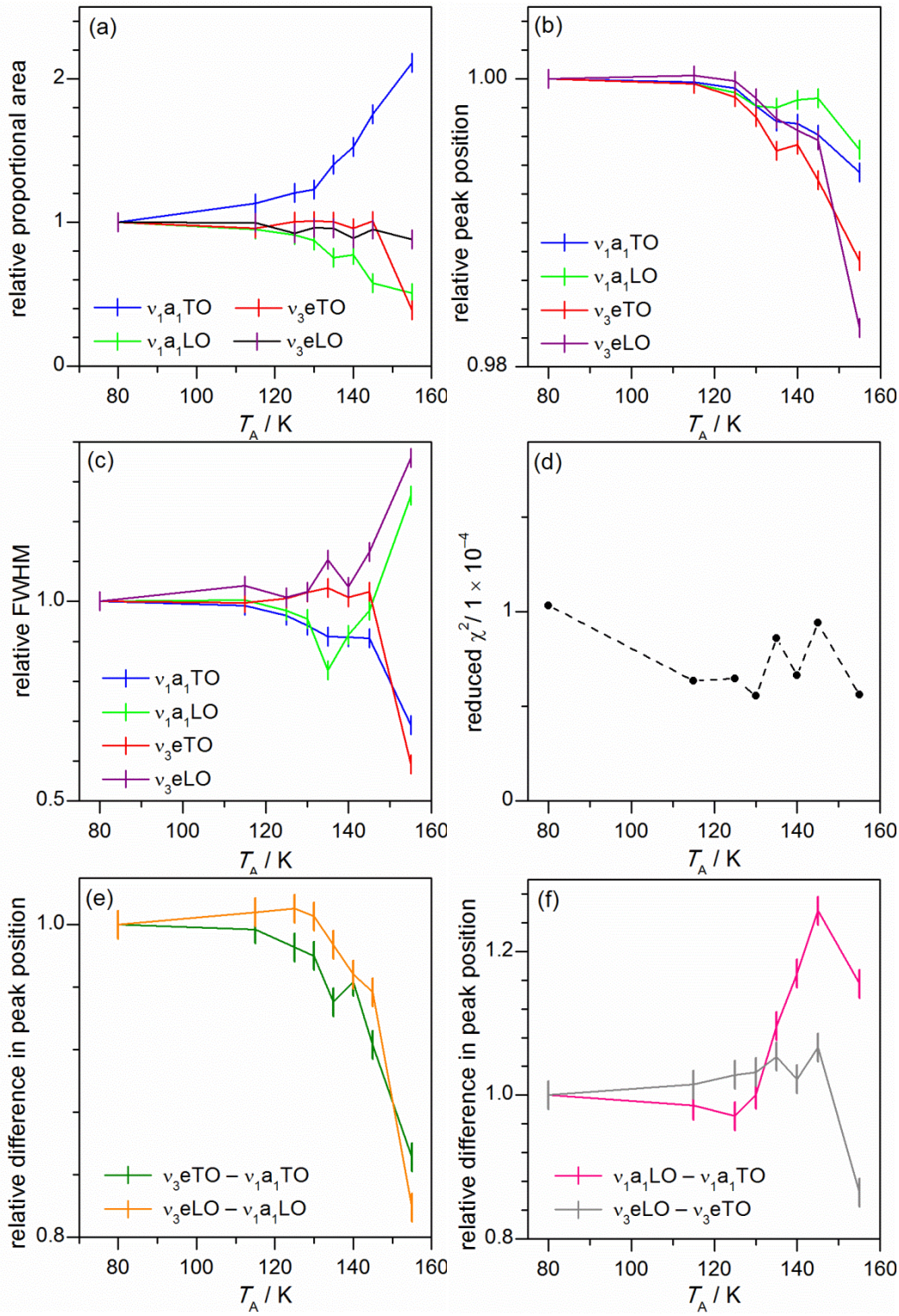

Figure 4.5 A comparison of the proportional peak area (a), position (b), width (c), goodness of fit (d), ν_1a_1-ν_3e splitting (e), and TO-LO splitting (f) obtained by fitting the Figure 4.4a spectra of ASW with 5 pseudo-Voigt peaks.[229,231] The peak fit parameters are shown relative to the values obtained for 'as-prepared' ASW (T_A = 78 K) to highlight the changes which occurred upon thermal annealing. The parameters for the ν_1b_1 absorption which gave a very weak/broad signal at ~3483 cm^{-1} in ASW and a weak signal in ice I at 3420 cm^{-1} are not shown.

In general, the spectral changes associated with precrystallisation relaxations, and crystallisation are harder to distinguish in the ν(OH) spectra than in the μ(O–D) spectra (Figures 4.1 and 4.3), presumably due to the coupling which averages the structure over a longer length scale than for the μ(O–D) absorptions. However, decomposing the ν(OH) spectra does allow the changes associated with precrystallisation relaxations to be separated from those occurring during crystallisation. For example, whilst the relative proportional area and positions vary consistently with T_A and must therefore be associated with the precrystallisation relaxations, the changes in width predominantly occurred after annealing at 155 K, and are thus associated with crystallisation. Overall the most pronounced change in the fitted peak parameters is the increase in the proportional area of the $\nu_1 a_1$ vibration. This is most likely to be related to the structural ordering occurring during relaxation which enables greater changes in polarisability during the coupled symmetric vibrations and increases Raman activity.

The changes in position of the peaks with thermal annealing were not entirely consistent, giving rise to changes in the splitting between antisymmetric and symmetric ($\nu_3 e$–$\nu_1 a_1$) vibrations and between TO and LO vibrations. The $\nu_3 e$–$\nu_1 a_1$ splitting (e) decreased consistently upon thermal annealing for both the TO and LO modes. The TO-LO splitting (f), was constant between 78 and 130 K, increased sharply between 130 and 150 K, then decreased between 145 and 155 K and was much more pronounced for $\nu_3 e$ than $\nu_1 a_1$ vibrations. Whilst the decreases in the $\nu_3 e$–$\nu_1 a_1$ splitting upon structural relaxation may also be related to increases in the structural order already identified, the changes in TO-LO splitting may be much more sensitive to the specific structures formed. This is because the increase in energy of the longitudinal vibrations relative to the transverse vibrations depends upon the size of the electric field produced by the coupled vibrations and is thus dependent on the local structural anisotropy.[240] Thus in general, and assuming that the peaks are correctly assigned, the increase in TO-LO splitting associated with the precrystallisation temperature region and subsequent decrease upon crystallisation may indicate that the structural motifs produced by the precrystallisation relaxations are more anisotropic than those in the 'as-prepared' ASW or in the ice I_{sd} produced upon crystallisation. Although, it may then seem logical to assign the increases in

TO-LO splitting to local structural anisotropy caused by cubic stacking sequences, which stack most efficiently in a diagonal direction,[37] the spectra of I_h has a very similar profile. Bond orientation order is the only potential source of structural anisotropy in ice I_h. Although it is not universally accepted, the net disorder of the bond orientations indicated by diffraction (H positions have a fractional occupancy = 0.5 in ice I_h) implies a range of different local and intermediate bond orientations which may well be anisotropic and give rise to TO-LO splitting.[229,231] Even if the orientations of neighbouring molecules were completely uncorrelated, randomly occurring patterned structures are likely to extend over length scales similar to the coupling and therefore be sufficiently large to perturb the anisotropy and the spectra.[229,231]

Unlike the changes in TO-LO splitting, which is mostly hidden from view by the overlapping peaks in the raw spectral data, the very different changes in width of TO and LO modes upon crystallisation is clearly evident. The peaks assigned to TO get sharper and those assigned to LO get broader. Whilst the sharpening of the TO peaks is in general agreement with the greater structural order of ice I relative to ASW, the widening of the LO peaks indicates an increase in the inhomeogeniety of the anisotropy. Interestingly, the TO-LO splitting also decreases upon crystallisation implying that although the range of different electric field perturbations varies more widely in ice I_{sd} than in annealed ASW, the average perturbation is less. These trends could imply that as ASW was annealed local correlations in bond orientational order were introduced, increasing the TO-LO splitting, but that the longer range periodicity introduced upon crystallisation removed the local correlations restoring the random uncorrelated distribution of bond orientational order of ice I_h. Theoretical work predicting the impact of specific bond orientational orderings or variations in H_2O stacking arrangements on the vibrational spectra of ice I would be desirable to future work in this direction.

4.2.3 Comparisons of LDA formed from ASW, uHDA, vHDA and eHDA

In this section, the Raman spectra of ASW presented in section 4.2.2 are compared with similar spectra for LDAs formed from high-pressure amorphous forms of ice: uHDA, vHDA and eHDA.

As the LDA formed from the high pressure forms are free of ASW's microporosity,[81,87] the comparison has enabled the spectral contribution of sintering relaxations in ASW to be better understood. Comparison of the annealed forms of the LDA starting materials has also enabled the metastable ergodicity of the LDA system to be examined, revealing more about the nature of the reversible change in heat capacity and the temperature required for the glass to liquid transition. This comparison has also allowed an interrogation of the structurally distinct states of LDA identified by Winkel *et al*. using neutron diffraction. [211]

Figure 4.6(a) shows Raman spectra of the ν(OH) region for uHDA, eHDA and vHDA recorded at 78 K. The peak maxima of the most intense features are at 3158 cm^{-1} (HDA), 3172 cm^{-1} (eHDA) and 3204 cm^{-1} (vHDA), respectively, which is in good agreement with previously reported values.[136,139,241-242] In order to transform the various HDAs to LDA the samples were heated in the cryostat while continuously monitoring spectral changes in the coupled ν(OH) stretching region. The transition temperatures to LDA were found at ~110 K (HDA), ~118 K (vHDA) and ~122 K (eHDA). This sequence of the transition temperatures is in good agreement with calorimetric studies.[140-141] A similar temperature cycling as used previously for ASW (Figure 4.3 and 4.4) was then performed to anneal these forms of LDA. Due to the large amount of spectral data collected the total integrated intensity, $A_{\nu(OH)}$, and the wavenumber of maximum intensity, ν(OH), which reflect the main spectral changes, were extracted from the spectra and used to compare the various forms of LDA.

Figure 4.6(b) and Figure 4.6(c) show comparisons of the $A_{\nu(OH)}$ and ν(OH) for LDA formed from ASW, uHDA, vHDA and eHDA. In general the ν(OH) and $A_{\nu(OH)}$ of the various LDAs follow the trend of ASW fairly well and show that a similar gradual structural relaxation process takes place in all the materials. This is not entirely unexpected as Suzuki *et al.* have observed similar peak shifts of the ν(OH) upon annealing LDA formed from uHDA, [243] and irreversible structural changes in LDA formed from uHDA have also been observed in ultrasound measurements.[244-246] The arrows in Figure 4.6(b) and (c) indicate the parameters obtained for materials corresponding approximately to the LDA-I and LDA-II states identified by Winkel *et al*.[211] Although the LDA-II

state indicated was formed by thermal annealing at ambient pressure and the LDA-II state probed in the neutron diffraction experiments was formed by the decompression route, it has recently been concluded by Winkel *et al.* that the two routes are equivalent.[204]

Based on the data shown in Figure 4(b) it is not possible to differentiate between LDA-I and LDA-II states. Although the ν(OH) of LDA-II is slightly greater than for LDA-I, their $A_{\nu(OH)}$ are almost identical implying that their structures are very similar if not identical. One explanation for the disagreement of our results and the conclusion drawn by Winkel *et al*, [211] could be that neutron diffraction is more sensitive to the subtle structural differences than ν(OH) and $A_{\nu(OH)}$ parameters extracted from the Raman spectra. An alternative explanation is that the LDA-II sample measured by neutron diffraction[211] has simply spent much more time at 140 K during the decompression and is therefore more structurally relaxed than the LDA-I sample which was heated to 140 K and immediately cooled back to 80 K. The time dependence of the relaxation process is illustrated in Figure 4.3 by the decrease in position and width of the μ(O-D) upon annealing at 122 K for two hours, which is much greater decrease than obtained after annealing at 130 K for 5 minutes.

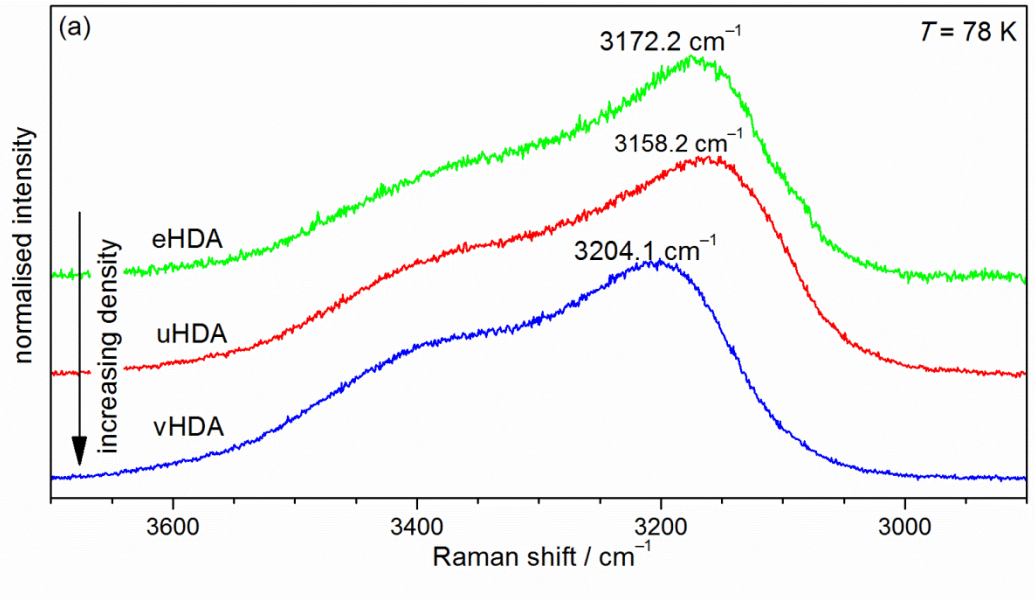

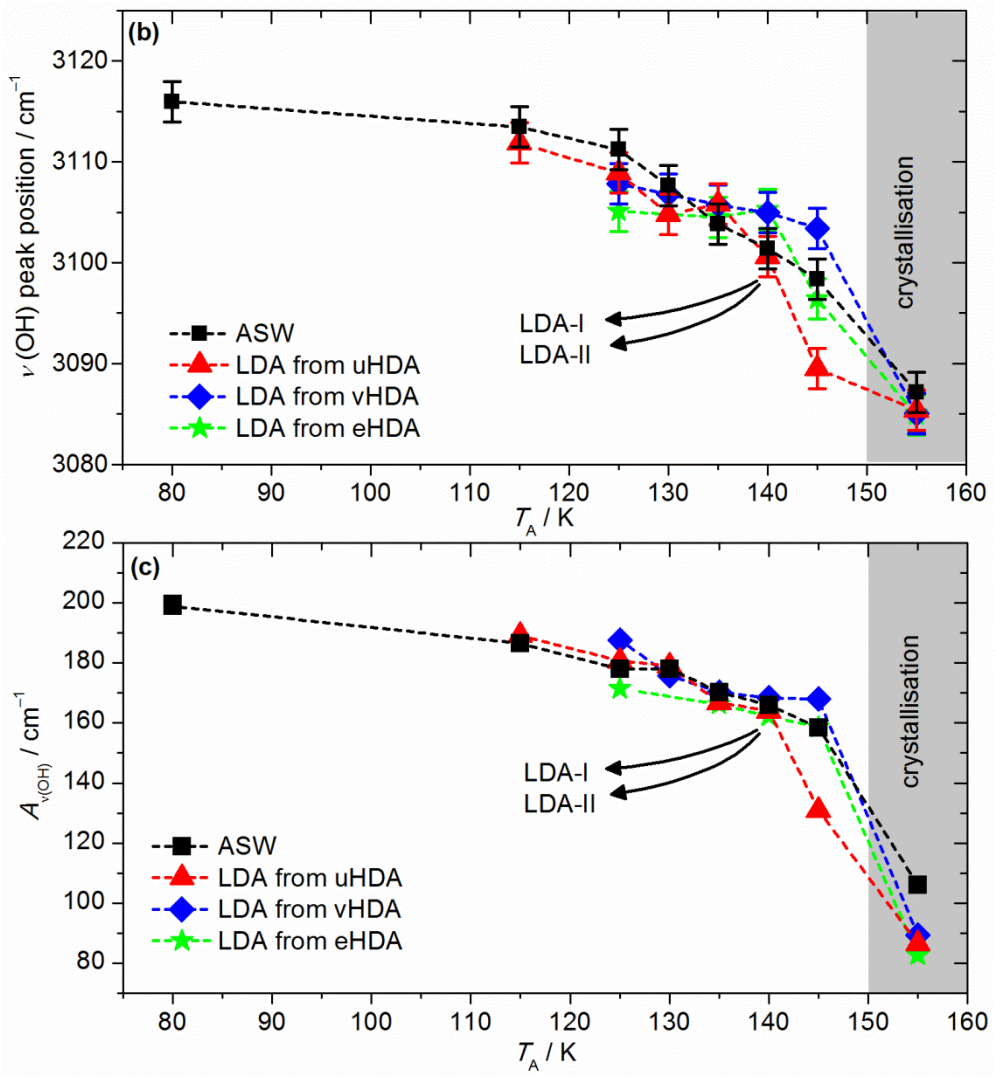

Figure 4.6 (a) Raman spectra of the OH stretching region of uHDA, eHDA and vHDA recorded at 78 K and (b) a comparison of the position of maximum intensity and (c) total integrated area extracted from the spectra of ASW and the LDA's formed from these HDA materials after sequential annealing steps.

There are, however, some differences in ν(OH) and $A_{\nu(OH)}$ between the different LDAs, particularly near the transitions from the HDAs states at 125 K and immediately preceding their crystallisation to ice I_{sd} at 145 K. The raw spectra show the much lower $A_{\nu(OH)}$ for uHDA annealed at 145 K was due to its partial crystallisation indicating a reduced thermal stability. Interestingly, the decrease in thermal stability of LDA from uHDA compared to LDA from eHDA and vHDA is consistent with calorimetric measurements.[218] The mechanisms increasing the thermal stability of ASW upon thermal annealing were discussed in section 4.2.1 and are likely to be similar to those stabilising HDAs annealed under pressure. To summarise, the greater thermal stability, may be

viewed as an increase in the effective height of the potential energy barrier as the structural state changes upon relaxation into the bottom of the energy basin. The structural state at the bottom of the basin may be characterised by frustrated cubic and hexagonal stacking sequences,[35-37] and locally correlated bond orientational order.[200] These forms of structural relaxations are supported by the crystal-like acoustic and thermal conductivity of LDA,[245-246 210,219] and the increase in TO-LO splitting observed in the Raman spectra of ASW upon thermal annealing (section 4.2.2).

4.3 Conclusions

Overall, it is difficult to reconcile the data presented in this chapter with the postulated glass transition of LDA before the onset of crystallisation.[85-87] By definition, after heating above a glass transition temperature ergodicity is reached, *i.e.*, the sample is in (metastable) equilibrium on the experimental time scale. This would be expected to dramatically accelerate the structural relaxation process observed here and bring it to completion. In particular, the pronounced impact of thermal history on the thermal stability of LDA and the spectral data (Figure 4.3) suggesting that the structural relaxation process in ASW takes place even while the sample crystallises would not be expected if 136 K was a true glass to liquid transition temperature. The suggestion that the heat-capacity increase of LDA *prior* to crystallisation is due to the kinetic unfreezing of the reorientation dynamics,[30] is perhaps more acceptable because the relaxation pathways available *via* this form of relaxation would be more limited. However, this cannot explain why sintering relaxations are active at much lower temperatures than crystallisation or the smooth continuous temperature profile of ASW's relaxation. These observations point towards the dynamics having a pronounced structural dependence with structural heterogeneity giving rise to dynamic heterogeneity and a broad temperature range of relaxation.

5 Structure in ASW/C_{60} 'Trapped Solutions'

5.1 INTRODUCTION

The ASW/C_{60} fullerene materials investigated in this chapter were prepared by co-depositing C_{60} and water vapour as thin films using the vapour deposition apparatus described in Chapter 3. The mixtures formed, referred to in this work as 'trapped solutions', contain C_{60} dispersed in an ASW matrix and are kinetically stable at liquid nitrogen (LN_2) temperatures. Their structural state is postulated to be similar to that of unstable aqueous solutions of water and C_{60} before precipitation (C_{60} has an extremely low solubility of 1×10^{-9} dm^{-3} [1247-248]). There are two motivations for studying these trapped solutions. Firstly, we are interested in the hydration of hydrophobic molecules in solution. Hydrophobic hydration is of great interest because of its fundamental importance to our understanding of hydrophobic effects.[1] The effects include an attractive force which forms between hydrophobic molecules and is thought to influence the folding of proteins and molecular self-assembly processes such as micelle formation.[12] C_{60} is the focus of several computer simulation studies of hydrophobic hydration,[249-254 255] and is expected to be a good model hydrophobe. Secondly, introducing C_{60} into the ASW matrix will allow us to investigate ASW's dynamics at different temperatures. C_{60} is thought to be an especially good probe of translational diffusion in ASW, previously demonstrated for small molecules,[256-258] and is thus also a good probe of a glass to liquid transition *prior* to crystallisation. This is because of its large size relative to H_2O (maximum C–C distance 7.10 Å and an 'outer' van der Waals diameter of 10.34 Å[259]) and a distinctive colour change which occurs when it aggregates.[260-261] In this work, temperature variations in C_{60}'s photoluminescence (phosphorescence and fluorescence) will also be investigated to reveal changes in the structure and dynamics of its hydration shell.

The low solubility of hydrophobic molecules, such as C_{60}, in water is due to the different polarities of the molecules; water being far more polar than C_{60} and with lone pairs positioned to favour a tetrahedral hydrogen bonding coordination. Figure 5.1 shows the DFT calculated (B3LYP 6-31G*) structure of H_2O and C_{60}. The directions of water's dipole moment, the approximate diameter of the molecules and the DFT-calculated 0.001 bohr $Å^{-3}$ isodensity surfaces colour mapped to show regions of positive and negative potential are also shown. The greater polarity of

water than C_{60} is indicated by the blue and red colouring of H_2O and entirely green colouring of C_{60}. H_2O has a permanent dipole moment of 1.854 D.[262] Despite the absence of dipole interactions nonpolar hydrophobic molecules do form van der Waals dispersion interactions with water. This is demonstrated by the different interfacial tensions of the water-air (72.8 mJ m^2), alkane-air (15-30 mJ m^2), and water-alkane (40-50 mJ m^2) interfaces. The most hydrophobic surface is the vapour interface with little or no interaction. The difference between the tension of the water-alkane and air-water interfaces (20 – 30 mJ m^2) indicates the extent of the van der Waals interaction between the hydrocarbon and water. Although similar surface tension information is not available for solids such as C_{60} (water surface contact angle of a porous film is ~60°[247]) C_{60} may be expected to have a slightly greater interaction with water than alkanes because of its delocalised π-electrons.[263]

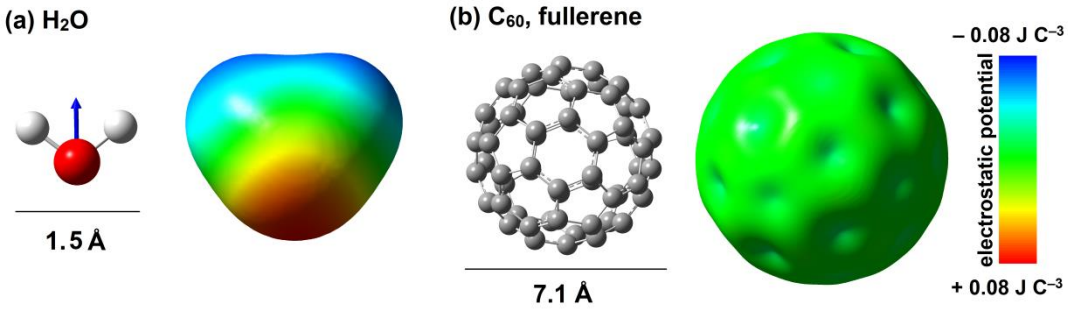

Figure 5.1 DFT calculated (B3LYP 6-31G*) structure of H2O and C60 molecules with 0.001 bohr cm–3 isodensity surfaces, colour mapped to show electrostatic potential. The direction of the dipole moment of H2O is indicated by the blue arrow.

On the basis of their different polarity it would seem intuitive to presume that separation of hydrophobic molecules from aqueous solutions would be solely due to a tendency to maximise favourable hydrogen bonding H_2O–H_2O interactions and minimise less favourable H_2O–C_{60} interactions. However, the situation is more complex. The orientational flexibility of the hydrogen bonding network allows it to form tetrahedral coordinated structures around hydrophobic molecules. This is most clearly indicated by the H_2O cage structures present in clathrate hydrates.[264] Frank and Evans were the first to suggest that similarly ordered hydration shells, they described as 'icebergs', may also form around hydrophobic molecules in the aqueous liquid.[3] The main evidence supporting the structural ordering of the hydrophobic hydration shells in the liquid are large positive solvation entropies and negative solvation enthalpies.[1,265-266] For water *n*-butane

at 25 °C Israelachvili quotes a ΔH_{mix} of -4.3 kJ mol^{-1} and ΔS_{mix} +28.7 kJ mol^{-1}. The higher entropy of the solution than the separated components reflects the reduced number of ways the water molecules may be positioned/orientated to contain the hydrophobic molecules and the decreased enthalpy reflects the greater hydrogen bonding between water molecules in the ordered hydration structures. However, this theory of hydrophobic hydration is not universally accepted.[1] Galamba has recently reviewed the literature,[267] pointing out that 'iceberg' hydration structures are not always reproduced by computer simulation,[1,266,268] and that other theories not requiring an 'iceberg like' ordered hydration shell may also be able to account for the positive entropy of solvation.[4,29,266,269-277] Unfortunately, there is no consensus about the extent of structural ordering which would be required to reproduce the calorimetric data. The main question remains whether hydrophobic hydration involves changes in the oxygen-oxygen distances, more subtle orientational ordering[29,269] or even if the mechanism may solely involve changes in the cooperativity[4 5] or H_2O dynamics.[278-279]

Nonetheless, attractive forces between hydrophobic surfaces separated by water and up to 100 nm apart are commonly observed with surface force apparatus,[280] and hydrophobes seem to aggregate at an unexpectedly rapid rate.[12] The relationship between these hydrophobic effects and hydrophobic hydration was first proposed by Kauzmann.[281] He suggested that a force develops because the entropically disfavoured hydration zones support two or more hydrophobic molecules without a proportional energetic penalty, making overlap of hydration shells favourable. In general, this would be supported by increases in the attractive force between hydrophobic surfaces found to occur with increases in temperature,[12] but a structural or dynamic perturbation over large enough distances to account for the attractive force seems very unlikely in a dynamic liquid.[266] Furthermore, experimental studies do not find significant structural or dynamic perturbations over extended distance ranges. Structural investigations have been carried out by X-ray absorption spectroscopy[282] neutron diffraction,[283-290] and dynamic investigations have primarily employed dielectric relaxation,[291-292] nuclear magnetic resonance (NMR)[293-296] and quasielastic neutron scattering techniques.[297] However, the systems examined in these studies may not be ideal for

identifying a subtle hydrophobic perturbation. Due to the low solubility of hydrophobic molecules, these studies of the equilibrium state were restricted to solutions of amphiphilic molecules or small gas molecules under pressure. The water perturbation in these systems would be expected to be much less than for an ambient pressure hydrophobe/water system which is very unstable and in the act of precipitating.

It has also been argued that structural or dynamic perturbations may be difficult to observe using techniques with low spatial or temporal resolution. In other words, the physical signature of the mixing thermodynamics may not be observable unless techniques are able to selectively probe the hydration shell and examine the different independent structural states occurring rather than the average. Techniques with improved spatial or temporal resolution used to study hydrophobic effects include Sum Frequency Generation (SFG) spectroscopy,[298] polarization-resolved mid-infrared pump-probe IR,[299-300] 2D IR,[279] and NMR ^{1}H spin-echo.[301] These studies report that molecules in the immediate hydration shell of hydrophobic molecules display much slower dynamics and weaker net hydrogen bonding interactions. This disconnection between molecules in the immediate hydration shell and those further from the hydrophobe may then imply that the physical signature of the hydrophobic effects and the origin of the positive entropy of solvation may be associated with reduced molecule correlations resulting from the excluded volumes filled by the hydrophobic molecules and their immediate hydration shell. In other words, the pathways for concerted molecular reorientations may be frustrated by the excluded volumes, significantly affecting how the remaining network rearranges over extended length scales.

However, water structure in solutions of purely hydrophobic molecules may not yet have been adequately measured with amphiphilic molecules[288] or gases under pressure[283] not providing a sufficiently large perturbation for the structural signature to be observable. It may also be important that spectroscopic data, such as that obtained from SFG, can tell us little about bond orientational ordering. The 'trapped solutions' approach taken here circumvents sensitivity issues related to C_{60} being only sparingly soluble because the dispersed mixtures prepared have much higher concentrations than available in saturated room temperature solutions. Figure 5.2 shows the

average intermolecular separation between the centres of C_{60} molecules in a saturated solution and in our 'trapped solutions' compared with the distance range over which attractive forces between hydrophobic surfaces have been reliably measured (20 nm).[280] The average separation between the C_{60} molecules can be approximated using the Wigner-Seitz radius, $r_s = \sqrt[3]{(3/4\pi n)}$ where n is the density of C_{60} in ASW with total density assumed to be unchanged from that of pure ASW (0.938 g cm^{-3}).[185] The average C_{60}-C_{60} separation calculated between the outer surface of the C_{60} molecules is assumed to be 10.34 Å less than twice the Wigner-Seitz radius. The smaller average C_{60}-C_{60} separation in our 'trapped solutions' than the distance over which hydrophobic effects operate suggests that perturbations to the water structure, if they exist, should permeate the entire structure of even the most dilute of our 'trapped solutions'. In this Chapter, the results of X-ray diffraction, small angle neutron diffraction (SANS) and transmission FT-IR studies carried out to search for the structural perturbation in these trapped solutions are presented.

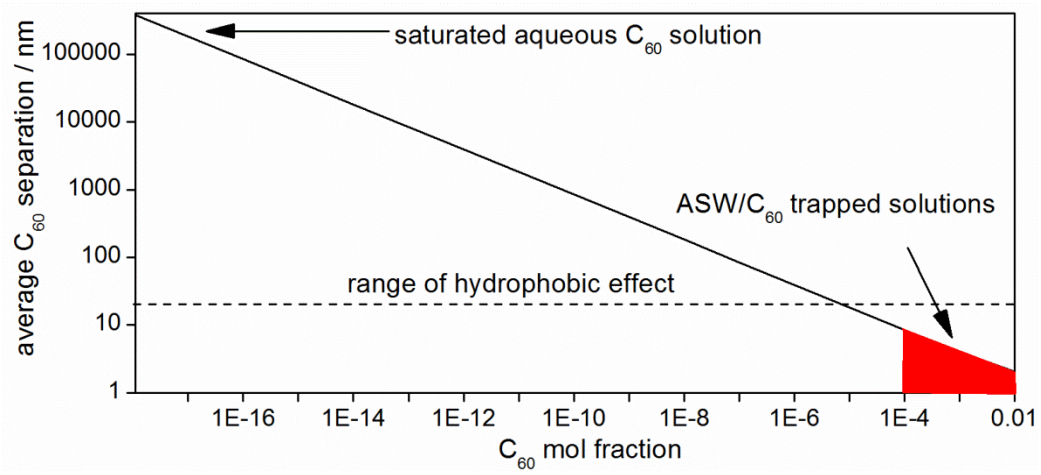

Figure 5.2 Comparison of the average separation between the centres of C_{60} molecules in a saturated room temperature solution and in the ASW/C_{60} 'trapped solutions' studied here with the distance limit of hydrophobic effects reported by Meyer *et al*.[280]

In the second part of this chapter, the optical absorbance and photoluminescence of the ASW/C_{60} 'trapped solutions' have been used to examine the temperature dependence of C_{60} diffusion in the ASW matrix and changes in the structure and dynamics of the hydration shell. The optical absorbance spectroscopy of C_{60} solutions has been studied in some detail, [248,260-261,302-305] and is fairly well understood.[302] Figure 5.3(a) shows the DFT calculated (B3LYP 6-31G*) optical

absorbance spectrum of isolated C_{60} indicating the approximate position of C_{60}'s 'dipole allowed' $\pi \rightarrow \pi^*$ transitions. These predictions reproduce experimental data for C_{60} dispersed in organic solvents which show maxima at ~210, ~256 and ~328 nm.[303] Also indicated in Figure 5.3(a) is the approximate spectral range corresponding to transitions between the electronic ground state (A_g symmetry, electronic configuration of h_u^{10}, singlet spin state, S_0) and the dipole forbidden,[304] excited spin singlet (S_1) states. These 'dipole forbidden' transitions, not predicted by DFT, are, however, observed weakly in optical absorbance spectra of C_{60}. The position of the absorption edge (0-0 transition or band gap) has been reported between 622 nm and 645 nm for C_{60} dispersed in different solvents. [306 307] The dipole forbidden transitions are understood to be weakly allowed due to the symmetry breaking influence of Herzberg-Teller coupling on the transition dipole moment.[302] Interestingly, the intensity of absorptions in the spectral region between 300 and 600 nm depend upon the solvent and the aggregation state of C_{60}.[248,261,308] C_{60} dissolved in 'good' solvents such as toluene or benzene has a pink-purple colour but in 'poor' solvents the activity of the absorptions increases and the solution turns brown. Although the mechanisms by which the absorptions become activated is unknown, the similar absorptions of C_{60}^{3-},[308] the negative surface charge and the unexpected colloidal stability of C_{60} aggregates in water,[309] point towards a very different surface chemistry for aggregated and dispersed C_{60}.[182,248,310-311]

The energy level diagram shown in Figure 5.3(b) provides a framework for discussing C_{60}'s photoluminescence. Near absorption edge excitation, such as that achieved with the He-Ne laser used in this work, is indicated by the red vertical arrow. Subsequent thermal relaxations are indicated by the green arrows. These non-radiative processes occur much more rapidly than radiative emissions causing C_{60} emission spectra produced using different excitation energies, to be very similar.[306] The excited spin singlet (S_1) to excited spin triplet (T_1) state transitions (intersystem crossings) are shown by the orange, nearly horizontal arrow. Dresselhaus states that for C_{60} the intersystem crossing to the T_1 state with μs lifetime is nearly 100 % efficient.[302] Radiative emissions from S_1 (fluorescence) and from T_1 (phosphorescence) are indicated by purple and blue arrows, respectively. For both fluorescence and phosphorescence there are several emissions with

different energies which correspond to relaxations into different vibrational excited states of the electronic ground state.[304,307] The different energy associated with relaxations into IR and Raman active fundamental, overtone and combination vibrational modes typically gives the emission spectra many bands which are referred to as 'vibronic progressions'. Due to the efficiency of the intersystem crossing and the high population of the T_1 state, C_{60}'s photoluminescence is mostly phosphorescence.

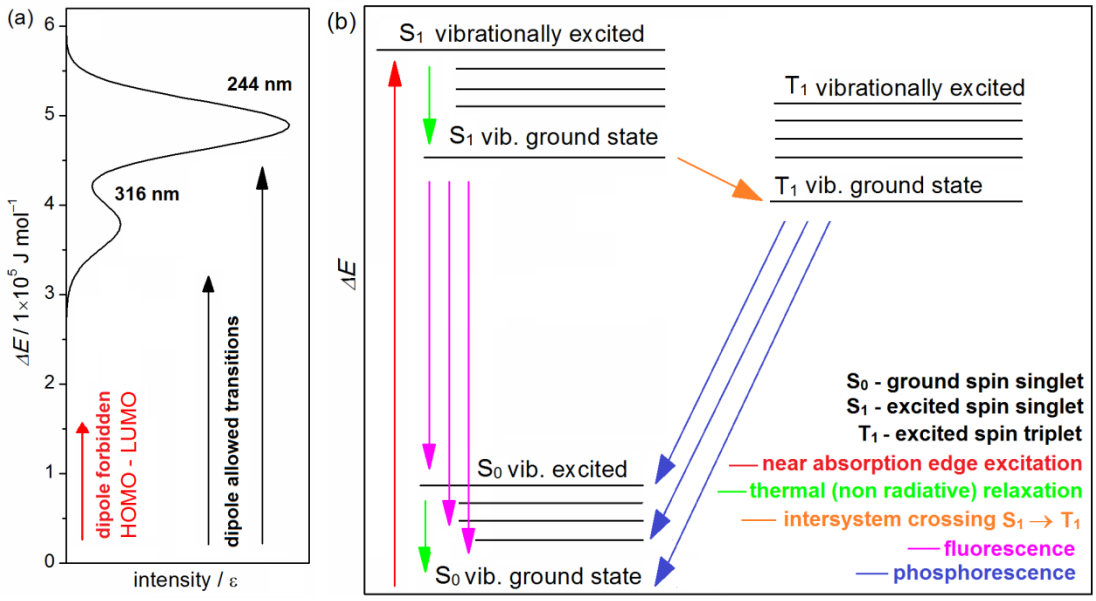

Figure 5.3 (a) DFT calculated (B3LYP 6-31G*) optical absorbance spectrum of isolated C_{60} and (b) a schematic diagram of C_{60}'s photoluminescence transitions.

Several groups have attempted to assign the emission spectra of isolated C_{60}.[304,306,312-316] [302,304,306-307,316] The assignments are difficult because of uncertainty in assigning the 0-0 transition which is particularly weak and the overlap of the individual vibronic peaks. Assignments are given by Wang *et al.*[307] but deviations from the measured Raman and IR frequencies are significant. More generally the profile may be viewed as comprising of two broad bands whereby the higher energy band corresponds to relaxations into states characterised by C_{60}'s fundamental vibrational modes and the lower energy band correspond to relaxations into overtone or combinational vibrational states. The suitability of C_{60} photoluminescence as a probe of local environment stems from the relationship between the intensity of the different transitions to the electric field environment and the potential for specific solvent interactions to cause non-radiative relaxation of

the T_1 state, quenching its photoluminescence. In this chapter the changes in C_{60}'s optical absorbance and photoluminescence upon thermal annealing and with changes in temperature are discussed in relation to potential changes in the electric field environment and quenching mechanisms. This has allowed hypotheses about structure and dynamics of H_2O in the immediate hydration shell of C_{60} to be formed.

5.2 RESULTS AND DISCUSSION

5.2.1 X-RAY DIFFRACTION OF ASW/C_{60} 'TRAPPED SOLUTIONS'

ASW/C_{60} 'trapped solutions' for X-ray diffraction (XRD) were deposited onto single crystal Si 'zero background' substrates (cut in 511) then transferred into the X-ray cryostat at 90 K. The samples were prepared using a H_2O dose rate of 0.4 g h^{-1} and a deposition time of 2.5 h. Figure 5.4 shows XRD patterns for 'trapped solutions' with C_{60} mole fractions (X_{C60}) of 0.0006, 0.0014 and 0.0028. These concentrations correspond to average C_{60}-C_{60} distances of 4.0, 2.6 and 1.9 nm. Peaks at 43.2 and 50.2 ° 2θ correspond to the copper metal of the X-ray cryostat body and the feature at 24.4 ° corresponds to a small (~0.3 weight %) amount of a crystalline ice I_h impurity which formed on the surface of the deposit during its transfer from liquid nitrogen into the cold cryostat.

Overall, the XRD patterns of the 'trapped solutions' with broad peak maxima at 2θ angles of 24 and 43° look similar to those previously reported for ASW. [59,143,156] There is, however, a subtle difference in the shape of the first peak for samples with different C_{60} concentrations. With increases in X_{C60} the intensity between 28 and 33° increases and the intensity between 23 and 26° decreases. However, it is difficult to comment on the extent to which this reflects changes in ASW structure as the change could be solely due to the presence of C_{60} and its intramolecular C-C correlations. The films were also heated in the cryostat to search for further structural differences upon thermal annealing and changes upon crystallisation. Data for X_{C60} = 0.0028 is shown in Figure 3.11 but the entire data set is not given. The much shorter scans recorded during heating did not show any significant differences with changes in X_{C60}. At temperatures above 200 K the H_2O

rapidly evaporated from the 'trapped solutions' leaving a deposit of C_{60} behind. The black line in Figure 5.4 shows the corresponding diffraction pattern for the *post* evaporation C_{60} film prepared from the 'trapped solution' with X_{C60} = 0.0028. The reflections of the C_{60} material correspond closely to those of crystalline C_{60} (space group $Pa\bar{3}$),[317] and are similar shape to those of nanocrystaline C_{60} formed at high pressures.[181,318] A Debye-Scherer analysis indicated that the nanocrystaline material formed here had a particle size of ~12 nm.

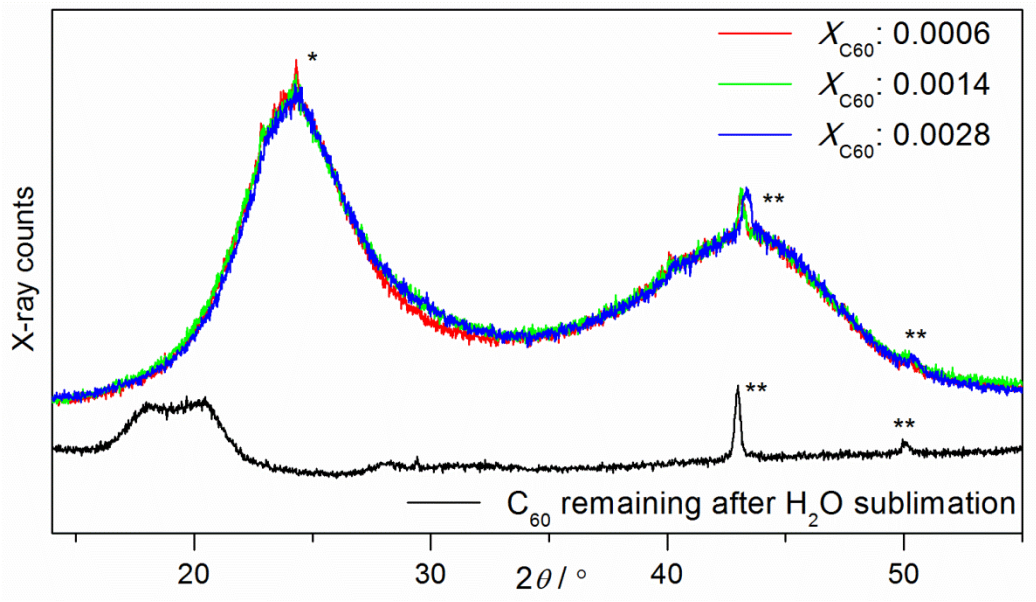

Figure 5.4 X-ray diffraction patterns of ASW/C_{60} 'trapped solutions' with C_{60} mole fractions of 0.0006, 0.0014 and 0.0028. Also indicated (offset vertically) is the diffraction pattern for the nanocrystalline C_{60} formed by evaporating the H_2O at 200 K. * a small amount (0.3 %) of crystalline ice impurity introduced during the transfer into the cryostat. ** reflections from the copper surfaces inside the cryostat.

5.2.2 NEUTRON DIFFRACTION OF ASW/C_{60} 'TRAPPED SOLUTIONS'

The influence of C_{60} on the ASW structure was also examined in a series of neutron scattering measurements carried out on the Small Angle Neutron Diffractometer for Liquids and Amorphous Solids (SANDALS) at the ISIS spallation source (Didcot, UK). For these measurements, ASW and ASW/C_{60} 'trapped solution' films with large thicknesses (~2 g total H_2O chamber dose) were deposited onto the deposition plate using a deposition rate of 0.4 g h^{-1}. Before their recovery, these materials were thermally annealed by allowing the temperature of the deposition plate to increase to 105 K at ~2 K min^{-1} and then immediately cooling it back to 77 K. This was carried out in order

to reduce the material's porosity and relax its intermolecular structure. For a deposition stage temperature of 105 K the surface of these thick deposits is estimated to be ~115 K. The material was recovered into liquid nitrogen, stored for around 30 days and then loaded into the neutron diffraction sample containers (volume of 2.88 mL). In total nine different samples with different C_{60} concentrations and H/D isotopic ratios were measured. A discussion of isotopic substitution difference techniques for neutron diffraction is given in section 1.1.5. Three different C_{60} concentrations were investigated: $X_{C60} = 0$ (pure ASW), $X_{C60} = 0.0065$ and $X_{C60} = 0.003$. These correspond to average C_{60}-C_{60} distances of 3.5 and 1.8 nm, respectively. For each C_{60} concentration, three samples were produced with an ASW matrix comprised of either H_2O, D_2O, or a 1:1 mixture of these, H_2O:D_2O. This combination was intended to enable the scattering data to be separated into partial structure factors [$S(Q)_{C\text{-}C}$, $S(Q)_{C\text{-}O}$, $S(Q)_{C\text{-}H}$, $S(Q)_{O\text{-}O}$, $S(Q)_{O\text{-}H}$ and $S(Q)_{H\text{-}H}$] and corresponding partial radial distribution functions, $g(r)$s, using the empirical potential structural refinement (EPSR) software.[154] Unfortunately, however, small amounts of crystalline ice were observed in several of the samples, preventing the analysis which requires that samples with different isotopic ratios have an identical structure. The contamination was later discovered to have resulted from a nitrogen leak in the deposition apparatus which caused additional readsorption and heating. A description of the EPSR technique used to separate partial structure factors from total structure factors (also used in later chapters on chloroform and the chloroform-acetone azeotrope) and the relationship between structure factors and radial distribution functions is given in Chapter 1.

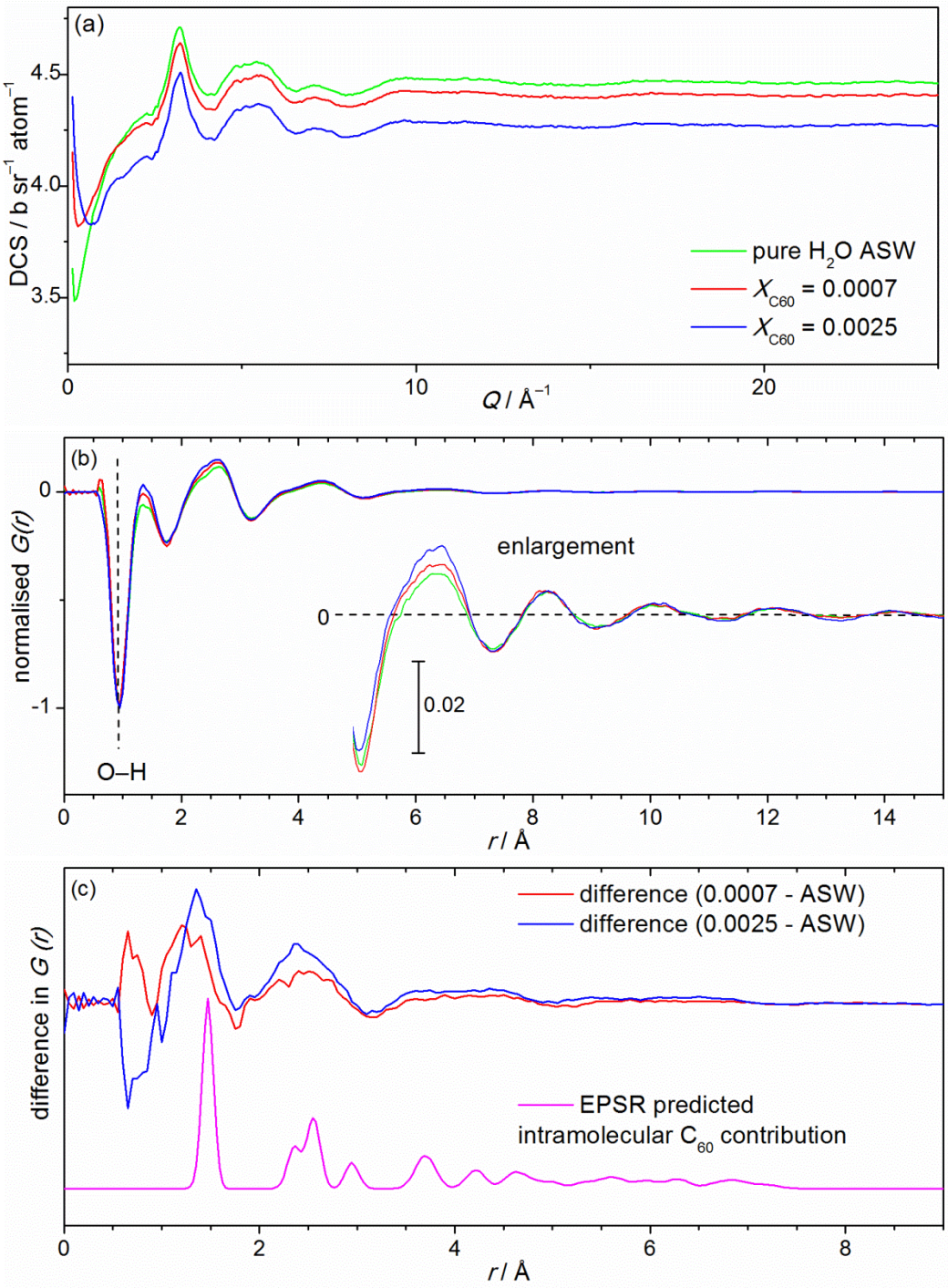

Figure 5.5 (a) DCS data for H_2O ASW and H_2O ASW/C_{60} 'trapped solutions' with X_{C60}=0.007 and 0.0025 corrected for attenuation, multiple scattering and inelastic pertubations. (b) the $G(r)$ obtained by Fourier transform of the $F(Q)$ data and normalised by negative intensity at 0.95 Å. The negative feature due to intramolecular O–H distance correlations is indicated by the dashed line and enlargement of the $G(r)$ at distances between 5 and 15 Å are provided. (c) a comparison of the difference between the normalised $G(r)$ shown in (b) and the EPSR predicted intramolecular C_{60} $g_{C\text{-}C}(r)$.

In Appendix 7 the weightings of the individual atom pairs to the scattering data of all nine samples are provided. Also shown are merged differential scattering cross sections (DCS) showing the variation in scattered intensity with the wavevector transfer, *Q*. Two different correction procedures were applied to the merged DCS data using the GudrunN software. In the first, the data were corrected for attenuation and multiple scattering using considerations of the cryostat geometry. For these data, given in Appendix 8, the variation in intensity with scattering angle, $I(\theta)$, and neutron wavelength, $I(\lambda)$, contain perturbations due to inelastic collisions. The data are therefore presented as $I(Q_e)$ reflecting that *Q* has been calculated by assuming elastic collisions. The extent of the inelastic perturbations is significantly larger for hydrogen than for deuterium, oxygen or carbon. In the second series of merged DCS presented in Appendix 9, the perturbation to the data caused by inelastic neutron collisions has been estimated and subtracted using the '*iterate gudrun*' subroutine in the GudrunN software. This uses a minimum intermolecular separation constraint (0.75 Å) and the differences between the $I(Q)$ and $I(\lambda)$ data to estimate the perturbation. The estimate is then refined in an iterative process. After the inelastic correction has been applied the merged DCS correspond to elastic scattering and the axis is labelled $I(Q)$.

Figure 5.5(a) shows the merged and corrected DCS data for the three protiated samples, which were free of ice contamination. The greater overall scattering of pure ASW than the 'trapped solutions', indicated by the greater DCS at high *Q*, is due to the greater bound scattering cross section of hydrogen (82.02 barn) than carbon (5.551 barn). The corresponding distance correlations obtained from the DCS data by sine Fourier transform are shown in Figure 5.5(b). These total radial distribution functions, $G(r)$s, were obtained by: (1) subtracting the average scattered intensity from the merged DCS data to give the interference function, $F(Q)$, (2) sine Fourier transform (FT), (3) Lorch smoothing to remove termination ripples introduced by FT artefacts and (4) normalisation to the negative intensity at 0.95 Å. The $G(r)$ of multicomponent systems, such as these mixtures of C, O, and H atoms is related to the $g(r)$'s for the individual atom pairs by their fractional occurrence and combined scattering length. Due to the negative scattering length of H and positive scattering length of C and O, negative features in the $G(r)$ correspond to H-O and H-C

atom pairs and positive features correspond to H-H, O-O, C-O and C-C. The undulating profile of the $G(r)$s for pure ASW giving maxima at 2.0, 5.4, 7.1 $Å^{-1}$ and minima at 4.0, 6.6 and 7.8 $Å^{-1}$ and the extent of the oscillations at greater distances correspond well with those previously reported for ASW.[154] The pronounced oscillation of the $G(r)$, indicating structural correlations over several molecular shells, is typical for materials with well-defined local order. The neutron diffraction analysis of Bowron *et al*. [154] indicated that ASW has a predominantly tetrahedral next neighbour environment.

To examine the structural differences between ASW and the trapped solutions the $G(r)$s have been normalised by the minimum intensity at 0.95 Å (O-H intramolecular bond). This normalisation counteracts decreases in the weighting toward H-H, O-H, O-O atom pairs with increases in C_{60} concentration which occurs due to their lower fractional occurrence. The differences between the normalised $G(r)$ shown in Figure 5.5(c) thus reflect only the perturbation to ASW's structure (fully subtracted if zero perturbation) and the combined profile of the individually weighted C-C, C-O and C-H $g(r)$s. Also shown in (c) is the EPSR simulated intramolecular $g(r)_{C\text{-}C}$ for the C_{60} molecule produced using the C_{60} structure given by Dresselhaus.[259] Interestingly, the profile of the predicted intramolecular $g_{C\text{-}C}(r)$ is very similar to the measured differences between the normalised $G(r)$ data for ASW and the 'trapped solutions'. This suggests that the differences shown in Figure 5.5(c) have a large contribution from the intermolecular C–C distance correlations of C_{60} itself. The remaining features may well correspond to distance correlations between C_{60} and water in its immediate hydration shell or perturbations to the ASW structure. However these effects are small and cannot be determined from these data due to the low concentration of C_{60}, overlapping nature of the $g(r)$s and influence of Lorch smoothing. The absence of a significant perturbation to ASW's extended structure may indicate that long range hydrophobic effects involve subtle orientational ordering not observable in diffraction data or arise due to changes in the dynamics of the ergodic liquid with a structural signal thus not present in ASW.

The total scattered intensity in neutron diffraction experiments is dependent upon the sample's composition, its density and how effectively it is packed into the container used for the measurements. For liquids, a packing fraction of 1 is possible but for powders the space between particles gives packing fractions < 1. For solids with known density and composition the packing fraction can be calculated from the measured DCS. Assuming the density to be unchanged from ASW (0.938 g cm^{-3})[185] the packing fractions obtained for these nine samples were between 0.24 and 0.45 with an average packing fraction of 0.36. Alternatively, for porous ASW, it may be more intuitive to assume that a particular packing fraction had been achieved and calculate the effective density of the materials. For a packing fraction of 0.8 this calculation gives an average effective density of ~0.4 g cm^{-3} and suggests that the materials measured were highly porous. Interestingly, the high porosity is also indicated by the increase in scattered intensity at Q < 0.3 Å present in the merged DCS data for all nine samples. The intensity at low-Q is caused by the large changes in scattering length density at the pore boundaries (greatest for D_2O) and correlations across the pore volume.[319] This low-Q intensity indicates that thermal annealing to ~115 K during sample preparation was insufficient to fully structurally relax the ASW.

To further investigate the temperature dependence of sintering and pore collapse in these materials, scattering data of the D_2O 'trapped solution' with X_{C60} of 0.0034 was monitored as the cryostat was heated from 80 to 180 K at 0.4 K min^{-1}. The merged DCS collected at 10 minute intervals is shown as overlapping diffraction patterns in Figure 5.6(a) and as contour plots with different scales in (b) and (c). In (a), Q is shown on a $\log_{10}$ scale to highlight the changes which occurred at Q < 0.3 Å. In (b) and (c) the intensity is shown on a $\log_{10}$ scale to highlight the small change in the diffraction occurring *prior* to crystallisation. Two pronounced changes can be observed in the merged DCS data with increases in temperature. At ~115 K the intensity at Q < 0.3 Å begins to decrease and the intensity of the first peak at 1.65 $Å^{-1}$ begins to increase. At ~160 K, the low-Q intensity stops changing and Bragg reflections, associated with the crystalline structure of ice I, emerge at 1.65 2.75, 3.40 and 4.35 $Å^{-1}$. The decreases in low-Q intensity, associated with increases in the homogeneity of scattering length density, indicate that the pores within the ASW

matrix began to collapse at ~115 K but were not completely eliminated until ~160 K. It is interesting that the first peak at 1.65 $Å^{-1}$ increases in intensity over the same temperature range. This may be due to increases in medium-range correlations as the effective density increased due to compaction. Alternatively, it may be due to the ordering influence of ASW's structural relaxations *prior* to crystallisation.

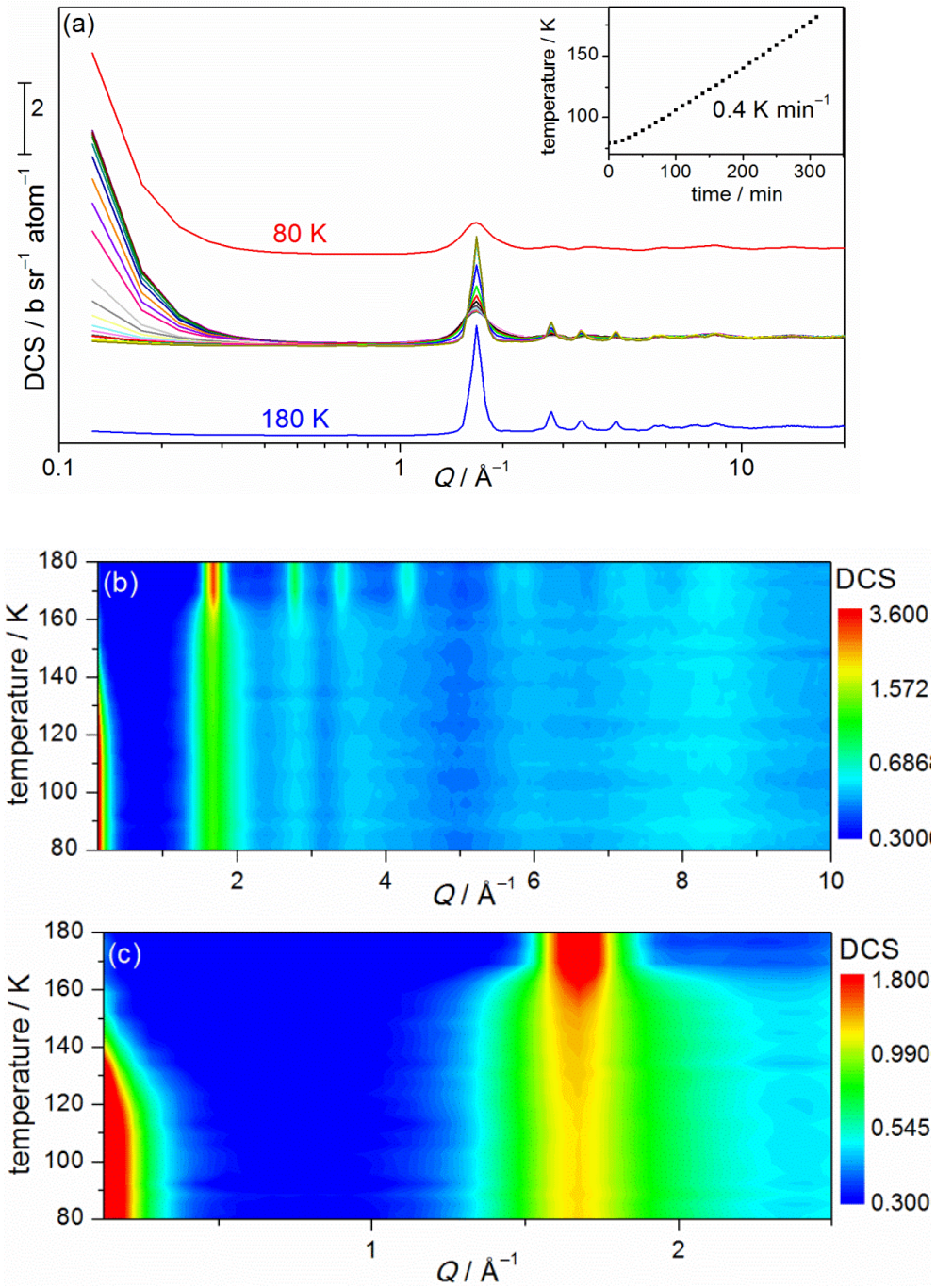

Figure 5.6 (a) neutron diffraction DCS of D_2O ASW/C_{60} 'trapped solution' with X_{C60} = 0.0034 accumulated over 10 minute intervals as the cryostat was heated from 80 to 180 K at 0.4 K min^{-1}, 80 K and 180 K data are offset vertically. Contour plots showing the temperature variation in DCS on log DCS scales (b) between 0.3 and 3.6 b sr^{-1} $atom^{-1}$ and (c) between 0.3 and 1.8 b sr^{-1} $atom^{-1}$

The temperature at which the low-*Q* intensity began to drop (115 K) coincides with the temperature to which the material was thermally annealed *prior* to the measurement. This may suggest that the rate of sintering is highly dependent on the temperature and that the porosity had already been significantly reduced by sintering during the sample preparation thermal annealing. Perhaps a certain temperature is required to close a pore of a given size with smaller pores requiring higher temperatures. This would be consistent with theoretical consideration of the correlation length and dynamic heterogeneity discussed in Chapter 4. The observation that crystallisation occurs immediately after sintering has finished is also in agreement with a model of ASW whereby the structure and dynamics are closely related. As smaller and smaller pores (very small pores are essentially structural defects) are closed with increasing temperature it would stand to reason that the bulk relaxation required for crystallisation would occur when the critical pore size reached zero. Overall, the sintering behaviour of the ASW matrix observed here is in stark contrast to what would be expected if ASW were to behave like a liquid, as has been postulated to be the case at temperatures above 136 K.[87] Significant low-*Q* intensity at temperatures > 150 K clearly indicates that the ASW/C_{60} material measured here is unrelaxed until its crystallisation.

5.2.3 FT-IR SPECTROSCOPY OF ASW/C_{60} 'TRAPPED SOLUTIONS'

In this section, the influence of C_{60} on the IR absorbance spectra of ASW is discussed. As for the FT-IR data of ASW presented in section 4.2.1 the ASW/C_{60} 'trapped solutions' investigated here were prepared with deuterium as an isotopic impurity (91.0 mol% H_2O + 9.0 mol% HDO) and deposited as thin films onto MgF_2 substrates. The isotopic substitution allowed features due to decoupled μ(O–D) modes to be observed. Figure 5.7 shows FT-IR absorbance spectra of the μ(O–D) mode for ASW (green lines) and for 'trapped solutions' with X_{C60} = 0.0040 (red line) and X_{C60} = 0.0208 (blue line). These correspond to average C_{60}–C_{60} outer shell distances of 1.60 and 0.75 nm, respectively. The more concentrated 'trapped solution' was a brown colour indicating a significant amount of aggregated C_{60} was present. The spectra have been normalised to the maximum intensity and the two curves presented for each C_{60} composition correspond to repeat measurements of

different ASW/C_{60} coated MgF_2 substrates. The spectra presented in Figure 5.7 (a) were recorded immediately after transfer of the substrates into the cryostat, (b) shows spectra recorded at 78 K after the films had been thermally annealed at 145 K (heating/cooling rate of ~5 K min^{-1}) and (c) shows 78 K spectra after thermal annealing at 190 K, which is above ASW's $T_{crystallisation}$.

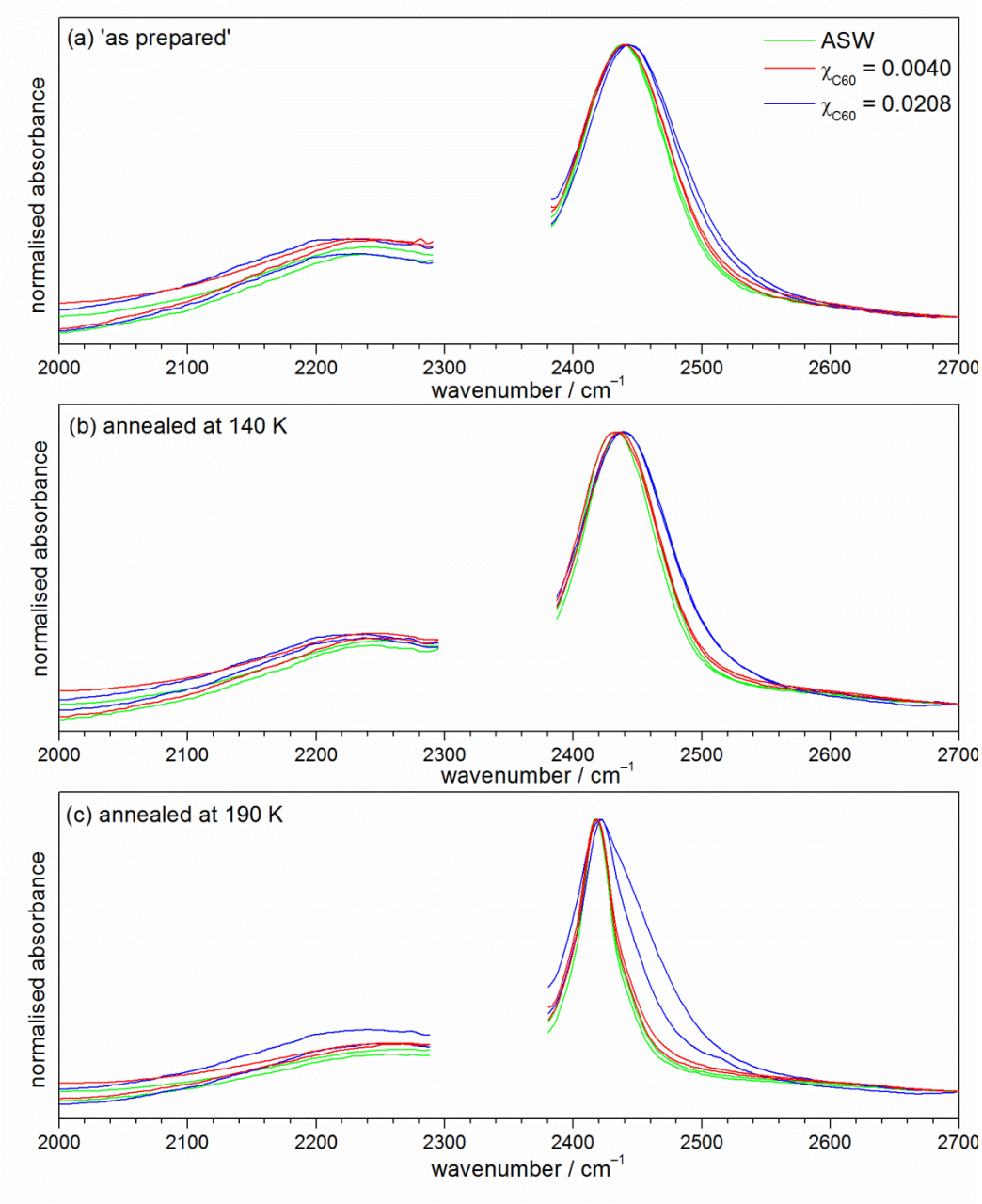

Figure 5.7 Transmission FT-IR spectra of the μ(O–D) absorption for ASW (green lines) and ASW/C60 'trapped solutions' with X_{C60} = 0.0040 (red line) and X_{C60} = 0.0208 (blue line). Spectra of (a) 'as-prepared' material recorded immediately after their transfer into the cryostat (b) annealed to 145 K and (c) 190 K.

Interestingly, the spectra of the ASW/C_{60} trapped solutions are significantly different from those of ASW in (a), (b) and (c). In each the μ(O–D) absorption for ASW containing C_{60} is wider with a greater intensity on the high wavenumber side of the peak. This suggests that on average the hydrogen bonding interaction was weaker in the ASW containing C_{60} than in pure ASW. This is consistent with the SFG results of the water-alkane interface,[298] and neutron spectroscopy of methane hydrates under pressure.[283] Furthermore, the similar peak shape on the low wavenumber side of the absorption suggest that the spectral difference upon introducing C_{60} giving increases in intensity ~2500 cm^{-1} is due to a small proportion of the HOD molecules in the ASW matrix forming weaker hydrogen bonds rather than a perturbation to the entire ASW structure. The extra absorptions between 2450 and 2550 cm^{-1} almost certainly correspond to HOD molecules in the immediate hydration shell of the C_{60}. Interestingly, the differences between the spectra for different C_{60} concentrations become more pronounced upon thermal annealing. This appears to be predominantly caused by a shift of the main absorption peak to lower wavenumber due to the structural relaxation of the ASW matrix. The position of the higher wavenumber C_{60} hydration-related absorptions does not appear to change much upon thermal annealing. The position of the hydration-shell-related absorptions are similar to those in liquid water at room temperature (*c.f* Figure 4.2) which may indicate that the average coordination number required to contain the hydrophobe in the hydration shell was similar to that found in liquid water (3.6). It is particularly interesting that even after annealing at 190 K and crystallisation of the ASW matrix to ice I the high wavenumber absorption are still present. This indicates that H_2O in the immediate hydration shell of the C_{60} did not form into consistent ice I crystals at 190 K. It may be that C_{60} retained an amorphous hydration layer or that the matrix about the C_{60} was comprised of very small crystallites with significant numbers of structural defects.

These results support a model of hydrophobic hydration whereby the water molecules in the first shell are somewhat disconnected from the remainder of the cooperative hydrogen bonding network. This theory is able to reproduce calorimetric data,[4] and is in good agreement with the many studies reporting structural and dynamics perturbations of the first hydration shell. Of

particular importance to this study, a disconnection between molecules in the shell and in the bulk may cause their structure/dynamics to have very different temperature dependence. This has been demonstrated experimentally by NMR relaxation measurements of supercooled solutions of amphiphilic molecules[5,320] which showed that the slower dynamics in the hydration shell of hydrophobic molecules at room temperature is reversed upon supercooling. This effect postulated to be caused by the insensitivity of the disconnected hydration shell to the slowing down of the bulk dynamics which occurs with decreasing temperature as the correlation length increases.[320] This would be in agreement with the sintering behaviour of ASW whereby interfacial H_2O at the surface of hydrophobic pores are more mobile at a given temperature than H_2O in the ASW bulk. The dynamics of the water molecules in the C_{60} hydration shells is explored further in the following section.

5.2.4 Optical Properties of ASW/C_{60} 'Trapped Solutions'

To investigate the optical properties of the ASW/C_{60} 'trapped solutions', thin films with a X_{C60} = 0.0010 or 0.0029 were again deposited onto MgF_2 substrates at a H_2O dose rate of 0.4 g h^{-1} for 1 h. These C_{60} concentrations correspond to average C_{60}-C_{60} separations of 3.0 and 1.9 nm, respectively. Two substrates were recovered from each deposition experiment. The first was used to perform optical absorbance measurements and the second to record their photoluminescence spectra. Optical absorbance was measured in transmission using a standard UV-VIS-NIR spectrometer and photoluminescence was recorded using a Raman microscope equipped with a He-Ne laser. The He-Ne laser provided a 'near absorption edge' excitation energy of 632.8 nm. No photoluminescence was observed when the excitation wavelength was changed to 735 nm. The corresponding absorbance and emission spectra for X_{C60} = 0.0010 are presented in Figure 5.8 and 5.9. A heating cycle was employed whereby the temperature of the cryostat was increased to sequentially higher temperatures for a 5 minute time period during spectral acquisition then reduced to 78 K in order to record a second spectrum (heating/cooling rate = ~5 K min^{-1}). Figure 5.8 (a) and Figure 5.9(a) show the spectra recorded at the annealing temperatures. Figure 5.8(b) and Figure 5.9(b) show

those recorded after recooling the cryostat to 78 K. This temperature profile enabled the reversible effects of temperature to be separated from the structural relaxations which occurred during thermal annealing steps and become 'frozen in' upon cooling. Figure 5.8(c) and (d) show an enlargement of the near absorption edge (630-650 nm) spectral range containing features due to C_{60}'s weak dipole forbidden predominantly S_0–S_1 excitations. The 632.8 nm excitation wavelength is indicated by the green line.

The most pronounced change in the optical absorbance (Figure 5.8) of the ASW/C_{60} films occurred after being heated to 220 K. At these temperatures, H_2O evaporates from the films, the C_{60} aggregates and the colour of the films change from pink-purple to brown. The total loss of water from the films annealed to 220 K was confirmed by loss of a near infrared (NIR) absorption peak at 1950 cm^{-1} (data not shown). The colour change upon aggregation is associated with the increases in absorption between 300 and 650 nm observed in the Figure 5.8 spectra. Increases in absorbance in this region of the spectrum were not observed at lower temperatures in either the X_{C60} = 0.0010 or X_{C60} = 0.0029 films suggesting that C_{60} did not diffuse in the ASW or crystalline ice matrices. Interestingly, the position of the optical absorptions for the nanocrystalline C_{60} remaining on the substrate has a strong temperature dependence becoming much more intense at ~700 nm at 220 K than at 78 K. Only small subtle changes can be observed in the spectra upon annealing at lower temperatures. There is a gradual and consistent increase in the width of the main absorption peaks centred at 326 and 256 nm with increasing temperature, and the peaks contributing to the features in the region of the absorption edge, indicated in Figure 5.8(c) and Figure 5.8(d), broaden slightly during crystallisation at annealing temperatures between 140 and 160 K. The subtle changes in shape of features in the region of the absorption edge reflect changes in the environment of C_{60} molecules during crystallisation. The increased width of the features implies that the C_{60} molecules were situated in a more diverse range of electric field environments in the crystalline matrix than in ASW. Perhaps this indicates an incoherent nature of the crystallites at the grain boundaries which presumably form around the C_{60}, molecules. This explanation would also be consistent with the

FT-IR measurements of section 5.2.4 which showed 'high wavenumber' OD related absorptions, even after annealing at temperatures as high as 190 K.

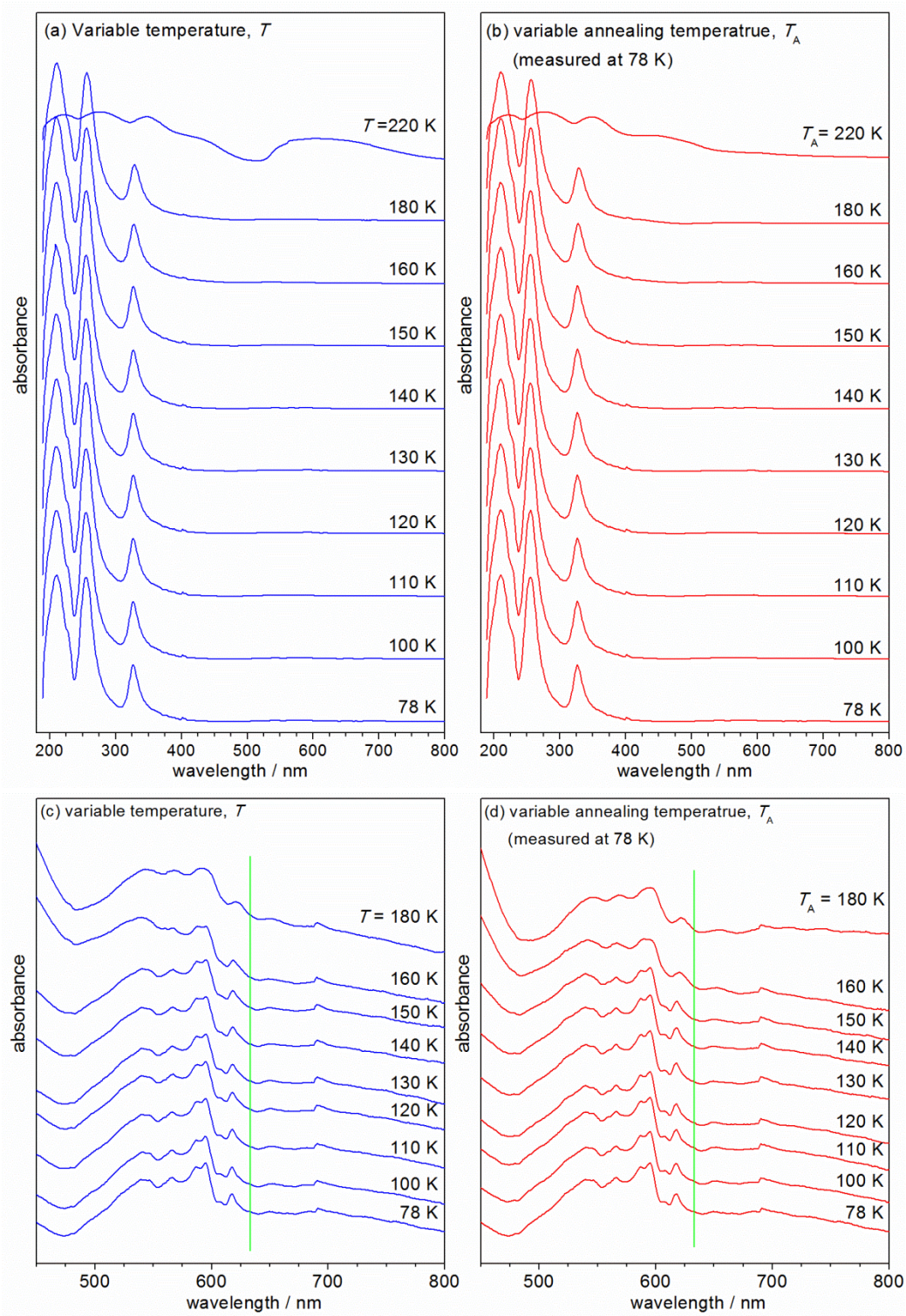

Figure 5.8 Optical absorbance spectra of an ASW/C_{60} trapped solution with X_{C60} = 0.0010 recorded at the T temperatures indicated (a and c) and at 78 K after being annealed for 5 minutes at the T_A temperatures indicated (b and d). The green line shows the wavelength of the He-Ne laser excitation used to record photoluminescence spectra.

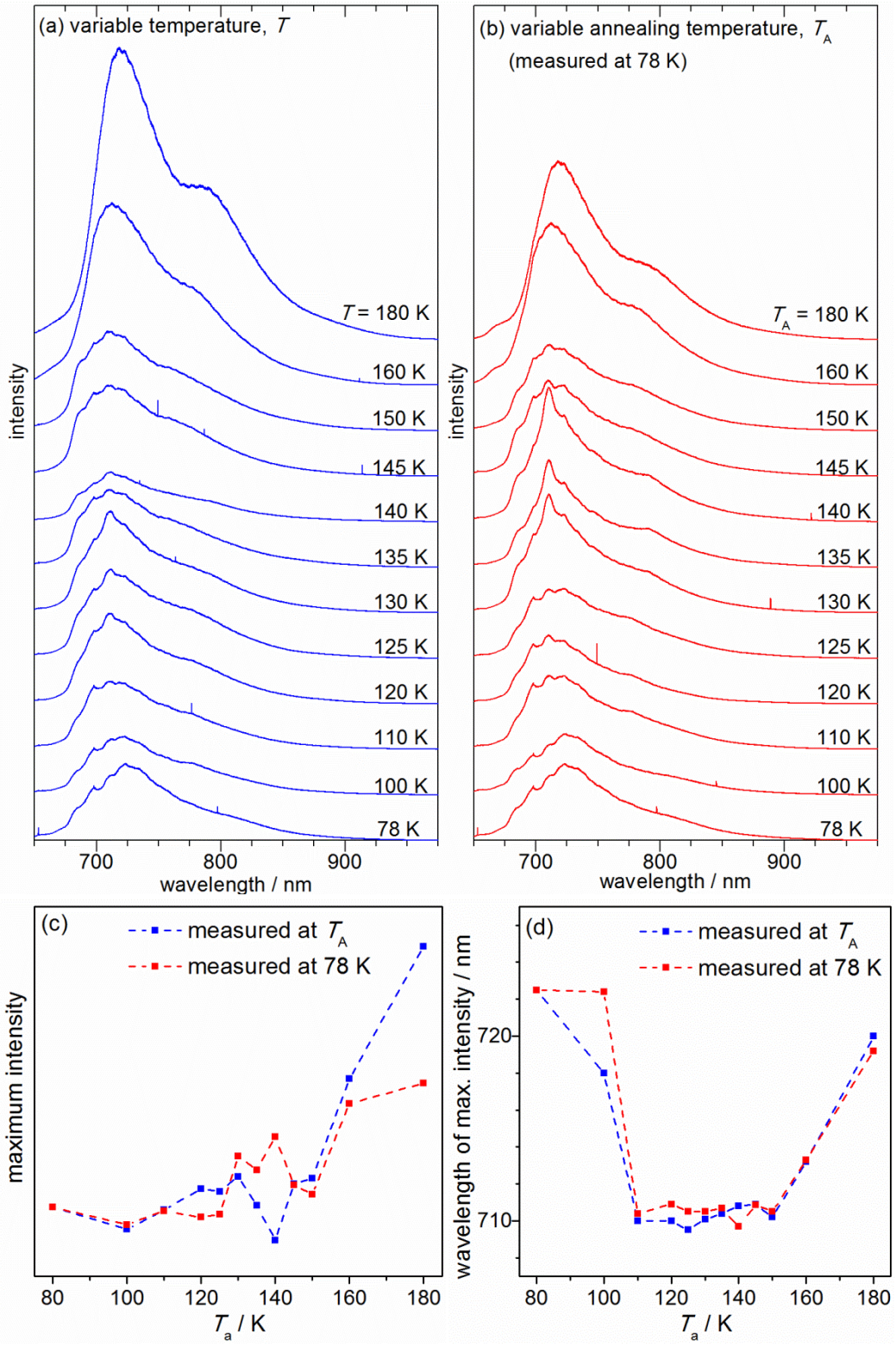

Figure 5.9 Photoluminescence spectra of an ASW/C_{60} trapped solution with X_{C60} = 0.0010 recorded at the T temperatures indicated (a) and at 78 K after being annealed for 5 minutes at the T_A temperatures indicated (b). The maximum intensity (c) and position of maximum intensity (d) extracted from the T and T_A spectra.

The photoluminescene spectra shown in Figure 5.9 look similar to those of C_{60} dispersed in organic solvents.[306] [302] Many of the small features visible in the 78 K spectra correspond exactly to T_1–S_0 phosphorescent transitions described by Wang et al.[307] Unlike the absorption spectra which showed only subtle changes with changes in temperature, T, or annealing temperature, T_A, there are quite considerable changes in photoluminescence. This confirms that C_{60}'s photoluminescence is sufficiently affected by changes in its local environment that it is well-suited to report on the nature of its hydration shell. As discussed in the introduction to this chapter, the influence of the chemical environment on the spectra depends upon the activity of non-radiative decay processes and the configuration coordinate cross over between excited and relaxed states, and may therefore be difficult to understand entirely for this system. However, confidence in the interpretation of the changes in the photoluminescence spectra may be improved by considering the trends which occur with increasing T and T_A. Three temperature ranges with different spectral variation can be identified. At temperatures between 78 K and 130 K the T and T_A spectra look similar and do not change much with increases in T or T_A. At temperatures between 130 K and 140 K the spectra show different variations with T and T_A. Whilst the spectra recorded at the annealing temperature, T, decrease in intensity those recorded at 78 K for different T_A look similar to the spectra recorded for T_A of 130 K with a sharp pronounced feature at 710 nm. For temperatures between 145 and 180 K the spectra again look similar for T and T_A. In this temperature range the intensity of the photoluminescence increases and the peaks get much broader. The T and T_A variations in maximum intensity and position of maximum intensity are summarised in Figure 5.9(c) and Figure 5.9 (d).

The spectral dependence on T and T_A outlined above suggests that the nature of the C_{60} hydration shells changed at ~130 and at ~145 K. The changes at 145 K are most likely to be related to ASW's crystallisation. The increasing width of the emissions corresponds well with the increasing width of the optical absorptions in the same temperature range and indicates that C_{60} in the crystalline ice matrix was in a diverse range of different environments. The changes in the nature of the hydration shell at 130 K are, however, not likely to be associated with crystallisation. As C_{60}'s 'near edge' absorptions do not change over this temperature range (Figure 5.8c and Figure

5.8d), the changes in photoluminescence must reflect changes in the interaction between C_{60}'s excited T_1 state and its local environment. The decreasing intensity with increasing temperature between 130 and 140 K may indicate that quenching mechanisms became increasingly available in this temperature range. This might indicate that the hydration shell was much more mobile at temperatures above 130 K. Although this is speculative, quenching mechanisms are typically increased in dynamic systems which better allow specific interaction geometries required for non-radiative relaxations. This hypothesis would also be supported by variations in the spectra recorded after the cryostat had been recooled to 78 K. The spectra recorded at 78 K after being annealed to temperatures of 130, 135 and 140 K are very similar with a single sharp feature at 710 nm. This indicates that the structure of the C_{60} hydration shell obtained upon cooling was identical (*i.e.* ergodicity at temperatures above 130 K) and the sharpening of the 710 nm feature is likely to be closely associated with the consistent and relaxed hydration structure formed.

The lower temperature required to mobilise water in the C_{60} hydration shells than in the bulk suggested by these data may be due to local heating effects concomitant with the quenching mechanisms, but would also be consistent with the connection between structural and dynamic heterogeneity already discussed whereby molecules in structurally unrelaxed environments, adjacent to hydrophobes or analogously small pores or at structural defects are more mobile than molecules in the bulk, which are structurally more relaxed.

5.3 CONCLUSIONS

In this chapter the structure of ASW/C_{60} 'trapped solutions' has been investigated using a wide range of techniques. X-ray and neutron diffraction data indicates that C_{60} does not measurably perturb the structure of ASW over length scales consistent with the distance range of hydrophobic effects. Very high concentrations of C_{60} were required to observe a change in the shape of the ASW OD stretching related absorption by FT-IR. These data suggest that the structural signature of hydrophobic hydration in ASW is a weakening of the hydrogen bonding interaction in only the first hydration layer. Based on this new understanding that the extended matrix is unperturbed by the

hydrophobe, a neutron scattering experiment to probe the immediate hydration shell could be envisaged whereby the scattering length density of a hydrophobic molecule (X) is varied to enable complete subtraction of the interference scattering from the matrix and separation of the X-O and X-H partial radial distribution functions. The low availability of large hydrophobic species with different isotopic scattering length contrast is, however, a significant obstacle.

The absence of a perturbation to ASW's extended structure found in this study may indicate that long range hydrophobic effects in liquid water may arise due to changes in the concerted nature of the dynamics which may allow local and perhaps intermediate structures to access specific relaxed states. This view is supported by measurements of C_{60} photoluminescence as a 'trapped solution' was thermally annealed, which suggest motion of water molecules in the C_{60} hydration shells at temperatures between 130 and 140 K, lower than in the bulk. The extensive temperature range of the sintering process, revealed in this chapter may, in fact, be the clearest manifestation of this dynamic character with unrelaxed molecules either adjacent to hydrophobes (or analogously small pores) being more mobile than molecules in the bulk which are structurally more relaxed. This structurally derived dynamic heterogeneity could provide another explanation for the weak heat capacity increase observed for ASW at 136 K and postulated to be associated with the glass to liquid transition.[87] Overall, a greater understanding of the potential energy landscape is needed to explain the link between these excluded volumes, changes in dynamic character, and forces such as the hydrophobic effects observed in liquid water. This would allow the distance range over which the rate of molecular motions and structure are interrelated to be described. Although studies of liquid structure and liquid dynamics are often considered separately, recent discoveries of mesoscale structural ordering,[321] and theories indicating structural mechanisms for dynamic arrest at the glass transition,[200] suggest that a more closely aligned perspective may be needed to answer some of the most challenging and important problems in liquids research.

6 Self-Associations in Liquid Chloroform

6.1 Introduction

This structural investigation of liquid chloroform ($CHCl_3$) has primarily been carried out to better understand the nature of interactions in the chloroform-acetone azeotrope. However, chloroform's structure is of significant independent interest. It is a widely used solvent due to its volatility and miscibility with polar and non-polar substances[322-324] It is also a commonly used chemical reagent and an effective anaesthetic.[7,325-326] In addition to its production for industrial purposes, chloroform vapour is present in the Earth's atmosphere at low levels, due to its production in forests and by marine plants.[327] Chloroform is also of fundamental interest because of its complex charge separation, whereby a region of positive electrostatic potential forms at the distal end of each chlorine atom, termed a "σ-hole" and a ring of negative charge forms around the circumference.[328] The interactions in the liquid which arise due to σ-hole formation, termed halogen bonding,[328-330] are thought to be fundamental to the stability of many proteins,[331] the activity of some pharmaceuticals,[332] and are being increasingly exploited for crystal-engineering applications.[333-335] Figure 6.1 shows the DFT-calculated (B3LYP 6-31G*) structure of chloroform and 0.001 electron $bohr^{-3}$ isodensity surface, colour mapped to show regions of positive and negative electrostatic potential. The atom labels and axes directions defined here are those used throughout the chapter. The measured vapour phase dipole moment of chloroform is 1.04 D.[262] Its direction is parallel to the *z*-axis as indicated by the blue arrow in Figure 6.1. Chloroform's properties have been described by Lide.[336]

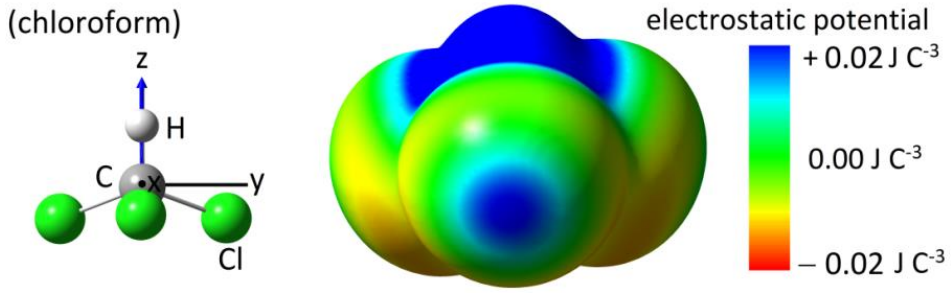

Figure 6.1 DFT-calculated (B3LYP 6-31G*) structure of the chloroform molecule, colour mapped to show electrostatic potential on the 0.001 electron $bohr^{-3}$ isodensity surface.

The intermolecular structure of liquid chloroform has primarily been studied using computer simulation,[111,337-344] diffraction,[345-349] and spectroscopic methods.[350-351] The diffraction and computer simulation studies mainly produced RDFs to describe the liquid structure, but ultimately found it difficult to characterise the 3D arrangements in the liquid using just radially averaged 2D functions. The diffraction studies by Pothoczki *et al.*,[348-349] did attempt to go beyond a radially averaged analysis by examining a 3D structural model, but neglected the true symmetry of chloroform in their analysis, instead using an approach first used to investigate the perfectly tetrahedral CCl_4.[352] They also found evidence for very ordered molecular arrangements in the first shell, which seem unlikely. A recent simulation by Yin *et al*, also went further than 2D RDFs and compared the relative interaction energies of several different 3D dimer conformers.[343] On the basis of electrostatic and dispersion forces they found dipole aligned pairs separated at a C–C distance of 4.0 Å to be the most stable. The spectroscopic studies,[350-351] carried out almost 60 years ago, postulated the self-association of chloroform in the liquid from changes in spectral band shape observed upon introducing chloroform into other solvent media. In many of the computer simulations studies of $CHCl_3$, particular attention has been given to reproducing the partitioning of chloroform into lipid membranes with the aim of better understanding its anaesthetic properties.[325-326,353]

In this chapter, the measured neutron diffraction structure factors for $CHCl_3$, $CDCl_3$ and a 1:1 mixture of these, $C(H/D)Cl_3$, are presented along with a full structural analysis of a 3D model produced using EPSR and consistent with the scattering data. The structural details of the model are described using intermolecular radial distribution functions (RDFs), spatial density functions (SDFs) and orientational correlation functions (OCFs). From these, several favourable molecular arrangements inherent to the liquids structure have been identified. Furthermore, chloroform's self-association has been investigated by analysis of the relative abundance of the most favourable arrangements. Some of the main findings presented in the Chapter are also reported by Shephard *et al.*[354]

6.2 Results and Discussion

6.2.1 Neutron Scattering of Chloroform Liquid

Neutron scattering structure factors for $CHCl_3$, $CDCl_3$ and $C(H/D)Cl_3$ have provided a good confidence in the distribution of H–H pair distances in liquid chloroform. Weighting factors ($b_A b_B c_A c_B$) indicating the corresponding contribution to the scattering data from the different atom pairs for the mass measured composition of the liquids are given in Appendix 10. A further series of measurements adjusting the scattering length of chlorine would be expected to improve the accuracy of the model but the cost of preparing chlorine isotope enriched chloroform was prohibitive. Also shown in Appendix 10 are the average measured differential cross sections (DCSs), the total coherent, $\langle b \rangle^2$, and total, $\langle b^2 \rangle$, cross sections. The scattering data over the entire *Q*-range measured (0.1 – 50 $Å^{-1}$) and the subtracted components, indicating the inelastic perturbations to the data are shown in Appendices 13–14.

The scattering data are presented over a reduced *Q*-range in Figure 6.2. In (a) the DCS has been corrected for attenuation and multiple scattering, in (b) the inelastic perturbations to the data have also been subtracted and (c) shows the FT of the corrected data after normalisation by $\langle b \rangle^2$. The data in (a) and (b) show an increase in average DCS with the hydrogen content of the liquid caused by the greater incoherent scattering length of H relative to D. The differences between (a) and (b), shown more clearly in Appendix 14, indicate the inelastic perturbations to the scattering data, which are most pronounced at low *Q* in the $CHCl_3$ data. The inelasticity correction procedure also unexpectedly removed the negative slope present in all three of the uncorrected data sets. The similar profile of the subtracted component for all three liquids suggests that this element of the uncorrected data may be due to inelastic collisions with chlorine or carbon atoms. Bertagnoli *et al.*,[346] observed a similar slope in their neutron scattering measurements of chloroform liquid. Alternatively, the slope may be due to the large neutron capture cross section of ^{37}Cl and its impact upon the Gudrun data corrections, for which absorption cross sections are assumed to depend linearly on wavelength.[123] In the work of Tao *et al.* on CCl_4 a more complex function was used to

model the attenuation in their corrections which employed a different software package.[355] The corrections carried out in this work using the Gudrun software are described in section 1.1.5.

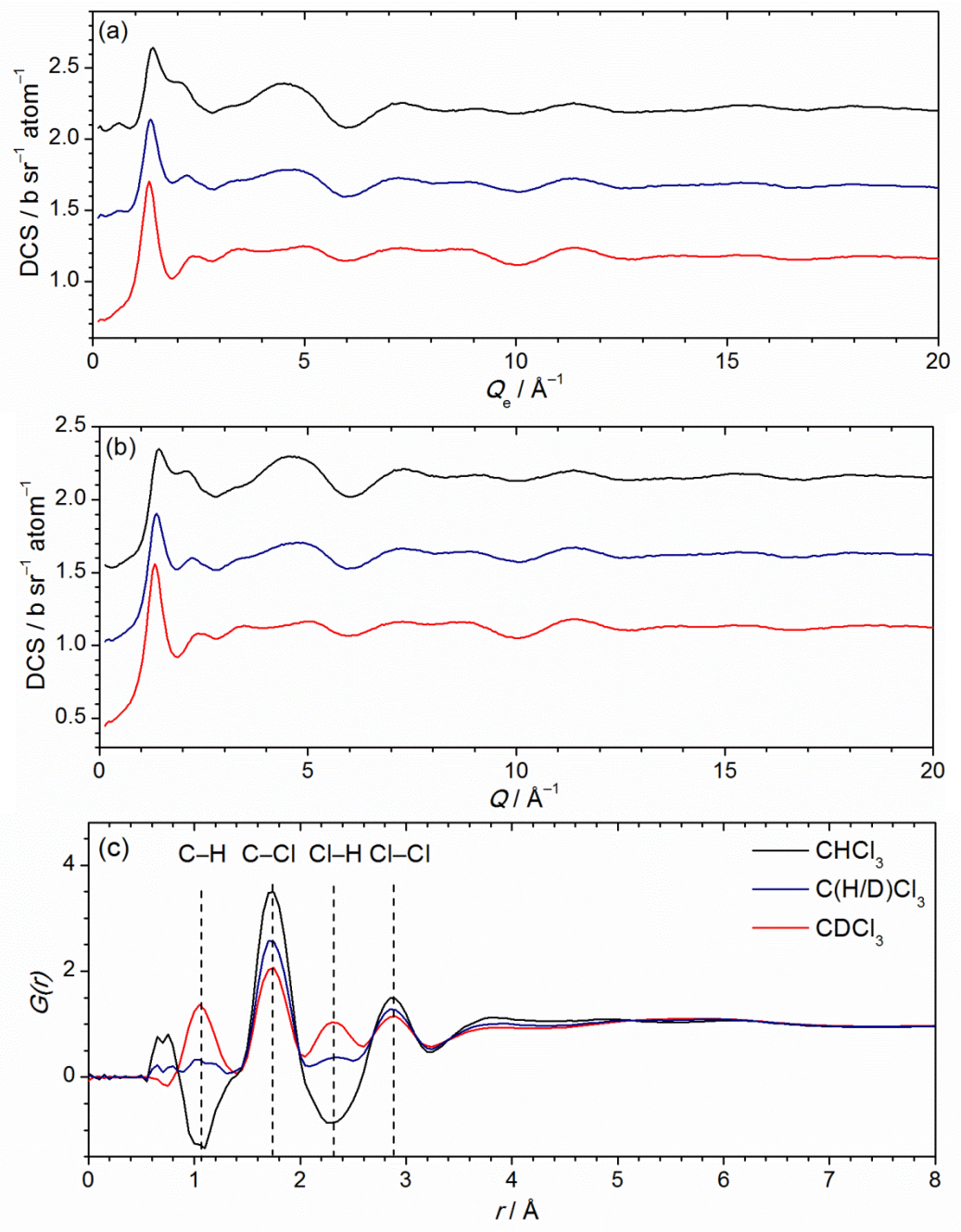

Figure 6.2 The measured scattering data for the chloroform liquids. (a), corrected for attenuation and multiple scattering, (b), also corrected for inelastic collisions and (c), the smoothed FT of the corrected scattering data normalised by $\langle b \rangle^2$.

6.2.2 Building Structural Models of Liquid Chloroform

Several different 3D structural models of liquid chloroform were produced by Monte Carlo simulation. For these, the bond lengths, angles, Lennard-Jones (LJ) distance and energy parameters, and the values of the monopole partial charges were taken from the parameterisation study of liquid chloroform carried out by Barlette *et al*.[111] These are given in section 2.1.15 with details of the adjustable EPSR parameters and box size. The intramolecular distances were originally found from microwave experiments,[356] and the partial charges were found from their fit to a DFT description of the electric field using CHELPG,[357] This arrangement gives a slightly larger dipole moment (1.32 D) than reported for the vapour (1.04 D).[111,262] The effectiveness of the CHELPG fitting procedure for reproducing the electric field around chloroform has been investigated by Torri *et al*..[358-359] The LJ distances, σ, were from Jorgenson *et al*.[360]. The LJ energy values, ε, were found by Barlette *et al.* using iterative adjustments within their simulation to reproduce the liquids density and molar enthalpy of vapourisation.[111] In this work, three models of liquid chloroform were produced; a model created using repulsive intermolecular potentials (term 1 in Equation 1.2) to reduce molecular overlap and representing the most efficient packing of the molecules, termed the hard sphere (HS) model; a model created from the LJ parameters (term 2 in Equation 1.2) and partial charges (term 3 in Equation 1.2), termed the LJ+C model; and a model created with EPSR by introducing EPs to improve the fit between simulated and measured scattering data. Comparisons of these three structural models have been used to better understand the nature of the interactions influencing the structure of the liquid.

6.2.3 Interference Functions of Liquid Chloroform

In Figure 6.3, interference functions, $F(Q)$, prepared from the corrected DCS by subtracting the average scattering level, are compared with interference functions simulated from the HS (blue), LJ (black), and EPSR (red) models. Large differences between simulation and experiment can be observed for the HS model, reflecting the influence of the electrostatic and more specific intermolecular interactions on the structure of liquid chloroform. For the LJ model, only small

differences can be observed in the *Q*-region between 1 and 4 $Å^{-1}$. This indicates that the LJ parameters and monopole partial charges of the model are able to reproduce many structural aspects of the liquid. The differences are further reduced in the EPSR model reflecting the additional descriptive power of the EPs and the directing influence provided by the experimental diffraction data. However, slight differences in the shape of the second diffraction peak can still be observed upon close inspection. These differences may suggest a small systematic error in the measured $F(Q)$ data or that the EPs are unable to entirely overcome errors in the force field introduced with the LJ parameters and monopole partial charges. In EPSR, this may arise due to the underdetermined nature of the system or because the pairwise EPs may be unable to account for multibody correlations or the orientation-dependence of specific interactions.[9] Nonetheless, the improved fit of the EPSR model relative to the LJ model (sum of absolute difference between the simulation and experiment are 4.14 and 3.13 b sr^{-1} $atom^{-1}$, respectively) indicates that the EPSR model is a closer representation of the liquid structure than possible by parameterised Monte Carlo simulation.

6.2.4 The Intramolecular Structure of Liquid Chloroform

The first analysis carried out was to examine the range of geometries taken by molecules within the EPSR model. The separation of the $F(Q)$ and $G(r)$ of the EPSR model into intra- and intermolecular $S(Q)$ and $g(r)$ are given in Appendix 19. These plots show the overlap of intra- and intermolecular RDFs, the bond length distributions without the influence of Lorch smoothing, and structure factors without the influence of the atoms scattering lengths. Bond length statistics, calculated from the intramolecular RDFs are given in Table 6.1. The bond angles statistics were found directly from the distribution of angles between the atom pairs in the model. These values are similar to those calculated for chloroform from neutron diffraction data collected by Bertagnoli *et al.*[345] and fall within the ranges expected for chloroform based upon analysis of the structures of chloroform-containing materials in the Cambridge Structural Database (CSD).

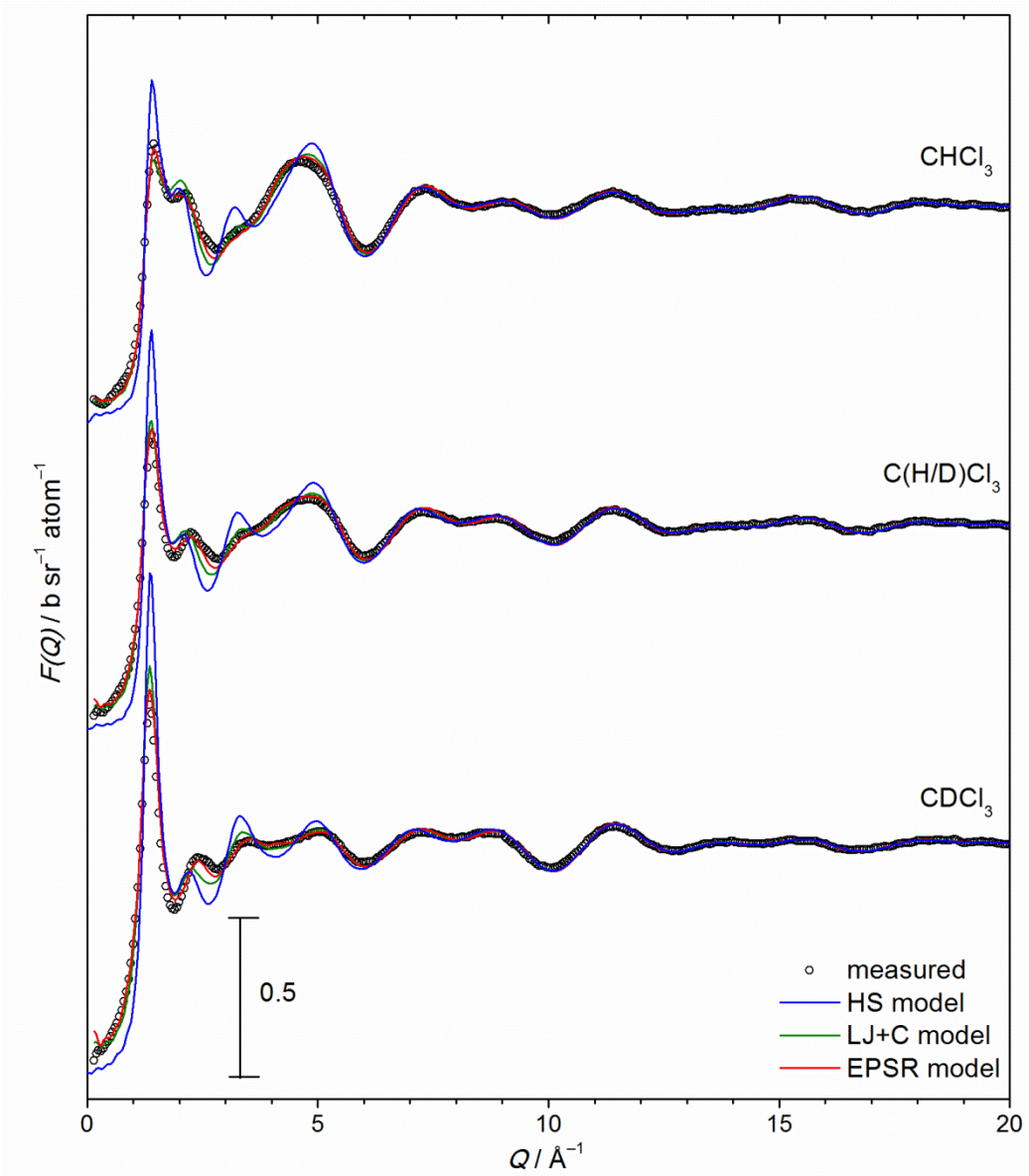

Figure 6.3 Comparison of the measured interference functions, $F(Q)$, with simulated data for the HS, LJ+C and EPSR models. The traces have been offset vertically for clarity.

Table 6.1 Average bond lengths and angles of chloroform molecules in the model structures. The numbers in parentheses give the standard deviations of all the distances/angles in the accumulated model structures.

	bond length / Å		angles / °
C-H	1.088 (0.071)	Cl-C-Cl	111.02 (5.24)
C-Cl	1.759 (0.062)	Cl-C-H	107.96 (8.78)

6.2.5 Radial Distribution Functions of Liquid Chloroform

The next stage in the structural analysis of the 3 models was to compare the intermolecular RDFs extracted from each. The RDFs of the HS (blue line), LJ+C (green line), and EPSR (red line) models are shown in Figure 6.4. Average coordination numbers of a central molecule in the EPSR model, calculated (Equation 1.4) from the RDFs over specified distance ranges are given in Table 6.2. The ranges were chosen according to local minima in the RDFs. The data for C–C atom pairs indicate that the closest approach between molecule centres (defined here as the C atom rather than the centre of mass) is ~3.5 Å, and that the first molecular shell contains an average of 12.7 nearest neighbours and extends to ~7.5 Å with a modal distance of ~5.3 Å. These values are in good agreement with the minimum energy conformer analysis of Yin *et al*.[343] The RDF oscillations at greater distances, with maxima at 10.0 and 14.6 Å, indicate some positional ordering in the subsequent two molecular shells, containing an average of 48 and 93 molecules, respectively.. Interpretation of the RDFs for the other atom pairs, further from the molecule's centre are more difficult, as their profile is more sensitive to the relative orientation of molecules within the coordination shells. However, it is conspicuous that the first peak in the H–Cl RDF corresponds to an average H–Cl coordination number of 3.1 and that the low-*r* profile of H–Cl and Cl–Cl RDFs indicate intermolecular distances which are much closer than would be expected to occur as a result of purely dispersive interactions.[110] The sum of van der Waals radii for H–Cl and Cl–Cl are 2.95 and 3.5 Å, respectively.[109]

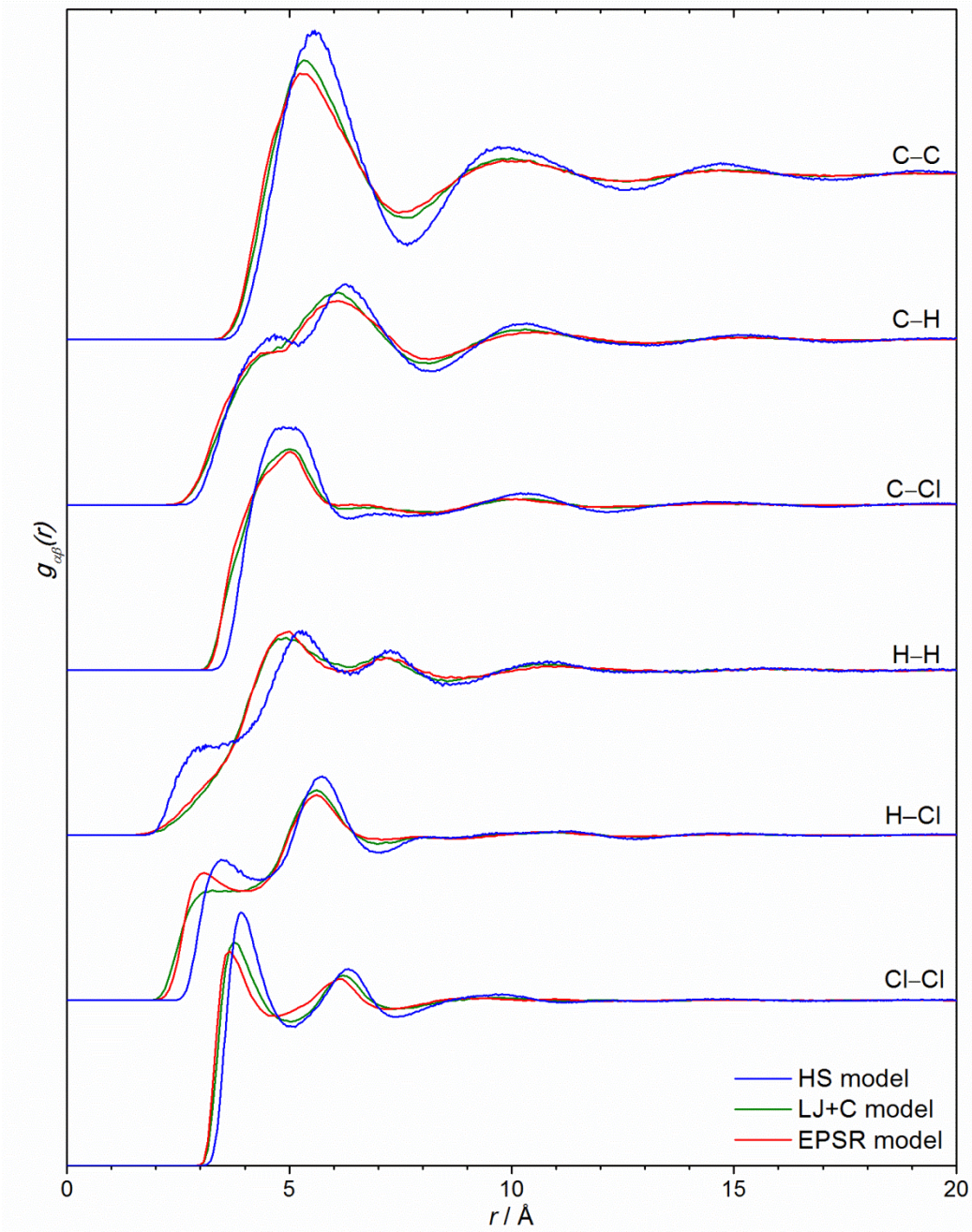

Figure 6.4 Intermolecular radial distribution functions extracted from the HS, LJ+C and EPSR models. The traces have been offset vertically for clarity.

Table 6.2 Average coordination numbers extracted from the EPSR model. Values in parentheses indicate the distance ranges in Å and the coordination numbers given are for atoms listed 2nd about atoms listed 1st.

C–C	(3–7.5)	12.7	(7.5–12.5)	47.6	(12.5–17)	92.7
C–H	(2–5)	2.5	(5–8)	13.0	(8–13)	52.5
C–Cl	(2–6)	18.0	(6–8.5)	36.4	(8.5–12)	105.5
H–H	(1.5–3.5)	0.3	(3.5–6)	5.5	(6–8.5)	12.7
H–Cl	(1.5–4)	3.1	(4–7)	26.7		
Cl–Cl	(2–4.5)	5.7	(4.5–7.2)	26.8		

Whilst the C–C RDFs of the EPSR, LJ+C and HS models have a similar profile, there are greater differences between the RDFs of the other atom pairs, which are most pronounced in the RDFs for H–H, H–Cl and Cl–Cl. The similarity of the C–C RDFs for the different models indicates that the overall shape of the first and second coordination shells is strongly influenced by the size and shape of the molecules. Similar observations have been made from the molecular centre RDFs of many molecular liquids. The greater differences for atom pairs further from the molecule's centre reveal the influence of intermolecular interactions on the relative alignment of molecules in the different shells. The nature of the interactions can be understood by comparing the RDFs of the EPSR and HS models. For example, the decreased intensity of the H–H RDF at distances between 2–3.5 Å in the EPSR model relative to the HS model demonstrates the repulsion between positively charged H atoms which act upon the orientation of the molecules to reduce the unfavourable electrostatic interaction.

The RDFs of the EPSR model may be compared with those found in earlier studies of liquid chloroform. In many respects, the RDFs determined here are similar to those reported in the RMC[361] study carried out by Pothoczki et al. [348] However, the H–H, C–H and H–Cl RDFs in the model produced by Pothoczki *et al*. contained sharp features at low *r*, indicating strong orientational ordering in the first shell. In the RDFs of the present study only broad features are observed at these positions, indicating more orientational disorder. This description is more consistent with models produced by computer simulation methods, which were reviewed for this purpose by Yin *et al*.[343] To further test the reasons for the differences between the structural models produced by EPSR and by RMC modelling procedures, the neutron scattering data of the present study were also fitted using the RMC approach. The high-*Q* SANDALS data was difficult to fit using RMC as the atom moves (EPSR primarily makes molecule moves) were found to distort intramolecular distances. Thus, without the constraining influence of high *Q* data in the earlier study, which used window constraints to compensate for a *Q*-max of 8 $Å^{-1}$, it is possible that these distortions may have gone unnoticed in the earlier study.

The RDFs shown here are also similar to those produced in a Monte Carlo simulation by Torii in which additional atomic quadrupoles were used to describe the charge separations in chloroform.[358] In this study, several different methods for describing the charge separation were tested and atomic quadrupoles positioned on the chlorine atoms were found to have a large impact on the shape of the RDFs. This reflects the relationship between the liquid structure and the molecular charge separation as the atomic quadrupoles enabled chloroform's σ-hole to be reproduced more accurately. Interestingly, the differences in the RDFs produced by Torri *et al*. are very similar to the differences between the RDFs of the LJ+C and EPSR models shown here. This suggests that the primary role of the experimentally derived EPs in the present simulation is to improve the spatial description of the electric field around the chlorine atoms of the chloroform molecules.

Differences in the Cl–Cl and H–Cl RDFs are particularly important to consider in this respect as they show the impact of the negative monopole partial charge values placed on the Cl atoms by the CHELPG fitting procedure. Specifically, the increased repulsion between chlorine atoms causes a shift in the first peak of the Cl–Cl RDF to greater distances in the LJ+C model relative to the EPSR model, for which the effect has been corrected. Also, the increased attraction between chlorine and hydrogen atoms appears to have disrupted the first feature in the H–C RDF of the EPSR model, which corresponds to an average chlorine coordination of 3.1 atoms. This implies that the EPs cause the H atoms to point into the recess between the three Cl atoms rather than towards a specific Cl atom. These observations suggest that for the accurate Monte Carlo simulation of molecules containing halogen atoms, atomic quadrupole parameters or additional EPs should be included.

6.2.6 Spatial Density Functions of Liquid Chloroform

The origin of features in the RDFs and the spatial position of neighbouring molecules can be better understood by an examination of 3D spatial density functions, SDFs. As for the RDFs, these plots show the distribution function, g. But rather than showing its variation with distance, r, the

variation with spherical coordinates r, φ_1 and θ_1 are indicated. Thus, SDFs show the most likely positions of a second molecule relative to a reference molecule with a fixed orientation (defined here as: C→H in line with z-axis, Cl atom placed in zx-plane). The axes definitions and origin of the spherical coordinates are shown schematically in Figure 2.1. As the exact variations in g are difficult to show in 3D, the distributions of spatial arrangements within the models are presented using fractional isosurface levels (FSL). These surfaces, which form lobes in 3D, indicate the smallest volume containing a specified fraction of atoms, and equate to an intrinsically scaled probability level. The shaded regions inside the lobes can be considered as the tips of the peaks in the intermolecular $g(r)$s, when plotted in 3D. In an effort to unambiguously show the structure within the first intermolecular shell, several FSLs of 0.1, 0.3, 0.5 and 0.8 have been used and the shell has been divided into 4 distance ranges with equal values for their integrated $g(r)$. This extensive approach avoids problems associated with curtailing the data at chosen distances or FSL levels. The images of Figure 6.5 (a) show C–C SDFs extracted from the EPSR model over distance ranges of 3–4.9, 4.9–5.5, 5.5–6.2 and 6.2–7.2 Å; (b) shows the same series of C–C SDFs but extracted from the HS model; The SDFs in (c), show data for C–H atom pairs extracted from the EPSR model over distance ranges of 2.1–4.5, 4.5–5.4, 5.4–6.2 and 6.2–7.1 Å; and the SDFs in (d) show data for C–Cl atom pairs extracted from the EPSR model over distance ranges of 2.8–4.5, 4.5–5.2, 5.2–6.2 and 6.2–7.2 Å.

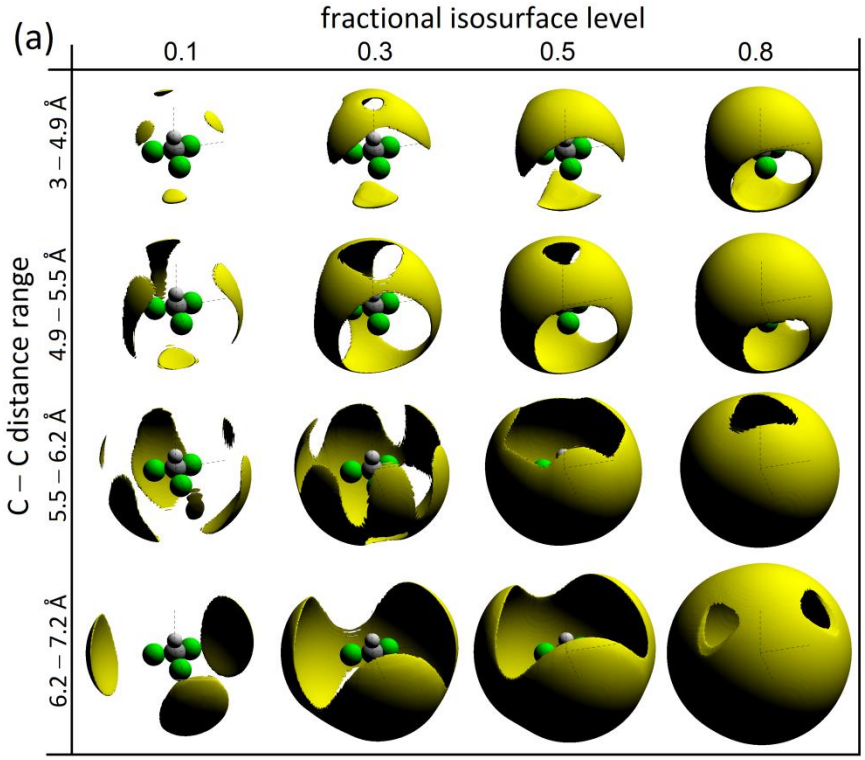
(a)
fractional isosurface level
0.1
0.3
0.5
0.8
C – C distance range
3 – 4.9 Å
4.9 – 5.5 Å
5.5 – 6.2 Å
6.2 – 7.2 Å

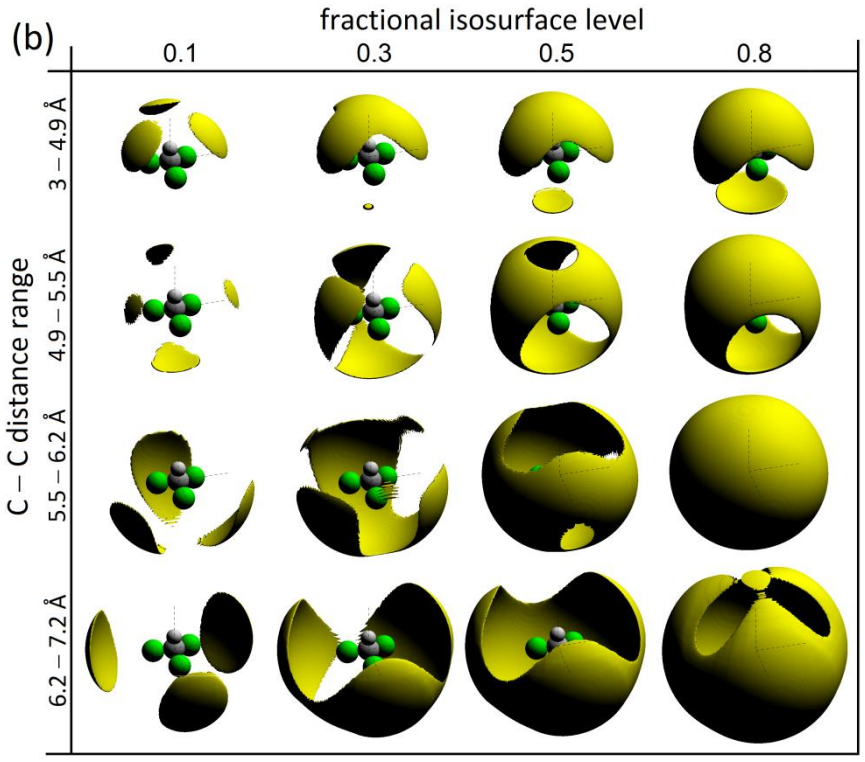
(b)
fractional isosurface level
0.1
0.3
0.5
0.8
C – C distance range
3 – 4.9 Å
4.9 – 5.5 Å
5.5 – 6.2 Å
6.2 – 7.2 Å

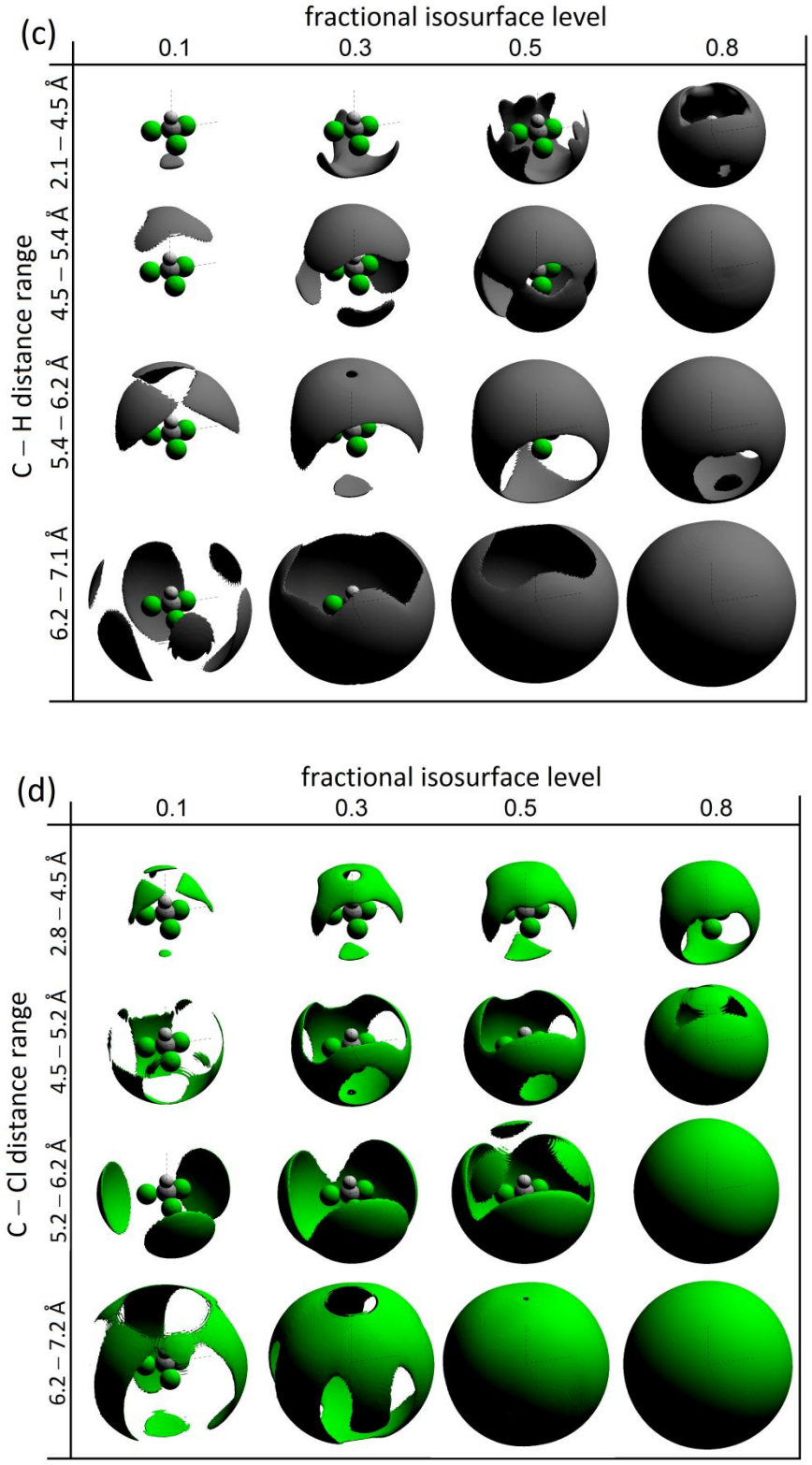

Figure 6.5 3D SDFs for FSLs of 0.1, 0.3, 0.5 and 0.8 over distance ranges chosen to give equal integrated $g(r)$. The SDFs shown in (a) are for C–C distances within the EPSR model; (b) C–C distances in the HS model; (c) C–H distances in the EPSR model; and (d) C–Cl distances in the EPSR model.

One of the most noticeable features in these plots is the similar shape of lobes in the C–C SDFs for the EPSR and HS models. This observation extends into 3D an understanding of the impacts of packing constraints on the molecular arrangements within coordination shells, concluded from the position of peaks in the radially averaged RDFs. These 3D plots indicate that the molecule's shape also appears to have a dominating influence on the spatial position of molecules in the first coordination shell. The shaded lobes in these C-C SDF plots also show a general trend of increasing volume with increasing FSL level and distance. Whilst the greater volume contained within the lobes at greater FSL levels reflects the shape of the distribution of probable positions, the increase in volume with distance reflects the tendency of the liquid to become more disordered, with a lower spatial homogeneity, towards the edge of the first molecular shell. In addition to these general observations for C–C atom pairs, the position of the lobes in the 0.1 FSL level plots for C–H and C–Cl, indicating their most likely positions about the reference, reveal the nature of several favourable molecular arrangements at different characteristic C–C distances. These arrangements are discussed below.

The position of lobes in the 0.1 FSL C–C SDF plot for the EPSR model (Figure 6.5a) over the 3–4.9 Å range indicates that the most closely approaching carbon atoms are positioned below (-*z*), and above (+*z*) the reference molecule. The lobes at +*z* appear as three separate lobes positioned between the chlorine atoms of the reference molecule. The stabilisation of molecules in this arrangement is also reflected in the C–C RDF which shows a subtle low-*r* shoulder on the first peak. The relative orientations of these closely approaching molecules can be better understood by considering the C–H and C–Cl SDF plots over the shortest distance ranges of 2.8–4.5 Å and 2.1–4.5 Å, respectively. The most likely position for chlorine atoms (above) and hydrogen atoms (below) indicate molecules stacked with a fairly parallel dipole alignment. This stacked arrangement gives rise to the low-*r* feature in H–Cl RDF and contributes to the first main peak in the H–H RDF at ~5 Å. The different position of lobes above and below the reference indicates that the most preferred arrangement has a relative dipole alignment slightly offset from parallel. This arrangement is shown as structure (a) in Figure 6.6.

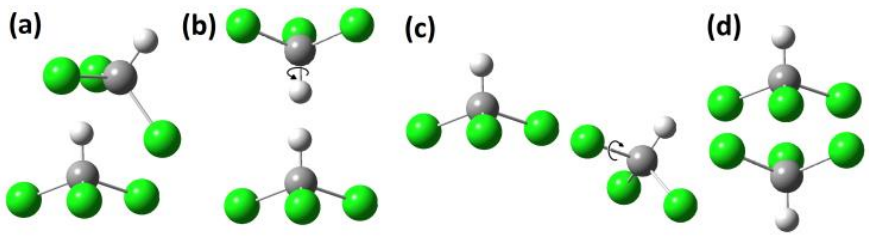

Figure 6.6 Molecular arrangements extracted from the EPSR model. The crystalline phases of chloroform are described by Dziubek *et al*.[362]

A similar observation about the most favoured arrangement was also made in the RMC study of Pothoczki *et al*..[348] Treating chloroform as tetrahedral, they argued that edge to face interactions are particularly likely at short C–C distances. However, the analysis carried out in the present study shows that it is specifically this arrangement of the dipole which is favoured, rather than any of the several possible edge to face interactions available for a regular tetrahedron. At first, this finding also appears to be in agreement with the early diffraction work of Bertagnoli *et al*.,[346] who stated that "the most satisfactory figuration is one in which the molecule dipole axes are inclined with respect to each other and the hydrogen atom is tilted toward the hollow between two chlorine atoms of the next molecule". However, upon closer inspection, the arrangements suggested in their work (*c.f.* Figure 8a produced by Bertagnoli *et al.*[346]) are different from those extracted from this EPSR model. These differences are likely due to an assumption about the minimum intermolecular C–C separation of 3.21 Å used in the earlier study to separate intra- and intermolecular contributions to the structure factor.[345] Based on our findings this distance is too large and thus the analysis of Bertagnoli *et al*. would have removed scattering data corresponding to the inclined dipole arrangement.

Upon going to greater distances, the position of the lobes changes, reflecting both different favourable arrangements and 'exclusion zones' which form as the most closely approaching arrangements block certain arrangements in subsequent shells. The 4.5–6.2 Å C–H SDF plot shows a change in the most favoured arrangement with increasing distance. The lobes above the reference (+z) in this plot indicate a change from a fairly parallel to a more antiparallel dipole alignment. The antiparallel dipole arrangement giving rise to closely approaching H atoms is shown as structure (b)

in Figure 6.1. Although the characteristically close H–H contacts of these antiparallel aligned arrangements are visible in the RDFs of this work and several of the earlier structural studies of chloroform liquid,[111,339,348-349] it is not immediately clear how this arrangement is stabilised. It may be favoured as the indirect consequence of another more favourable arrangement or to balance the electrostatics of the liquid isotropically.

A third type of specific arrangements is indicated by the changing position of lobes in the C–Cl SDFs with increasing distance. These arrangements may be characterised by the multiplicity of the Cl–Cl interaction involved: Cl_1–Cl_1, Cl_1–Cl_2, Cl_2–Cl_2, Cl_1–Cl_3 or Cl_2–Cl_3. Within the shortest C–Cl distance range (2.8–4.5 Å SDF) the lobes positioned in the recesses between the atoms of the reference molecule indicate Cl_1–Cl_3 and Cl_1–Cl_2 contacts. For the next greatest C–Cl distance range (4.5–5.2 Å SDF) the lobes are positioned in the recess between the two chlorine atoms of the reference indicating an increase in the number of Cl_1–Cl_2 and Cl_2–Cl_2 contacts. These arrangements would be expected to be favoured by the electrostatic interaction between the σ-hole of the approaching Cl and the most negatively charged region of the reference molecule on the underside of the chlorinated face (Figure 6.1).

Over the greater distance range of 5.2–6.2 Å, the position of the lobes changes further, now indicating Cl_1–Cl_1 interactions. The position of similar shaped lobes in the C–C SDF (5.2–6.2 Å), which also appears to cap the chlorine atoms of the reference molecule, indicates that in these arrangements the C–Cl bonds of adjacent molecules are aligned. This arrangement is shown as (c) in Figure 6.6. This arrangement would not be expected to be favoured through electrostatic interactions of the σ-hole as the interaction between the positive charges at the terminal ends of the approaching chlorine atoms would be unfavourable. It may be that this arrangement is stabilised by dispersion effects, which have been calculated to contribute almost equally to the overall interaction energy of the chloroform-formaldehyde dimer.[330] However, the position of these lobes may also form due to the ‘exclusion zones’ created by the favoured arrangements at shorter C–C

distances which are held in position more tightly than those towards the edge of the molecular shell which experience weaker intermolecular interactions.

6.2.7 Orientation Correlations of Liquid Chloroform

The arrangements in the first molecular shell have also been investigated using orientational correlation functions (OCFs). These indicate the variation in the most likely relative alignments (φ_2, θ_2) of the molecules with C–C distance *(r)* for specified θ_1 angles of the 2nd molecule about the reference (the data are averaged for variations in φ_1 and only φ_2 = 90 or 270° are considered). The axis definitions, spherical coordinates and Euler rotations are shown schematically in Figure 2.1. OCF plots at θ_1 positions of 0, 45, 90, 135 and 180° for the EPSR and HS models are shown in Figure 6.7. These indicate changes as one moves progressively from above the reference (north pole, θ_1 = 0°) around the side (equator, θ_1 = 90°) to a position below the reference (south pole, θ_1 = 180°). Also shown are 2D C–C SDFs plots, indicating the relative occurrence of 2nd molecules as a function of θ_1. Although it is necessary to average over φ_1 in these 2D SDF plots, plotting in 2D enables the FSL levels of the 3D SDF plots of Figure 6.5 to be replaced by contours, which more clearly show the variation in g with distance and θ_1. Whereas the position of lobes in the 3D plots are intrinsically normalised, the contours in the 2D plots display the values of g and thus enable the degree of correlation in the different models to be compared. As indicated in the Key, variations with distance and θ_1 in the SDF 2D plots of Figure 6.7 can be followed by measuring the distance of features from the origin and their angular offset from 12 o'clock, respectively. Due to the isotropic nature of the liquid, contours drawn with clockwise and anti-clockwise rotations are symmetric in the plots. A value of 1 has been chosen for the minimum scale, such that the coloured contours indicate arrangements with g >1 and thus identify the positional correlations. In the OCF plots, contours for g >1 are again used to show only the more favoured arrangements, and the distance between molecule centres may be measured from the origin. However, in the OCF plots, clockwise and anticlockwise rotations are no longer equivalent. Clockwise rotations from 12 o'clock show variations in the relative orientation, θ_2 (equivalent to the cosine similarity), for 2nd

molecules with φ_2 = 90° and anti-clockwise rotations show θ_2 for φ_2 = 270°. This distinction enables molecules with dipoles pointing generally ‘away from’ or ‘towards’ the reference, to be examined independently.

In general, the 2D SDF plots for the HS and EPSR models shown in Figure 6.7 indicate similar spatial correlations to the 3D SDF plots. However, the different intensity of features, only visible in the 2D plots, show that spatial position correlations are significantly more pronounced in the HS model than in EPSR model. The lower spatial homogeneity of the EPSR model reflects the disordering influence of specific intermolecular interactions on the most efficiently packed structure. Conversely, correlations between the alignments of molecules, shown by the colour intensity of contours in the OCFs, are more pronounced in the EPSR model than in the HS model. The dipole correlations for molecules at θ_1 = 0 and θ_1 = 180° corresponding to directly above (+z) and below (–z) the reference are particularly strong in the EPSR model. The position of the most intense contours over a θ_1 range between 0 and 40° in these 2 plots indicate a strong tendency for molecules to form arrangements with parallel dipole alignment. At first these data appear to contradict the 3D SDF plots of Figure 6.5, which indicated an inclined dipole arrangement to be most favoured. However, this can be explained by the fact that the 2D plots are averaged over φ rotations and the 3D plots are not. The difference is essentially due to the dipole inclined arrangement only being favoured over discrete φ ranges as a result of the favourable electrostatic interaction between the hydrogen atom and the negatively charged circumference of two chlorine atoms.

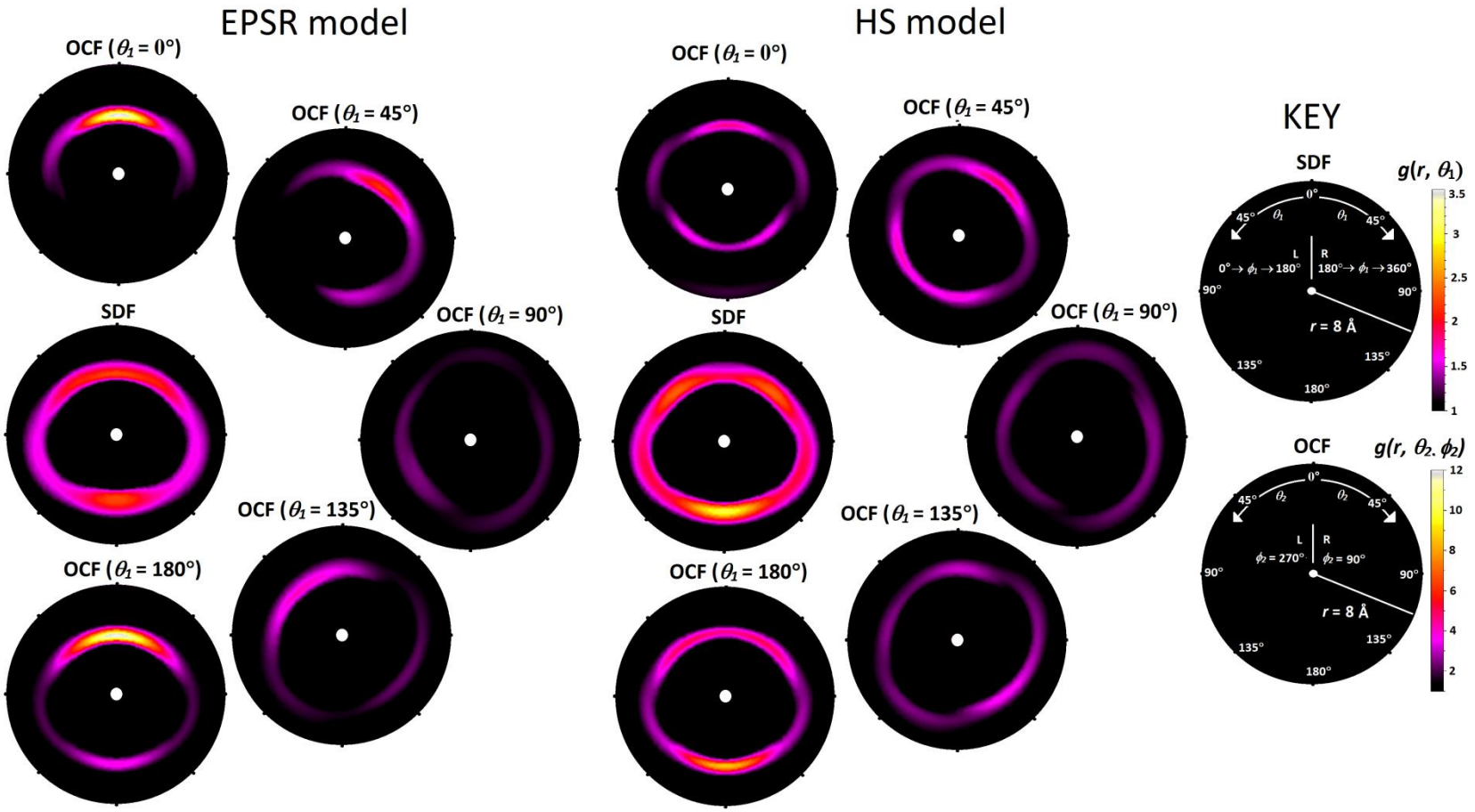

Figure 6.7 2D C–C SDFs and OCFs for the EPSR and HS models. OCFs are drawn at θ_1 = 0, 45, 90, 135 and 180°. Details on how to read the plots are provided in the Key. The origin representing the C atom at the centre of the reference molecule is indicated by a white spot. The C–C distances are indicated by the distance of features to the origin. The angles θ_1 (SDFs) and θ_2 (OCFs) correspond to rotations about the plots from 12 o'clock; clockwise for φ_1 = 0–180° (SDF) and φ_2 = 90° (OCF) and anticlockwise for φ_1 = 180–360° (SDF) and φ_2 = 270° (OCF).

Contours over a θ_2 range between 160 and 180° at a distance of ~7.0 Å in the OCF for a θ_1 angle of 180° also reveal an arrangement not discussed in the earlier 3D SDF section. This intensity corresponds to an arrangement with antiparallel dipole alignment in which the faces formed by three chlorine atoms on two molecules approach closely. This arrangement, shown as (d) in Figure 6.6, may not be expected to be particularly favoured through σ-hole interactions, even for a staggered arrangement, as the close contact between the negatively charged circumference of the chlorine atoms would be unfavourable. It is more likely that these antiparallel dipole aligned arrangements are favoured due to the energetic gain associated with balancing the longer range electrostatics isotropically.

At θ_1 angles of 45, 90, 135° (*i.e.* not in line with the *z*-axis of the reference), the less intense colour of features in the OCF plots indicate less pronounced orientation correlations. These plots also display differences between the left and right sides due to the different occurrence of relative orientations in which the molecules point toward or away from the reference. For the OCF plot drawn at θ_1 = 45° the most intense feature at ~ 4.5 Å, in a θ_2 range between 10 and 40° is on the right side (clockwise, φ_2 = 90°) indicating that the dipole moment of these molecules point upwards and generally away from the reference. This correlation may be due to the contribution of the inclined dipole arrangement at this θ_1 position (Figure 6.6a). In the OCF plot for θ_1 = 135° the position of the most intense contour indicates dipole orientations pointed upwards and towards the reference molecule. This arrangement would enable the favourable interaction between the H atom of the second molecule and the Cl atoms of the reference molecule. In the OCF plot for θ_1 = 90°, corresponding to molecules centres positioned around the 'equator' of the reference molecule, the broad, dim ovoid seen indicates that there are few orientation correlations for these molecules. However, the ovoid shape of the feature reveals a connection between distance and orientation correlations; molecules positioned around the 'equator' with 'perpendicular' dipole alignment (θ_2 = 45–135°) approach the reference more closely than those with parallel (θ_2 = 0–45°) or antiparallel (θ_2 = 135–180°) dipole alignments. This reflects the shape of the molecules which are more plate like than tetrahedral due to relative size of Cl and H atoms. This is also supported by the similar

shape of features in the corresponding $\theta_1 = 90°$ plot for the HS model, which is determined solely by the most efficient packing of the chloroform molecules.

A comparison of the OCF data extracted for the EPSR model of chloroform with the OCFs for other small polar molecules such as HF,[363] HCl, [364-365]HBr,[366] HI,[106] H_2O,[124] H_2S,[367] CHF_3[368] and CH_3F. [368] suggests that the dominance of orientation correlations in line with the z-axis may be a somewhat unique aspect of chloroforms structural character. HCl is the only other molecule showing strong orientation correlations along the axis of the dipole moment. [364-365] At a reduced temperature of 0.59 the maximum value of $g_{COM-COM}(r, \theta_2)$ was found to be ~13 in the first coordination shell and at θ_1=0° (Fig. 7 by Andreani *et al.*[365]). The corresponding value for $CHCl_3$ from the EPSR model presented here is 14.9 at a comparable reduced temperature of 0.56.[354] The significant orientational correlations in liquid chloroform is an even more remarkable finding considering its relatively small gas phase dipole moment. The most significant of chloroform's structural characteristic stabilising the correlation may be its molecular shape, which is dominated by the large chlorine atoms, and the direction of its dipole moment, which is in line with the shortest molecular axis (*z*). This combination allows a much closer approach in the *z*-axis favouring in line (at the poles) dipole-dipole correlations over those between molecules positioned in the *xy*-plane (around the equator). Furthermore the extensive spatial distribution of negative charge density formed in the vicinity of the chlorine atoms (Figure 6.1) provides a wide range of favourable $H^+ \rightarrow Cl^-$ interaction geometries, stabilising dipole aligned molecules against thermal agitations.

6.2.8 Self-Associations and Dipole Correlations in Liquid Chloroform

In this final section, the pronounced dipole alignments found in the OCFs of the EPSR model have been further characterised by examination of the C–C $h(110;00;r)$ function from the spherical harmonic expansion of the EPSR model and also independently by examining the proportion of dipole aligned molecules in the model forming as 'stacks' using the *chains* EPSR subroutine. The

spherical harmonic expansion is discussed in section 2.1.16. The $h(110;00;r)$ function is closely related to the Kirkwood correlation factor, g_K, used in the theory of dielectrics to account for the influence of orientation correlations on the dielectric constant of liquids.[369] The relation of this scalar correlation factor to the relative dipole alignment of the molecules is given as Equation 6.1.[370] N is the number of contributing molecular dipole moments and $\langle \cos\theta_2 \rangle$ is the average of the cosine similarity between dipole vectors, already discussed in the OCF analysis. For a liquid with a tendency for parallel dipole alignment $g_K > 1$, and for liquids with a tendency for antiparallel dipole alignment, $g_K = 0–1$.

$$g_k = 1 + N\langle \cos\theta_2 \rangle.$$

Equation 6.1

As well as being available from our model, this factor may also be estimated from the vapour phase dipole moment, μ_0, the dipole density, ρ, the static dielectric constant, ε, and dielectric constant at infinite frequency, ε_∞, using the Kirkwood-Fröhlich equation, given as Equation 6.2.[371] k is the Boltzmann constant.

$$\frac{(\varepsilon-\varepsilon_\infty)(2\varepsilon+\varepsilon_\infty)}{\varepsilon(\varepsilon_\infty+2)^2} = g_K \frac{4\pi\rho\mu_0^2}{9kT}.$$

Equation 6.2

Using values of $\rho = 0.00748$ A^{-3}, $\mu_0 = 1.04$ D, $\varepsilon = 4.80$,[262] and $\varepsilon_\infty = 2.17$,[372] gives $g_K = 1.26$. This value indicates a tendency for parallel dipole alignment in liquid chloroform and supports the validity of the EPSR structural model. However, the value of ε_∞, included to account for contributions to the dielectric from molecular polarisation is difficult to measure accurately due to the potential frequency overlap of contributions from molecular polarisations and vibrations.[372] This experimental difficulty makes it difficult to predict the uncertainty in the value of g_K obtained in this manner.

The Kirkwood correlation factor, g_K may also be calculated from the $h(110;00;r)$ spherical harmonic function which accrues dipole alignment information during the simulations accumulation period. The $h(110;00;r)$ function is related to the correlation function $g_K(r)$,

describing the variation in $N\langle\cos\theta_2\rangle$ with intermolecular distance, r, by the number of molecules in a spherical shell at the given radius, $\rho 4\pi r^2$, and a constant of the spherical harmonics, $C = (\sqrt{3})^{-1}$. The relationship is expressed by Equations 6.3 and 6.4. [124]

$$g_K(r) = 1 + N\langle\cos\theta_2\rangle(r).$$

Equation 6.3

$$N\langle\cos\theta_2\rangle(r) = \frac{C}{3}\,\rho 4\pi r^2\, h(110;00;r).$$

Equation 6.4

This correlation function, $g_K(r)$, may then be integrated over chosen limits of intermolecular separation to give g_K, the Kirkwood correlation factor. However, the estimation of g_K from a model structure using EPSR also has several limitations: (1), the spherical harmonic functions of the model may only be derived over finite distance range (0–20 Å) and (2), the molecules centre of mass (COM), about which the molecules rotate in the liquid, cannot currently be used by EPSR to define the intermolecular separation, r. For this analysis the average chlorine position (~0.07 Å from COM) has been used to define r. A modification to EPSR allowing intermolecular distances based on the COM is currently being pursued.

A function indicating the variation in the average cosine of dipole vectors with r, $\langle\cos\theta_2\rangle(r)$, may also be obtained from the spherical harmonic expansion of the model by dividing $h(110;00;r)$ by $h(000;00;r)$ as shown in Equation 6.5.[105] The $h(000;00;r)$ function corresponds to the Av.Cl–Av.Cl RDF and contains the pairwise information about N .

$$\langle\cos\theta_2\rangle(r) = \frac{C}{3}\,\frac{h(110;00;r)}{h(000;00;r)}.$$

Equation 6.5

The distance variation in the average cosine of dipole vectors $\langle\cos\theta_2\rangle(r)$ extracted from the EPSR model is shown in Figure 6.8(a). The Kirkwood correlation function, $g_K(r)$, is shown in Figure 6.8(b) along with the running integral of $g_K(r)$ showing the value of g_K over different distance ranges. The error bars show the standard deviation of the mean value obtained during the 125 different model structures produced during 625 iterations of the simulation (1 in 5). In the plot

of average cosine similarity, the error is greatest at r < 4 Å due to the small number of molecules counted at these close Av.Cl–Av.Cl distances. However the negative cosine similarity at these short distances indicates that these molecules have an antiparallel dipole alignment and thus correspond to arrangement (d) of Figure 6.6. The dipole aligned molecules then contribute to the positive average cosine similarity between 4 and 5 Å. The maximum in $\langle\cos\theta_1\rangle$ is at ~4.1 Å.

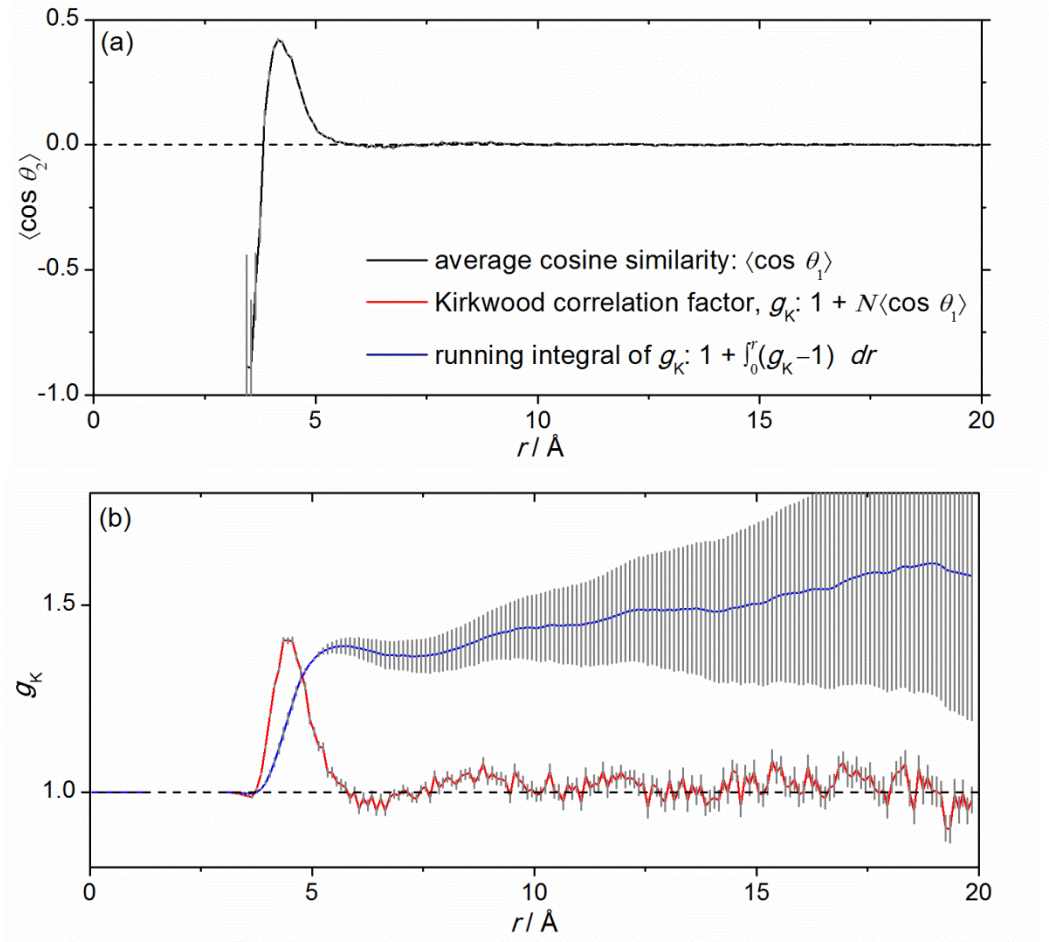

Figure 6.8 Functions describing the relative dipole alignment of molecules in the EPSR model. (a) the average cosine similarity $\langle\cos\theta_1\rangle$ (black), (b) the Kirkwood correlation factor, g_K, shown as a function of Av.Cl–Av.Cl distance (red) and as a running integral (blue).

The extent of the dipole alignment is shown more clearly by the Kirkwood correlation function, $g_K(r)$ given in Figure 6.8(b). This function, which indicates the variation in the number of dipole aligned molecules with separation, oscillates in a series of shallow peaks and troughs to distances up to ~12–13 Å, beyond which oscillations become insignificant. The maxima of the peaks are at ~4.4 and ~8.8 Å and the minima of the troughs are at ~3.5 and ~6.5. These oscillations

reflect the characteristic intermolecular separations of the most favoured arrangements and their persistence within the first two molecular shells. Whilst antiparallel arrangements, as shown in Figure 6.6(b) and (d), contribute to the negative features at short and long distances within each molecular shell, dipole aligned molecules (Figure 6.6a), contribute to the main feature with positive g_K with a characteristic distance in-between that of the two antiparallel arrangements.

The running integral of $g_K(r)$ also shown in Figure 6.8 (b), indicates the impact of the integration range on the magnitude of g_K. The error bars again indicate the standard deviation of the mean. Interestingly, the average value of the running integral continues to increase beyond a distance range corresponding to the first two coordination shells (12.5 Å). This indicates that dipole alignments at distances beyond the second shell occurred in the model during the accumulation. This result may be understood to indicate the occurrence of slightly ferroelectric regions, with *radii* up to 20 Å. Chloroform is known to form a ferroelectric crystalline phase at 0.6 GPa and low temperatures,[362] but this result is unexpected for the liquid phase on the basis of the g_K value (1.26) predicted from the measured dielectric constants of the liquid. However, it may be important to consider that as the maximum distance of the EPs in these simulations was 12 Å, correlations beyond these distances are only extracted from the scattering data as the sum of multiple local ordering events. The EPs are not able to account for the multibody interactions and polarisations which likely influence the formation of extended stacks in the real liquid. For a distance range between 0 and 12.5 Å including molecules in the first two coordination shells the model predicts a dipole correlation, g_K (0–20 Å) = 1.56 ± 0.35 and dielectric constant of the liquid, ε = 5.32 ± 0.78. The slightly greater g_K and ε values than found experimentally (1.26 and 4.80, respectively) may imply that dipole correlations have been overestimated in the model or the difference may be due to errors introduced from using the average chlorine position to define the intermolecular separation rather than the COM.

The degree of dipole alignment in the EPSR model has also been examined independently of the spherical harmonic approach using an EPSR auxiliary routine (*chains*) to calculate the proportion of molecules forming as linked ‘chains’ of dipole-aligned molecules. The C···H

distances between atoms and the enclosed H····C–H angle were used as constraints to define connected molecules in the chain distribution analysis. Figure 6.8(a) shows the variation in probability for a range of H····C–H angles and H···C distances within the first coordination shell used to determine values for the constraints. The sharp feature in this plot with maximum at 2.8 Å and C····C–H angles close to 180° again reveals the prevalence of dipole aligned arrangements in the EPSR model. The black lines drawn at the edge of the main peak indicate the molecules included in the chain analysis. These have *r*(H···C) = 2–4.2 Å and ∠H···C–H = 150–180°.

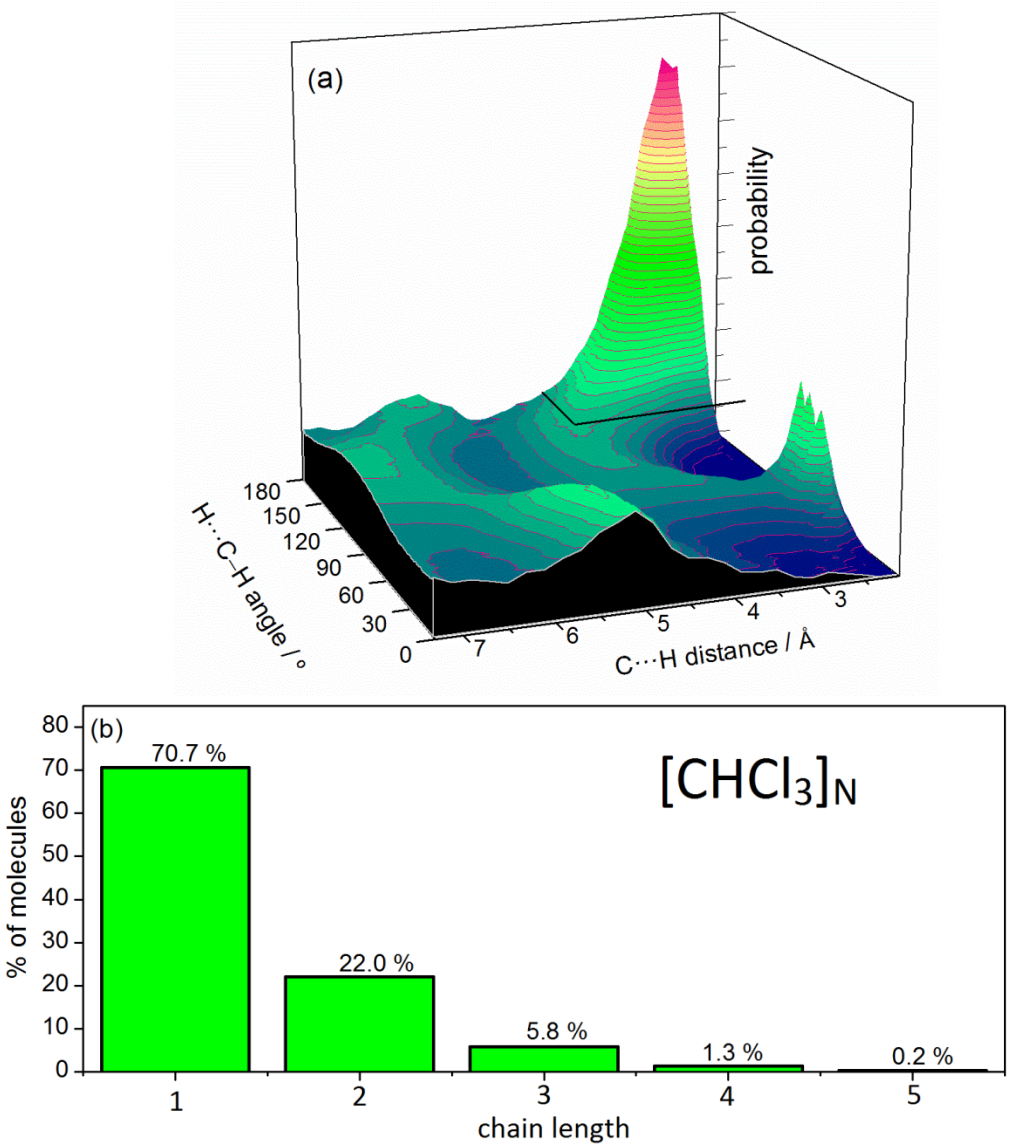

Figure 6.9 Chains analysis applied to the EPSR model of chloroform liquid. (a) the variation in probability of finding atoms within the accumulated model with H····C–H angle and C–H distances within the 1st molecular shell and (b), the chain length distribution, $[CHCl_3]_N$, for r(H····C) = 2–4.2 Å and ∠H····C–H = 150–180° constraints, also indicated by the black lines in (a).

The results of the chain distribution analysis are shown in Figure 6.9 (b). These indicate that ~ 29 % (Σ CC + CCC + CCCC + CCCCC) of the molecules in the EPSR model have a dipole-aligned neighbour in the first molecular shell and that ~7 %(Σ CCC + CCCC+CCCCC) also have a dipole-aligned neighbour in the second molecular shell. As the proportion of molecules in the chains was found to remain constant for further model accumulation, these values are a good representation of the average structure of the simulation box and thus reflect the accuracy of the EPs and the temperature of the simulation (298 K). It is, however, more difficult to comment with certainty that chains of molecules exist in chloroform liquid. Although the chains are consistent with the measured diffraction data, it is disquieting that this mid-range structure has been produced in the model as an extrapolation of EPs truncated at 12 Å. It is therefore interesting to examine the relative probability, and hence the cooperative nature, of the stacking events in the first and second coordination shells. From the chains distribution analysis the probability of a molecule being involved in chains with >2 and >3 molecules are 0.294 ± 0.002 and 0.0740 ± 0.002, respectively. For a chain formation process for which the connections are independent of the connections in other coordination shells the probability for chains containing >3 molecules would be expected to be $0.294^2 = 0.0867 \pm 0.0013$. The lower probability found in the model (0.073 ± 0.002) shows that the EPs captured a tendency for chloroform to form dimers rather than extended chains and suggests chain formation in $CHCl_3$ is anti-cooperative in nature events (*i e.* chain linking events are not entirely independent and are supressed by dimer formation). This in turn implies that multibody terms and polarisation effects may prohibit the formation of extended chains of molecules in the liquid and that the confidence in the chain length distribution analysis may be improved by extending the distance range of the EPs to include the third and fourth coordination shells.

6.3 Conclusions

A structural model of liquid chloroform has been prepared using EPSR. It shows a greater consistency with neutron total scattering data for $CHCl_3$, $CHCl_3$ and $C(H/D)Cl_3$ than can be achieved by parameterized Monte Carlo simulation. Several ‘inherent’ structural arrangements

contributing to the liquid's structure were identified. The most common of these is a structure in which the dipole axes of adjacent molecules are 'in line' and form as nanometer-sized chains of linked molecules. Our data suggests that liquid chloroform has the most pronounced orientation correlations along the direction of the dipole moment of all the small polar molecules investigated to date. The chains are favoured through interactions between the positively-charged hydrogen atom and the most negatively-charged region of a neighboring chloroform molecule, between the three chlorine atoms. Due to the 'plate like' shape of the molecules this arrangement gives the closest approach of two molecules thereby giving the greatest electrostatic interaction of all possible coordination geometries. Comparisons of the models produced using different potentials suggest that interactions involving the σ-holes of the chlorine atoms also contribute to the liquids structure. A total scattering/EPSR study is now planned to investigate the nature of this halogen-bonding interaction in several different halomethanes. The accepted SANDALS proposal is included as Appendix 31.

The influence of the liquid's structure on its properties has also been considered. Due to the parallel alignment of the dipole moments, the chains of chloroform molecules have net dipole moments greater than those of individual chloroform molecules. The calculations of net dipole are given in Appendix 21. These 'super-dipoles' may be a significant factor in explaining the outstanding properties of chloroform as a solvent whereby the chains polarize the electron clouds of nearby organic solutes providing a favourable enthalpic contribution to the dissolution processes. These 'super dipoles' may also be expected to interfere with the cell membranes and ion channels of nerve cells and could be linked to chloroform's potent anesthetic properties.[325-326,353] Of particular importance to the anesthetic mechanism may be the reversibility of chloroform's electrostatic interaction, whereby their aggregation into 'super dipoles' causes the interference but the low overall polarity of the isolated molecules allows them to migrate into the membrane to reach anesthetically effective concentrations.

7 Intermolecular Interactions in the Chloroform-Acetone Azeotrope

7.1 Introduction

Mixtures of chloroform and acetone form a minimum pressure azeotrope with liquid and vapour compositions containing an acetone mole fraction of 0.405 at room temperature and at ambient pressure.[97,102] This system is often used as the physical chemistry text book example of a negative pressure azeotrope.[373] The pressure-composition isotherm (PXY plot) for the room temperature binary mixture is given as Appendix 1. Also given in the Appendix 1 is the pressure-composition isotherm (PXY plot) for the binary mixtures of benzene and methanol which form a positive pressure azeotrope. In section 7.2.14 the structural differences between the two systems has been briefly considered. Intermolecular structure in the chloroform-acetone (CA) azeotrope has been studied by computer simulation techniques,[374-375] statistical analysis of thermodynamic excess functions,[97,376-377] NMR,[103,378-380] investigations of dielectric properties,[381-384] and by vibrational spectroscopy.[103,385-386] In these studies, there is a general agreement that the non-ideal mixing behaviour is connected to the formation of C–H donor hydrogen bonds between the oxygen atoms of acetone and the hydrogen atoms of chloroform, as first proposed Glasstone in 1937.[387] A complex since found to be stable in the solid state,[379,383] and supported to exist in the liquid mixtures by shifts in chloroform's proton NMR signal,[103,378-380] and C–H related absorptions in vibrational spectra.[103,385-386] DFT calculated (B3LYP 6-31G*) structures of acetone and chloroform molecules, and isodensity surfaces of colour mapped to show electrostatic potential are shown in Figure 7.1. The atom labels and axis definitions shown here are those used in the later results sections. Chloroform and acetone have gas phase dipole moments of 1.04 and 2.88 D, respectively with directions indicated by the blue arrows.[336] The magnitude of these values suggest that the molecular arrangements in the azeotrope will also be constrained by longer range electrostatic forces which are lowest in energy when balanced isotropically.

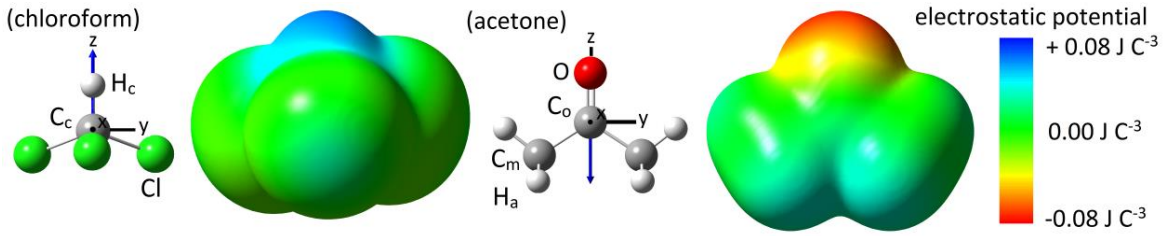

Figure 7.1 DFT predicted structure and the 0.004 bohr A^{-3} isodensity surfaces of acetone and chloroform molecules colour mapped to show electrostatic potential.

The structural analysis carried out by Apelblat *et al.*,[97] and based on a review of thermodynamic excess functions, explored the evidence for several different hydrogen bonded complexes. The complexes considered in their study are reproduced in Figure 7.2 as (a), (b) and (c). Complexes (a) and (b) have either one or two chloroform molecules bonded to the lone-pair electrons of the oxygen atom on acetone, termed AC and AC_2. In complex (c), termed ACC, a chloroform–chloroform self-association has also been included. This was originally suggested on the basis of thermodynamic evidence for the non-equivalence of hydrogen bonds found for AC and AC_2 complexes.[376-377] However, the more recent analysis by Apelblat *et al.*[97] found an equivalent $\Delta H°$ for OH bond formation (~10 kJ mol^{-1}) in the AC and AC_2 complexes and discounted arrangement (c) from their model describing the variation in composition (A + C + AC + AC_2) with temperature and acetone mole fraction.

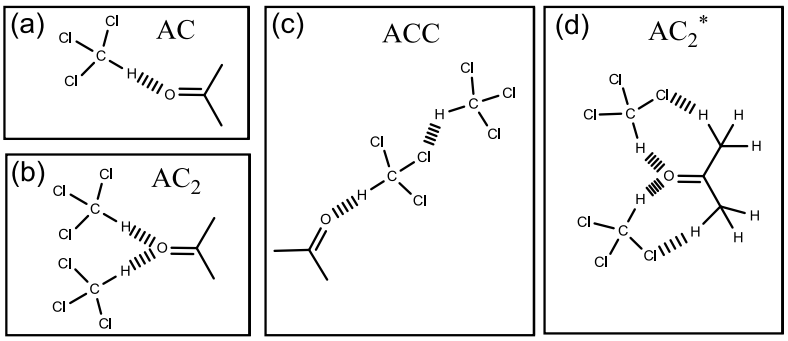

Figure 7.2 Acetone-chloroform complexes considered by Apelblat *et al.*[97] and Jalian *et al.*[103]

More recently, a Monte Carlo simulation has reproduced the azeotropic vapour pressure behaviour and characterised the interspecies association in their simulation box.[375] This study found a majority of AC complexes and a 'small number' of AC_2 complexes. They report a fairly large

average O–H bond length of 2.4 Å, indicating a weak hydrogen bonding interaction, and a $\angle C_oOH_c$ angle of 120°. The preference for 120° is interesting as the LJ parameters and partial charges of the model did not have any angular dependence. The preference for 120° has resulted from combinations of the spherical pairwise potentials. It is not straightforward to determine which of the parameters constrain these values in their simulation, as the LJ energies of the central carbon atoms were used as adjustable parameters to reproduce the azeotropic vapour pressure behaviour. In a more recent NMR and FT-IR study,[103] the dynamic nature of the AC_2 complex has also been considered. In this study the authors argue that bonding interactions between Cl atoms and the H atoms of acetone may constrain the rotation of the hydrogen bonded chloroform molecules in the complex. This arrangement is shown as (d) in Figure 7.2. However, such interpretation of spectral differences is difficult as interspecies interactions may only be revealed in this way if the AA and CC interactions are unchanged in the mixture and thus give rise to spectral contributions which are fully subtracted. This assumption is not likely to be true for these mixtures as the change in dielectric environment will impact strongly upon the molecular polarisations and thus the shape of the molecules, their bond strengths and vibrational spectra. In particular, it might be expected that chloroform's self-associations into dipole aligned chains may be different in the pure liquid than in the azeotrope.

The aim of the present structural investigation is to determine the composition, structure and concentration of the complexes in the azeotrope and to gain a better understanding of how interspecies associations are related to negative pressure azeotropy. The analysis given here is in two sections. In the first, Raman spectra for acetone, chloroform and the azeotrope are presented. In this section a H/D isotopic substitution procedure has been used to improve the separation of spectral features relative to earlier spectroscopic studies. In the second section, neutron diffraction data for seven azeotropic liquid mixtures with different H/D composition have been used to construct a 3D structural model consistent with the diffraction data using EPSR. The model is then analysed by comparison of RDFs, SDFs and OCFs. Functions describing acetone–acetone (AA)

and chloroform-chloroform (CC) correlations in the model are compared with those for the pure liquids. Data for pure acetone liquid has been taken from the EPSR study of McLain *et al.*[105] and the data for liquid chloroform are reproduced from Chapter 6 of the present thesis. The nature of the acetone-chloroform interactions in the azeotrope are then considered through a comparison of the model's chloroform-acetone RDFs and SDFs with those extracted from a model produced from the unperturbed LJ parameters and monopole partial charges, termed LJ+C, and a model representing the most efficient packing of the molecules, termed HS.

7.2 Results and Discussion

7.2.1 Raman Spectroscopy of the CA Azeotrope

The Raman spectra of acetone, chloroform and the azeotrope are shown in Figure 7.3. To enable comparisons between the spectra of the liquids and azeotrope, the intensity of features in the pure liquid spectra have been normalised to give equal integrated intensity of features at 260 cm^{-1} (chloroform) and 2926 cm^{-1} (acetone). The difference between the sum of these normalised spectra and the spectrum of the azeotrope then reveals the spectral changes associated with the non-ideality of the azeotropic liquid mixture. Table 7.1 gives the position of peaks in the three spectra. Spectral assignments for chloroform and acetone from Shurvell,[388] and by Williams *et al.*[389] respectively, are described below.

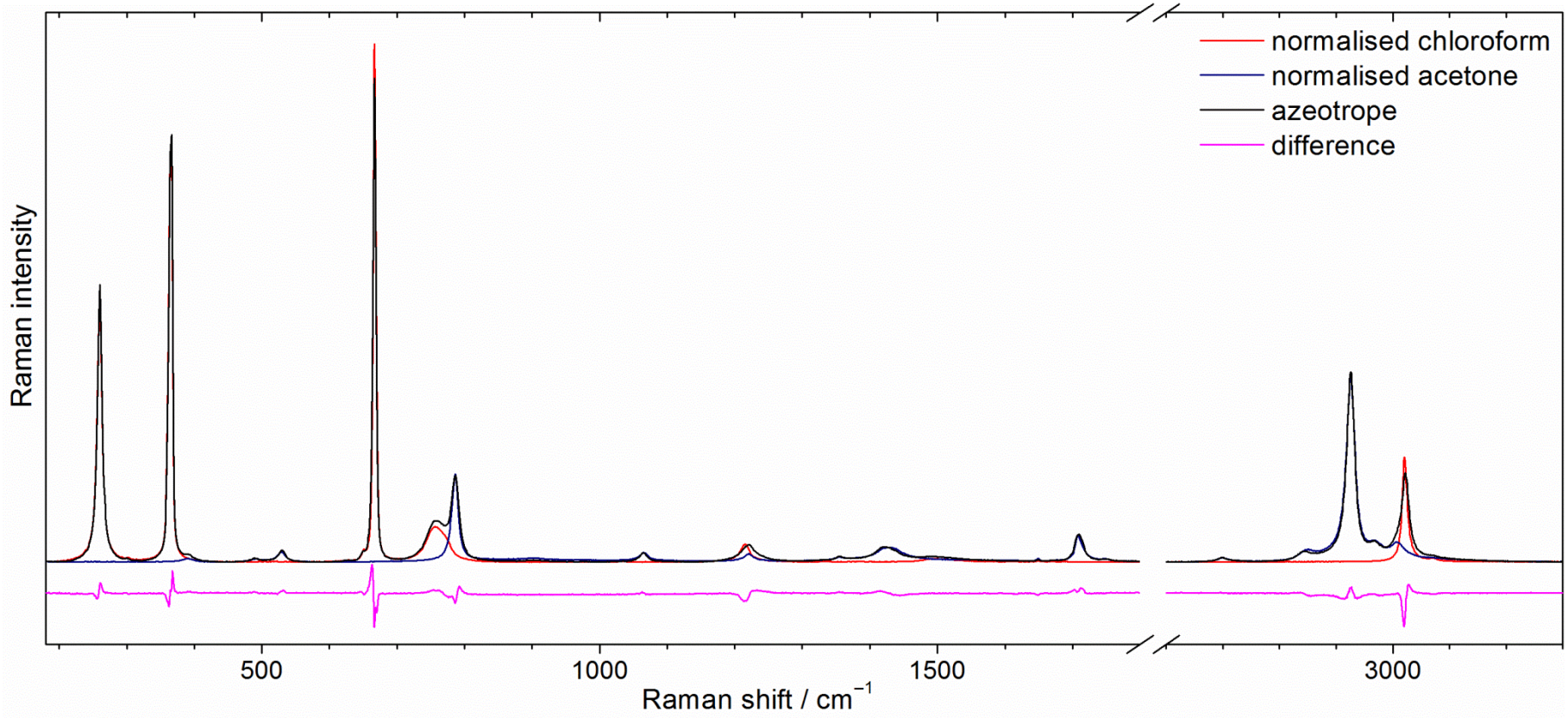

Figure 7.3 Raman spectra of acetone (blue), chloroform (red) and the chloroform-acetone azeotrope (black). The intensity of the acetone and chloroform spectra have been normalised, respectively, to the integrated intensity of peaks at 2926 and 260 cm^{-1} in the azeotrope spectrum. The impact of introducing the molecules into the liquid mixture is indicated by the difference spectrum (pink), obtained by subtracting the spectrum of the azeotrope from a spectrum formed by the direct weighted sum of the normalised spectra of the pure chloroform and acetone liquids.

Table 7.1 Raman shift in cm^{-1} of peak maxima in the spectra of chloroform, acetone and the azeotrope.

acetone	chloroform	azeotrope	Δ
	260.0	260.0	0
	365.9	365.9	0
390.4		mixed	-
491.5		489.2	-2.3
529.4		530.2	+0.8
	667.0	667.0	0
	757.0	mixed	-
786.3		mixed	-
1066.0		1065.2	–0.8
	1216.11	mixed	-
1220.9		mixed	-
1355.3		1354.5	-0.7
1429.5		1421.6	-7.9
	1499.0	mixed	-
1707.7		1709.3	+1.6
2700.3		2700.3	0
2850.5		2844.8	-6.7
2925.9		2925.9	0
2968.2		2968.2	0
3008.5		Mixed	-
	3020.7	Mixed	-
	3070.9	Mixed	-

The most intense feature in the Raman spectrum of liquid acetone is related to the in-phase symmetric stretching vibration of the methyl groups and occurs at a Raman shift of 2926 cm^{-1}. There are also less intense features in the vicinity of this primary mode due to coupled antisymmetric stretching modes. The weak feature at 1707 cm^{-1} is due to the stretching of C_o=O bonds. Features between 1300 and 1500 cm^{-1} are due to the deformations of methyl groups and those at 390, 531, 786, 1066 and 1221 cm^{-1} are due to more mixed molecular deformations. Liquid chloroform has several intense features in the Raman spectrum which are related to the vibrations of the C_c–H_c and C_c–Cl bonds; those at higher and lower wavenumber primarily involving C_c–H_c and C_c–Cl bonds, respectively. The features with large contributions from C_c–Cl vibrations show some asymmetry due to the different Raman shifts for molecules containing different combinations of $^{35/37}$Cl isotopes.

The difference spectrum of Figure 7.3 indicates small wavenumber down shifts in the position of vibrational modes involving C_c–Cl at 260, 366 and 667 cm^{-1} in the azeotrope. Conversely, the feature at ~3020 cm^{-1} indicates a slight upshift in the position of the C_c–H_c

stretching mode. There are also some changes in the shape of acetone-related features and change in the relative intensity of the C_m–H_a stretching modes. The feature at 1429 cm^{-1}, related to the antisymmetric deformation of methyl groups, shifts to a lower wavenumber position. There also appears to be a change in the shape of the feature at 1707 cm^{-1}, associated with C_o=O stretching which is consistent with $C_2H_6O\cdots HCCl_3$ hydrogen bonding.[385] Although, these spectral differences are clearly significant and indicative of the different environment of the molecules in the azeotrope relative to the pure liquid, it is difficult to interpret the changes with confidence due to the overlap of chloroform and acetone related features and the unknown influence of intermolecular coupling.

To overcome this problem, a novel approach of H/D isotopic substitution has been adopted. The different reduced masses of C–H and C–D, and associated decrease in the frequency of fundamental vibrational modes upon deuteration has been used to move one component of the overlapping C–H stretch feature to a lower wavenumber. In addition, the influence of intermolecular coupling has been removed by partially substituting the remaining protiated component with a 0.95 mole fraction of its deuterated counterpart giving a mixture with mole fractions: CD_3COCD_3 = 0.405, $CDCl_3$ = 0.565 and $CHCl_3$ = 0.030, and a mixture with mole fractions: CD_3COCD_3 = 0.385, CH_3COCH_3 = 0.020 and $CDCl_3$ = 0.595. Figure 7.4 shows the comparison of these azeotrope spectra with spectra for the partially deuterated pure liquids, normalised to give equal integrated intensity over the C–H stretching region. Figure 7.4(a) shows the separated C_m–H_a stretching mode of acetone and Figure 7.4(b) shows the C_c-H_c stretching mode of chloroform. The corresponding difference spectra then indicate the impact of introducing the liquids into the mixture.

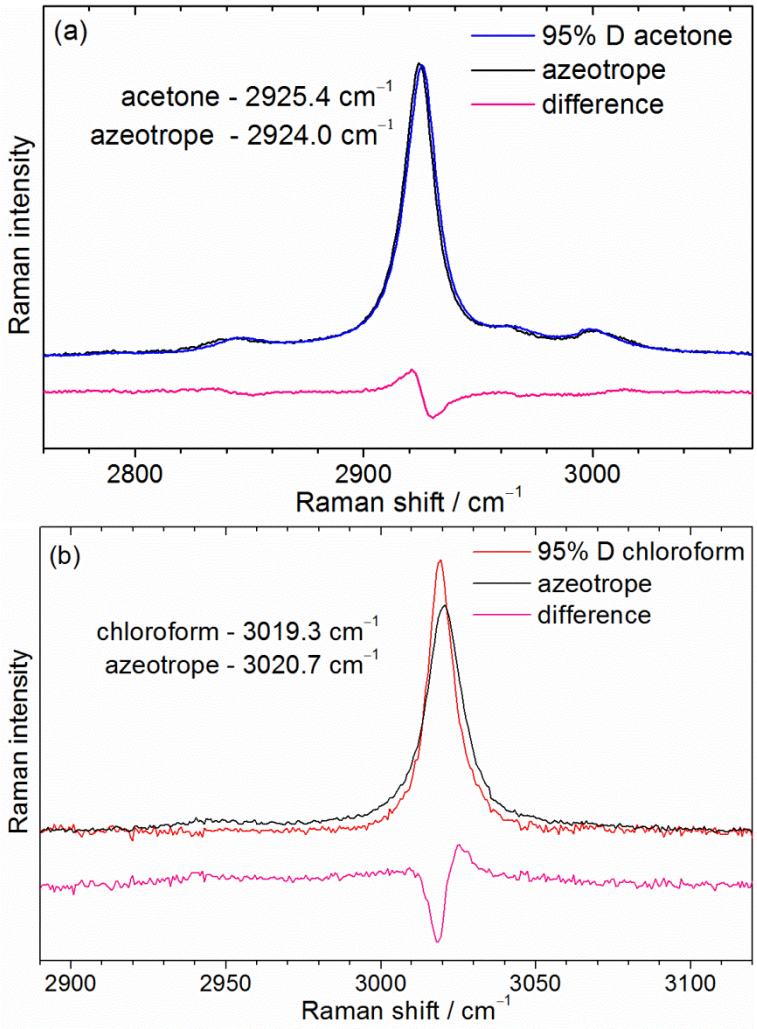

Figure 7.4 Raman spectra in the C–H stretching spectral regions for mixtures of protiated and deuterated chloroform and acetone liquids. (a), a comparison of CD_3COCD_3 = 0.385, CH_3COCH_3 = 0.020 and $CDCl_3$ = 0.595 (azeotrope, black line) with CD_3COCD_3 = 0.950 and CH_3COCH_3 = 0.050 (95 % D acetone). (b) a comparison of CD_3COCD_3 = 0.405, $CDCl_3$ = 0.565 and $CHCl_3$ = 0.030 (azeotrope, black line) with $CDCl_3$ = 0.950 and $CHCl_3$ = 0.050 (95 % D chloroform, red line). Spectral differences are shown (pink) offset vertically for clarity.

The spectra of Figure 7.4 indicate a ~1.4 cm^{-1} downshift in the C_m–H_a symmetric stretching vibration of the methyl groups and a ~1 cm^{-1} upshift of the C_c–H_c stretching mode of chloroform. The full width at half maximum (FWHM) of this peak (C_c–H_c) also increase from 10.2 to 13.7 cm^{-1}. Whilst the decrease in wavenumber of the C_m–H_a vibration is in agreement with the FT-IR results of Jalilan *et al.*,[103] they report a 1 cm^{-1} downshift in the C_c–H_c stretch of chloroform rather than the 1 cm^{-1} upshift and broadening found here. However, their values correspond to the peak maxima of overlapping features in FT-IR spectra and are thus not directly comparable. The shifts found in the present study are expected to be more accurate because of the reduced influence of intermolecular

coupling afforded by the H/D substitution. Substitution also gives a much greater degree of confidence in the width of the features and reveals pronounced peak-broadening of the C_c–H_c vibration. The increased width implies a wider distribution of environments for chloroform in the azeotrope than in the pure liquid. This may include molecules bonded to acetone *via* O···H_c hydrogen bonds with weaker C_c–H_c bonds and molecules with fewer associations than found in the pure liquid, with correspondingly stronger bonds. This suggests that the extent of chloroform's self-associations into dipole-aligned chains, found in the EPSR model of pure chloroform liquid, may be reduced in the azeotrope. It may be possible to find the wavenumber position of hydrogen bonded and free C_c–H_c oscillators from the Raman spectra of chloroform mixed with an excess of a hydrogen bonding or non-hydrogen bonding solvent.

7.2.2 Neutron Scattering of the CA Azeotrope

Seven liquid mixtures with different H/D substitutions were used to investigate the structure of the azeotrope by neutron diffraction. The substitution of hydrogen positions on acetone and on chloroform provides a good confidence in the H–H pair distance distributions. As many aspects of the molecular arrangements are thought to be constrained by the distribution of H–H atom pairs, these measurements have enabled detailed information about the intermolecular arrangements and molecular associations in the azeotrope to be extracted from a 3D EPSR model. The isotopic composition and weighting factors for each of the atom pairs in the liquid mixtures are given in Appendix 11.The measured scattering data over the entire *Q*-range (0.1 – 50 $Å^{-1}$) are given in Appendix 15 (corrected for attenuation and multiple scattering) and 16 (also corrected inelasticity).

The scattering data are presented over a reduced *Q*-range in Figure 7.5. In (a) the DCS has been corrected for attenuation and multiple scattering, in (b) the inelastic perturbations to the data have also been subtracted and (c) shows the FT of the corrected data after normalisation by $\langle b \rangle^2$. These data show an increase in average DCS with hydrogen content due to the greater neutron scattering cross sections of H relative to D, and indicate the inelastic perturbations to the scattering data which are most pronounced at low-*Q* in the most protiated mixtures. The low-*Q* intensity, which may be used to identify de-mixing in liquid mixtures under certain conditions of scattering

length contrast, is relatively low for all measurements. However, the data show a systematic change in slope at low *Q* with the level of acetone H/D substitution. The slope is close to zero for CD_3COCD_3 containing mixtures, positive for CH_3COCH_3, and negative for 1:1 mixtures of CD_3COCD_3 with CH_3COCH_3. The FT (c) shows the distribution of bond lengths present in chloroform and acetone weighted by the normalised scattering lengths (Appendix 11) and broadened slightly by Lorch smoothing.

7.2.3 Building Structural Models of the CA Azeotrope

Several structural models of the azeotrope have been prepared by Monte Carlo simulations. The differences between these three models, termed HS, LJ+C and EPSR, are the same as for chloroform, and were described Chapter 6. In these models of the azeotrope, the $CHCl_3$ parameters of Barlette *et al*,[111] successfully applied to pure chloroform liquid in the earlier chapter, were used again here. The parameters for acetone were taken from the EPSR study of pure acetone liquid carried out by McLain *et al.*[105] The partial charges in their study originated from semi-empirical quantum mechanical calculations of Wellington *et al.*[390] and give rise to a dipole moment (2.7 D) slightly lower than measured in the gas phase (2.88 D). The LJ parameters for C_o and O atoms were optimized by Jorgenson *et al.*[391] to heats of vaporisation and the parameters for the methyl groups were optimised by Ferrario *et al.*[392]. The origin of the bond distances and angles used for acetone are not described in the McLain study, but they report a good fit to neutron scattering data up to *Q* = 50 Å indicating that the shape of the molecules in the pure liquid are described well in their model. However, there is a mismatch in the angles describing the methyl groups which are not related exactly by natural cosines ($\angle C_oC_mH_a = 113°$, $\angle H_aC_mH_a = 110°$) suggesting that one of these parameters may have been adjusted in order to fit the neutron scattering data at high-*Q*. In the present study the *ecore* value was changed from the 3 (EPSR suggested value) to 1 in order to give a satisfactory fit to the measured data of the azeotrope at high-*Q*. The LJ potentials and partial charges of Kamath *et al*.[375] parameterised to reproduce the azeotrope vapour pressure were also tested, but found to give a worse fit to the measured diffraction data.

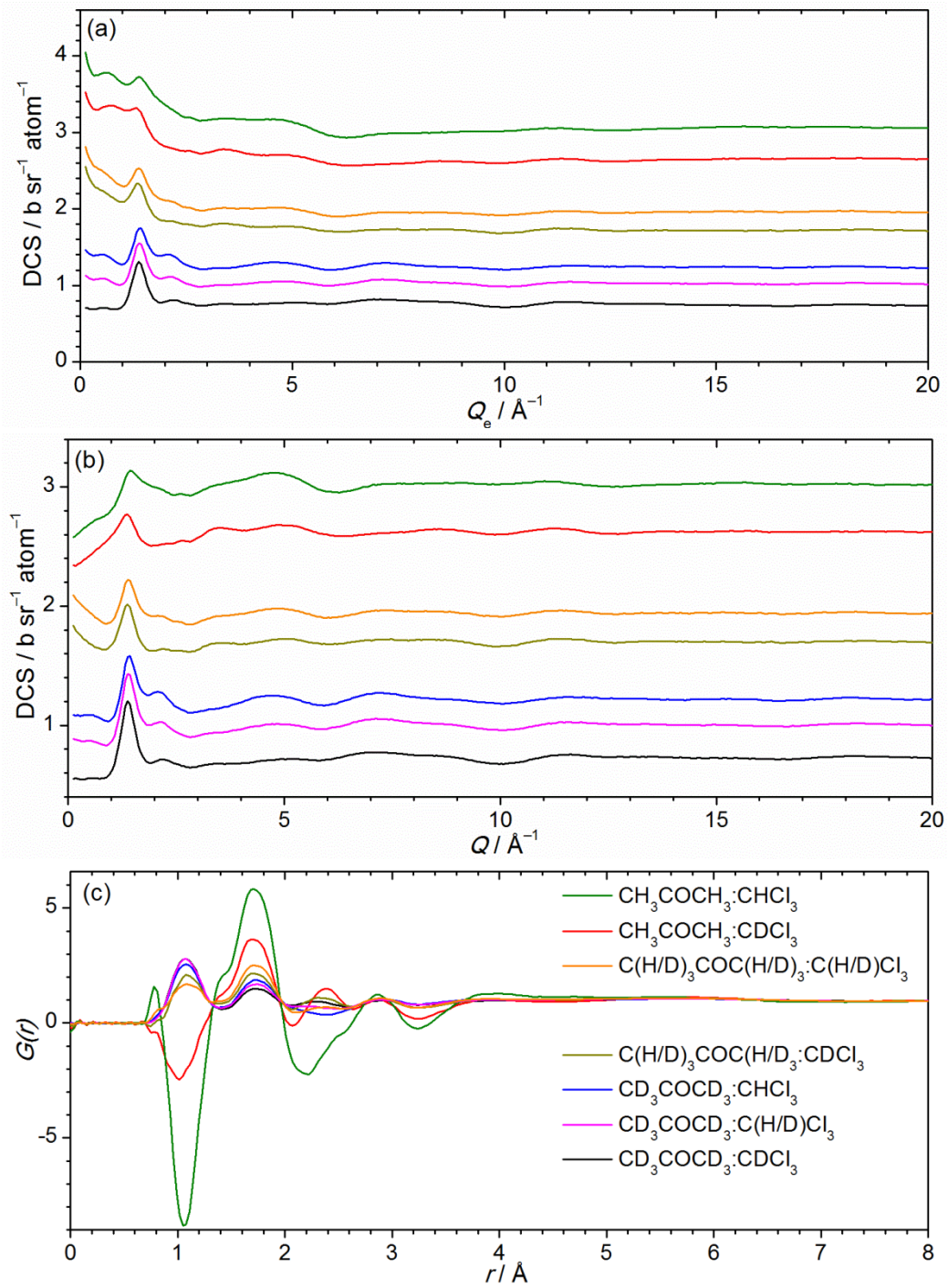

Figure 7.5 The measured scattering data for the azeotropic liquid mixtures of chloroform and acetone. (a) DCS corrected for attenuation and multiple scattering, (b) also corrected for inelasticity and (c) the smoothed FT of the corrected scattering data normalised by $\langle b \rangle^2$.

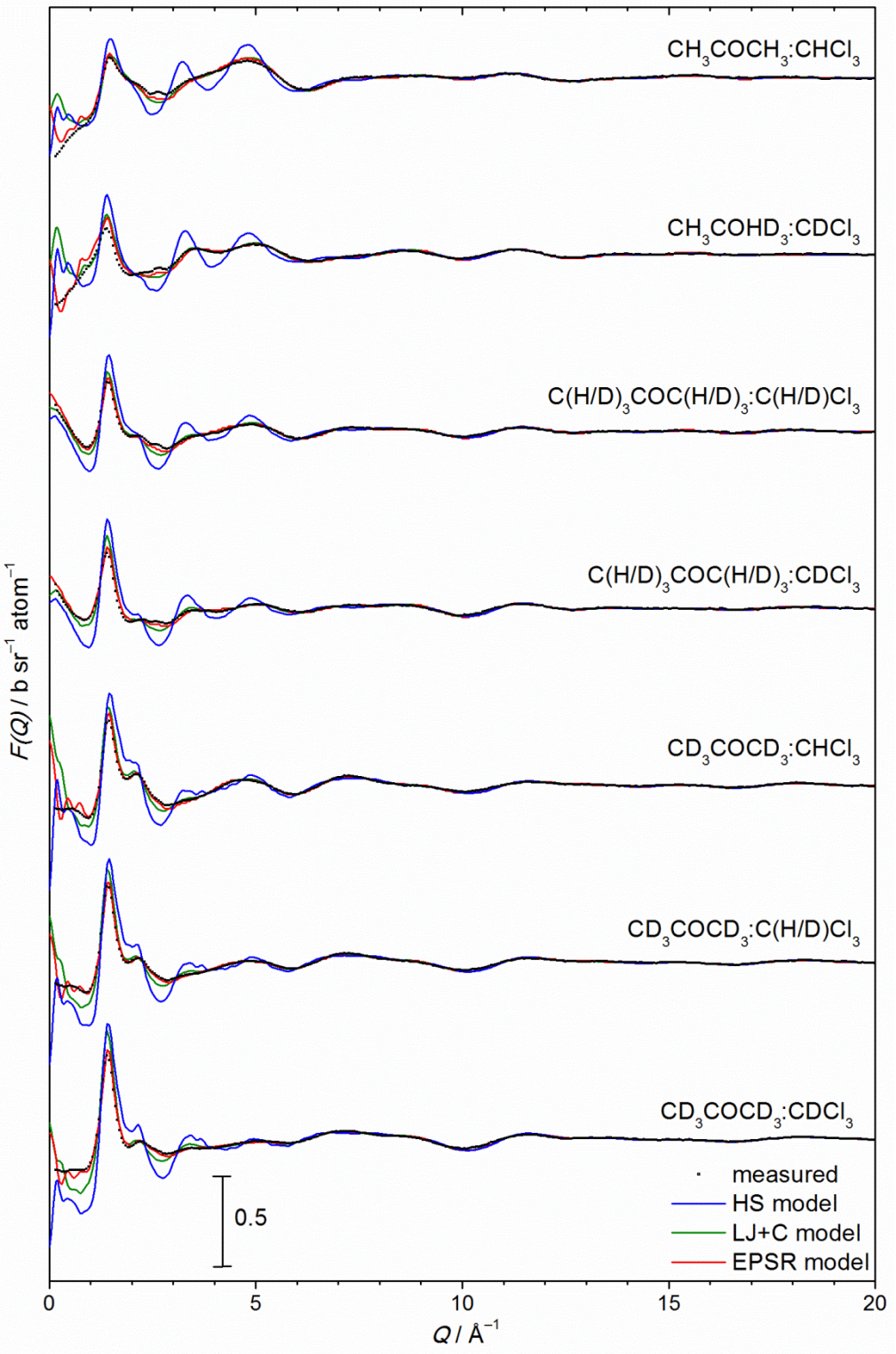

Figure 7.6 Measured *F(Q)* for the azeotrope liquid mixtures (points), and simulated *F(Q)* for the HS (blue line), LJ+C (green line) and EPSR (red line) models.

The simulated diffraction patterns for the HS, LJ+C and EPSR models are compared with the measured DCSs in Figure 7.6. The HS model gave a poor fit to the measured scattering data, the LJ+C model gave a far better fit and the EPSR model the best fit. As for liquid chloroform, the

final EPSR model of the azeotrope did not reproduce the measured diffraction data exactly, with the greatest residuals in the *Q*-range between 2.5 and 3 Å. However, the model does reproduce both large and small features in the scattering data better than the LJ+C model indicating that the EPs improved the accuracy of the model over the best estimate achievable using the LJ+C potentials alone. The imperfect fit of the EPSR model may be associated with the lack of orientation dependence of the potentials or be related to the limited degree of scattering length contrast achievable by H/D isotope substitution in this system.

7.2.4 Intramolecular Structure of the CA Azeotrope

The intramolecular structure of the molecules in EPSR model has been examined. The separation of intra- and intermolecular RDFs and structure factors are shown in Appendix 20. The average and standard deviations of the bond lengths and intramolecular angles of molecules in the model are given in Table 7.2. To determine their plausibility the average values have been compared with the structures of molecules in the crystalline compounds in the Cambridge Structural Database. The average values for chloroform molecules in the model are similar to the most preferred values found for molecules in the database. The average C_o–O bond length is also in agreement with the results of the database search. However, the $\angle C_mC_oC_m$ angle (115.9°) and C_o–C_m bond lengths (1.514 Å) deviate significantly from the modal values for compounds in the database, 118° and 1.48 Å, respectively. The average $\angle C_mC_oC_m$ (115.9°) and $\angle OC_oC_m$ (118.1°) angles of the acetone molecules indicate deviation from a planar geometry. If the molecules are assumed to have an average geometry which is planar, the average $\angle C_mC_oC_m$ angle may be written as (360–115.9)/2 = 122.05° and the average deviation from planar 122.05–118.1 = ~3.95°. The shape of the molecules in the model and differences to those in the database reflect the choice of input parameters and the inherent difficulty in reproducing SP2 hybridised molecular structures using only the one set of harmonic potentials available in EPSR. However, small errors in the intramolecular structure at high-*Q* are thought to impact weakly on intermolecular structure in EPSR simulations.

Table 7.2 Average bond lengths and angles of acetone and chloroform molecules in EPSR model structures. The numbers in parenthesise give the standard deviations of all the distances in the accumulated model structures.

bond length / Å		angles / °	
C_c–H_c	1.090 (0.072)	∠ClC_cCl	111.27 (5.31)
C_c–Cl	1.762 (0.062)	∠ClC_cH_c	107.66 (8.34)
C_o–O	1.218 (0.056)	∠$C_mC_oC_m$	115.93 (7.03)
C_o–C_m	1.514 (0.056)	∠OC_oC_m	118.13 (7.44)
C_m–H_a	1.095 (0.072)	∠$C_oC_mH_a$	111.09 (9.64)
		∠$H_aC_mH_a$	108.04 (11.10)

7.2.5 Acetone-Acetone RDFs of the CA Azeotrope

In the following three sections, the arrangements formed between acetone molecules in the EPSR model of the azeotrope are compared with those for the EPSR model of the pure liquid reported by McLain *et al.*.[105] In McLain's model the relative orientations of closely approaching molecules were found to be strongly correlated. This is thought to be a consequence of the electrostatic interactions between permanent dipoles, which are much larger for acetone (2.88 D) than for chloroform (1.04 D). It was also proposed that there may be weak hydrogen bonding between oxygen and the methyl hydrogen atoms. In Figure 7.7, McLain's intermolecular acetone-acetone RDFs (available to 9 Å) are compared with those extracted from the EPSR model of the azeotrope. The position of the first minima in the C_o–C_o RDF indicates that the first coordination shell extends to ~ 7.0 Å in acetone and the azeotrope. Although the two RDFs are fairly similar, the intensity of each feature in the azeotrope RDFs are lower than for the RDFs of the pure liquid.

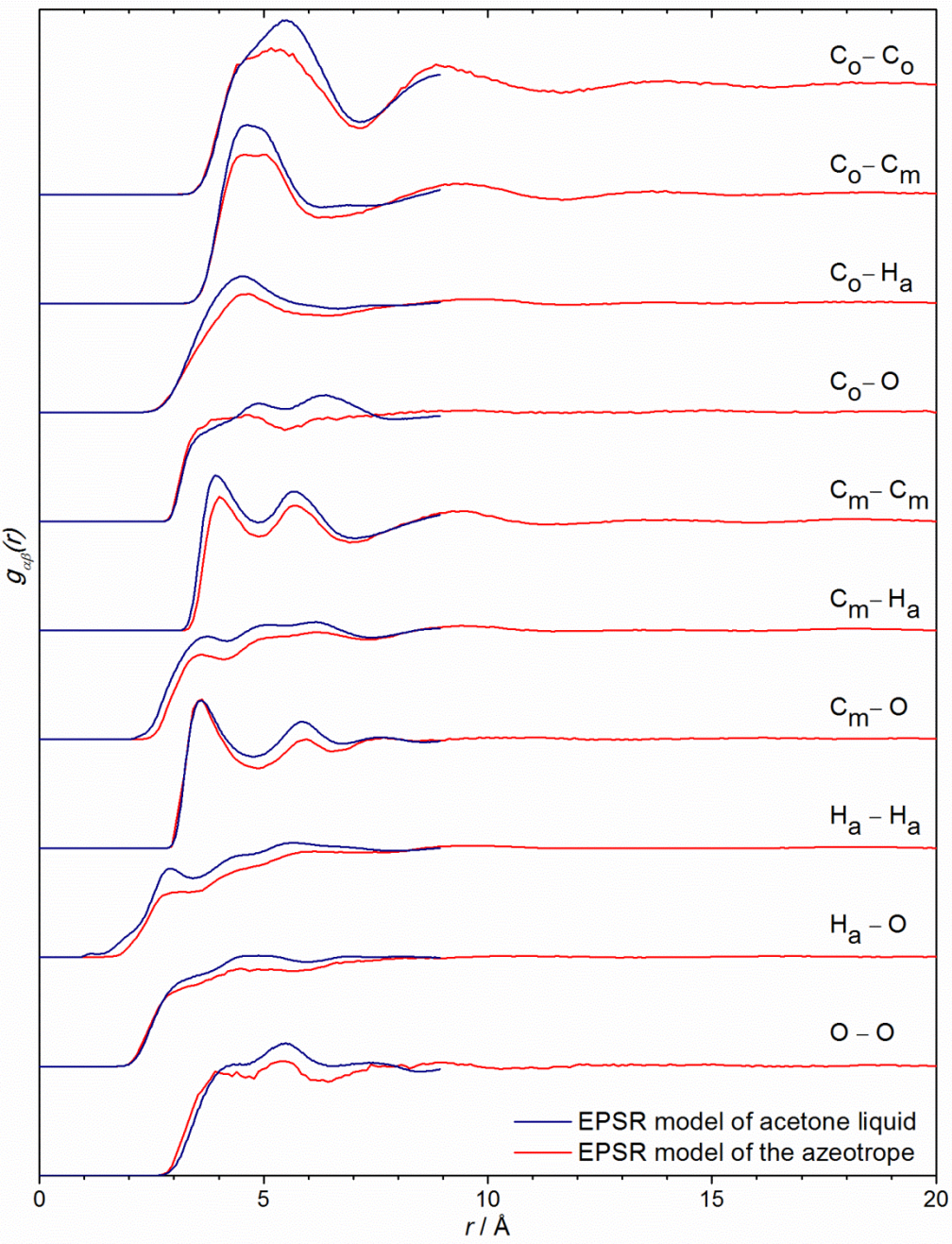

Figure 7.7 Intermolecular acetone-acetone RDFs extracted from the EPSR model of the azeotrope (red) and from the EPSR model of liquid acetone, reported by McLain *et al.* (blue).[105]

As $g(r)$ functions are inherently normalised by the liquid's composition and density, the low-r profile of the RDFs for the azeotrope indicate both the nature of the acetone-acetone intermolecular arrangements and the degree of chloroform-acetone interspecies mixing. Through comparison with the pure liquid data, the relationship between the intensity of features in the RDFs and the relative strength of AA, CC and AC interactions may be understood on a molecular level.

For mixtures characterised by a negative excess enthalpy, such as chloroform-acetone, the greater strength of AC interactions (relative to AA and CC) and the formation of AC complexes reduces the number of AA and CC associations contributing to the first shell RDF data. This is shown to be the case for AA in the present section and also for CC in section 7.2.8. The opposite case is expected for mixtures with positive excess enthalpy of mixing, such as benzene-methanol. In these systems the greater strength of BB and MM interactions over BM interactions would cause a partial demixing, whereby the intensity of BB and MM first shell RDF data would be greater in the mixture than in the pure liquids. The comparison of neutron scattering data for AC and BM systems is explored further in Section 7.2.14. Due to this influence of interspecies associations on the isospecies associations it is difficult to give more detailed structural interpretations of the acetone-acetone RDFs. In the following section the acetone-acetone associations are characterised through examinations of SDFs and OCFs.

7.2.6 Acetone-Acetone SDFs of the CA Azeotrope

In Figure 7.8, 3D acetone-acetone (C_o-C_o) SDFs extracted from the EPSR model of the azeotrope are compared with those reported for the pure liquid.[105] The distance ranges and FSL levels were chosen to reproduce the figures in McLain's study. The lobes in the upper panels, $r(C_o–C_o)$ = 0–5 Å, indicate the spatial positions of the most closely approaching acetone molecules. Lobes in the lower panels, $r(C_o–C_o)$ = 5–7 Å, indicate the most likely positions for molecules at the edge of the first coordination shell. The lobes are drawn for FSL levels of 0.7 and 0.15, respectively to offset the greater spatial inhomogeneity at larger $C_o–C_o$ distances. From the shape of the corresponding feature in the $C_o–C_o$ RDFs, which have a pronounced low-*r* shoulder, it may be anticipated that these distance ranges would capture two different molecular arrangements. This is supported by the different position of lobes in the SDF plots for the two distance ranges.

The position of the lobes is very similar for the azeotrope (left column) and the pure liquid (right column). In the plots for closely approaching molecules (1st row), the lobes are positioned in a cap surrounding the oxygen atom above (+*z*) the reference molecule and around its sides (+*x*; –*x*). For molecules further toward the edge of the first molecular shell (2nd row), the lobes common to plots of acetone and azeotrope, are positioned underneath (-*z*) and around the sides (+*y*; –*y*) of the reference molecule. Based on these observations, it would appear that chloroform has little impact on the packing and associations of acetone in the azeotrope. However, in the SDF plot of the azeotrope there are two lobes in the *zy*-plane at θ_1 = ~45° which may indicate that a different acetone-acetone packing is required to accommodate AC complexes involving O–H_c hydrogen bonds.

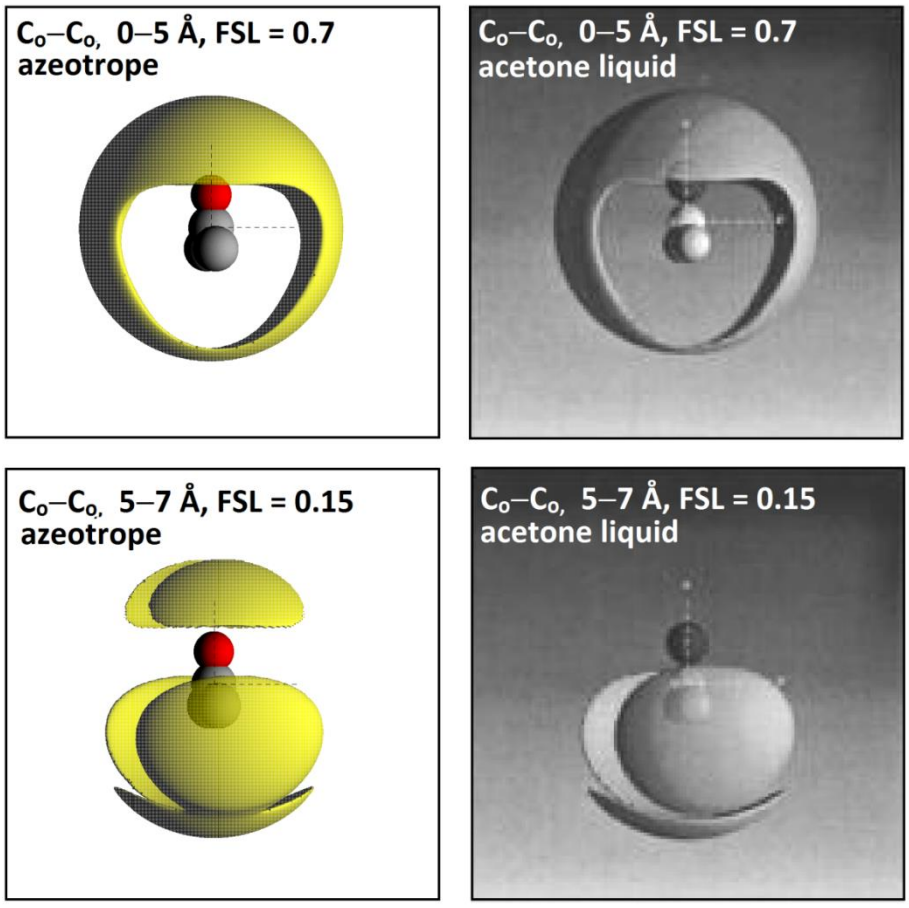

Figure 7.8 Acetone–Acetone (C_o–C_o) SDFs for the EPSR model of the azeotrope and the EPSR model of the pure liquid, reported by McLain *et al*.[105] The distance ranges and FSL levels plotted are those chosen in the study of the pure liquid.

7.2.7 Acetone-Acetone OCFs of the CA Azeotrope

The orientation correlations of acetone molecules in the EPSR model of the azeotrope has also been investigated in a series of 2D C_o–C_o SDF and OCF plots. These are shown in Figure 7.9 over two pages. Due to the two fold rotational axis of acetone, correlations in the *zx*- and *zy*-planes of the reference molecule have been examined independently. This has been accomplished by fixing the value of φ_1 to 0° (*zx*) or 90° (*zy*). These plots, shown in Figure 7.9(a) and (b), respectively, extend the analysis of McLain's study in which orientation correlations were only reported for the *zx*-plane.[105] The SDFs are shown on the left sides of each figure and the OCFs are shown on the right. OCFs are drawn for θ_1 = 0, 45, 90, 135, 180°. The columns correspond to different χ_2 Euler rotations of the second molecule which governs the rotational offset between the z'' axis of the reference and second molecules. Its consideration allows more detail about the arrangements between acetone molecules in the first coordination shell to be revealed. The central column indicates OCFs obtained by averaging over all χ_2 rotations; OCFs in the left hand columns are for χ_2 = 0°; and OCFs in the right hand column are for χ_2 = 90°.

There are pronounced differences between the SDF plots of the *zx* and *zy*-planes, which indicate the different approach distances of molecules possible in the two planes. Molecules approach the origin more closely in the *zx*- than *zy*-plane and reproduce the general shape of the acetone molecules. This indicates the importance of geometric packing on the first coordination shell. There are also pronounced differences in the OCF plots for 'off-centre' θ_1 = 45, 90 and 135° angles (OCFs plots for θ_1 = 0 and 180° refer to the same polar coordinates in both the *zx*- and *zy*-planes and the plots are identical). The greater intensity of features in the OCF plots of the *zx*-plane for θ_1 = 45, 90 and 135° indicate more pronounced orientation and hence dipole correlations than for molecules in the *zy*-plane. The greater dipole correlations of closely approaching molecules can be explained by the rapid ($1/r^3$) decay of electrostatic permanent-dipole to permanent-dipole interactions with distance.[373]

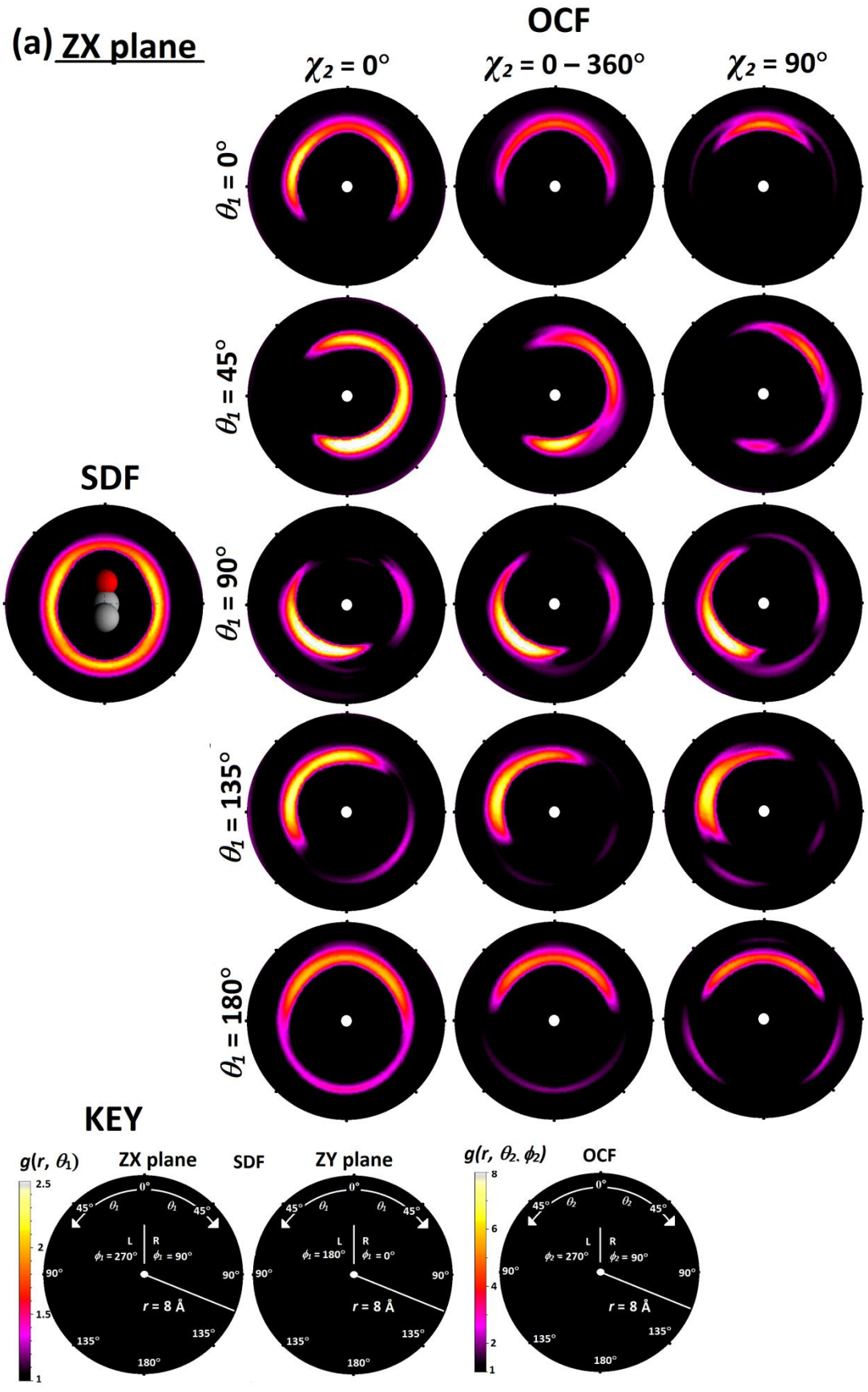
(a) ZX plane
OCF
χ_2 = 0°
χ_2 = 0 – 360°
χ_2 = 90°
θ_1 = 0°
θ_1 = 45°
θ_1 = 90°
θ_1 = 135°
θ_1 = 180°
SDF
KEY
$g(r, \theta_1)$
ZX plane
SDF
ZY plane
$g(r, \theta_2, \phi_2)$
OCF
ϕ_1 = 270°
ϕ_1 = 90°
ϕ_1 = 180°
ϕ_1 = 0°
ϕ_2 = 270°
ϕ_2 = 90°
r = 8 Å
L
R

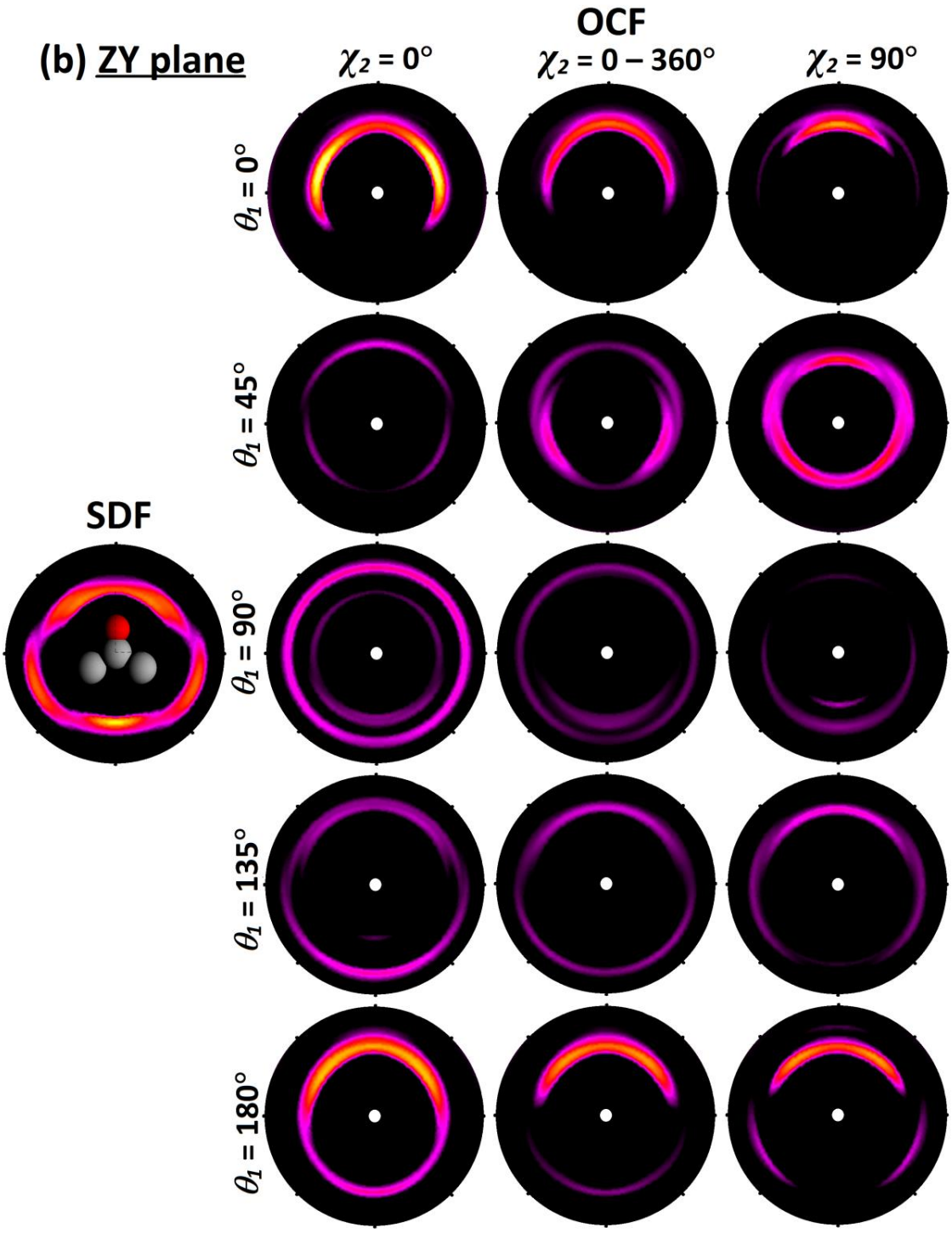

Figure 7.9 2D plots of the C_o-C_o SDF and OCFs for θ_1 = 0, 45, 90, 135 and 180° showing acetone-acetone associations in the EPSR model of the chloroform-acetone azeotrope. These are examined independently for the *zx*- (opposite) and *zy*-planes and OCFs are shown for χ_2= 0° (left column), 0–360°(central column), and 90° (right column).

In the following section, the dipole correlations of second molecules positioned at different θ_1 angles about the *zx*-plane are examined independently and compared with the 3D OCFs of pure liquid acetone reported by McLain *et al*..[105] The most likely orientation of molecules positioned above the reference (+*z*) are indicated by the contours in the OCF for $\theta_1 = 0$ and $\chi_2 = 0–360°$. The arrowhead-shaped intensity indicates that molecules at this position are mostly orientated with their *z*-axis pointing 'away from' the reference. The different shape of contours in the OCFs plotted for fixed $\chi_2 = 0°$ and $\chi_2 = 90°$ then reveals the specific arrangements in more detail. Intensity at $\theta_2 = 0°$, indicating a preference for parallel dipole orientation, is only present for molecules with for $\chi_2 = 90°$, indicating staggered methyl groups. For $\chi_2 = 0°$ the intensity is centred at $\theta_2 = \sim 70°$. This indicates T-shaped arrangements in which the z-axis of the reference points towards a second molecule with fairly perpendicular dipole alignment and with parallel *zy*-planes. These arrangements are shown as structures (a) and (b) in Figure 7.10. The position of lobes in McLain's OCFs for $\theta_1 = 0°$ indicates that a T-arrangement is also favoured in the pure liquid. [105]

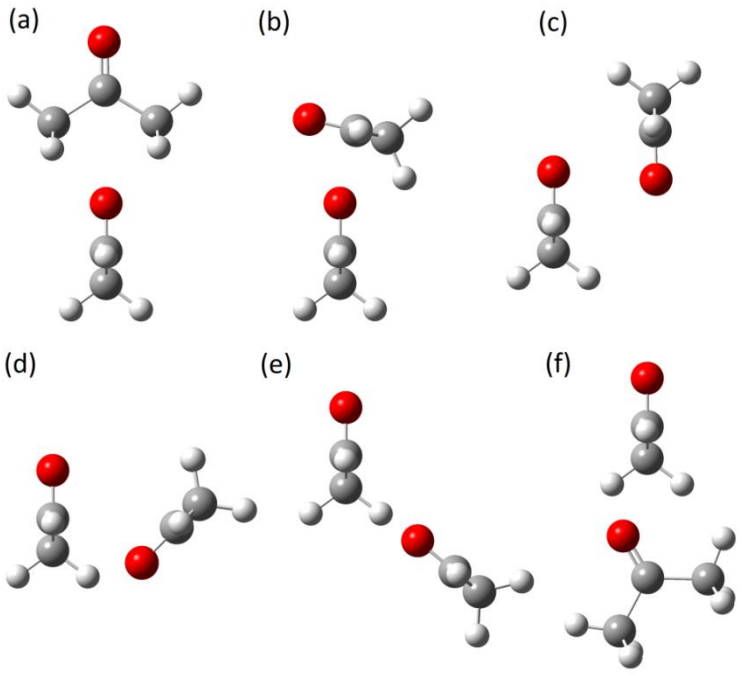

Figure 7.10 Acetone-acetone associations extracted from the EPSR model of the chloroform-acetone azeotrope. The arrangements in the crystalline phases are described by Allan *et al*.[393]

At θ_1 = 45, 90 and 135°, the OCF plots are not symmetrical and show correlations in which molecules point generally 'towards' (anticlockwise rotation, φ_2 = 270°) or 'away from' (clockwise rotation, φ_2 = 90°) the reference molecule on their left and right sides, respectively. At θ_1 = 45° in the *zx*-plane the greatest intensity in the OCF for χ_2 = 0–360° is centred at θ_2 = 180° indicating molecules with an antiparallel dipole alignment. McLain's 3D OCFs also indicates that this antiparallel arrangement is favoured in pure liquid acetone. The different intensity of features in the OCF plots for fixed χ_2 = 0° and χ_2 = 90° show that this antiparallel arrangement is also characterised by a χ_2 = 0° rotational offset and that the zy-planes of these molecules are parallel. This arrangement is shown as structure (c) in Figure 7.10. For θ_1 = 90° and χ_2 = 0–360°, the most intense features at θ_2 = 140° and φ_2 = 270° indicate molecules with antiparallel dipoles and *z*-axes angled toward the reference. This arrangement is shown as structure (d) in Figure 7.10. A very similar orientation correlation was observed in McLain's model of pure liquid acetone. At this position, fixing χ_2 has minimal influence on the features of the OCF plot, indicating an arrangement with freely varying χ_2. For θ_1 = 135° and χ_2 = 0–360° the features are also most intense on the left of the plot (φ_2 = 270°) indicating molecules pointing 'towards' the reference, but cover a wider θ_2 range, θ_2 = 0–120° at this θ_1 position. Fixing χ_2, again, has only a small influence on the shape of the feature at this θ_1 position. The greatest intensity and thus the most favoured orientation is at θ_2 = 50–80° indicating arrangements like structure (e) shown in Figure 7.10. In McLain's model of the pure liquid the most favoured orientation is ~30° indicating molecules with more parallel alignment. This difference may be due to the impact of chloroform molecules on the electrostatic balance of charge in the first coordination shell.

The orientation correlations of molecules positioned below (-*z*) the reference molecule are shown in the θ_1 = 180° OCFs. The greatest intensity at θ_2 = 0° in the plot for χ_2 = 0–360° indicates arrangements with parallel dipole alignment. A similar correlation was reported for the pure liquid by McLain *et al.* The OCF plots for fixed χ_2 = 0° and χ_2 = 90° reveal that the χ_2 rotational offset of these molecules is related to their orientation. Whilst for χ_2 = 0° the contours cover a wide θ_2 range

between 0 – 90°, for $\chi_2 = 90°$, the contours cover a smaller θ_2 range and are most intense at $\theta_2 = 30°$. The corresponding arrangement is shown as (f) in Figure 7.10. The smaller range of orientations explored by molecules with a 90° χ_2 rotational offset may be due to the obstructing influence of the 2nd molecule's methyl groups, which interfere with the reference molecule at more inclined θ_2 angles.

7.2.8 Chloroform–Chloroform RDFs of the CA Azeotrope

In the following three sections the arrangements between chloroform molecules in the EPSR model of the azeotrope are compared with those found in the pure liquid and presented in Chapter 6. In this section the intermolecular chloroform-chloroform RDFs are compared. These are shown in Figure 7.11. As already discussed for acetone, the chloroform-chloroform RDFs for the azeotrope are very similar to those of the pure liquid. A decrease in the intensity of features in the first shell RDFs of the azeotrope relative to those of the pure liquid is also observed for the chloroform-chloroform RDFs. As discussed in section 8.2.5, this effect is caused by the non-ideal interspecies mixing in the azeotrope: the negative enthalpy of mixing manifesting structurally as an increase in AC and decreases in AA and CC first shell coordination numbers relative to that of a randomly mixed liquid. This can be quantified from the presented RDFs as the average coordination number expected for a randomly mixed regular two-component liquid mixture may be estimated by multiplying the pure liquid values by the component's mole fraction in the mixture. For acetone-acetone, $12.1 \times 0.405 = 4.90$ (0–7 Å) and for chloroform-chloroform, $12.7 \times 0.595 = 7.56$. (0–7.5 Å) The corresponding average coordination numbers for the EPSR model of the azeotrope are significantly lower: 4.15 for acetone-acetone, and 6.60 for chloroform-chloroform. Interestingly, the opposite trend is found for the HS model with average coordination numbers of 5.40 for acetone-acetone, and 8.01, for chloroform-chloroform. This indicates that the interspecies associations are the result of specific interactions rather than just due to the different packings of AA, CC and AC combinations.

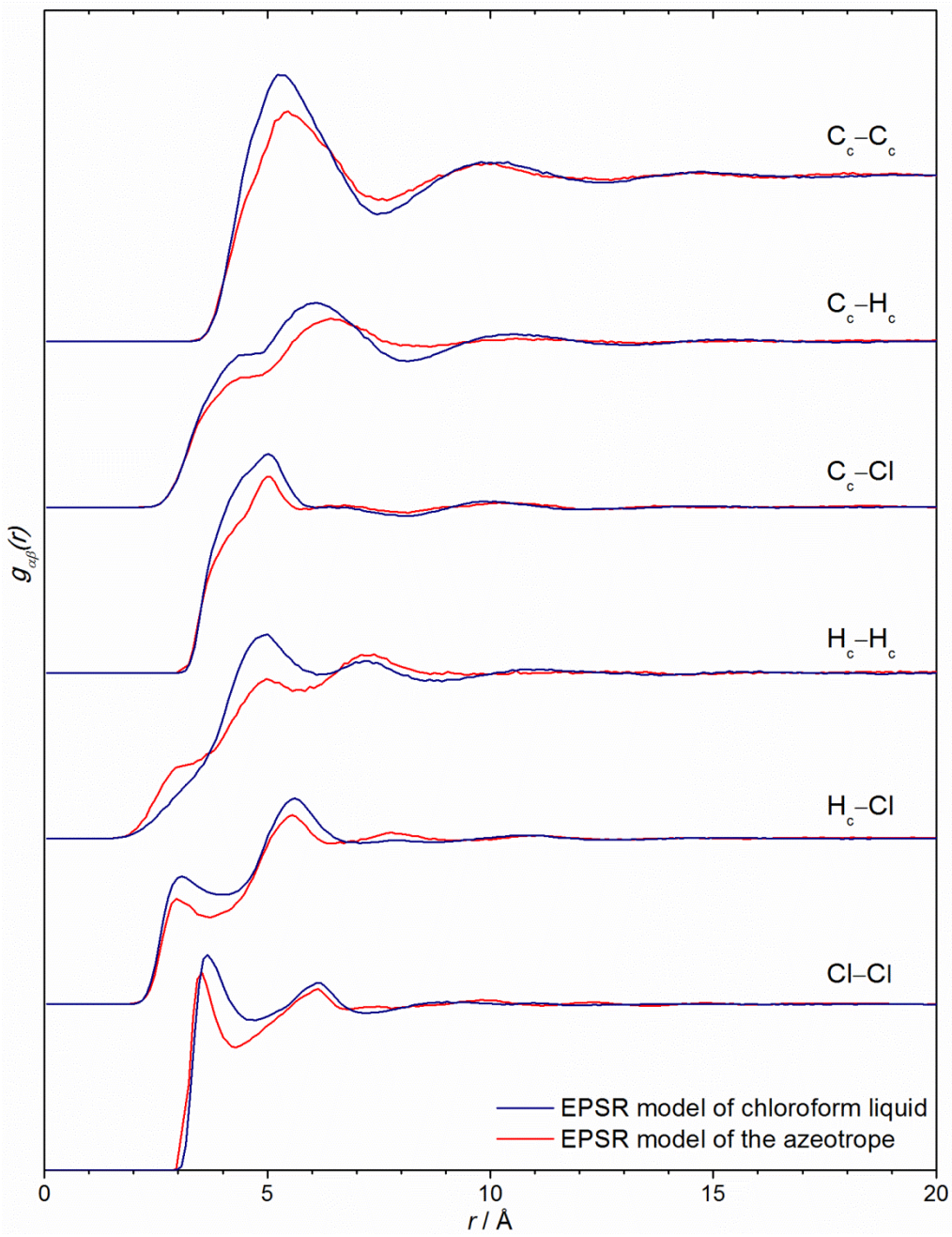

Figure 7.11 Chloroform-chloroform RDFs extracted from the EPSR model of the chloroform-acetone azeotrope and the EPSR model of pure liquid chloroform (also presented in Chapter 6).

In addition to this most striking difference, there are also more subtle differences between the RDFs of pure chloroform liquid and the azeotrope. The shape of the first feature in the H–H, H–Cl and Cl–Cl RDFs are different in the two models. The low-*r* shoulder of the first feature of the H–H RDF is much larger and the maxima of the first features in the H–Cl and Cl–Cl RDFs are at shorter distance in the azeotrope model than in the pure liquid. The low-*r* shoulder in the H–H

RDF may indicate the formation of AC_2 complexes, in which two chloroform molecules point towards a single acetone and thus have closely approaching H atoms (Figure 7.2b). The shorter distances in the azeotrope RDFs may indicate that whilst chloroform self-associations characterised by very close H–Cl and Cl–Cl distance are still found in the azeotrope, those with weaker interactions and greater H–Cl and Cl–Cl distances are lost in the mixture.

7.2.9 Chloroform–Chloroform SDFs of the CA Azeotrope

In this section, spatial density functions showing the positions of chloroform molecules about a centrally placed chloroform reference molecules are compared for the EPSR models of the azeotrope and pure liquid. To help this, the distance ranges and FSL levels of chapter 6 are used again here. The SDF plots for pure chloroform liquid are reproduced in Figure 7.12(a) and corresponding SDF plots for azeotrope are shown in Figure 7.12(b). Due to the intrinsic normalisation involved in creating FSL levels the much smaller number of molecules in the first coordination shell of the azeotrope (~6.6) compared to the pure liquid (~12.7) does not influence the size of the lobes.

In general, the area covered by SDF lobes is greater in the azeotrope than for the pure liquid. This indicates a greater spatial inhomegeniety between chloroform molecules in the azeotrope. Some lobes characterising the most favoured arrangements in the SDF plots of the pure liquid are also less well defined or missing in the plots of the azeotrope. For example, the lobe below (-*z*) the reference molecule in the SDF plot of the pure liquid at an FSL of 0.1 and 0.3 and distance range of 3–4.9 Å (indicative of the parallel aligned stacks), is absent in the azeotrope. The lobe is also absent at the greater FSL level of 0.3. Both observations suggest that the self-association of chloroform into dipole-aligned stacks in the pure liquid is significantly reduced in the azeotrope. This supports the interpretation of the Raman spectra given in section 8.2.1. However, for the greater distance range of 6.2–7.2 Å the spatial homogeneity is similar for the two models and the lobes capping the chlorine atoms of the reference are reproduced almost exactly in the SDFs of the pure liquid. As similar lobes were also found for the HS model of the pure liquid, this may indicate

that at these distances (*i.e* in the first coordination shell) the molecular packing of chloroform is similar in the azeotrope and in the pure liquid.

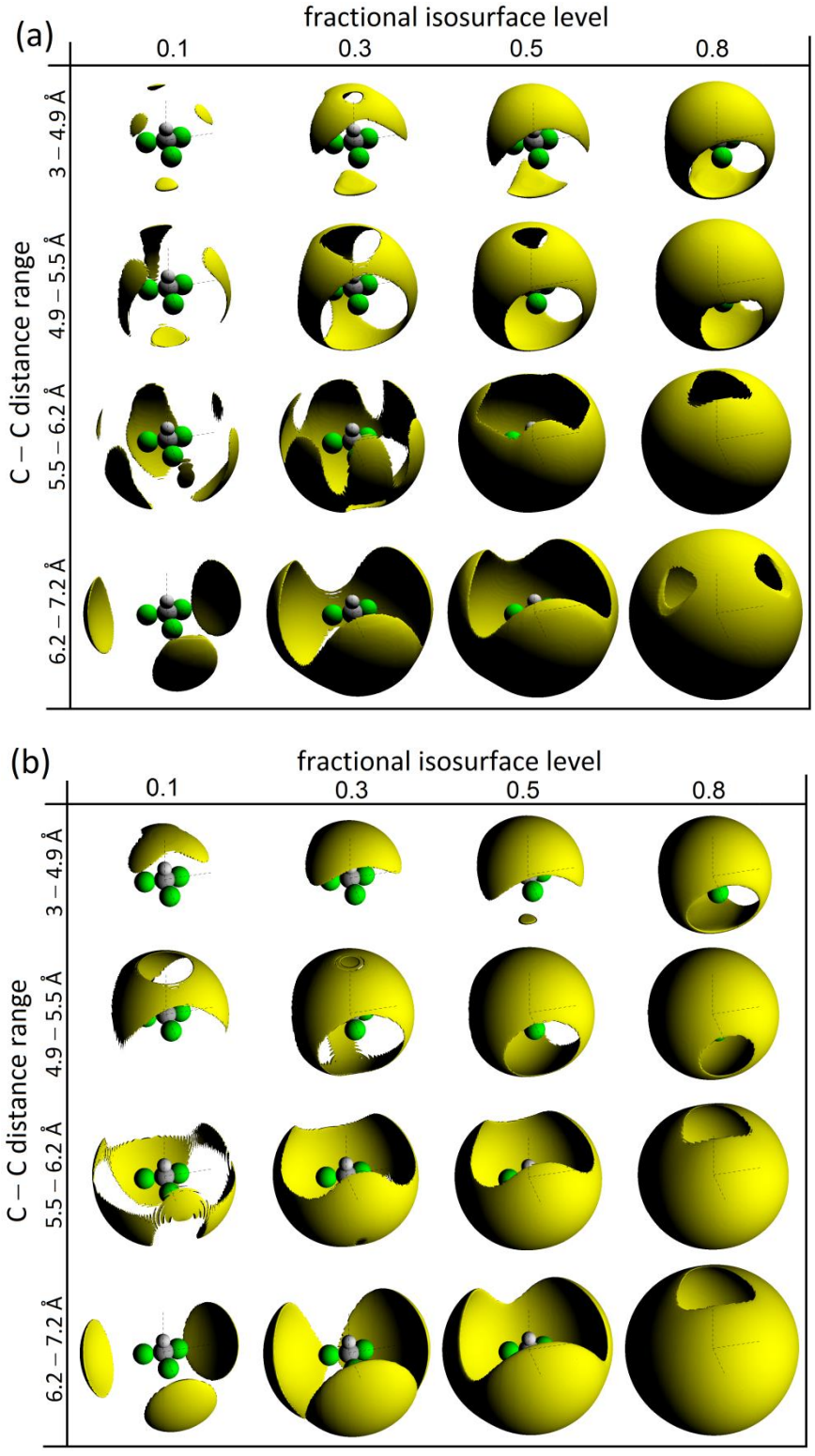

Figure 7.12 3D SDFs for C–C distance ranges covering the first coordination shell extracted from the EPSR models of (a), pure liquid chloroform (also presented in Chapter 6) and (b), the chloroform-acetone azeotrope. The distance ranges correspond to equal integrated $g(r)$ in the EPSR model of pure liquid chloroform.

7.2.10 Chloroform–Chloroform OCFs of the CA Azeotrope

The self-associations of chloroform in the EPSR models of the azeotrope and pure liquid have been more closely examined using 2D SDF and OCF plots, which are shown in Figure 7.13. Unlike the 3D plots of the *prior* section, intrinsically scaled using FSLs, these 2D plots indicate the variation in *g*. The intensity of features in these 2D plots thus reflects the lower relative amount of chloroform-chloroform coordination in the azeotrope than in the pure liquid which was described in Section 7.2.8. The comparison given in the present section will therefore focus on the shape of the features in the OCF and SDF plots.

Although the shape of most features in these 2D SDF plots is similar for chloroform liquid and azeotrope models there are a few key differences. Firstly, the feature at $\theta_1 = 180°$ is less pronounced in the azeotrope than the pure liquid, more clearly showing the origin of the missing lobe in the 3D SDF plots (section 7.2.9). In the azeotrope model there are far fewer molecules positioned directly below (-z) the reference. However, interestingly, the orientation correlations of these molecules, as indicated by the shape of the feature in the OCF for $\theta_1 = 180°$, are similar for the azeotrope and pure liquid. This suggests that although a preference for chloroform's dipole alignment is maintained in the azeotrope, the property of dipole aligned stacks is greatly reduced. There are also differences in the OCF for $\theta_1 = 45°$. An additional feature at $\theta_2 = 90°$ for ($\varphi_2 = 270°$) indicates an arrangement in which the 2nd molecule is directed towards the reference and the molecule's dipole axes are approximately perpendicular. Interestingly, this orientation correlation would be expected for chloroform molecules arranged in the AC_2 complex of Figure 7.2(b). This provides further confidence that interspecies interactions are impacting the isospecies arrangements in the chloroform-acetone azeotrope. Interspecies associations are considered in the following sections.

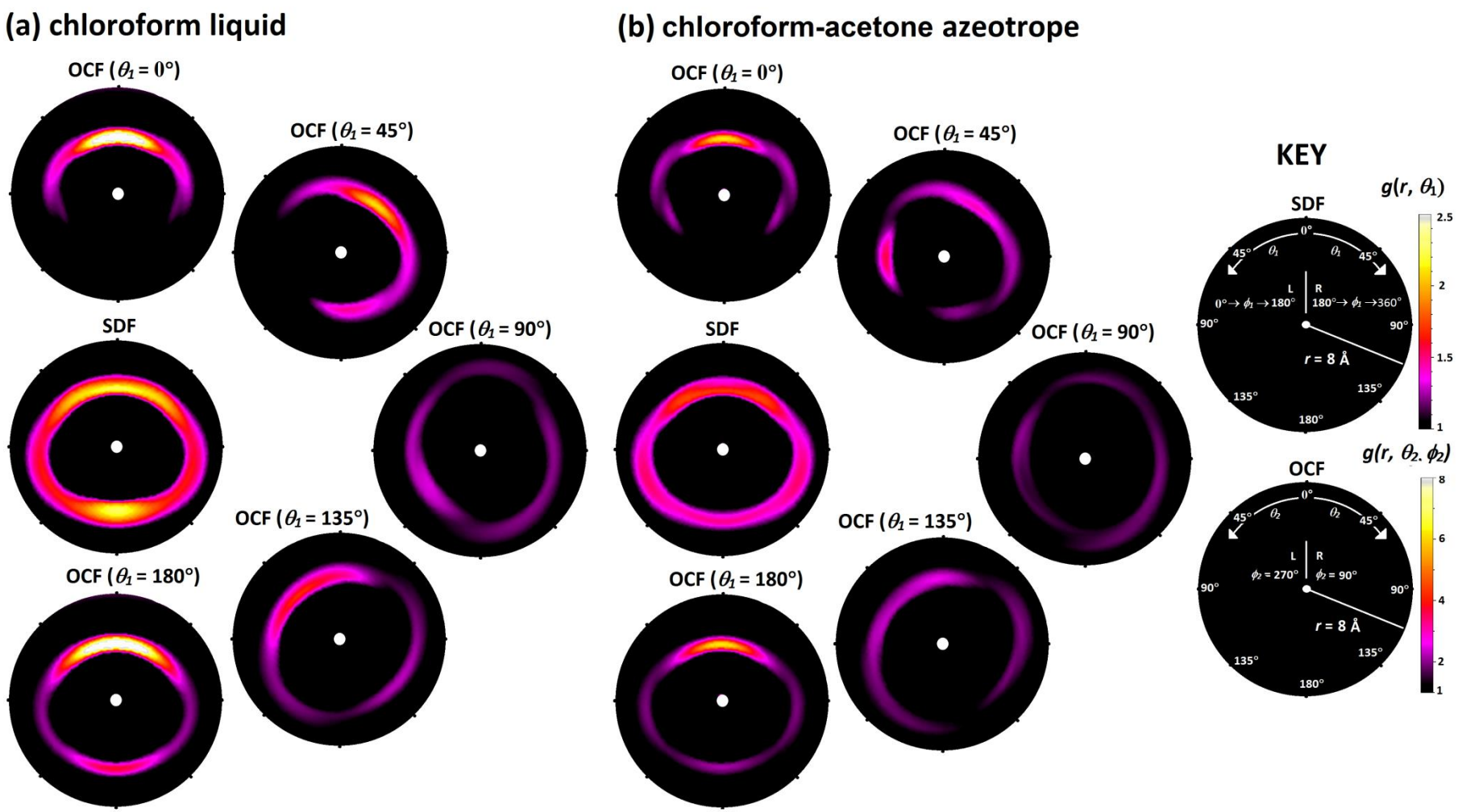

Figure 7.13 A comparison of 2D chloroform-chloroform (C_c-C_c) SDFs and OCFs for the EPSR models of the (a) pure liquid chloroform (also presented in Chapter 6) and (b) the chloroform-acetone azeotrope. The θ_1 positions (0, 45, 90, 135 and 180°) examined in the OCFs plots are roughly indicated by their position around the centrally placed SDF.

7.2.11 Interspecies RDFs of the CA Azeotrope

In this section, chloroform-acetone RDFs are examined to investigate the interspecies associations in the models of the azeotrope. RDFs are presented for the HS (blue line), LJ+C (black line) and EPSR (red line) models in Figure 7.14. The RDFs of the HS model represents the most efficient way to pack the chloroform and acetone molecules. The RDFs of the LJ+C model indicates the associations arising from the Lennard-Jones parameters and monopole partial charges ascribed to the molecules in studies of the pure liquids, and discussed in sections 6.2.2 (chloroform) and 7.2.3(acetone). The RDFs of the EPSR model represent a set of interspecies associations which give a good fit to the measured diffraction data. Differences between the RDFs of the EPSR and LJ+C models indicate the structural perturbations arising from the introduction of empirical potentials between the atom pairs and thus indicate the influence of the diffraction data on the structure. The differences between the RDFs of the three models, which have interspecies interactions as their origin, are discussed below.

The most pronounced difference in the RDFs for the EPSR and HS models is the strong maximum at 2.08 Å in the O–H_c RDF, which is absent in the HS model. The feature is consistent with a hydrogen-bonding interaction between acetone and chloroform. Sharp features in many of the other RDFs arise from the dominating influence of this interaction over other interspecies arrangements. Interestingly, no sharp low-*r* feature is seen in the H_a–Cl RDF. This suggests that the AC complexes formed in the model do not constrain the rotation of the methyl groups, as suggested by Jalian *et al*. and shown as arrangement (d) in Figure 7.2(d).[103] Due to the complexity of the RDFs and the nature of the complexes formed, the arrangements are more easily examined in 3D using SDFs and through statistical analysis. These are presented in the following sections. The C_o–C_c RDFs contains the remaining information about the composition of chloroform and acetone coordination shells. The first coordination shell about acetone contains an average of 4.1 acetone molecules and 7.5 chloroform molecules. The first coordination shell about chloroform contains an average of 5.1 acetone molecule and 6.6 chloroform molecules. We therefore observe a greater number of interspecies contacts than would be expected in a randomly mixed liquid.

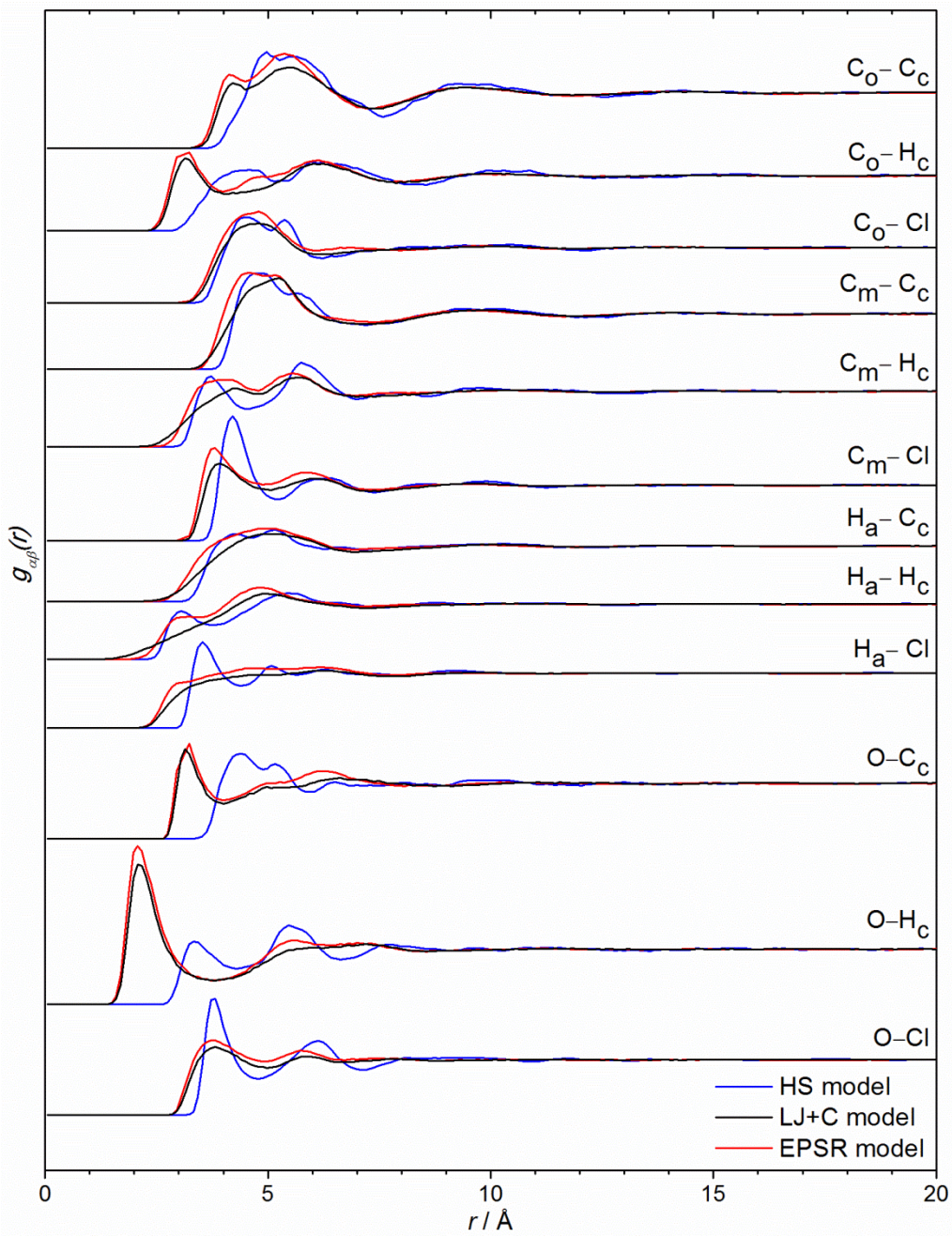

Figure 7.14 Chloroform-acetone RDFs extracted from the HS (blue line), LJ (black line) and EPSR (red line) models. The traces have been offset vertically for clarity.

Due to the low weighting of O–H_c atom pairs to the diffraction data (1% in the deuterated azeotrope) the simulation parameters and the influence of the diffraction data on the simulation have been closely considered. To maximise the sensitivity of the model to the diffraction data the data sets were independently weighted proportionally to their H_a/H_c composition and a high overall weighting was used.. Although, it may appear that the low O–H_c weighting would prohibit an accurate description of the hydrogen bonding interactions in the azeotrope, it is clear from the

RDFs that AC_n complex formation impacts many of the RDFs and hence has a strong drive from the measured diffraction data. It is also reassuring that the distance of maximum intensity for the first feature in the O–H_c RDF is slightly shorter and its intensity slightly greater in the EPSR model than in the LJ+C model. This implies that EPs produced from the measured diffraction data perturbed the structure sufficiently to increase the number and average strength of hydrogen bonding interactions in the model. However, the differences are small, which may suggest that the low contribution of the data in describing the O–H_c RDF may have limited the perturbation.

The impact of the measured diffraction data on the model was also independently examined using the approach of McLain *et al.*.[105] In their study, several EPSR models based upon different LJ+C parameters and partials charges were found to converge upon a single structure, confirming the influence of the data on the model structure. We therefore also applied a LJ+C model using the parameters of Kamath *et al.*,[375] originally produced to give accurate calculated partial vapour pressures. Kamath's potentials produced a model with much longer hydrogen bond distances (maximum at ~2.7 Å). Disappointingly, the position of the feature did not decrease significantly with subsequent EPSR simulation, indicating that the EPs produced from the measured diffraction data were not able to overcome the inaccuracies in Kamath's potentials. This may be due to the large electrostatic forces contributing to the hydrogen bond which would require larger EPs to enact a structural perturbation than for acetone in McLain's study. In essence, the magnitude of the potentials available in EPSR to perturb the structure is limited by their potential to cause unwanted side effects; large spherical potentials may be able to shift the feature, but their influence on other aspects of the structure needs also to be considered. This reinforces the importance of accurate LJ+C models as starting points in EPSR simulation. The accuracy impacts upon the magnitude of the EPs needed to reproduce the scattering data and this in turn impacts upon the suitability of the potentials to describe the intermolecular interactions of the system.

7.2.12 Interspecies SDFs of the CA Azeotrope

In this section, the most likely position of chloroform's H atom about a centrally positioned acetone molecule in the EPSR model of the azeotrope are probed using 3D SDFs. The Cambridge Structural Database (CSD) has also been used to investigate the nature of similar ketone–HX hydrogen bonding contacts in crystalline compounds. Plots which look very similar to the EPSR-produced SDF plots of liquids but showing the distribution of different arrangements in all the appropriate compounds of the database are available *via* the *Isostar* software. The sum of van der Waals radii for oxygen and hydrogen (1.2 Å + 1.52 Å = 2.72 Å) from Bondi *et al.*[109] has been used to define the O–H_c contacts forming a hydrogen bond and the distance range examined in the SDF plots. Intrinsically scaled FSL levels of 0.1, 0.3 0.5 and 0.8 showing the spatial distribution of different arrangements are used in this section.

The arrangements between ketone and hydrogen bonding species extracted from the CSD are shown in Figure 7.15. The three images of Figure 7.15(a) show the relationship between the orientation of the hydrogen bonding contacts (indicated by sticks, hydrogen atoms represented by the white terminus) and the overlap of their van der Waals radii. The spatial distribution of hydrogen bonding contacts decreases significantly with distance such that for distances < 3.22 Å the contacts are widely distributed while for distances < 2.22 Å the contacts form a cap of contacts with hydrogen atoms pointing exclusively towards the oxygen. The 3D surface plots of Figure 7.15(b) then show the spatial distribution of the contacts for the compounds of the database within a distance range corresponding to the sum of van der Waals radii (2.72Å). The white lobes in the image drawn at an FSL of 0.1 indicate the most favoured positions for hydrogen bonded contacts, in line with the oxygen lone pairs.

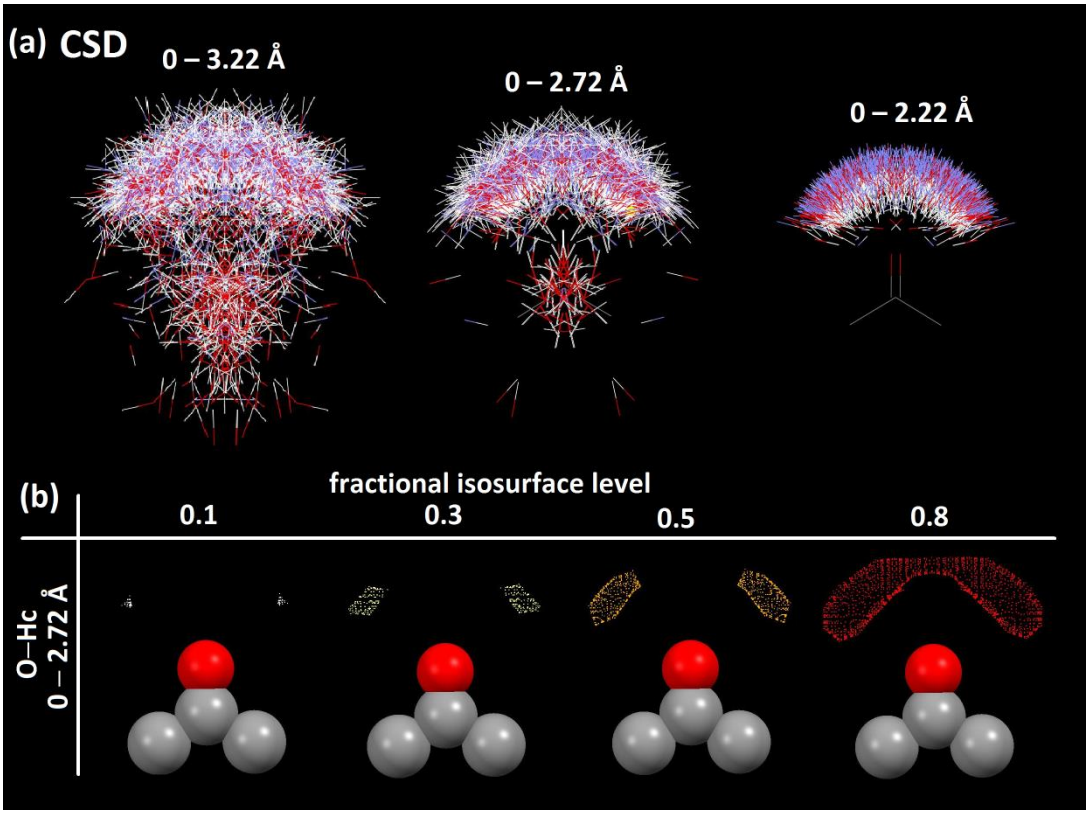

Figure 7.15 Associations between ketone (C(sp3)COC(sp3)) groups and hydrogen bonding species (HX; H shown in white)in the crystalline compounds of the Cambridge Structural Database. (a) Stick plots showing the associations at interatomic distances <2.22, <2.72 and <3.22 Å and (b) intrinsically scaled contour plots showing the spatial distribution of arrangements.

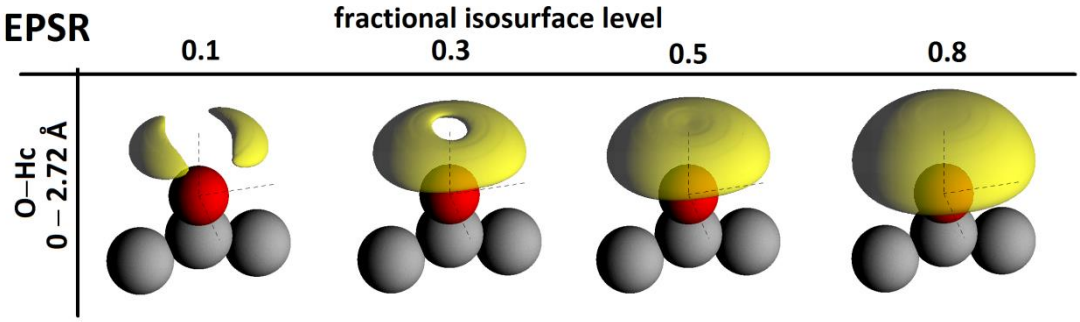

Figure 7.16 O–H_a SDFs extracted from the EPSR model of the chloroform-acetone azeotrope. The distance range corresponds to the sum of van der Waals radii of oxygen and hydrogen.[109] FSLs of 0.1, 0.3, 0.5 and 0.8 show the spatial distribution of arrangements in the model.

The corresponding distribution in spatial position for H_c about O in the EPSR model of the azeotrope is shown in Figure 7.16. The position of the lobes in these plots indicates a far greater spatial inhomeogeniety in the azeotrope than found in the crystalline compounds of the CSD. Although the lobes are centred on the lone pairs for an FSL of 0.1, at greater FSL levels the lobes

form a cap around the oxygen atom. This indicates that the majority of O–H_c contacts within the sum of van der Waals radii have no positional preference towards the lone pair electrons. Thus although the EPs contain the pairwise information to reproduce the interspecies association of the CSD their magnitude is insufficient to constrain the interspecies association against the disordering influence of thermal motion. To some extent this would be expected for a liquid which will be more greatly affected by thermal motions than the crystalline compounds of the CSD. Alternatively, the difference may reflect the inadequacies of the EPs to manipulate the fine detail of the structural model. Work is underway to include an additional X-Ray diffraction data set into the simulation to provide scattering length contrast on the chlorine positions. This will enable a greater confidence in the interspecies associations of the model.

7.2.13 Interspecies Associations in the CA Azeotrope

The intermolecular associations in the EPSR model of the azeotrope have also been investigated through a statistical analysis of the arrangements in the simulation box. This has enabled the number and type of AC_N complexes in the model to be characterised and enables acetone's impact on chloroform's self-association to be better understood. This analysis is based upon the chain distribution analysis of the chloroform model, presented in Chapter 6, and used identical constraints. However, for the azeotrope, three separate chain distribution analyses were carried out and compared. In the first only the connections between chloroform molecules were considered (CC); in the second, connections between the acetone and chloroform molecules with O–H_c distances less than 2.72 Å were also considered (AC). The third chain distribution analysis only considered these AC connections and ignored CC connections. This combination of chain length distributions has then enabled the number of C_N, AC_N and $A(C_N)_2$ complexes in the model to be determined.

The proportion of acetone, chloroform and acetone and chloroform molecules involved in the different associations found in the EPSR model of the azeotrope are shown in Figure 7.17. Overall ~52 % of the chloroform and acetone molecules form an association within the given

constraints. AC complexes are by far the most likely and involve ~36 % of the chloroform and acetone molecules in the simulation box. AC_2 complexes were also present involving ~9 % of the molecules. ACC and a small number of ACCC complexes involved ~4 % of all the molecules in the simulation box. However, the most striking result of this analysis is the low proportion of self-associated chloroform molecules in the model with only ~4 % of the chloroform molecules involved in a dipole-aligned stack. This is greatly reduced from 29 % found in the EPSR model of pure chloroform liquid.

The reduction in the extent of chloroform self-association in the azeotrope relative to the pure liquid, reinforced by shifts in chloroforms vibrational spectra, supports the validity of Apelblat's,[97] model of the azeotrope. However, our data suggest that a more accurate description of the interactions in the azeotrope may be obtained in their model if ACC complexes were to be included.

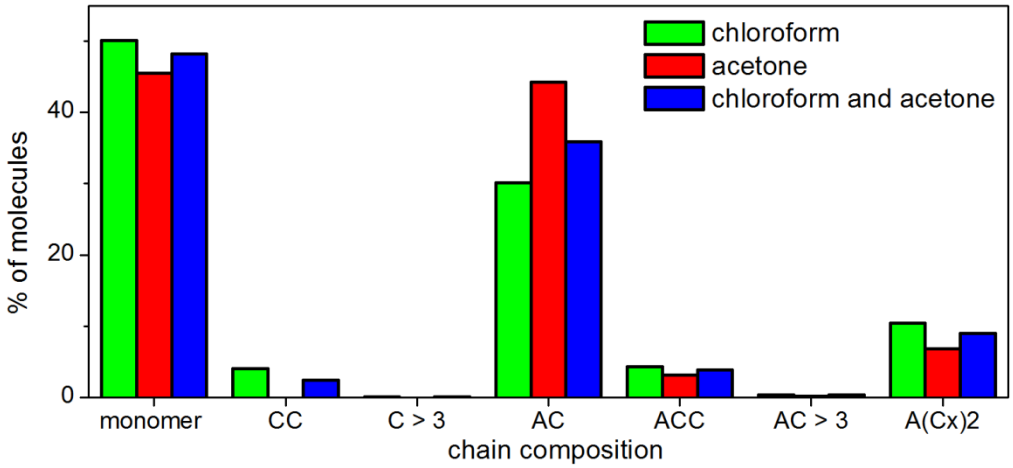

Figure 7.17 Intermolecular associations in the EPSR model of the chloroform-acetone azeotrope obtained from chain length distribution analysis for CC, CC and AC, and AC connections. CC connections were defined by a C–H distance 2–4.2 Å and H···C–H angle 150–180°. AC connections were defined by C-H_c distance < 2.72 Å (the sum of van der Waals radii for oxygen and hydrogen).

7.2.14 Comparison with Neutron Diffraction data for the Benzene-Methanol Azeotrope

Nine liquid mixtures with different H/D substitutions were used to investigate the structure of the benzene-methanol azeotrope ($X_{methanol}$ = 0.550),[98-100] by neutron diffraction. The isotopic composition and weighting factors for each of the atom pairs in the liquid mixtures are given in Appendix 12. The measured scattering data over the entire *Q*-range (0.1 – 50 Å^{-1}) are given in Appendix 17 (corrected for attenuation and multiple scattering) and 18 (also corrected for inelasticity). EPSR structural modelling of this system has not yet been completed but Figure 7.18 compares *F*(*Q*)s for several isotopic compositions carried out to test the general hypothesis that the benzene-methanol azeotrope, being thermodynamically much closer to demixing, will show isospecies aggregation. In Figure 7.18(a) the *F*(*Q*)s for the differently substituted liquid-mixtures are overlaid. In Figure 7.18(b) the *F*(*Q*) for the fully deuterated azeotrope is compared with a hypothetical *F*(*Q*) obtained by summing *F*(*Q*) data for the pure deuterated liquids.

Interestingly, as indicated in Figure 7.18(a), the slope of the low-*Q* intensity for the BM liquids was found to increase proportionally with the ratio of benzene to methanol scattering length density. Although a lower minimum *Q* and greater *Q*-resolution than available on SANDALS would be required to model the fluctuations in scattering length density in 3D, this trend indicates significant spatial fluctuations in the concentration of benzene and methanol, and supports the partial molecular demixing predicted for positive pressure azeotropes in section 7.2.5.[319] The much closer state of the positive azeotrope to demixing is also supported by their very different crystallisation behaviour observed by X-ray diffraction as the azeotropes were cooled to 80 K (Appendices 22 and 23). Whilst the benzene-methanol azeotrope separated and crystallised, the chloroform-acetone azeotrope formed a glass. The close agreement between *F*(*Q*) data for the fully deuterated azeotrope with hypothetical *F*(*Q*) data for a combination of the pure liquids (Figure 7.18b) suggests that the intermolecular structure in the azeotrope at low *r* is somewhat similar to the pure liquids. This situation would only occur if the liquid structure contained a significant proportion of benzene clusters and methanol clusters. This also implies that (in an opposite way to

the negative pressure chloroform-acetone azeotrope) the partial radial distribution functions for interspecies correlations have low intensity at low *r* and that partial radial distribution functions for isospecies correlations have a high intensity at low *r*. These data are very much in disagreement with studies suggesting distinct benzene-methanol clusters with defined stoichiometry.[104,394-395] We expect that EPSR modelling of the benzene methanol azeotrope (in progress) will reveal the size of the clusters and the nature of the benzene–benzene[396-400] and methanol–methanol[119,401-407] interactions which give rise to the partial demixing.

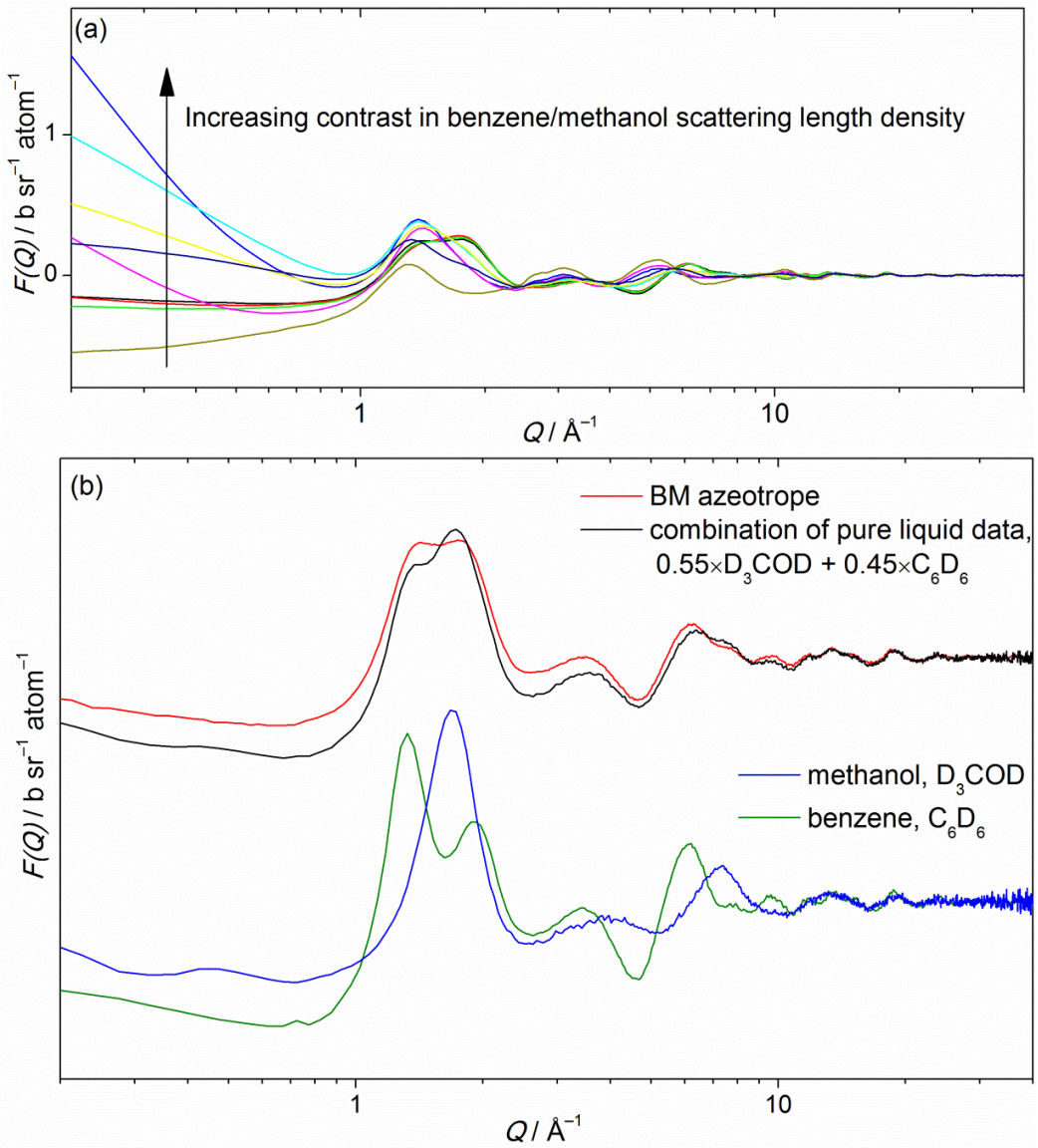

Figure 7.18(a) Neutron scattering *F(Q)* data for nine benzene-methanol azeotropic liquid mixtures with different H/D substitutions. A trend of increasing low-*Q* intensity gradient with increasing benzene/methanol scattering length density contrast is indicated by the arrow, (b) a comparison of measured *F(Q)* data for the fully deuterated benzene-methanol azeotrope (red) with a trace for a hypothetical liquid mixture (black) formed by summing data of pure deuterated benzene (green) and methanol (blue) liquids weighted by the azeotropic composition.

7.3 Conclusions

The intermolecular structures of the negative pressure chloroform-acetone azeotrope and the positive pressure benzene-methanol azeotrope have been studied by neutron diffraction and Raman spectroscopy. A structural model of the chloroform-acetone azeotrope was prepared using EPSR. This model indicated that a structure strongly influenced by favourable $C_2H_6O\cdots HCCl_3$ and $Cl_3H\cdots\cdots Cl_3H\cdots\cdots Cl_3H$ intermolecular interactions are consistent with neutron scattering data recorded with isotopic substitution. The model showed a reduced number of dipole aligned chloroform self-associations in the azeotrope relative to the pure liquid; this is in agreement with changes in Raman spectra of pure chloroform liquid and as a component of the azeotrope. The modelling also identified several AC_N complexes not always considered, such as ACC, and found the complexation to influence the overall mixing character of the azeotrope. Neutron scattering data for the benzene–methanol azeotrope also indicates that intermolecular interactions influence mixing in this system. Whilst the negative pressure azeotrope shows a partial or transient complexation, for the positive pressure azeotrope there is evidence for partial demixing. It is particularly pleasing to observe this negative excess entropy of mixing (a regular mixture showing the greatest entropy of mixing) in the structural data. Going forward it is expected that more detailed insights into microscopic mixing phenomena may be gained through comparisons of Kirkwood-Buff integrals,[408-411] calculated from the EPSR derived structural models of the chloroform-acetone and benzene-methanol azeotropes.

Final Conclusions

In this work it is shown how the intermolecular interactions in liquids, and resulting liquid properties, depend intimately on the size, shape and charge distribution of the molecules as well as on temperature and pressure. This work also contributes to one of the most exciting areas of current liquids research aimed at understanding the contribution of dynamic and structural correlations to a liquid's properties and phase behaviour.[199]

For aqueous systems, the spatial correlations are especially pronounced due to the strength and directionality of hydrogen bonding interactions which significantly structures the low temperature and ambient liquids. It has even recently been suggested that transient regions of profoundly different structural ordering may exist in liquid water affecting properties such as its glass transition,[17,200] and nucleation behaviour.[43] Water's structural and dynamic correlations have been probed in this work through temperature annealing studies of amorphous solid water (ASW), a metastable form of H_2O prepared by vapour deposition at 77 K. The changes that take place as ASW is heated provide a different perspective on the nature of water's glass transition and crystallisation, which are typically studied as the ambient liquid is cooled. The data shown herein indicate that upon heating, ASW relaxes towards the structure of ice I_h in several sequential stages: pore collapse, local structural relaxations, crystallisation to ice I_{sd} and then transformation to ice I_h. Although there are many interesting aspects of this behaviour, the local structural relaxations which occur *prior* to crystallisation are particularly thought-provoking; rather than accelerating the rate of crystallisation, the thermal annealing hinders subsequent crystallisation, suggesting that the relaxed structures forming are somewhat unrelated to the structure of ice I. Whilst these structures may closely reflect the structure of the inaccessible liquid at these temperatures, the time dependence of these relaxations indicate that the material is not liquid-like, at least until its crystallisation to ice I at 150–160 K, which likely occurs concomitantly with the glass to liquid transition. This conclusion is in disagreement with reports of a glass to liquid transition in ASW at 136 K,[87,144] It might, however, be possible to access the liquid by heating ASW if crystallisation can be

prevented, using, for example, the close confinement methods applied successfully upon cooling.[54] IR Spectroscopic data presented in this work indicates that the hydration shells surrounding C_{60} molecules in ASW retain a water-like character after being annealed to 190 K, which suggests that this may indeed be possible.

The behaviour of micropores and of C_{60} molecules in ASW is also particularly intriguing. The data presented here confirm that sintering relaxations, which close the micropores, proceed at much lower temperatures than required for the more local structural relaxations occurring *prior* to crystallisation. It is also shown that water molecules in the hydration shells of C_{60} become mobile at lower temperatures than water molecules in the bulk. These observations highlight a relationship between structure and dynamics, whereby the energy of the transition state for molecular reorientation is greater in the bulk than at the surface of a pore or in the hydration shell of a hydrophobic C_{60} molecule. Indeed the local structural relaxations occurring *prior* to crystallisation, and crystallisation itself, may also be related to this phenomenon. Upon heating, mobility will initially increase near hydrogen bonding defects giving the local structural relaxations, and then at higher temperatures in the bulk material, allowing crystal nucleation and growth. In this regard, it is remarkable that the mobility of water in the hydration shell of hydrophobes relative to that in the bulk is reversed as the temperature is increased, becoming much less mobile than in the bulk at ambient temperatures.[5] This suggests an effective way to further investigate hydrophobic effects, thought to be intricately linked to changes in dynamics,[267] may be to examine hydrophobic behaviour in the supercooled regime under conditions in which the mobility in the bulk and in the hydration shell become equal and when hydrophobic effects could potentially vanish.

Mixtures of small polar molecules also display interesting properties related to their specific intermolecular interactions. The combination of neutron scattering and computer simulation, made possible by the Empirical Potential Structural Refinement (EPSR) software[6] used in this study, is capable of providing much more information about liquid structure than can be learned from vibrational spectroscopy or by examination of macroscopic properties such as relative permittivity or the average dipole moment of their components. The collinear self-association of

chloroform molecules discovered in the pure liquid using this approach makes this most evident as well as demonstrating the connection between intermolecular interactions and liquid properties. In particular, the self-association is proposed to explain its excellent solvent properties, as local increases in polarity about the coordinated stacks provide a positive enthalpic contribution to dissolution and extraction processes.[354] This structural characteristic may also be relevant to chloroform's anaesthetic activity, which may be caused by the interference of these aggregated 'super dipoles' with mammalian nerve cells.[353]

Whilst it is very appealing to prepare structural models of liquids which are consistent with pairwise diffraction data, this work also shows some of the limitations of the approach. In particular, the models may not reproduce the exact nature of the true inherent structures if they are constrained only by small deviations in the one dimensional pair distribution data. This effect is the most likely cause of an unexpected feature in the model of the chloroform-acetone azeotrope whereby the $O_{acetone}$–$H_{chloroform}$ hydrogen bonding interaction, giving rise to the negative pressure azeotropy of these mixtures, did not show a pronounced preference for an orientation allowing overlap of molecular orbitals containing the oxygen lone pair electrons. In addition to highlighting the caution required whilst interpreting the fine detail of these models, this work also demonstrates that it is possible to test their accuracy to measurable quantities using theories of a liquid's dielectric permittivity.[369] There are likely to be many other ways to independently investigate the validity of these models. For example, the preferential solvation displayed by the azeotropic mixtures studied in this work can be related to measureable thermodynamic quantities using the Kirkwood-Buff theory of liquids.[408-409] In addition to providing a useful check on the accuracy of the models, this applied theoretical approach to model analysis may also be the most productive in identifying the connections between structure and liquid properties, which will ultimately lead to the new understandings needed in order design more effective, efficient and environmentally conscious solvents.

References

1. Blokzijl, W.; Engberts, J. B. F. N., Hydrophobic Effects: Opinion and Fact. *Angew. Chem., int. Ed. Engl.* **1993,** *32* (11), 1545-79.

2. Shephard, J. J.; Evans, J. S. O.; Salzmann, C. G., Structural Relaxation of Low-Density Amorphous Ice Upon Thermal Annealing. *J. Phys. Chem. Lett.* **2013,** *4* (21), 3672–3676.

3. Frank, H. S.; Evans, M. W., Free Volume and Entropy in Condensed Systems. 3. Entropy in Binary Liquid Mixtures; Partial Molal Entropy in Dilute Solutions; Structure and Thermodynamics in Aqueous Electrolytes. *J. Chem. Phys.* **1945,** *13*, 507-32.

4. Gill, S. J.; Dec, S. F.; Olofsson, G.; Wadsoe, I., Anomalous Heat Capacity of Hydrophobic Solvation. *J. Phys. Chem.* **1985,** *89*, 3758.

5. Qvist, J.; Halle, B., Thermal Signature of Hydrophobic Hydration Dynamics. *J. Am. Chem. Soc.* **2008,** *130*, 10345-10353.

6. Soper, A. K., Partial Structure Factors from Disordered Materials Diffraction Data: An Approach Using Empirical Potential Structural Refinement. *Phys. Rev. B* **2005,** *72*, 104204.

7. Stratmann, L., *Chloroform. The Quest for Oblivion*. Sutton Publishing: Stroud, 2003.

8. Rowlinson, J. S.; Swinton, F. L., *Liquids and Liquid Mixtures*. Third ed.; Butterworth Scientifics: London, 1982; p 1-11.

9. Gray, C. G.; Gubbins, K. E., *Theory of Molecular Fluids*. Clarendon Press: Oxford, 1984; Vol. 1: Fundementals.

10. Murrell, J. N.; Jenkins, A. D., *Properties of Liquids and Solutions*. 2nd ed.; Wiley: New York, 1982; p 14-37.

11. Ohmine, I.; Saito, S., Water Dynamics: Fluctuation, Relaxation, and Chemical Reactions in Hydrogen Bond Network Rearrangement. *Acc. Chem. Res.* **1999,** *32* (9), 741–749.

12. Israelachvili, J., *Intermolecular and Surface Forces*. Second ed.; Elsevier: San Diego, 1992; p 282-286.

13. Rowlinson, J. S.; Swinton, F. L., *Liquids and Liquid Mixtures*. Third ed.; Butterworth Scientifics: London, 1982; p 106-107.

14. Chaplin, M. Water Structure and Science. http://www1.lsbu.ac.uk/water/ (accessed 26.3.2014).

15. Stillinger, F. H., Water Revisited. *Science* **1980,** *209* (4455), 451-457.

16. Cho, C. H.; Singh, S.; Robinson, G. W., Understanding All of Water's Anomalies with a Nonlocal Potential. *J. Chem. Phys.* **1997,** *107*, 7979.

17. Tanaka, H., Simple Physical Explanation of the Unusual Thermodynamic Behavior of Liquid Water. *Phys. Rev. Lett.* **1998,** *80*, 5750-5753.

18. Vedamuthu, M.; Singh, S.; Robinson, G. W., Properties of Liquid Water: Origin of the Density Anomalies. *J. Phys. Chem.* **1994,** *98* 2222-2230.

19. Vedamuthu, M.; Singh, S.; Robinson, G. W., Accurate Mixture-Model Densities for D_2O. *J. Phys. Chem.* **1994**, 8591-8593.

20. Mallamace, F.; Corsaro, C.; Mallamace, D.; Vasic, C.; Stanleyd, H. E., The Thermodynamical Response Functions and the Origin of the Anomalous Behavior of Liquid Water *Faraday Discuss.* **2013,** *167*, 95-108.

21. Soper, A. K., The Radial Distribution Functions of Water as Derived from Radiation Total Scattering Experiments: Is There Anything We Can Say for Sure. *ISRN Physical Chemistry* **2013**, 279463.

22. Teixeira, J.; Luzar, A., Physics of Liquid Water. Structure and Dynamics. *NATO Science Series, Series A: Life Sciences* **1999** *305* (Hydration Processes in Biology), 35-65.

23. Soper, A. K., The Radial Distribution Functions of Water and Ice from 220 to 673 K and at Pressures up to 400 MPa. *Chem. Phys.* **2000,** *258*, 121-137.

24. Elliot, S. R., *Physics of Amorphous Solids* second ed.; Longman Scientific and Technical: New York, 1990; p 340-350.

25. Yagasaki, T.; Saito, S., Molecular Dynamics Simulation of Nonlinear Spectroscopies of Intermolecular Motions in Liquid Water. *Acc. Chem. Res.* **2009,** *42* (9), 1250-1258.

26. Laage, D.; Stirnemann, G.; Sterpone, F.; Rey, R.; Hynes, J. T., Reorientation and Allied Dynamics in Water and Aqueous Solutions. *Annu. Rev. Phys. Chem.* **2011,** *62*, 395-416.

27. Heyden, M.; Sun, J.; Funkner, S.; Mathias, G.; Forbert, H.; Havenith, M.; Marx, D., Dissecting the THz Spectrum of Liquid Water from First Principles Via Correlations in Time and Space. *Proc. Natl. Acad. Sci. U.S.A* **2010,** *107* (27), 12068–12073.

28. Marsh, K. N., *Recommended Reference Materials for the Realization of Physicochemical Properties*. Blackwell Scientific Publications: Oxford, 1987.

29. Stillinger, F. H., Structure in Aqueous Solutions of Nonpolar Solutes from the Standpoint of Scaled-Particle Theory. *J. Solution Chem.* **1973,** *2*, 141.

30. Salzmann, C. G.; Radaelli, P. G.; Slater, B.; Finney, J. L., The Polymorphism of Ice: Five Unresolved Questions. *Phys. Chem. Chem. Phys.* **2011,** *13*, 18468-18480.

31. Bernal, J. D.; Fowler, R. H., A Theory of Water and Ionic Solution, with Particular Reference to Hydrogen and Hydroxyl Ions. *J. Chem. Phys.* **1933,** *1*, 515–549.

32. Blackman, M.; Lisgarten, N. D., The Cubic and Other Structural Forms of Ice at Low Temperature and Pressures. *Proc. R. Soc. Lond. A* **1957,** *239*, 93-107.

33. Shilling, J. E.; Tolbert, M. A.; Toon, O. B.; Jenson, E. J.; Murray, B. J.; Bertram, A. K., Measurements of the Vapour Pressure of Cubic Ice and Their Implications for Atmospheric Clouds. *Geophys. Res. Lett.* **2006,** *33*, L17801.

34. Shallcross, F. V.; Carpenter, G. B., X-Ray Diffraction Study of the Cubic Phase of Ice. *J. Chem. Phys.* **1957,** *26*, 782-784.

35. Kuhs, W. F.; Sippel, C.; Falentya, A.; Hansen, T. C., Extent and Relevance of Stacking Disorder in “Ice Ic”. *Proc. Natl. Acad. Sci. U.S.A* **2012,** *109*, 21259-21264.

36. Kuhs, W. F.; Bliss, D. V.; Finney, J. L., High-Resolution Neutron Powder Diffraction Study of Ice I_c. *J. Phys. Colloq., C1* **1987,** *48*, 631-636.

37. Malkin, T. L.; Murray, B. J.; Brukhno, A. V.; J., A.; Salzmann, C. G., Structure of Ice Crystallized from Supercooled Water. *Proc. Natl. Acad. Sci. USA* **2012,** *109*, 1041-1045.

38. Silonov, V. M.; Chubrov, V. V., Diffuse X-Ray Scattering by Ice in the Vicinity of the Melting Point. *Moscow Univ. Chem. Bull.* **2011,** *66* (4), 369-374.

39. Hansen, T. C.; Koza, M. M.; Kuhs, W. F., Formation and Annealing of Cubic Ice: I. Modelling of Stacking Faults *J. Phys.: Condens. Matter* **2008,** *20*, 285104.

40. Loveday, J. S.; Nelmes, R. J., High-Pressure Gas Hydrates. *Phys. Chem. Chem. Phys.* **2008,** *10*, 937-950.

41. Kuo, J.-L.; Ciobanu, C. V.; Ojamäe, L.; Shavitt, I.; Singer, S. J., Short H-Bonds and Spontaneous Self-Dissociation in Effects of H-Bond Topology *J. Chem. Phys.* **2003,** *118* (8), 3583-3588.

42. Henchman, R. H.; Cockramb, S. J., Water's Non-Tetrahedral Side. *Faraday Discuss.* **2013,** *167*, 529-550.

43. Bullocka, G.; Molinero, V., Low-Density Liquid Water Is the Mother of Ice: On the Relation between Mesostructure, Thermodynamics and Ice Crystallization in Solutions *Faraday Discuss.* **2013,** *167*, 371-388.

44. Stanley, H. E.; Angell, C. A.; Essmann, U.; Hemmati, M.; Poole, P. H.; Sciortino, F., Is There a Second Critical Point in Liquid Water? *Physica A* **1994,** *205*, 1.

45. Stanley, H. E.; Buldyrev, S. V.; Canpolat, M.; Mishima, O.; Sadr-Lahijany, M. R.; Scalaa, A.; Starra, F. W., The Puzzling Behavior of Water at Very Low Temperatures. *Phys. Chem. Chem. Phys.* **2000,** *2*, 1551-1558.

46. Mishima, O.; Suzuki, Y., Propagation of the Polyamorphic Transition of Ice and the Liquid-Liquid Critical Point. *Nature* **2002,** *419*, 599-603.

47. Poole, P. H.; Sciortino, F.; Essmann, U.; Stanley, H. E., Phase Behavior of Supercooled Water. *Nature* **1992,** *360*, 324-328.

48. Holten, V.; Bertrand, C. E.; Anisimov, M. A.; Sengers, J. V., Thermodynamics of Supercooled Water. *J. Chem. Phys.* **2012,** *136*, 094507.

49. Poole, P. H.; Sciortino, F.; Grande, T.; Stanley, H. E.; Angell, C. A., Effect of Hydrogen Bonds on the Thermodynamic Behavour of Liquid Water. *Phys. Rev. Lett.* **1994,** *73* (12), 1632.

50. Speedy, R., Evidence for a New Phase of Water: Water II. *J. Phys. Chem.* **1992,** *96*, 2322-2325.

51. Tanaka, H., Phase Behaviors of Supercooled Water: Reconciling a Critical Point of Amorphous Ices with Spinodal Instability *J. Chem. Phys.* **1996,** *105*, 5099

52. Poole, P. H.; Sciortino, F.; Essmann, U.; Stanley, H. E., Spinodal of Liquid Water. *Phys. Rev. E* **1993,** *48* (5), 3799-3817.

53. Murata, K. i.; Tanaka, H., Liquid–Liquid Transition without Macroscopic Phase Separation in a Water–Glycerol Mixture. *Nat. Mater.* **2012,** *11*, 436-443.

54. Soper, A. K., Structural Transformations in Amorphous Ice and Supercooled Water and Their Relevance to the Phase Diagram of Water. *Mol. Phys.* **2008,** *106*, 2053-2076.

55. Nelmes, R. J.; Loveday, J. S.; Strässle, T.; Bull, C. L.; Guthrie, M.; Hamel, G.; Klotz, S., Annealed High-Density Amorphous Ice under Pressure. *Nature Physics* **2006,** *2*, 414-418.

56. Koop, T.; Luo, B.; Tsias, A.; Peter, T., Water Activity as the Determinant for Homogeneous Ice Nucleation in Aqueous Solutions. *Nature* **2000,** *406*, 611-614.

57. Mayer, E.; Brüggeller, P., Vitrification of Pure Liquid Water by High-Pressure Jet-Freezing. *Nature* **1982,** *298*, 715-718.

58. Mayer, E., New Method for Vitrifying Water and Other Liquids by Rapid Cooling of Their Aerosols. *J. Appl. Phys.* **1985,** *58*, 663-667.

59. Burton, E. F.; Oliver, W. F., X-Ray Diffraction Patterns of Ice. *Nature* **1935,** *135*, 505-506.

60. Mayer, E.; Pletzer, R., Polymorphism in Vapor Deposited Amorphous Solid Water. *J. Chem. Phys.* **1984,** *80*, 2939-2952.

61. Sceats, M. G.; Rice, S. A., Amorphous Solid Water and Its Relationship to Liquid Water: A Random Network Model for Water. In *Water, a Comprehensive Treatise*, Franks, F., Ed. Plenum Press: New York, 1982; Vol. 7, pp 83-214.

62. Mishima, O.; Calvert, L. D.; Whalley, E., 'Melting Ice' I at 77 K and 10 Kbar: A New Method of Making Amorphous Solids. *Nature* **1984,** *310*, 393-395.

63. Mishima, O.; Calvert, L. D.; Whalley, E., An Apparently First-Order Transition between Two Amorphous Phases of Ice Induced by Pressure. *Nature* **1985,** *314*, 76-78.

64. Mishima, O., Relationship between Melting and Amorphization of Ice. *Nature Lett.* **1996,** *384*, 546-549.

65. Mishima, O., Liquid-Liquid Critical Point in Heavy Water. *Phys. Rev. Let.* **2000,** *85* (2), 334 - 336.

66. Amann-Winkel, K.; Gainaru, C.; Handle, P. H.; Seidl, M.; Nelson, H.; Böhmer, R.; Loerting, T., Water's Second Glass Transition. *Proc. Natl. Acad. Sci. U.S.A* **2013,** *110*, 17720–17725.

67. Strässle, T.; Klotz, S.; Hamel, G.; Koza, M. M.; Schober, H., Experimental Evidence for a Crossover between Two Distinct Mechanisms of Amorphization in Ice under Pressure *Phys. Rev. Lett.* **2007,** *99*, 175501.

68. Klug, D. D.; Tulk, C. A.; Svensson, E. C.; Loong, C. K., Dynamics and Structural Details of Amorphous Phases of Ice Determined by Incoherent Inelastic Neutron-Scattering. *Phys. Rev. Lett.* **1999,** *83*, 2584-2587.

69. Smith, R. S.; Petrik, N. G.; Kimmel, G. A.; Kay, B. D., Thermal and Nonthermal Proccesses in Nanoscale Films of Amorphous Solid Water. *Acc. Chem. Res.* **2012,** *45*, 33-42.

70. Smith, R. S.; Zubkov, T.; Dohnalek, Z.; Kay, B. D., The Effect of the Incident Collision Energy on the Porosity of Vapor-Deposited Amorphous Solid Water Films. *J. Phys. Chem. B* **2009,** *113* (13), 4000-4007.

71. Johari, G. P., Phase Transitions and Entropy of Amorphous Ice. *J. Chem. Phys.* **1995,** *102*, 6224.

72. Johari, G. P., An Estimate for the Gibbs Energy of Amorphous Solid Waters and Differences between the Low-Density Amorph and Glassy Water. *J. Chem. Phys.* **2000,** *112*, 8573-8580.

73. Johari, G. P.; Andersson, O., Vibrational and Relaxational Properties of Crystalline and Amorphous Ices. *Thermochim. Acta* **2007,** *461*, 14-43.

74. Loerting, T.; Winkel, K.; Seidl, M.; Bauer, M.; Mitterdorfer, C.; Handle, P. H.; Salzmann, C. G.; Mayer, E.; Finney, J. L.; Bowron, D. T., How Many Amorphous Ices Are There? *Phys. Chem. Chem. Phys.* **2011,** *13*, 8783-8794.

75. Elliot, S. R., *Physics of Amorphous Solids* second ed.; Longman Scientific and Technical: New York, 1990; p 30-34.

76. Angell, A.; Ngai, K. L.; Mcmillan, P. F.; Martin, S. W., Relaxation in Glassforming Liquids and Amorphous Solids. *J. Appl. Phys.* **2000,** *88*, 3113-3157.

77. Angell, C. A., Insights into Phases of Liquid Water from Study of Its Unusual Glass-Forming Properties. *Science* **2008,** *319*, 582-587.

78. Mishima, O.; Stanley, H. E., The Relationship between Liquid, Supercooled and Glassy Water. *Nature* **1998,** *396*, 329-335.

79. Burke, D. J.; Brown, W., Ice in Space: Surface Science Investigations of the Thermal Desorption

of Model Interstellar Ices on Dust Grain Analogue Surfaces. *Phys. Chem. Chem. Phys.* **2010,** *12*, 5947–5969.

80. Hagen, W.; Tielens, A. G. G. M.; Greenberg, J. M., The Infrared Spectra of Amorphous Solid Water and Ice Ic between 10 and 140 K. *J. Chem. Phys.* **1981,** *56* (3), 367-79.

81. Mayer, E.; Pletzer, R., Astrophysical Implications of Amorphous Ice-a Microporous Solid. *Nature* **1986,** *319*, 298-301.

82. Tielens, A. G. G. M.; Hagen, W.; Greenberg, J. M., Interstellar Ice. *J. Phys. Chem.* **1983,** *87* (21), 4220-9.

83. Sunshine, J. M.; Groussin, O.; Schultz, P. H.; A'Hearn, M. F.; Feaga, L. M.; Farnham, T. L.; Klaasen, K. P., The Distribution of Water Ice in the Interior of Comet Tempel 1. *Icarus* **2007,** *190*, 284–294.

84. Feaga, L. M.; A'Hearn, M. F.; Farnham, T. L.; Bodewits, D.; Sunshine, J. M.; Gersch, A. M.; Protopapa, S.; BinYang; Drahus, M.; Schleicher, D. G., Uncorrelated Volatile Behavour During the 2011 Apparation of Comet C/2009 P1 Garrardd. *Astron. J.* **2014** *147* (1), ID 24.

85. Johari, G. P.; Hallbrucker, A.; Mayer, E., The Glass-Liquid Transition of Hyperquenched Water. *Nature* **1987,** *330*, 552-553.

86. Hallbrucker, A.; Mayer, E.; Johari, G. P., The Heat Capacity and Glass Transition of Hyperquenched Glassy Water. *Phil. Mag. B* **1989,** *60*, 179-187.

87. Hallbrucker, A.; Mayer, E.; Johari, G. P., Glass-Liquid Transition and the Enthalpy of Devitrification of Annealed Vapor-Deposited Amorphous Solid Water: A Comparison with Hyperquenched Glassy Water. *J. Phys. Chem.* **1989,** *93*, 4986-4990.

88. Löw, F.; Amann-Winkel, K.; Loerting, T.; Fujara, F.; Geil, B., Ultra-Slow Dynamics in Low Density Amorphous Ice Revealed by Deuteron Nmr: Indication of a Glass Transition. *Phys. Chem. Chem. Phys.* **2013,** *15*, 9308-9314.

89. Cukierman, S. l., Grotthuss! And Other Unfinished Stories. *Biochim. Biophys. Acta Bioenerg.* **2006,** *1757* (8), 876-885.

90. Lobban, C.; Finney, J. L.; Kuhs, W. F., The Structure and Ordering of Ices III and V. *J. Chem. Phys.* **2000,** *112*, 7169-7180.

91. Bjerrum, N., Structure and Properties of Ice. *Science* **1952,** *115* (2989), 385-390.

92. Salzmann, C. G.; Radaelli, P. G.; Finney, J. L.; Mayer, E., A Calorimetric Study on the Low Temperature Dynamics of Doped Ice V and Its Reversible Phase Transition to Hydrogen Ordered Ice XIII. *Phys. Chem. Chem. Phys.* **2008,** *10*, 6313-6324.

93. Struebing, H.; Ganase, Z.; Karamertzanis, P. G.; Siougkrou, E.; Haycock, P.; Piccione, P. M.; Armstrong, A.; Galindo, A.; Adjiman, C. S., Computer-Aided Molecular Design of Solvents for Accelerated Reaction Kinetics. *Nat. Chem.* **2013,** *5*, 952.

94. Murrell, J. N.; Jenkins, A. D., *Properties of Liquids and Solutions*. 2nd ed.; Wiley: New York, 1982; p 140-146.

95. DuPont http://www2.dupont.com/Vertrel/en_US/. (accessed 3.4.2014).

96. Busato, G. A.; Bashein, G., The Halothane/Ether Azeotrope - a Reconsideration. *Update Anaesth.* **2004,** *18*, 36-38.

97. Apelblat, A.; Tamir, A.; Wagner, M., Thermodynamics of Acetone-Chloroform Mixtures. *Fluid Phase Eq.* **1980,** *4*, 229-255.

98. Scatchard, G.; Wood, S. E.; Mochel, J. M., Vapour-Liquid Equilibrium. VI Benzene-Methanol Mixtures. *J. Am. Chem. Soc.* **1946,** *68* (10), 1957-1960.

99. Miyano, Y.; Hayduk, W., Solubilities of Butane, Vapor Pressures, and Densities for Benzene + Cyclohexane, Benzene + Methanol, and Methanol + Cyclohexane Solutions at 298 K. *J. Chem. Eng. Data* **1993,** *38* (2), 277-381.

100. Butcher, K. L.; Medani, M. S., Thermodynamic Properties of Methanol–Benzene Mixtures at Elevated Temperatures. *J. Appl. Chem.* **1968,** *18*, 100-107.

101. Campbell, A. N.; Kartzmark, E. M.; Feisen, H., The Equilibrium Diagrams, Heats of Mixing, Dipole Moments, Densities, and Boiling Points of the System Acetone-Chloroform-Benzene. *Can. J. Chem.* **1961,** *39*, 735-744.

102. Zawidzki, V., Uber Die Dampfdrucke Binarer Flussigkeitsgemische. *Z. Phys. Chem.* **1900,** *35*, 129.

103. Jalilian, M. R.; Alibabaei, L., Spectra and Structure of Binary Azeotropes I. Acetone-Chloroform. *Spectrochim. Acta Mol.* **2005,** *62*, 322-325.

104. Jalilian, M. R.; Tayyari, S. F., Spectra and Structure of Binary Azeotropes VI. Benzene-Methanol. *Spectrochim. Acta Mol.* **2009,** *73*, 828-832.

105. McLain, S.; Soper, A. K.; Luzar, A., Orientational Correlations in Liquid Acetone and Dimethyl Sulfoxide: A Comparative Study. *J. Chem. Phys.* **2006,** *124*, 074502.

106. Soper, A. K.; Andreani, C.; Nardone, M., Reconstruction of the Orientational Pair-Correlation Function from Neutron-Diffraction Data: The Case of Liquid Hydrogen Iodide. *Phys. Rev. E* **1993,** *47* (4), 2598-2605.

107. Allen, M. P.; Tildesley, D. J., *Computer Simulation of Liquids*. Oxford University Press: Oxford, 1987; p 110-135.

108. Elliot, S. R., *Physics of Amorphous Solids* second edition ed.; Longman Scientific and Technical: New York, 1990; p 151-169.

109. Bondi, A., Van Der Waals Volumes and Radii. *J. Phys. Chem.* **1964,** *68* (3), 441.

110. Alvarez, S., A Cartography of Van Der Waals Territories. *Dalton. Trans.* **2013,** *42*, 8617-8636.

111. Barlette, V. E.; Garbujo, F. L. L.; Freitas, L. C. G., Monte Carlo Study of Structural and Thermodynamic Properties of Liquid Chloroform Using a Five Site Model. *Mol. Eng.* **1997,** *7*, 439-455.

112. Pimentel, G. C.; McCellan, A. L., *The Hydrogen Bond*. W. H. Freeman and Company: San Francisco, 1971.

113. Murrell, J. N.; Jenkins, A. D., *Properties of Liquids and Solutions*. 2nd ed.; Wiley: New York, 1982; p 161-169.

114. Keen, D. A., A Comparison of Various Commonly Used Correlation Functions for Describing Total Scattering. *J. Appl. Cryst.* **2001,** *34*, 172-177.

115. Silva, D. S., *Elementary Scattering Theory for X-Ray and Neutron Users*. Oxford Univeristy Press: Oxford, 2011.

116. Pynn, R. The Mathamatical Foundations of Neutron Scattering. https://www.fas.org/sgp/othergov/doe/lanl/pubs/00326652.pdf (accessed 1/4/2014).

117. Fischer, H. E.; Barnes, A. C.; Salmon, P. S., Neutron and X-Ray Studies of Liquids and Glasses. *Rep. Prog. Phys.* **2006,** *69*, 233-299.

118. Sears, V. F., Neutron Scattering Lengths and Cross Sections. *Neutron News* **1992,** *3* (3), 26-37.

119. Yamaguchi, T.; Hidaka, K.; Soper, A. K., The Structure of Liquid Methanol Revisited: A Neutron Diffraction Experiment at -80 C and +25 C. *Mol. Phys.* **1999,** *96* (8).

120. Kameda, Y.; Sasaki, M.; Usuki, T.; Otomo, T.; Itoh, K.; Suzuya, K.; Fukunaga, T., Inelasticity Effect on Neutron Scattering Intensities of the Null-H_2O. *J. Neut. Res.* **2003,** *11* (3), 153-163.

121. van Hook, W. A., Condensed Matter Isotope Effects. In *Isotope Effects in Chemisty and Biology*, Kohen, A.; Limbach, H. H., Eds. Taylor and Francis: Florida, 2006; pp 119-152.

122. Soper, A. K., Recent Advances in Structure Refinement for Liquids and Disordered Materials. In *Local Structure from Diffraction*, Billinge, S. J.; Thorpe, M. F., Eds. Plenum Press: New York, 1998.

123. Soper, A. K., Inelasticity Corrections for Time-of-Flight and Fixed Wavelength Neutron Diffraction Experiements. *Mol. Phys.* **2009,** *107*, 1667-1684.

124. Soper, A. K., Orientational Correlation Function for Molecular Liquids: The Case of Liquid Water. *J. Chem. Phys.* **1994,** *101* (8), 6888-6901.

125. Bowron, D. T.; Finney, J. L.; Soper, A. K., The Structure of Liquid Tetrahydrofuran. *J. Am. Chem. Soc.* **2006,** *128*, 5119-5126.

126. Soper, A. K.; Luzar, A., A Neutron Diffraction Study of Dimethyl Sulphoxide-Water Mixtures. *J. Chem. Phys.* **1992,** *97*, 1320.

127. Botti, A.; Bruni, F.; Imberti, S.; Ricci, M. A.; Soper, A. K., Ions in Water: The Microscopic Structure of Concentrated Sodium Hydroxide Solutions. *J. Chem. Phys.* **2004,** *120* (21), 10154-10162.

128. Imberti, S.; Botti, A.; Bruni, F.; Cappa, G.; Ricci, M. A.; Soper, A. K., Ions in Water: The Microscopic Structure of Concentrated Hydroxide Solutions *J. Chem. Phys.* **2005,** *122* (19), 194509.

129. Burton, R. C.; Ferrari, E. S.; Davey, R. J.; Finney, J. L.; Bowron, D. T., The Relationship between Solution Structure and Crystal Nucleation: A Neutron Scattering Study of Supersaturated Methanolic Solutions of Benzoic Acid. *J. Phys. Chem. B* **2010,** *114*, 8807-8816.

130. Soper, A. K., Tests of the Empirical Potential Structure Refinement Method and a New Method of Application to Neutron Diffraction Data on Water. *Mol. Phys.* **2001,** *99* (17), 1503-1516.

131. Soper, A. K., On the Uniqueness of Structure Extracted from Diffraction Experiments on Liquids and Glasses. *J. Phys.: Condens. Matter* **2007,** *19* (41), 415108.

132. OerlikonLeybold www.oelikon.com (accessed 2.1.2014).

133. Mathews, C. K.; Baba, M. S.; Narasimhan, T. S. L.; Balasubramanian, R.; Sivaraman, N.; Srinivasan, T. G.; Rao, P. R. V., Vaporization Studies on Buckminsterfullerene. *J. Phys. Chem.* **1992,** *96* (9), 3566-8.

134. Kroeger, F. R.; Swenson, C. A., Absolute Linear Thermal-Expansion Measurements on Copper and Aluminum from 5 to 320 K. *J. Appl. Phys.* **1977,** *48* (3), 853-64.

135. Wang, K.; Reeber, R. R., The Perfect Crystal, Thermal Vacancies and the Thermal Expansion Coefficient of Aluminium. *Philos. Mag. A* **2000,** *80* (7), 1629-1643.

136. Loerting, T.; Salzmann, C.; Kohl, I.; Mayer, E.; Hallbrucker, A., A Second Distinct Structural "State" of High-Density Amorphous Ice at 77 K and 1 Bar. *Phys. Chem. Chem. Phys.* **2001,** *3*, 5355-5357.

137. Giovambattista, N.; Stanley, H. E.; Sciortino, F., Phase Diagram of Amorphous Solid Water: Low-Density, High-Density, and Very-High-Density Amorphous Ices *Phys. Rev. E* **2005,** *72*, 031510.

138. Salzmann, C. G.; Mayer, E.; Hallbrucker, A., Effect of Heating Rate and Pressure on the Crystallization Kinetics of High-Density Amorphous Ice on Isobaric Heating between 0.2 and 1.9 GPa. *Phys. Chem. Chem. Phys.* **2004,** *6* (22), 5156-5165.

139. Salzmann, C. G.; Loerting, T.; Klotz, S.; Mirwald, P. W.; Hallbrucker, A.; Mayer, E., Isobaric Annealing of High-Density Amorphous Ice between 0.3 and 1.9 GPa: In Situ Density Values and Structural Changes. *Phys. Chem. Chem. Phys.* **2006,** *8*, 386-397.

140. Handa, Y. P.; Mishima, O.; Whalley, E., High-Density Amorphous Ice. III. Thermal Properties. *J. Chem. Phys.* **1986,** *84*, 2766-2770.

141. Winkel, K.; Mayer, E.; Loerting, T., Equilibrated High-Density Amorphous Ice and Its First-Order Transition to the Low-Density Form. *J. Chem. Phys. B* **2011,** *115*, 14141-14148.

142. Urquidi, J.; Benmore, C. J.; Neuefeind, J.; Tomberli, B.; Tulk, C. A.; Guthrie, M.; Egelstaff, P. A.; Klug, D. D., Isotopic Quantum Effects on the Structure of Low Density Amorphous Ice *J. Phys.: Condens. Matter* **2003,** *15*, 3657-3664.

143. Burton, E. F.; Oliver, W. F., The Crystal Structure of Ice at Low Temperatures. *Proc. R. Soc. London, Ser. A* **1935,** *153*, 166-172.

144. Handa, Y. P.; Klug, D. D., Heat Capacity and Glass Transition Behavior of Amorphous Ice. *J. Phys. Chem.* **1988,** *92*, 3323-3325.

145. Johari, G. P., Liquid State of Low-Density Pressure-Amorphized Ice above Its T_g. *J. Phys. Chem. B* **1998,** *102*, 4711-4714.

146. Smith, R. S.; Kay, B. D., The Existence of Supercooled Liquid Water at 150 K. *Nature* **1999,** *398*, 788-791.

147. Seidl, M.; Elsaesser, M. S.; Winkel, K.; Zifferer, G.; Mayer, E.; Loerting, T., Volumetric Study Consistent with a Glass-to-Liquid Transition in Amorphous Ices under Pressure. *Phys. Rev. B* **2011,** *83*, 100201.

148. Velikov, V.; Borick, S.; Angell, C. A., The Glass Transition of Water, Based on Hyperquenching Experiments. *Science* **2001,** *294*, 2335-2338.

149. Yue, Y.; Angell, C. A., Clarifying the Glass-Transition Behaviour of Water by Comparison with Hyperquenched Inorganic Glasses. *Nature* **2004,** *427*, 717-720.

150. Swallen, S. F., Organic Glasses with Exceptional Thermodynamic and Kinetic Stability. *Science* **2007,** *315*, 353-356.

151. Singh, S.; Ediger, M. D.; Pablo, J. J. d., Ultrastable Glasses from *in Silico* Vapour Deposition. *Nat. Mater.* **2013,** *12*, 139-144.

152. Angell, C. A., Amorphous Water. *Annu. Rev. Phys. Chem.* **2004,** *55*, 555-583.

153. Hallbrucker, A.; Mayer, E., Unexpectedly Stable Nitrogen, Oxygen, Carbon Monoxide and Argon Clathrate Hydrates from Vapour-Deposited Amorphous Solid Water: An X-Ray and Two-Step Differential Scanning Calorimetry Study. *J. Chem. Soc. Faraday Trans.* **1990,** *86*, 3785.

154. Bowron, D. T.; Finney, J. L.; Hallbrucker, A.; Kohl, I.; Loerting, T.; Soper, A. K., The Local and Intermediate Range Structures of the Five Amorphous Ices at

80 K and Ambient Pressure: A Faber-Ziman and Bhatia-Thornton Analysis. *J. Chem. Phys.* **2006,** *125*, 194502.

155. Stevenson, K. P.; Kimmel, G. A.; Dohnalek, Z.; Smith, R. S.; Kay, B. D., Controlling the Morphology of Amorphous Solid Water. *Science (Washington, D. C.)* **1999,** *283* (5407), 1505-1507.

156. Dowell, L. G.; Rinfret, A. P., Low-Temperature Forms of Ice as Studied by X-Ray Diffraction. *Nature* **1960,** *188*, 1144-8.

157. Narten, A. H.; Venkatesh, C. G.; Rice, S. A., Diffraction Pattern and Stucture of Amorphous Solid Water at 10 and 77 K. *J. Chem. Phys.* **1976,** *64*, 1106-1121.

158. Jenniskens, P.; Blake, D. F., Structural Transitions in Amorphous Water Ice and Astrophysical Implications. *Science* **1994,** *265* (5173), 753-556.

159. Laffon, C.; Lacombe, S.; Bournel, F., Radiation Effects in Water Ice: A near Edge X-Ray Absorption Fine Structure Study. *J. Chem. Phys.* **2006,** *125*, 204714.

160. Guillot, B.; Guissani, Y., Investigation of Vapor-Deposited Amorphous Ice and Irradiated Ice by Molecular Dynamics Simulation. *J. Chem. Phys.* **2004,** *120* (9), 4366-4382.

161. Kimmel, G. A.; Dohnalek, Z.; Stevenson, K. P.; Smith, R. S.; Kay, B. D., Control of Amorphous Solid Water Morphology Using Molecular Beams. 1. Experimental Results. *J. Chem. Phys.* **2001,** *114* (12), 5284-5294.

162. Raut, U.; Famá, M.; Teolis, B. D.; Baragiol, R. A., Characterization of Porosity in Vapor-Deposited Amorphous Solid Water from Methane Adsorption. *J. Chem. Phys.* **2007,** *127*, 204713.

163. Tomlinson-Phillips, J.; Davis, J.; Ben-Amotz, D., Structure and Dynamics of Water Dangling Oh Bonds in Hydrophobic Hydration Shells. Comparison of Simulation and Experiment. *J. Phys. Chem. A,* **2011,** *115* (23), 6177–6183.

164. Rowland, B.; Fisher, M.; Devlin, J. P., Probing Icy Surfaces with the Dangling-OH-Mode Absorption: Large Ice Clusters and Microporous Amorphous Ice. *J. Chem. Phys.* **1991,** *95* (2), 1378-1384.

165. Cholette, F.; Zubkov, T.; Smith, R. S.; Dohnalek, Z.; Kay, B. D.; Ayotte, P., Infrared Spectrscopy and Optical Constants of Porous Amorphous Solid Water. *J. Phys. Chem. B* **2009,** *113*, 4131-4140.

166. Brown, D. E.; George, S. M.; Huang, C.; Wong, E. K. L.; Rider, K. B.; Smith, R. S.; Kay, B. D., Water Vapour Condensation Coefficient and Refractive Index for Vapour-Deposited Ice from Molecular Beam and Optical Interference Measurements. *J. Phys. Chem.* **1996,** *100*, 4988-4995.

167. Dohnalek, Z.; Kimmel, G. A.; Ayotte, P.; Smith, R. S.; Kay, B. D., The Deposition Angle-Dependent Density of Amorphous Solid Water Films. *J. Chem. Phys.* **2003,** *118* (1), 364-372.

168. Ghormley, J. A., Thermal Behavour of Amorphous Ice. *J. Chem. Phys.* **1956,** *25*, 599-599.

169. Pershin, S. M.; Bunkin, A. F.; Luk'yanchenko, V. A., Evolution of the Spectral Component of Ice in the OH Band of Water at Temperatures from 13 to 99°C. *Quantum Electron.* **2010,** *40* (12), 1146-1148.

170. Smith, R. S.; Mathiesen, J.; Knox, J.; Kay, B. D., Crytallization Kinetics and Excess Free Energy of H_2O and D_2O Nanoscale Films of Amorphous Solid Water. *J. Phys. Chem. A* **2011,** *115*, 5908-5917.

171. edwardsvacuum www.edwardsvacuum.com (accessed 2.1.2014).

172. Lide, R., *Crc Handbook of Chemistry and Physics*. 77th ed.; CRC press: Boca Raton, 1996; p **4-**123.

173. White, G. K.; Collocott, S. J., Heat Capacity of Reference Materials. *J. Phys. Chem. Ref. Data* **1984,** *13* (4), 1251-1257.

174. Lide, R., *Crc Handbook of Chemistry and Physics*. 77th ed.; CRC press: Boca Raton, 1996; p **12-**172.

175. Vorob'ev, V. S.; Eletskii, A. V., Similarity Laws and Thermodynamic Quantities for Fullerite C_{60}. *Chem. Phys. Lett.* **1996,** *254*, 263-267.

176. Piacente, V.; Gigli, G.; Scardala, P.; Giustini, A.; Ferro, D., Vapor Pressure of C_{60} Buckminsterfullerene. *J. Phys. Chem.* **1995,** *99* (38), 14052-14057.

177. Abrefah, J.; Olander, D. R.; Balooch, M.; Siekhaus, W. J., Vapor Pressure of Buckminsterfullerene. *J. Appl. Phys.* **2002,** *60* (11), 1313-1314.

178. Korobov, M. V.; Sidov, L. N., Thermodynamic Properties of Fullerenes. *J. Chem. Thermodyn.* **1994,** *26*, 61-73.

179. Chen, H. S.; kortan, A. R.; Haddon, R. C.; Fleming, D. A., Thermodynamics of Fullerene (C_{60}) in Pure Oxygen, Nitrogen and Argon. *J. Phys. Chem.* **1992,** *96*, 1016-1018.

180. Nisha, J. A.; Sridharan, V.; Janaki, J.; Hariharan, Y.; Sastry, V. S.; Sundar, C. S.; Radhakrishnan, T. S., Studies of C_{60} Oxidation and Products. *J. Chem. Phys.* **1996,** *100*, 4503-4506.

181. Gao, M.; Zhang, H., Preparation of an Amorphous Fullerene Film. *Phys. Lett. A* **1996,** *213*, 203-206.

182. Millar, J. M.; Creegan, K. M.; Robbins, J. L.; Robbins, W. K.; Sherwood, R. D.; Tindall, P. J.; Cox, D. M., Chromatographic Separations of Fullerenes: Discovery and Characterization of C_{60} Mono-Epoxide. *Synt. Met.* **1993,** *59* (3), 317–331.

183. Sanna, T. G., *Introduction to Molecular Beams Gas Dynamics*. Imperial College Press: London, 2005.

184. Pfeiffer http://www.mpi-hd.mpg.de/gerda/TG04_TECHNICAL/manuals/bg805178be_d_web.pdf (accessed 14.4.2014).

185. Loerting, T.; Bauer, M.; Kohl, I.; Watschinger, K.; Winkel, K.; Mayer, E., Cryoflotation: Densities of Amorphous and Crystalline Ices. *J. Phys. Chem. B* **2011,** *115*, 14167-14175.

186. Kuhs, W. F.; Lehmann, M. S., The Structure of Ice-Ih. In *Science Reviews 2*, Franks, F., Ed. Cambridge University Press: 1986; Vol. 2, pp 1-65.

187. Bolina, A. S.; Wolff, A. J.; Brown, W. A., Reflection Absorption Infrared Spectroscopy and Temperature-Programmed Desorption Studies of the Adsorption and Desorption of Amorphous and Crystalline Water on a Graphite Surface. *J. Phys. Chem. B* **2005,** *109*, 16836-16845.

188. Kimmel, G. A.; Dohnalek, Z.; Stevenson, K. P.; Smith, R. S.; Kay, B. D., Control of Amorphous Solid Water Morphology Using Molecular Beams. 2. Ballistic Deposition Simulations. *J. Chem. Phys.* **2001,** *114* (12), 5295-5303.

189. Smith, R. S.; Huang, C.; Wong, E. K. L.; Kay, B. D., Desorption and Crystallization Kinetics in Nanoscale Thin Films of Amorphous Water Ice. *Surf. Sci. Lett* **1996,** *367* (1), 13-18.

190. Ayotte, P.; Smith, R. S.; Stevenson, K. P.; Dohnálek, Z.; Kimmel, G. A.; Kay, B. D., Effect of Porosity on the Adsorption, Desorption, Trapping, and Release of Volatile Gases by Amorphous Solid Water. *J. Geophys. Res.* **2001,** *106* (E12), 33387-33392.

191. May, R. A.; Smith, R. S.; Kay, B. D., The Molecular Volcano Revisited: Determination of Crack Propagation and Distribution During the Crystallization of Nanoscale Amorphous Solid Water Films. *J. Phys. Chem. Lett.* **2012,** *3* (3), 327-331.

192. Hornekaer, L.; Baurichter, A.; Petrunin, V. V.; Luntz, A. C.; Kay, B. D.; Al-Halabi, A., Influence of Surface Morphology on D_2 Desorption Kinetics from Amorphous Solid Water. *J. Chem. Phys.* **2005,** *122* (12), 124701.

193. Zubkov, T.; Smith, R. S.; Engstrom, T. R.; Kay, B. D., Adsorption, Desorption, and Diffusion of Nitrogen in a Model Nanoporous Material. 2. Diffusion Limited Kinetics in Amorphous Solid Water. *J. Chem. Phys.* **2007,** *127*, 184708.

194. Zubkov, T.; Smith, R. S.; Engstrom, T. R.; Kay, B. D., Adsorption, Desorption, and Diffusion of Nitrogen in a Model Nanoporous Material. 1. Surface Limited Desorption Kinetics in Amorphous Solid Water *J. Chem. Phys.* **2007,** *127*, 184707.

195. Smith, R. S.; Dohnálek, Z.; Kimmel, G. A.; Stevenson, K. P.; Kay, B. D., The Self-Diffusivity of Amorphous Solid Water near 150 K. *Chem. Phys.* **2000,** *258*, 291-305.

196. Steckelmacher, W., Knudsen Flow 75 Years On: The Current State of the Art for Flow of Rarefied Gases in Tubes and Systems *Rep. Prog. Phys.* **1986,** *49*, 1083-1107.

197. Milne, T. A.; Beachey, J. E.; Greene, F. T., Possible Errors in Vapour Composition Determinations Due to Dimer Formations in Noneffusive Expansions. *J. Chem. Phys.* **1972,** *57* (5), 2221-2222.

198. Debenedetti, P. G.; Stillinger, F. H., Supercooled Liquids and the Glass Transition. *Nature* **2001,** *410*, 259-267.

199. Malins, A.; Eggers, J.; Tanaka, H.; Royall, C. P., Lifetimes and Lengthscales of Structural Motifs in a Model Glassformer *Faraday Discuss.* **2013,** *167*, 405-423.

200. Tanaka, H., Bond Orientational Ordering in Liquids: Towards a Unified Description of Water-Like Anomalies, Liquid-Liquid Transition, Glass Transition, and Crystallization. *Eur. Phys. J. E* **2012,** *35*, 113.

201. Yuan, H.; Khatua, S.; Zijlstra, P.; Orrit, M., Individual Gold Nanorods Report on Dynamical Heterogeneity in Supercooled Glycerol. *Faraday Discuss* **2013,** *167*, 515-527.

202. Conde, M. M.; Vega, C.; Patrykiejew, A., The Thickness of a Liquid Layer on the Free Surface of Ice as Obtained from Computer Simulation. *J. Chem. Phys.* **2008,** *129*, 0149702 1-11.

203. Hohne, G. W. H., *Differential Scanning Calorimetry* Springer-Verlag: Heidelberg, 2010.

204. Amann-Winkel, K.; Löw, F.; Handle, P. H.; Knoll, W.; Peters, J.; Geil, B.; Fujara, F.; Loerting, T., Limits of Metastability in Amorphous Ices: The Neutron Scattering Debye-Waller Factor. *Phys. Chem. Chem. Phys.* **2013,** *14* (47), 16386.

205. Fisher, M.; Devlin, J. P., Defect Activity in Amorphous Ice from Isotopic Exchange Data: Insight into the Glass Transition. *J. Phys. Chem.* **1995,** *99* (29), 11584-90.

206. Salzmann, C. G.; Kohl, I.; Loerting, T.; Mayer, E.; Hallbrucker, A., The Low-Temperature Dynamics of Recovered Ice XII as Studied by Differential Scanning Calorimetry: A Comparision with Ice V. *Phys. Chem. Chem. Phys.* **2003,** *5*, 3507-3517.

207. Salzmann, C. G.; Mayer, E.; Hallbrucker, A., Thermal Properties of Metastable Ices IV and XII: Comparison, Isotope Effects and Relative Stabilities. *Phys. Chem. Chem. Phys.* **2004,** *6*, 1269-1276.

208. Brüggeller, P.; Mayer, E., Complete Vitrification in Pure Liquid Water and Dilute Aqueous Solutions. *Nature* **1980,** *288*, 569-571.

209. Tulk, C. A.; Klug, D. D.; Branderhorst, R.; Sharpe, P.; Ripmeester, J. A., Hydrogen Bonding in Glassy Liquid Water from Raman Spectroscopic Studies. *J. Chem. Phys.* **1998,** *109*, 8478-8484.

210. Andersson, O.; Inaba, A., Thermal Conductivity of Cystalline and Amorphous Ices and Its Implications on Amorphization and Glassy Water. *Phys. Chem. Chem. Phys.* **2005,** *7*, 1441-1449.

211. Winkel, K.; Bowron, D. T.; Loerting, T.; Mayer, E.; Finney, J. L., Relaxation Effects in Low Density Amorphous Ice: Two Distinct Structural States Observed by Neutron Diffraction. *J. Chem. Phys.* **2009,** *130*, 204502.

212. Winkel, K.; Elsaesser, M. S.; Mayer, E.; Loerting, T., Water Polyamorphism: Reversibility and (Dis)Continuity. *J. Chem. Phys.* **2008,** *128*, 044510.

213. Hage, W.; Hallbrucker, A.; Mayer, E.; Johari, G. P., Crystallization Kinetics of Water Below 150 K. *J. Chem. Phys.* **1994,** *100*, 2743-2747.

214. Gálvez, Ó.; Maté, B.; Herrero, V. J.; Escribano, R., Trapping and Adsorption of Carbon Dioxide in Amorphous Ice: A Fourier Transform Infrared Study. *Icarus* **2008,** *197* (2), 599-605.

215. Petrenko, V. F.; Whitworth, R. W., *Physics of Ice*. Oxford University Press: Oxford, 1999.

216. Palumbo, M. E.; Baratta, G. A.; Leto, G.; Strazzulla, G., H Bonds in Astrophysical Ices. *J. Mol. Struct.* **2010,** *972*, 64-67.

217. Safarik, D. J.; Mullins, C. B., The Nucleation Rate of Crystalline Ice in Amorphous Solid Water. *J. Chem. Phys.* **2004,** *121* (12), 6003-6010.

218. Elsaesser, M. S.; Winkel, K.; Mayer, E.; Loerting, T., Reversibility and Isotope Effect of the Calorimetric Glass Liquid Transition of Low-Density Amorphous Ice. *Phys. Chem. Chem. Phys.* **2010,** *12*, 708-712.

219. Andersson, O.; Suga, H., Thermal Conductivity of Amorphous Ices. *Phys. Rev. B* **2002,** *65*, 140201.

220. Li, J. C.; Jenniskens, P., Inelastic Neutron Scattering Study of High Density Amorphous Water Ice. *Planet. Space Sci.* **1997,** *45*, 469-473.

221. Tse, J. S.; Klug, D. D.; Tulk, C. A.; Swainson, I.; Svensson, E. C.; Loong, C.-K.; Shpakov, V.; Belosludov, V. R.; Belosludov, R. V.; Kawazoe, Y., The Mechanisms for Pressure-Induced Amorphization of Ice Ih. *Nature* **1999,** *400*, 647-649.

222. Schober, H.; Koza, M. M.; Tölle, A.; Masciovecchio, C.; Sette, F.; Fujara, F., Crystal-Like High Frequency Phonons in the Amorphous Phases of Solid Water. *Phys. Rev. Lett.* **2000,** *85*, 4100-4103.

223. Geil, B.; Koza, M. M.; Fujara, F.; Schober, H.; Natali, F., Absence of Fast Precursor Dynamics of Low-Density Amorphous Ice around Its Hypothetical Glass Transition Temperature. **2004,** *6*, 677-679.

224. Andersson, O., Dielectric Relaxation of Low-Density Amorphous Ice under Pressure. *Phys. Rev. Lett.* **2007,** *98*, 057602.

225. Tse, J. S.; Shaw, D. M.; Klug, D. D.; Patchkovskii, S.; Vanko, G.; Monaco, G.; Krisch, M., X-Ray Raman Spectroscopic Study of Water in the Condensed Phases. *Phys. Rev. Lett.* **2008,** *100*, 095502.

226. Murray, B. J.; Bertram, A. K., Inhibition of Solute Crystallisation in Aqueous H+, $HN4^{+}$, SO^{2-}, H_2O Droplets. *Phys. Chem. Chem. Phys.* **2008,** *10*, 3287–3301.

227. Servos, J. W., *Physical Chemistry from Ostwald to Pauling, the Making of a Science in America*. Princeton University Press: Princeton, 1990.

228. Whale, T. F.; Clark, S. J.; Finney, J. L.; Salzmann, C. G., DFT-Assisted Interpretation of the Raman Spectra of Hydrogen-Ordered Ice XV. *J. Raman Spectrosc.* **2013,** *44*, 290-298.

229. Whalley, E., A Detailed Assignment of the O-H Stretching Bands of Ice I. *Can. J. Chem.* **1977,** *55*, 3429-3441.

230. Bakker, H. J.; Skinner, J. L., Vibrational Spectroscopy as a Probe of Structure and Dynamics in Liquid Water. *Chem. Rev.* **2010,** *110*, 1498-1517.

231. Whalley, E.; Klug, D. D., Comment on TO-LO Splitting in Disordered Phases of Ice. *J. Chem. Phys.* **1979,** *71* (3), 1513-1513.

232. Nielson, G.; Rice, S. A., An Improved Analysis of the Hydroxyl Stretching Spectrum of Amorphous Solid Water. *J. Chem. Phys.* **1983,** *78* (8), 4824-7.

233. Sivakumar, T. C.; Schuh, D.; Sceats, M. G.; Rice, S. A., The 2500-4000 cm-1 Raman and Infrared Spectra of Low Density Amorphous Solid Water and of Polycrystalline Ice I. *Chem. Phys. Lett.* **1977,** *48*, 212.

234. Rice, S. A.; Bergren, M. S.; Belch, A. C.; Nielsen, G., A Theoretical Analysis of the Hydroxyl Stretching Spectra of Ice Ih, Liquid Water, and Amorphous Solid Water. *J. Phys. Chem.* **1983,** *87* (21), 4295-4308.

235. Sivakumar, T. C.; Rice, S. A.; Sceats, M. G., Raman Spectroscopic Studies of the OH Stretching Region of Low Density Amorphous Solid Water and of Polycrystalline Ice Ih *J. Chem. Phys.* **1978,** *69*, 3468.

236. Venkatesh, C. G.; Rice, S. A.; Bates, J. B., A Raman Spectral Study of Amorphous Solid Water *J. Chem. Phys.* **1975,** *63* (3), 1065-1071.

237. Minceva-Sukarova, B.; Sherman, W. F.; Wilkinson, G. R., The Raman Spectra of Ice (Ih, II, III, V, VI and IX) as Functions of Pressure and Temperature. *J. Phys. C* **1984,** *17*, 5833-5850.

238. Scherer, J. R.; Snyder, R. G., Raman Intensities of Single Crystal Ice *Ih*. *J. Chem. Phys.* **1977,** *67* (11), 4794-4811.

239. Li, F.; Skinner, J. L., Infrared and Raman Line Shapes for Ice Ih. II. H_2O and D_2O. *J. Chem. Phys.* **2010,** *133*, 244504.

240. Durman, R.; Favre, P.; Jayasooriya, U. A.; Kettle, S. F. A., Longitudinal Optical-Transverse Optical (L.O.-T.O)Splitting on Internal Modes in the Raman Spectra of Noncentric Crystals. *J. Cryst. Spectrosc.* **1987,** *17* (4), 431.

241. Klug, D. D.; Mishima, O.; Whalley, E., High-Density Amorphous Ice. 4. Raman Spectrum of the Uncoupled O-H and O-D Oscillators. *J. Chem. Phys.* **1987,** *86*, 5323-5328.

242. Kanno, H.; Tomikawa, K.; Mishima, O., Raman Spectra of Low- and High-Density Amorphous Ices. *Chem. Phys. Lett.* **1998,** *293*, 412-416.

243. Suzuki, Y.; Mishima, O., Raman Study of the Annealing Effect of Low-Density Glassy Waters. *J. Phys. Soc. Jpn.* **2003,** *72*, 3128-3131.

244. Gromnitskaya, E. L.; Stal'gorova, O. V.; Lyapin, A. G.; Brazhkin, V. V.; Tarutin, O., Elastic Properties of Deuterium Oxide Ices in Solid-State Amorphization and Transformations between Amorphous Phases. *J. Exp. Theor. Phys. Lett.* **2003,** *78* (8), 488-492.

245. Gromnitskaya, E. L.; Stal'gorova, O. V.; Brazhkin, V. V.; Lyapin, A. G., Ultrasonic Study of the Nonequilibrium Pressure-Temperature Diagram of Ice. *Phys. Rev. B* **2001,** *64*, 094205.

246. Gromnitskaya, E. L.; Lyapina, A. G.; Stalgorovaa, O. V.; Danilova, I. V.; Brazhkin, V. V., Ultrasonic Study of Solid Phase Amorphization and Polyamorphism in an H_2O–D_2O (1:1) Solid Solution. *J. Exp. Theor. Phys. Lett.* **2012,** *96*, 789-793.

247. Ma, X.; Wigington, B.; Bouchard, D., Fullerene C_{60}. Surface Energy and Interfacial Interactions in Aqueous Systems. *Langmuir* **2010,** *26* (14), 11886-11893.

248. Fortner, J. D.; Lyon, D. Y.; Sayes, C. M.; Boyd, A. M.; Falkner, J. C.; Hotze, E. M.; Alemany, L. B.; Tao, Y. J.; Guo, W.; Ausman, K. D.; Colvin, V. L.; Hughes, J. B., C_{60} in Water: Nanocrystal Formation and Microbial Response. *Environ. Sci. Technol.* **2005,** *43*, 4307-4316.

249. Rivelino, R.; de Mota, F., Band Gap and Density of States of the Hydrated C_{60} Fullerene System at Finite Temperature. *Nano Lett.* **2007,** *7* (6), 1526-1531.

250. Lambeth Jr., B. P.; Junghans, C.; Kremer, K.; Clementi, C.; Delle Site, L., On the Locality of Hydrogen Bond Networks at Hydrophobic Interfaces. *J. Chem. Phys.* **2010,** *133* (22), 221101.

251. Li, L.; Bedrov, D.; Smith, G. D., Water-Induced Interactions between Carbon Nanoparticles. *J. Phys. Chem. B* **2006,** *110* (21), 10509-10513.

252. Walther, J. H.; Jaffe, R. L.; Kotsalis, E. M.; Werder, T.; Halicioglu, T.; Koumoutsakos, P., Hydrophobic Hydration of C_{60} and Carbon Nanotubes in Water. *Carbon* **2004,** *42*, 1185-1194.

253. Weiss, D. R.; Raschke, T. M.; Levitt, M., How Hydrophobic Buckminsterfullerene Affects Surrounding Water Structure. *J. Phys. Chem. B* **2008,** *112* (10), 2981-2990.

254. Hotta, T.; Sasai, M., Fluctuating Hydration Structure around Nanometer-Size Hydrophobic Solutes 2. Caging and Drying around Single-Wall Carbon Nanotubes. *J. Phys. Chem. C* **2007,** *111* (7), 2861-2871.

255. Colherinhas, G.; Fonseca, T. L.; Fileti, E. E., Theoretical Analysis of the Hydration of C_{60} in Normal and Supercritical Conditions. *Carbon* **2010,** *49* (1), 187-192.

256. Souda, R., Interaction of Water with LiCl, LiBr, LiI in the Deeply Supercooled Region. *J. Chem. Phys.* **2007,** *127*, 214505.

257. Souda, R., Hydrophobic Hydration of Alkanes: Its Implication for the Property of Amorphous Solid Water. *J. Chem. Phys.* **2004,** *121* (18), 8676-8679.

258. Chazallon, B.; Oancea, A.; Capoen, B.; Focsa, C., Ice Mixtures Formed by Simultaneous Condensation of Formaldehyde and Water: An in Situ Study by Micro-Raman Scattering. *Phys. Chem. Chem. Phys.* **2008,** *10* (5), 702-712.

259. Dresselhaus, M. S.; Dresselhaus, G.; Eklund, P. C., *Science of Fullerenes and Carbon Nanotubes*. Acedemic Press: San Diego, 1996; p 60-66.

260. Catalan, J.; Saiz, J. L.; La, J. L.; Jagerovic, N.; Elguero, J., The Colours of C_{60} Solutions. *Angew. Chem. Int. Ed.* **1995,** *34* (1), 105-107.

261. Eletskii, A. V., Fullerenes in Solutions. *Phys. Usp.* **1998,** *41*, 1091-1114.

262. Hellwege, K. H., *Landolt-Bornstein, Numerical Data and Functional Relationships in Science and Technology*. Springer-Verlag: Heidelberg, 1974; Vol. 6: Molecular Constants.

263. Graziano, G.; Lee, B., Hydration of Aromatic Hydrocarbons. *J. Phys. Chem. B* **2001,** *105* (42), 10367-10372.

264. Englezos, P., Clathrate Hydrates. *Ind. Eng. Chem. Res.* **1993,** *32*, 1251-1274

265. Israelachvili, J., *Intermolecular and Surface Forces* 2nd ed.; Acedemic Press: San Diego, 1992; p 122-133.

266. Ball, P., Water as an Active Constituent in Cell Biology. *Chem. Rev.* **2008,** *108* (74), 74-108.

267. Galamba, N., Water's Structure around Hydrophobic Solutes and the Iceberg Model. *J. Phys. Chem. B* **2013,** *117*, 2153−2159.

268. Ashbaugh, H. S.; Paulaitis, M. E., Effect of Solute Size and Solute−Water Attractive Interactions on Hydration Water Structure around Hydrophobic Solutes. *J. Am. Chem. Soc.* **2001,** *123* (43), 10721–10728.

269. Southall, N. T.; Dill, K. A.; Haymet, A. D. J., A View of the Hydrophobic Effect. *J. Phys. Chem. B* **2002,** *106*, 521.

270. Chandler, D., Interfaces and the Driving Force of Hydrophobic Assembly. *Nature* **2005,** *437*, 640-647.

271. Lum, K.; Chandler, D.; Weeks, J. D., Hydrophobicity at Small and Large Length Scales. *J. Phys. Chem. B* **1999,** *103*, 4570.

272. Graziano, G., On the Size Dependence of Hydrophobic Hydration. *J. Chem. Soc. Faraday Trans.* **1998,** *94*, 3345.

273. Lee, B., Solvent Reorganization Contribution to the Transfer Thermodynamics of Small Nonpolar Molecules. *Biopolymers* **1991,** *31*, 993.

274. Hummer, G.; Garde, S.; Garcia, A. E.; Paulaitis, M. E.; Pratt, L. R., Hydrophobic Effects on a Molecular Scale. *J. Phys. Chem. B* **1998,** *102*, 10469.

275. Ashbaugh, H. S.; Truskett, T. M.; Debenedetti, P. G., A Simple Molecular Thermodynamic Theory of Hydrophobic Hydration. *J. Chem. Phys.* **2002,** *116*, 2907.

276. Ashbaugh, H. S.; Pratt, L. R., Colloquium: Scaled Particle Theory and the Length Scales of Hydrophobicity. *Rev. Mod. Phys.* **2006,** *78*, 159.

277. Ben-Amotz, D.; Underwood, R., Unraveling Water's Entropic Mysteries: A Unified View of Nonpolar, Polar, and Ionic Hydration. *Acc. Chem. Res.* **2008,** *41*, 957.

278. Titantah, J. T.; Karttunen, M., Long-Time Correlations and Hydrophobe-Modified Hydrogen-Bonding Dynamics in Hydrophobic Hydration. *J. Am. Chem. Soc.* **2012,** *134* (22), 9362-9368.

279. Bakulin, A. A.; Liang, C.; Jansen, T. l. C.; Wiersma, D. A.; Bakker, H. J.; Pshenichnikov, M. S., Hydrophobic Solvation: A 2D Infrared Spectroscopic Inquest. *Acc. Chem. Res.* **2009,** *42* (9), 1229–1238.

280. Meyer, E. E.; Rosenberg, K. J.; Israelachvili, J., Recent Progress in Understanding Hydrophobic Interactions. *Proc. Natl. Acad. Sci. U.S.A* **2006,** *103* (43), 15739-15746.

281. Kauzmann, W., Some Factors in the Interpretation of Protein Denaturation. *Adv. Protein Chem.* **1959,** *14*, 1-63.

282. Bowron, D. T.; Weigel, R.; Filipponi, A.; Roberts, M. A.; Finney, J. L., X-Ray Absorption Spectroscopy Investigations of the Hydrophobic Hydration of Krypton at High Pressure. *Mol. Phys.* **2001,** *99*, 761-765.

283. Buchanan, P.; Aldiwan, N.; Soper, A. K.; Creek, J. L.; Koh, C. A., Decreased Structure on Dissolving Methane in Water. *Chem. Phys. Lett.* **2005,** *415*, 89-93.

284. Bowron, D. T.; Soper, A. K.; Finney, J. L., Temperature Dependence of the Structure of a 0.06 Mole Fraction Tertiary Butanol-Water Solution. *J. Chem. Phys.* **2001,** *114* (14), 6203-6219.

285. Finney, J. L.; Bowron, D. T., Experimental Configurational Landscapes in Aqueous Solutions. *Phil. Trans. R. Soc. A* **2005,** *363*, 469-492.

286. Bowron, D. T.; Finney, J. L.; Soper, A. K., Structural Characteristics of a 0.23 Mole Fraction Aqueous Solution of Tetrahydrofuran at 20 °C. *J. Phys. Chem. B* **2006,** *110* (41), 20235-20245.

287. Burton, R. C.; Ferrari, E. S.; Davey, R. J.; Hopwood, J.; Quayle, M. J.; Finney, J. L.; Bowron, D. T., The Structure of a Super-Saturated Solution : A Neutron Scattering Study of Aqueous Urea. *Cryst. Growth Des.* **2008,** *8* (5), 1559–1565.

288. Bowron, D. T.; Finney, J. L., Association and Dissociation of an Aqueous Amphiphile at Elevated Temperatures. *J. Phys. Chem. B* **2007,** *111* (33), 9838–9852.

289. Finney, J. L.; Bowron, D. T.; Soper, A. K., The Structure of Aqueous Solutions of Tertiary Butanol. *J. Phys. Condens. Matter.* **2000,** *12*, 123.

290. Finney, J. L.; Bowron, D. T.; Daniel, R. M.; Timmins, P. A.; Roberts, M. A., Molecular and Mesoscale Structures in Hydrophobically Driven Aqueous Solutions. *Biophys. Chem.* **2003,** *105*, 391.

291. Wachter, W.; Buchner, R.; Hefter, G., Hydration of Tetraphenylphosphonium and Tetraphenylborate Ions by Dielectric Relaxation Spectroscopy. *J. Phys. Chem. B* **2006,** *110*, 5147.

292. Kaatze, U.; Gerke, H.; Pottel, R., Dielectric Relaxation in Aqueous Solutions of Urea and Some of Its Derivatives. *J. Phys. Chem.* **1986,** *90*, 5464.

293. Yoshida, K.; Ibuki, K.; Ueno, M., Pressure and Temperature Effects on ^{2}H Spin-Lattice Relaxation Times and ^{1}H Chemical Shifts in Tert-Butyl Alcohol- and Urea-D_2O Solutions. *J. Chem. Phys.* **1998,** *108*, 1360.

294. Ishihara, Y.; Okouchi, S.; Uedaira, H., Dynamics of Hydration of Alcohols and Diols in Aqueous Solutions. *J. Chem. Soc. Faraday Trans.* **1997,** *93*, 3337.

295. Shoichi Okouchi; Moto, T.; Ishihara, Y.; Numajiri, H.; Uedaira, H., Hydration of Amines, Diamines, Polyamines and Amides Studied by NMR. *J. Chem. Soc. Faraday Trans.* **1996,** *92*, 1853-1857.

296. Shimizu, A.; Fumino, K.; Yukiyasu, K.; Taniguchi, Y., Nmr Studies on Dynamic Behavior of Water Molecule in Aqueous Denaturant Solutions at 25°C: Effects of Guanidine Hydrochloride, Urea and Alkylated Ureas. *J. Mol. Liq.* **2000,** *85*, 269.

297. Russo, D.; Hura, G.; Head-Gordon, T., Hydration Dynamics near a Model Protein Surface. *Biophys. J.* **2004,** *86* (3), 1852–1862.

298. Scatena, L. F.; Brown, M. G.; Richmond, G. L., Water at Hydrophobic Surfaces: Weak Hydrogen Bonding and Strong Orientation Effects. *Science* **2001,** *292* (5518), 908-912.

299. Rezus, Y.; Bakker, H. J., Observation of Immobilized Water Molecules around Hydrophobic Groups. *Phys. Rev. Lett.* **2007,** *99* (14), 148301.

300. Rezus, Y. L. A.; Bakker, H. J., Effect of Urea on the Structural Dynamics of Water. *Proc. Natl. Acad. Sci. U.S.A* **2006,** *103* (49), 18417-18420.

301. Haselmeier, R.; Holz, M.; Marbach, W.; Weingaertner, H., Water Dynamics near a Dissolved Noble Gas. First Direct Experimental Evidence for a Retardation Effect. *J. Phys. Chem.* **1995,** *99*, 2243.

302. Dresselhaus, M. S.; Dresselhaus, G.; Eklund, P. C., *Science of Fullerenes and Carbon Nanotubes*. Acedemic Press: San Diego, 1996; p 464-490.

303. Zhang, F.; Zhang, X., Solvent-Induced Optical Properties of C_{60}. *J. Lumin.* **2010,** *130*, 787-791.

304. Tian, G.; Lu, Y., Fluorescence and Phosphorescence of Single C_{60} Molecules as Stimulated by a Scanning Tunneling Microscope. *Angew. Chem. Int. Ed.* **2013,** *52*, 4814 –4817.

305. Beeby, A.; Eastoe, J.; Heenanc, R. K., Solubilisation of C_{60} in Aqueous Micellar Solution *J. Chem. Soc. Chem. Commun.* **1994,** *10*, 173-175.

306. Catalan, J.; Elguero, J., Fluorescence of Fullerenes (C_{60} and C_{70}). *J. Am. Chem. Soc.* **1993,** *115* (20), 9249-52.

307. Wang, Y.; Holden, J. M.; Rao, A. M.; Eklund, P. C.; Venkateswaran, U. D.; Eastwood, D.; Lidberg, R. L.; Dresselhaus, G.; Dresselhaus, M. S., Optical Absorption and Photoluminescence in Pristine and Photopolymerized C_{60} Solid Films *Phys. Rev. B* **1995,** *51*, 4547.

308. Kwon, O. H.; Park, K.; Jang, D. J., Photoluminescence Dynamics and Spectra of C_{60} and C_{60}- in VPI-5 Molecular Cages. *Chem. Phys. lett.* **2001,** *346*, 195-200.

309. Alargova, R. G.; Deguchi, S.; Tsujii, K., Stable Colloidal Dispersions of Fullerenes in Polar Organic Solvents. *J. Am. Chem. Soc.* **2001,** *123*, 10460-10467.

310. Labille, J.; Masion, A.; Ziarelli, F.; Rose, J.; Brant, J.; Villiéras, F.; Pelletier, M.; Borschneck, D.; Wiesner, M. R.; Bottero, J. Y., Hydration and Dispersion of C_{60} in Aqueous Systems: The Nature of Water-Fullerene Interactions. *Langmuir* **2009,** *25* (19), 11232-11235.

311. Hirana, Y.; Tanaka, Y.; Niidome, Y.; Nakashima, N., Strong Micro-Dielectric Environment Effect on the Band Gaps of (N,M)Single-Walled Carbon Nanotubes. *J. Am. Chem. Soc.* **2010,** *37* (37), 13072-13077.

312. Hung, W. C.; Ho, C. D.; Liu, C. P.; Lee, Y. P., Laser-Induced Fluorescence and Phosphorescence of C_{60} Isolated in Solid Ne. *J. Phys. Chem.* **1996,** *100*, 3927-3932.

313. Sassara, A.; Zerza, G.; Chergui, M.; Negri, F.; Orlandi, G., The Visible Emission and Absorption Spectrum of C_{60}. *J. Chem. Phys.* **1997,** *107*, 8731-8741.

314. Sassara, A.; Zerza, G.; Chergui, M., Fluorescence Spectra of Isolated C_{60} Molecules in Neon and Argon Matrices: Assignment of the Lowest Emitting States. *J. Phys. B* **1996,** *29*, 4996-5013.

315. Cavar, E.; Blum, M.-C.; Pivetta, M.; Patthey, F.; Chergui, M.; Schneider, W. D., Fluorescence and Phosphorescence from Individual C_{60} Molecules Excited by Local Electron Tunneling. *Phys. Rev. Lett.* **2005,** *95*, 196102.

316. Heuvel, D. J. v. d.; Berg, G. J. B. v. d.; Groenen, E. J. J.; Schmid, J.; Holleman, I.; Meijer, G., Lowest Excited Singlet State of C_{60}: A Vibronic Analysis of the Fluorescence *J. Phys. Chem.* **1995,** *99*, 11644-11649

317. Agafonov, S. S.; Glazkov, V. P.; Kokin, I. F.; Somenkov, V. A., Polyamorphic Transition in Amorphous Fullerites. *Phys. Solid State* **2010,** *52*, 1329-1331.

318. Li, B.; Tao, X.; Kasai, H.; Oikawa, H.; Nakanishi, H., Size Control for Fullerene C_{60} Nanocrystals During the High Temperature

and High Pressure Fluid Crystallization Process. *Matter. Lett.* **2007,** *61*, 1738–1741.

319. Feigin, L. A.; Svergun, D. I., *Structure Analysis by Small Angle X-Ray and Neutron Scattering*. Plenum Press: New York, 1987.

320. Duboue-Dijon, D.; Fogarty, A. C.; Laage, D., Temperature Dependence of Hydrophobic Hydration Dynamics: From Retardation to Accelaration. *J. Phys. Chem. B* **2014,** *118*, 1574-1583.

321. Elliot, S. R., *Physics of Amorphous Solids* second ed.; Longman Scientific and Technical: New York, 1990; p 132-151.

322. Aguilar, M.; Cortina, J. L., *Solvent Extraction and Liquid Membranes: Fundamentals and Applications in New Materials*. CRC Press: 2008.

323. Puckner, A., The Extraction of Morphine with Immiscible Solvents. *J. Am. Chem. Soc.* **1901,** *23*, 470-473.

324. Solomon, M. J.; Crane, F. A., Critical Evaluation of Extraction Procedures in Determination of Atropine and Scopolamine from Datura Powder. *J. Pharm. Sci.* **1970,** *59*.

325. Vorobyov, I.; Bennet, W. F. D.; Tieleman, D. P.; Allen, T. W.; Noskov, S., The Role of Atomic Polarisation in the Thermodynamics of Chloroform Partitioning to Lipid Bilayers. *J. Chem. Theory Comput.* **2012,** *8*, 618-628.

326. Seeman, P., The Membrane Actions of Anesthetics and Tranquilizers. *Pharmacol. Rev.* **1972,** *24*, 583-655.

327. Laturnus, F.; Haselmann, K. F.; Borch, T.; Gron, C., Terrestrial Natural Sources of Trichloromethane (Chloroform) - an Overview. *Biogeochemistry* **2002,** *60*, 121-139.

328. Politzer, P.; Murray, J. S.; Clark, T., Halogen Bonding and Other Sigma-Hole Interactions: A Perspective. *Phys. Chem. Chem. Phys.* **2013,** *15*, 11178.

329. Riley, K. E.; Hobza, P., Investigations into the Nature of Halogen Bonding Including Symmetry Adapted Perturbation Theory Analyses. *J. Chem. Theory Comput.* **2008,** *4*, 232-242.

330. Metrangolo, P.; Resnati, G., *Halogen Bonding*. Springer-Verlag: Heidelberg, 2008; Vol. 126.

331. Scholfield, M. R.; Zanden, C. M. V.; Carter, M.; Ho, P. S., Halogen Bonding (X-Bonding): A Biological Perspective. *Protein Sci.* **2013,** *22* (2), 139-152.

332. Wilcken, R.; Zimmermann, M. O.; Lange, A.; Joerger, A. C.; Boeckler, F. M., Principles and Applications of Halogen Bonding in Medicinal Chemistry and Chemical Biology. *J. Med. Chem.* **2013,** *56* (4), 1363-1388.

333. Anthony, A.; Desiraju, G. R.; Jetti, R. K. R.; Kuduva, S. S.; MAdhavi, N. N. L.; Nangia, A.; Thaimattam, R.; Thalladi, V. R., Crystal Engineering: Some Further Strategies. *Cryst. Eng.* **1998,** *1*, 1-18.

334. Awwadi, F. F.; Willett, R. D.; Peterson, K. A.; Twamley, B., The Nature of Halogen-Halogen Synthons: Crystallographic and Theoretical Studies. *Chem. Eur. J.* **2006,** *12* (35), 8952-8960.

335. Gutzler, R.; Fu, C.; Dadvand, A.; Hua, Y.; MacLeod, J. M.; Rosei, F.; Perepichka, D. F., Halogen Bonds in 2D Supramolecular Self-Assembly of Organic Semiconductors *Nanoscale* **2012,** *4*, 5965-5971.

336. Lide, R., *Crc Handbook of Chemistry and Physics*. 77th ed.; CRC press: Boca Raton, 1996; p **6-**185.

337. Lamoureux, G.; Faraldo-Gomez, J. D.; Krupin, S.; Noskov, S. Y., Polarizable Model of Chloroform Based on Classical Drude Oscillators. *Chem. Phys. Lett.* **2009,** *468*, 270-274.

338. Evans, M. W., A Review and Computer Simulation of the Structure and Dynamics of Liquid Chloroform. *J. Mol. Liq.* **1983,** *25*, 211-260.

339. Bohm, J.; Ahlrichs, R., Molecular Dynamics Simulation of Liquid Dichloromethane and Chloroform with New Pair Potentials. *Mol. Phys.* **1985,** *54* (6), 1261-1274.

340. Martin, M. E.; Losa, A. M.; Galvan, I. F.; Aguilar, M. A., An ASEP/MD Study of Liquid Chloroform. *J. Mol. Struct.* **2006,** *775*, 81-86.

341. Chang, T.-M.; Dang, L. X.; Peterson, K. A., Computer Simulation of Chloroform with a Polarizable Potential Model. *J. Phys. Chem. B* **1997,** *101*, 3413-3419.

342. Fennell, C. J.; Li, L.; Dill, K. A., Simple Liquid Models with Corrected Dielectic Constants. *J. Phys. Chem. B* **2012,** *116*, 6936-6944.

343. Yin, C. C.; Li, A. H. T.; Chao, S. D., Liquid Structure from Computer Simulation with Full Ab Initio Intermolecular Interaction Potential. *J. Chem. Phys.* **2013,** *139*.

344. Caballero, N. B.; Zuriaga, M.; Carignano, M. A.; Serra, P., Molecular Kinetics of Solid and Liquid Chloroform. *Chem. Phys. Lett* **2013,** *585*, 69-73.

345. Bertagnolli, H.; Chieux, P., A Neutron Diffraction Study of a Hydrogen Containing Organic Liquid Chloroform as an Example. *Ber. Bunsenges. Phys. Chem.* **1980,** *84*, 1225 - 1231.

346. Bertagnolli, H.; Chieux, P., The Complete Set of Atom Pair Correlation Functions of Liquid Chloroform as Obtained from a Final Neutron Scattering Experiment with H/D Isotopic Substitution. *Mol. Phys.* **1984,** *51* (3), 617-631.

347. Takahashi, A.; Yano, Y. F.; Iijima, T., Structure of Liquid Chloroform as Investigated by Energy-Dispersive X-Ray Diffraction. *Bull. Chem. Soc. Jpn* **1998,** *71*, 2081-2086.

348. Pothoczki, S.; Temleitner, L.; Kohara, S.; Jovari, P.; Pusztai, L., The Liquid Structure of Haloforms: Chloroform and Bromoform. *J. Phys.: Condens. Matter* **2010,** *22*, 404211.

349. Pothoczki, S.; Temleitner, L.; Pusztai, L., Detailed Intermolecular Structure of Molecular Liquids Contianing Slightly Distorted Tetrahedral Molecules with C3V Symmetry: Chlororfom, Bromoform, and Methyl-Iodide. *J. Chem. Phys.* **2011,** *134*, 044521.

350. Nikuradse, A., Association State of Chloroform. *Z. Phys. Chem.* **1954,** *2*, 9-24.

351. Becker, E. D., Infrared Studies of the Self-Ascociation of Chloroform. *Spectrochim. Acta* **1959,** *15*, 743-746.

352. Rey, R., Quantitative Charachterization of Orientational Order in Liquid Carbon Tetrachloride. *J. Chem. Phys.* **2007,** *126*, 164506.

353. Campagna, J. A.; Miller, K. W.; Forman, S. A., Mechanisms of Actions of Inhaled Anesthetics. *New Engl. J. Med.* **2003,** *348*, 2110-2124.

354. Shephard, J. J.; Soper, A. K.; Imberti, S.; Evans, J. S. O.; Salzmanna, C. G., Polar Stacks of Molecules in Liquid Chloroform. *Angew. Chem. Int. Ed..* **2014**, under review.

355. Tao, J.; Benmore, C. J.; Worlton, T. G.; Carpenter, J. M.; Mikkelson, D.; Mikkelson, R.; Siewenie, J.; Hammonds, J.; Chatterjee, A., Time-of-Flight Neutron Total Scattering Data Analysis Implemented in the Software Suite *ISAW*. *Nucl. Instr. Meth. Phys. Res.* **2006,** *562*, 422 - 432.

356. Jen, M.; Lide Jr, D. R., Molecular Structure of Chloroform. *J. Chem. Phys.* **1962,** *36*, 2525.

357. Breneman, C. M.; Wiberg, K. B., Determining Atom-Centered Monopoles from Molecular Electrostatic Potentials. The Need for High Sampling Density in Formamide Conformational Analysis. *J. Comput. Chem.* **1990,** *11* (3), 361-373.

358. Torii, H., Atomic Quadrupolar Effect in Intermolecular Electrostatic Interactions of Chloroalkanes: The Case of Chloroform and Dichloromethane. *J. Mol. Liq.* **2005,** *119*, 31 - 39.

359. Torii, H.; Yoshida, M., Properties of Halogen Atoms for Representing Intermolecular Electrostatic Interactions Related to Halogen Bonding and Their Substituent Effects. *J. Comput. Chem.* **2010,** *31* (1), 107-116.

360. Jorgenson, W. L.; Briggs, J. M.; Contreras, M. L., Relative Partition Coefficients for Organic Solutes from Fluid Simulations. *J. Phys. Chem.* **1990,** *94*, 1683-1686.

361. Cliffe, M. J.; Dove, M. T.; Drabold, D. A.; Goodwin, A. L., Structure Determination of Disordered Materials from Diffraction Data. *Phys. Rev. Lett.* **2010,** *104*.

362. Dziubek, K. F.; Katrusiak, A., Polar Symetry in New High Pressure Phases of Chloroform and Bromoform. *J. Phys. Chem. B.* **2008,** *112*, 12001-12009.

363. McLain, S. E.; Benmore, C. J.; Siewenie, J. E.; Urquidi, J.; Turner, J. F. C., On the Structure of Liquid Hydrogen Fluoride. *J. Am. Chem. Soc.* **2004,** *43*, 1952-1955.

364. Andreani, C., Orientational Correlations in Liquid Hydrogen Halides: The Special Case of Hydrogen Chloride. *J. Mol. Liq.* **1998,** *78*, 217-223.

365. Andreani, C.; Ricci, M. A.; Nardone, M.; Ricci, M. A.; Soper, A. K., Orientational Correlations and Hydrogen Bonding in Liquid Hydrogen Chloride. *J. Chem. Phys.* **1997,** *107*, 214-221.

366. Andreani, C.; Menzinger, F.; Ricci, M. A.; Soper, A. K.; Dreyer, J., Neutron Diffraction from Liquid Hydrogen Bromide: Study of the Orientational Correlations. *Phys. Rev. B* **1994,** *49*, 3811-3820.

367. Santoli, G.; Bruni, F.; Ricci, M. A.; Soper, A. K., Orientational Correlations in Liquid Hydrogen Sulphide. *Mol. Phys.* **1999,** *97*, 777-786.

368. Neuefeind, J.; Fischer, H. E.; Schröer, W., The Structure of Fluid Trifluoromethane and Methylfluoride. *J. Phys.: Condens. Matter* **2000,** *12*, 8765-8776.

369. Deba, N.; Tiwaryb, A. S.; Mukherjee, A. K., Calculation of the Kirkwood–Frohlich Correlation Factor and Dielectric Constant of Methanol Using a Statistical Model and Density Functional Theory. *Mol. Phys.* **2010,** *108*, 1907-1917.

370. Johnson, L. E.; Barnes, R.; Drexler, T. W.; Eichinger, B. E.; Robinson, B. H., Dielectric Constants of Simple Liquids:Stockmayer and Ellipsoidal Fluids. *J. Phys. Chem.* **2010,** *114*, 8431-8440.

371. Valisko, M.; Boda, D., Dielectric Constant of the Polarizable Dipolar Hard Sphere Fluid Studied by Monte Carlo Simulation and Theories. *Condens. Matter Phys.* **2005,** *8*, 357-376.

372. Rosenthal, L. C.; Strauss, H. L., Rotational Correlations in Chloroform. *J. Chem. Phys.* **1976,** *64*, 282.

373. Atkins, P.; Paula, J. D., *Physical Chemistry*. Sixth ed.; Oxford University Press: Oxford, 1998.

374. Gupta, R.; Chandra, A., Structural, Single Particle and Pair Dynamical Properties of Acetone-Chloroform Mixtures with Dissolved Salts. *J. Chem. Phys.* **2011,** *383*, 41-49.

375. Kamath, G.; Georgiev, G.; Potoff, J. J., Molecular Modelling of Phase Behavour and Microstructure of Acetone-Chloroform-Methanol Binary Mixtures. *J. Phys. Chem. B* **2005,** *109*, 19463-19473.

376. Matsui, T.; Hepler, L. G.; Fenby, D. V., Thermodynamic Investigation of Complex Formation by Hydrogen Bondng Binary Liquid Systems. Chloroform with Triethyleamine, Dimethyl Sulfoxide and Acetone. *J. Phys. Chem.* **1973,** *77*, 2397.

377. Morcom, K. W.; Travers, D. N., Heat of Mixing of the System Acetone-Chloroform. Temperature Dependence and Deuterium Isotope Effect. *Trans. Faraday Soc.* **1965,** *61*, 230.

378. Huggins, C. M.; Pimental, G. C.; Schoolery, J. N., Proton Magnetic Resonence Studies of Chloroform in Solution. Evidence for Hydrogen Bond. *J. Phys. Chem.* **1955,** *23*, 1244.

379. Korinek, G. J.; Schneider, W. G., On the Proton Magnetic Resonence Shift Due to Hydrogen Bonding. *Can. J. Chem.* **1957,** *35*, 1157.

380. Reaves, L. W.; Schneider, W. G., Nuclear Magnetic Resonence Measurements of Complexes of Chloroform with Aromatic Molecules and Olefins. *Can. J. Chem.* **1957,** *35*, 251.

381. Shakhparonov, M. I.; Vakalov, I. A., Dielektriczeskiye Svojstva I Molekularnoe Stoyenie Raztrorov Aceton-Khloroform. *Zhum. Fiz. Khim.* **1964,** *38*, 1978.

382. Fischer, E.; Fessler, R., Dielektrische Relaxationszeit Und Assoziation II. *Z. Naturforsch.* **1953,** *8* (a), 177.

383. Campbell, A. N.; Kartzmark, E. M., The Energy of Hydrogen Bonding in the System: Acetone-Chloroform *Can. J. Chem.* **1960,** *38*, 652.

384. Durov, V. A.; Shilov, I. Y., Molecular Structure and Physicochemical Properties of Acetone-Chloroform Mixtures. *J .Chem. Soc. Faraday Trans.* **1996,** *92* (19), 3559-3563.

385. Denisolv, G. S., Hydrogen Bonding of Ketones with Chloroform as Revealed in the Band of the Carbonyl Group Stretching Vibration. *Opt. Spektrosk.* **1961,** *11*, 428.

386. Kagarise, R. E., Solvent Effects on Infrared Freaquencies. 4. The Effect of Acetone on the C-D Band of Some Deuterated Haloforms. *Spectr. Acta* **1963,** *19*, 629.

387. Glasstone, S., The Structure of Some Molecular Complexes in the Liquid Phase. *J. Chem. Soc. Faraday Trans.* **1937,** *33*, 200-214.

388. Shurvell, H. F., Raman Spectra and Crystal Structure of Solid $CHCl_3$ and $CDCl_3$. *J. Chem. Phys.* **1973,** *58* (12), 5807-5811.

389. Williams, J. W.; Hollaender, A., A Study of the Raman Effect in Acetone. *Proc. Natl. Acad. Sci. U.S.A* **1929,** *15*, 421-423.

390. Wellington, C. A.; Khowaiter, S. H., Charge Distributions in Molecules and Ions: Mindo 3 Calculations. An Alternative of the Charge Localisation Concept in Mass Spectrometry *Tetrahedron* **1978,** *34*, 2183-2190.

391. Jorgenson, W. L.; Swenson, C. J., Optimized Intermolecular Potential Functions for Amides and Peptides. Structure and Properties of Liquid Amides. *J. Am. Chem. Soc.* **1985,** *107*, 569.

392. Ferrario, M.; Haughney, M.; McDonald, I. R.; Klein, M., Molecular-Dynamics Simulations of Aqueous Mixtures: Methanol, Acetone, and Ammonia *J. Chem. Phys.* **1990,** *93*, 5156-5166.

393. Allan, D. R.; Clark, S. J.; Ibberson, R. M.; Parson, S.; Pulham, C. R.; Sawye, L., The Influence of Pressure and Temperature on the Crystal Structure of Acetone. *Chem. Commun.* **1999**, 751-752.

394. Matisz, G.; Kelterer, A.-M.; Fabian, W. M. F.; Kunsági-Máté, S., Coordination of Methanol Clusters to Benzene: A Computational Study. *J. Phys. Chem. A* **2011,** *115* (38), 10556-10564.

395. Garrett, A. W.; Severance, D. L.; Zwier, T. S., Multiphoton Ionization Studies of Benzene-Methanol Clusters. I. Comparisons with Benzene-Water Clusters. *J. Chem. Phys.* **1992,** *96*, 7245.

396. Baker, C. M.; Grant, G. H., The Structure of Liquid Benzene. *J. Comput. Chem.* **2006,** *2*, 947-955.

397. Headen, T. F.; Howard, C. A.; Skipper, N. T.; Wilkinson, M. A.; Bowron, D. T.; Soper, A. K., Structure of π–π Interactions in Aromatic Liquids. *J. Am. Chem. Soc.* **2010,** *132* (16), 5735-5742.

398. Jorgensen, W. L.; Severance, D. L., Aromatic-Aromatic Interactions: Free Energy Profiles for the Benzene Dimer in Water, Chloroform, and Liquid Benzene. *J. Am. Chem. Soc.* **1990,** *112*, 4786-4774.

399. Hobza, P.; Spirko, V.; Selzle, H. L.; Schlag, E. W., Anti-Hydrogen Bond in the Benzene Dimer and Other Carbon Proton Donor Complexes. *J. Phys. Chem. A* **1998,** *102* (15), 2501-2504.

400. Nishio, M.; Hiroto, M.; Umezawa, Y., *The CH/Pi Interaction. Evidence, Nature and Consequences*. Wiley-VCH: New York, 1998.

401. Haughney, M.; Ferario, M.; Mcdonald, I. R., Pair Interactions and Hydrogen-Bond Networks in Models of Liquid Methanol. *J. Mol. Phys.* **1986,** *58* (4), 849-853.

402. Haughney, M.; Farrario, M.; McDonald, I. R., Molecular Dynamics Simulations of Liquid Methanol. *J. Phys. Chem.* **1987,** *91*, 4934-4940.

403. Vrhovšek, A.; Gereben, O.; Pothoczk, S.; Tomšič, M.; Jamnik, A.; Kohara, S.; Pusztai, L., An Approach Towards Understanding the Structure of Complex Molecular Systems: The Case of Lower Aliphatic Alcohols. *J. Phys. Condens. Matter.* **2010** *22*, 404214.

404. Adya, A. K.; Bianchi, L.; Wormald, C. J., The Structure of Liquid Methanol by H/D Substitution Technique of Neutron Diffraction *J. Chem. Phys.* **2000,** *112*, 4231.

405. Handgraaf, J.-W.; Erp, T. S. v.; Meijer, E. J., Ab Initio Molecular Dynamics Study of Liquid Methanol. *Chem. Phys. Lett.* **2003,** *367*, 617-624.

406. Tanaka, Y.; Ohtomo, N.; Arakawa, K., The Structure of Liquid Alcohols by Neutron Diffraction. I. Molecular Structure of Methanol Alcohol. *Bull. Chem. Soc. Jpn* **1984,** *57*, 644-647.

407. Idrissi, A.; Oparin, R. D.; Krishtal, S. P.; Krupin, S. V.; Vorobiev, E. A.; Frolov, A. I.; Duboisa, L.; Kiselev, M. G., The Study of Correlations between Hydrogen Bonding Characteristics in Liquid, Sub- and Supercritical Methanol. Molecular Dynamics Simulations and Raman Spectroscopy Analysis. *Faraday Discuss.* **2013,** *167*, 551-566.

408. Ploetz, E. A.; Bentenitis, N.; Smith, P. E., Kirkwood-Buff Integrals for Ideal Solutions. *J. Chem. Phys.* **2010,** *132*, 164501.

409. Matteoli, E.; Lepori, L., Solute-Solute Interactions in Water. II. An Analysis through the Kirkwood-Buff Integrals for 14 Organic Solutes. *J. Chem. Phys.* **1983,** *80* (6), 2856-2863.

410. Perera, A.; Kežićab, B., Fluctuations and Micro-Heterogeneity in Mixtures of Complex Liquids. *Faraday Discuss.* **2013,** *167*, 145-158.

411. Donkersloot, M. C. A., The Structure of Binary Liquids. The Kirkwood Buff Theory of Liquid Mixtures. *J. Solution Chem.* **1979,** *8* (4), 293-307.

412. Jeffrey, G. A.; Ruble, J. R.; McMullan, R. K.; Pople, J. A., The Crystal Structure of Deuterated Benzene. *proc. Natl. Acad. Sci. Lond. A* **1987,** *414* (1846), 47-56.

413. Tauer, K. J.; Lipscomb, W. N., On the Crystal Structures, Residual Entropy and Dielectric Anomaly of Methanol. *Acta Cryst.* **1952,** *5*, 606-613.

414. Torrie, B. H.; Binbrek, O. S.; Straussa, M.; Swainsonc, I. P., Phase Transitions in Solid Methanol. *J. Solid State Chem.* **2002,** *166*, 415-420.

Appendices

Appendix 1 Chloroform-Acetone and Benzene-Methanol Pressure-Composition Isotherms

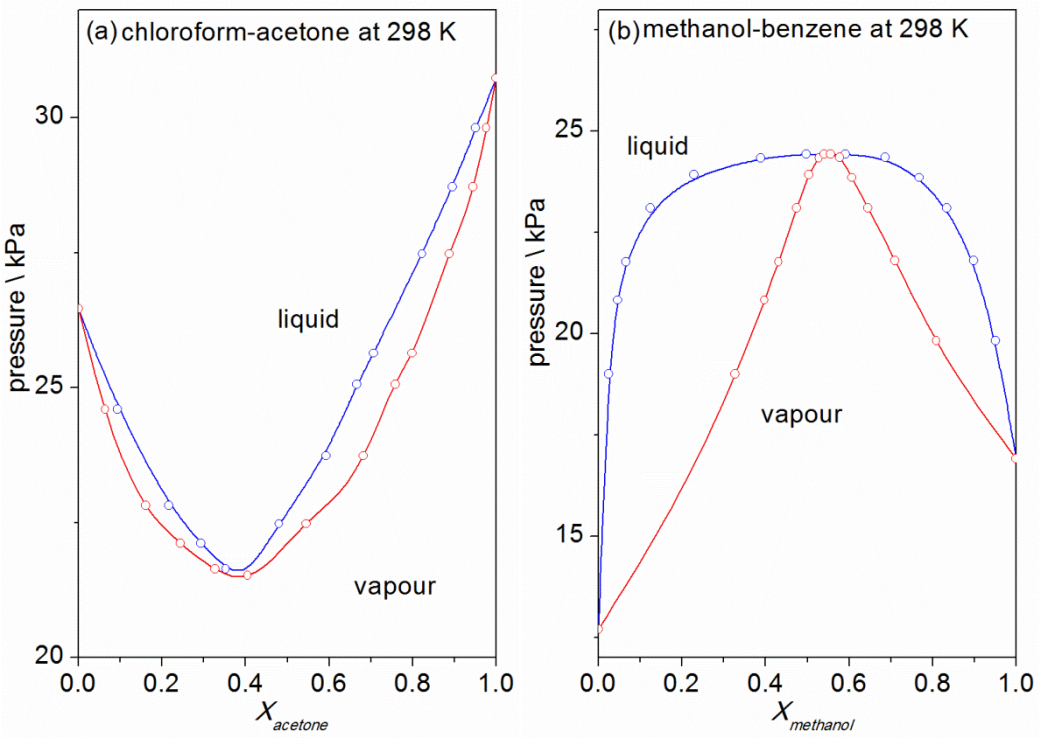

Appendix 1 Pressure-composition isotherms for room temperature binary mixtures of (a) chloroform-acetone,[97,102] and (b) methanol-benzene.[99]

APPENDIX 2 EVACUATION AND COOLING OF THE DEPOSITION APPARATUS

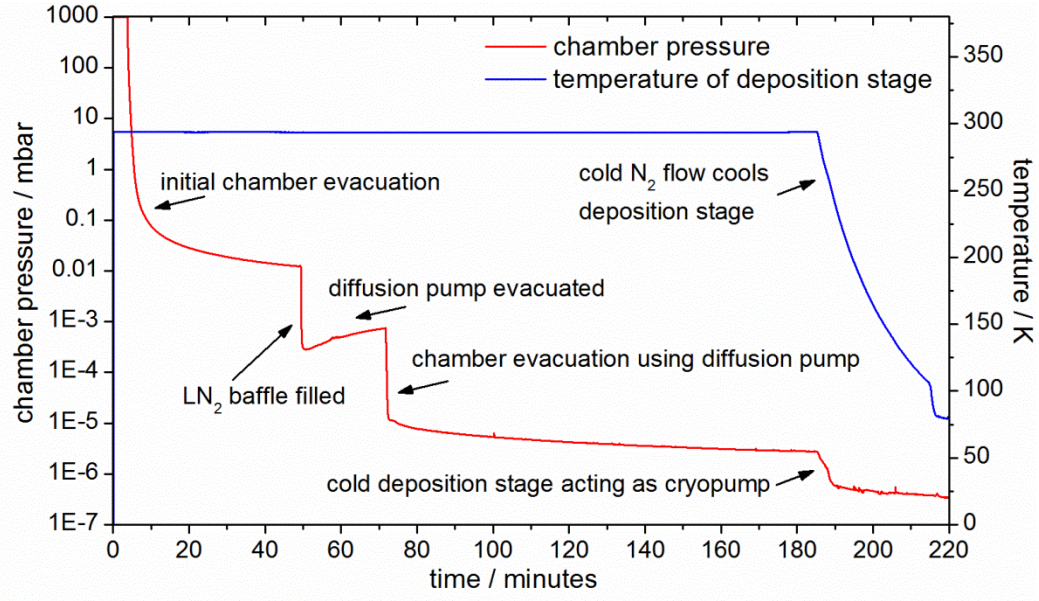

Appendix 2. Preparation of the apparatus for ASW deposition. Variation in chamber pressure (red line) and deposition stage temperature (blue line) with time. The methods are given in section 2.1.3.

Appendix 3 Scale Drawing of the Deposition Stage

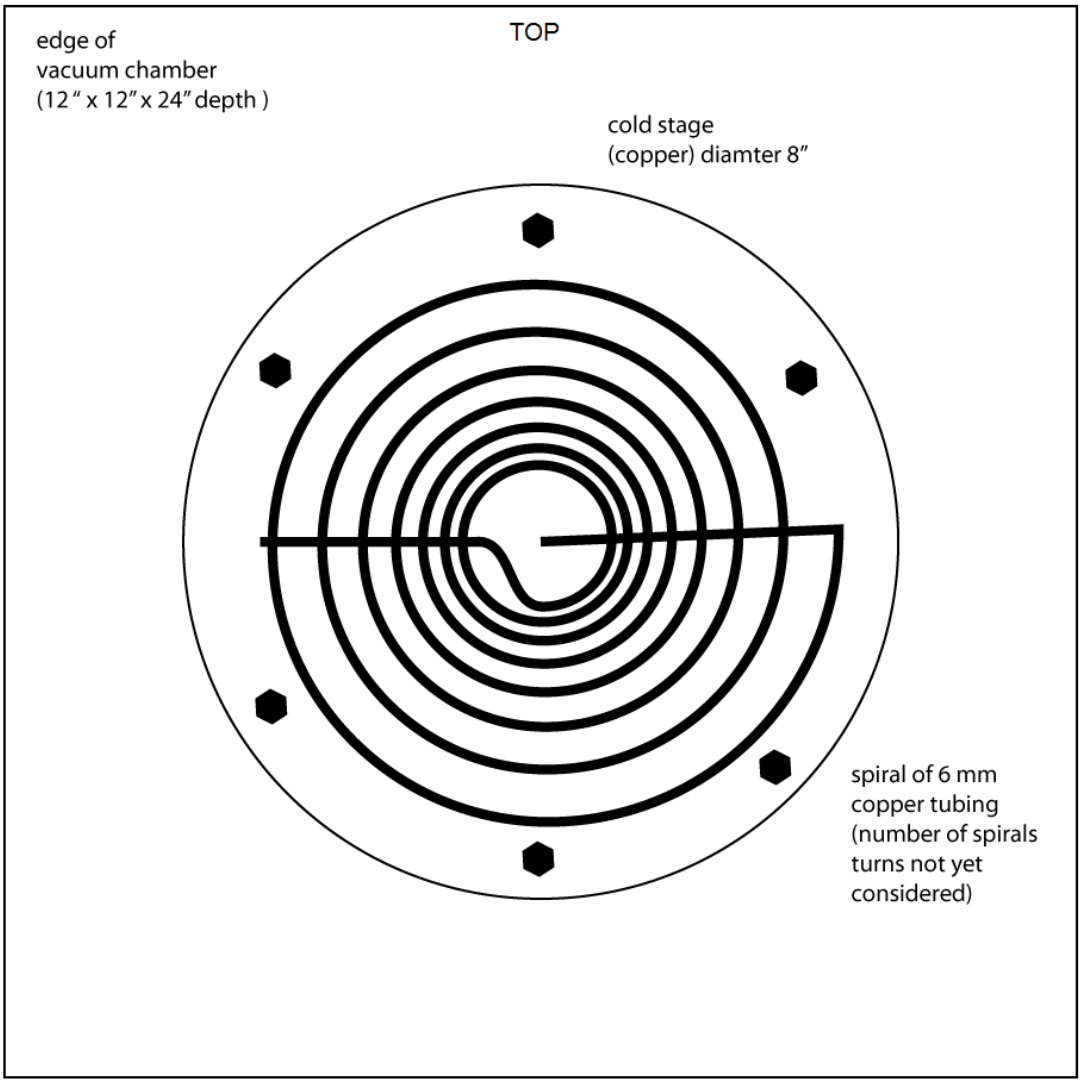

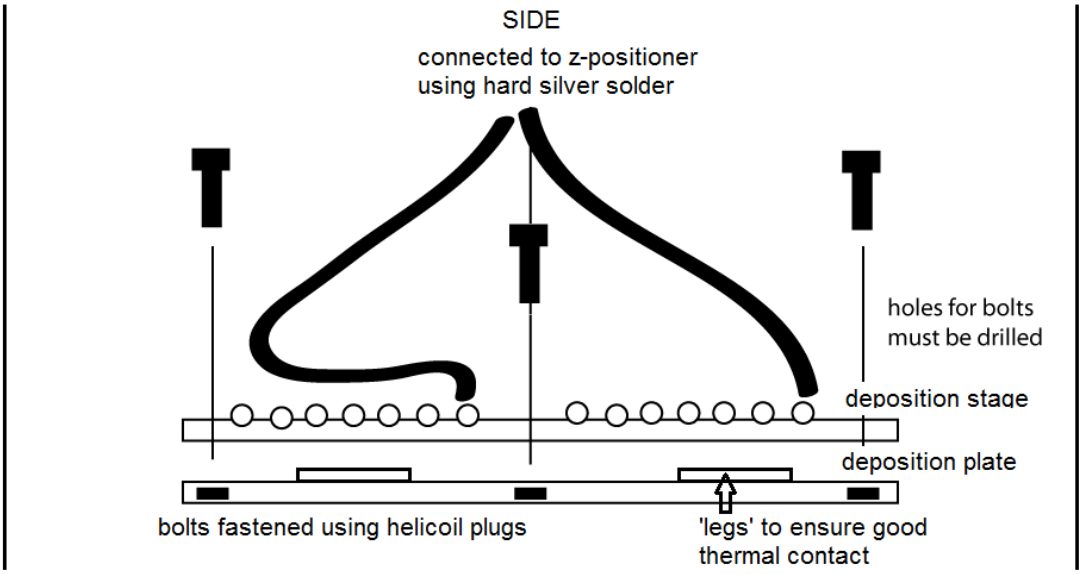

Appendix 3 Scale drawing of the deposition stage and deposition plate

APPENDIX 4 C_{60} SUBLIMATION DATA

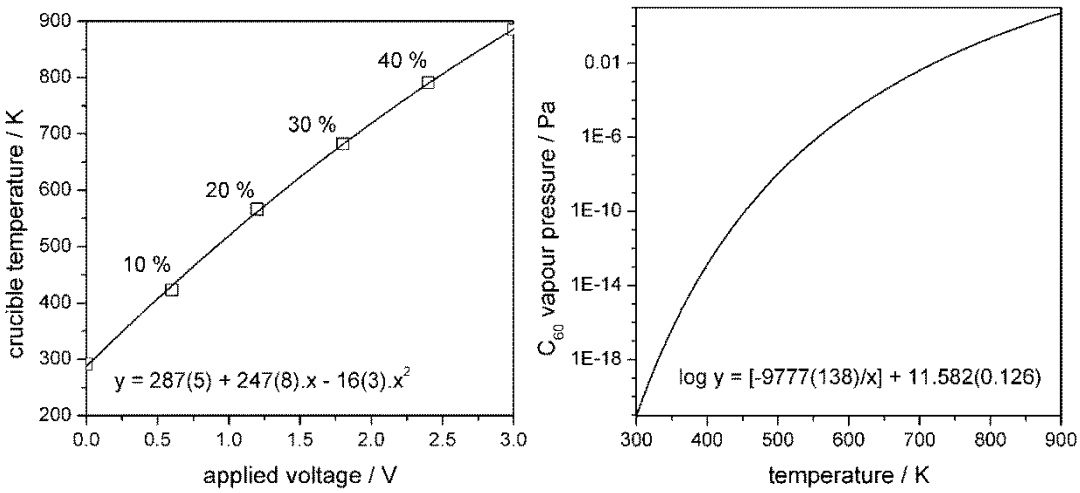

Appendix 4 (left) Variation in crucible temperature with applied potential, also shown are the percentile power settings used for each datum point and the fit to a polynomial function, and (right) the relationship between temperature and C_{60} vapour pressure, from the measurements of Mathews et al.[133] Standard errors are indicated in brackets.

APPENDIX 5 SOLID-STATE SNMR OF RAW AND VACUUM SUBLIMED C_{60}

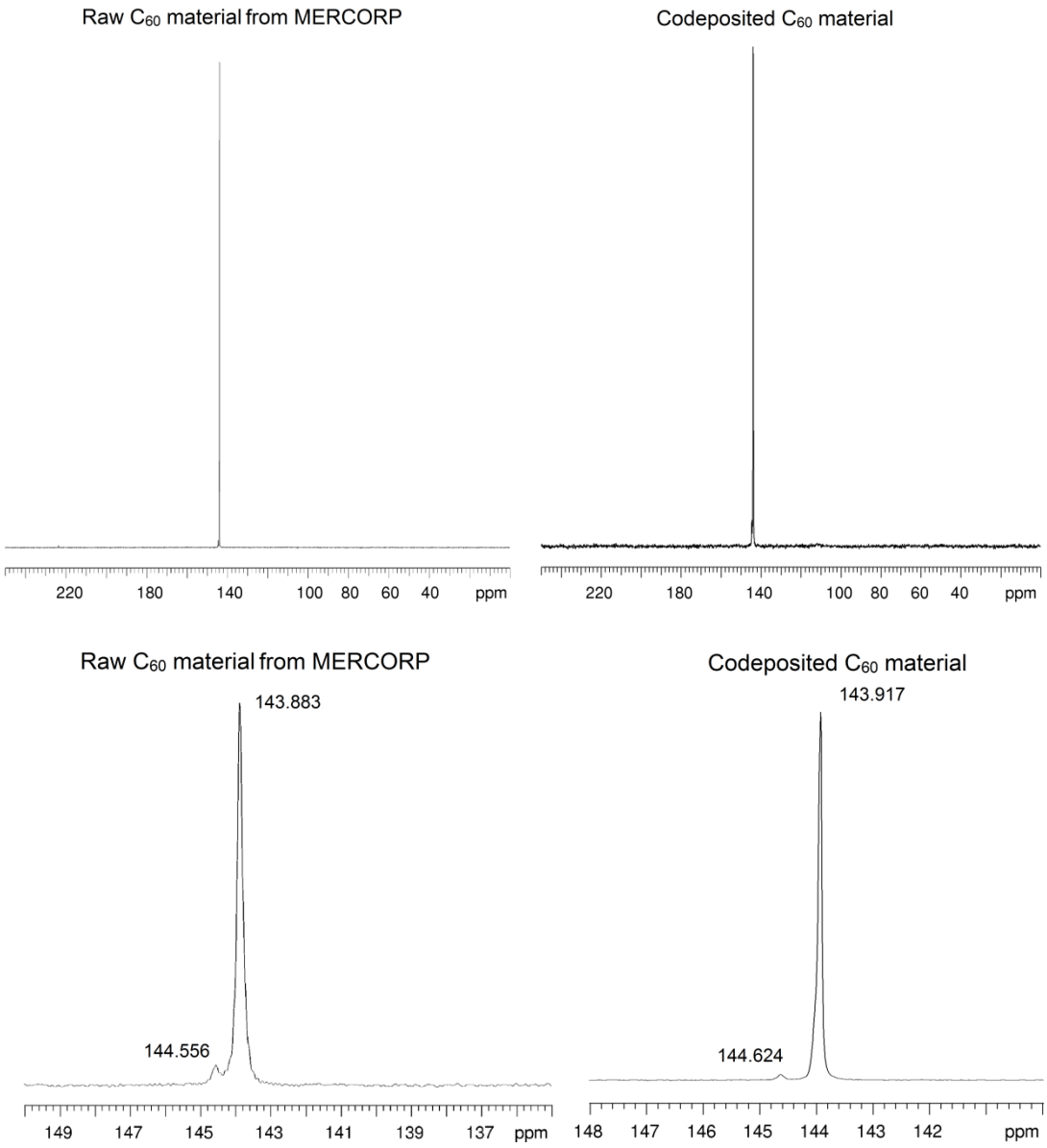

Appendix 5 Comparison of solid-state nuclear magnetic resonance (SSNMR) spectra of raw C_{60} material obtained from MERCORP (left) and that recovered after its codeposition with H_2O (right).

Appendix 6 Scale Drawing of the Codeposition Baseplate

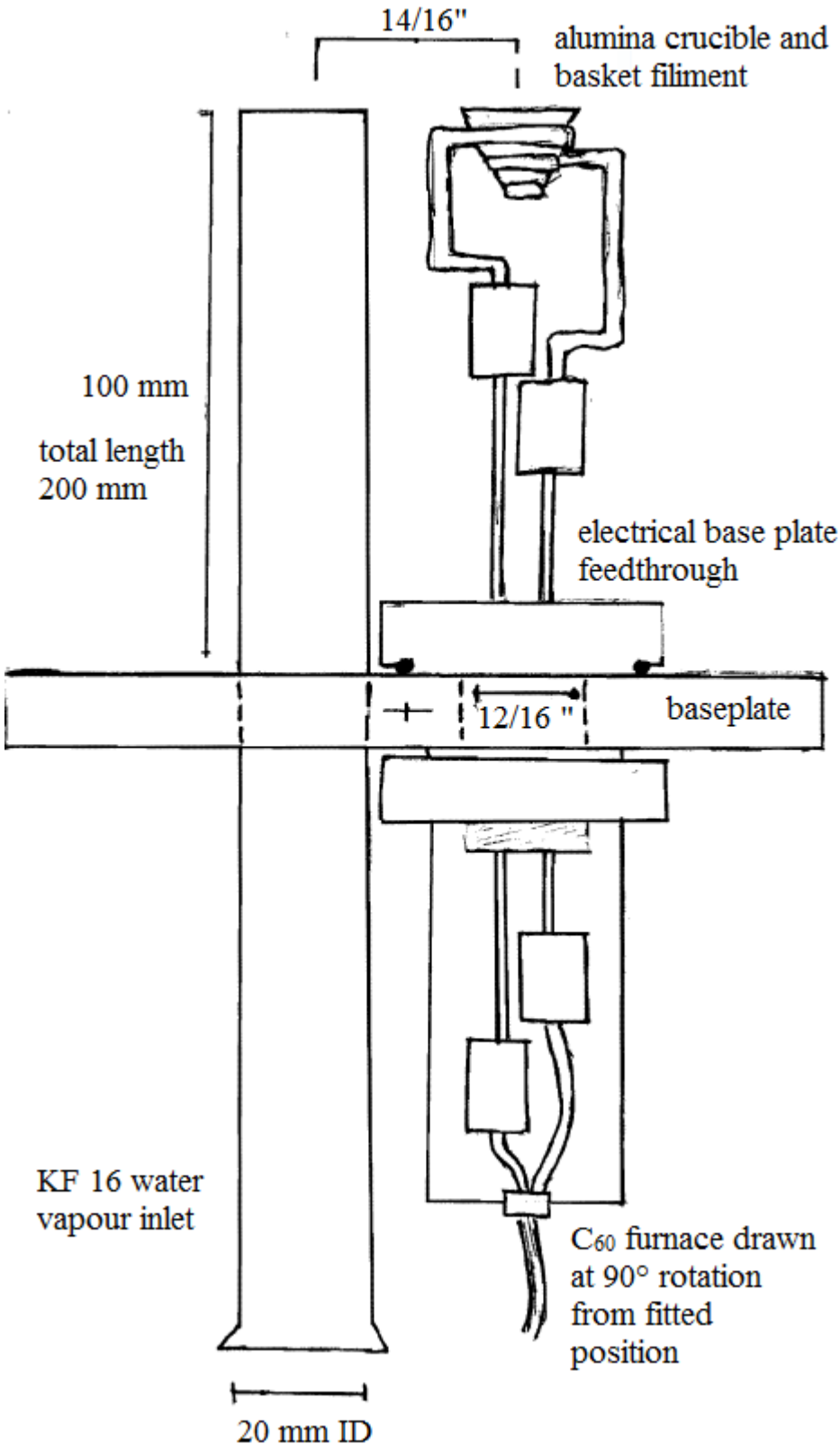

Appendix 6 Scale drawing of the codeposition baseplate. For the ASW baseplate, without C60 furnace (not shown) the water inlet has identical dimensions but is centrally placed

APPENDIX 7 NEUTRON WEIGHTS FOR ASW/C_{60} 'TRAPPED SOLUTIONS'

H_2O

X_{C60}	0		0.0007		0.0024	
C-C	0.0000	0	0.0001	4	0.0010	214
C-H	0.0000	0	-0.0046	-220	-0.0150	-3213
C-O	0.0000	0	0.0036	170	0.0117	2493
H-H	0.0622	1987	0.0604	2883	0.0564	12058
H-O	-0.0965	-3083	-0.0938	-4472	-0.0875	-18706
O-O	0.0374	1196	0.0364	1734	0.0339	7255
$\langle b \rangle^2$	0.0031		0.0021		0.0005	
$\langle b^2 \rangle$	4.4636		4.4069		4.2720	
packing	0.243		0.270		0.314	

H_2O:D_2O

X_{C60}	0		0.0007		0.0024	
C-C	0.0000	0.0%	0.0001	0.1%	0.0009	1.0%
C-H	0.0000	0.0%	0.0018	2.0%	0.0056	5.9%
C-O	0.0000	0.0%	0.0035	4.0%	0.0112	11.8%
H-H	0.0095	11.3%	0.0093	10.6%	0.0087	9.2%
H-O	0.0378	44.6%	0.0367	41.8%	0.0344	36.3%
O-O	0.0374	44.2%	0.0364	41.4%	0.0341	35.9%
$\langle b \rangle^2$	0.0847		0.0878		0.0949	
$\langle b^2 \rangle$	2.4906		2.4619		2.3974	
packing	0.449		0.452		0.383	

D_2O

X_{C60}	0		0.0006		0.0034	
C-C	0.0000	0.0%	0.0001	0.0%	0.0017	0.4%
C-H	0.0000	0.0%	0.0073	1.8%	0.0348	8.5%
C-O	0.0000	0.0%	0.0032	0.8%	0.0152	3.7%
H-H	0.1978	48.6%	0.1928	47.3%	0.1737	42.4%
H-O	0.1721	42.2%	0.1678	41.1%	0.1511	36.9%
O-O	0.0374	9.2%	0.0365	8.9%	0.0329	8.0%
$\langle b \rangle^2$	0.4073		0.4077		0.4094	
$\langle b^2 \rangle$	0.5176		0.5166		0.5128	
packing	0.364		0.414		0.337	

Appendix 7 Weighting factors in b sr^{-1} $atom^{-1}$ and weighting factors normalised by $\langle b \rangle 2 \times 10^{-2}$ indicating the contributions of each atom pair to the measured diffraction data of the ASW/C_{60} 'trapped solutions'. The coherent $\langle b^2 \rangle$ and total $\langle b^2 \rangle$ cross sections (b sr^{-1} $atom^{-1}$) are also indicated together with the packing fractions calculated from the measured DCS using a density of 0.094067 atom A^{-3}.

Appendix 8 DCS Data for the ASW/C_{60} 'Trapped Solutions'

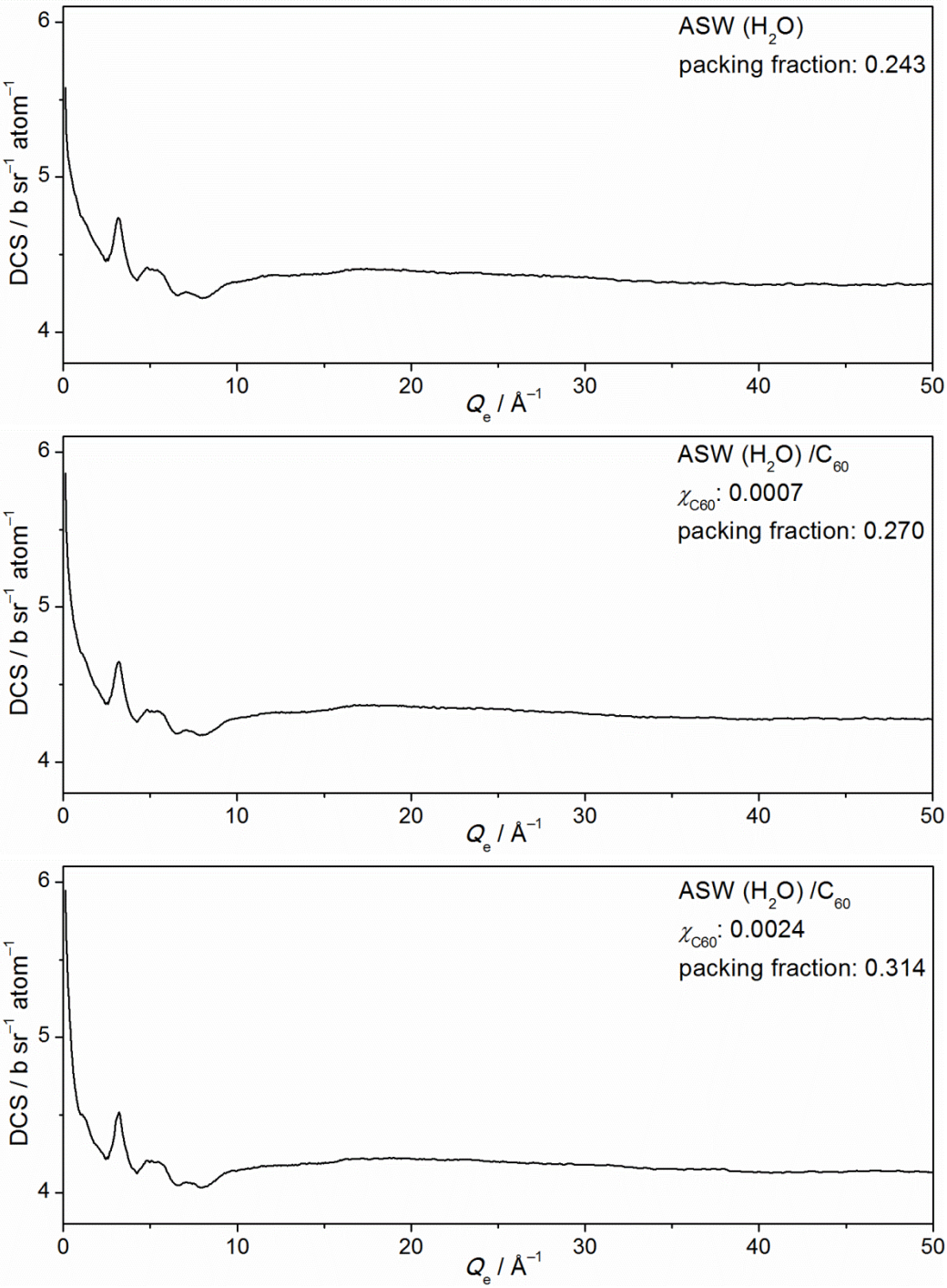

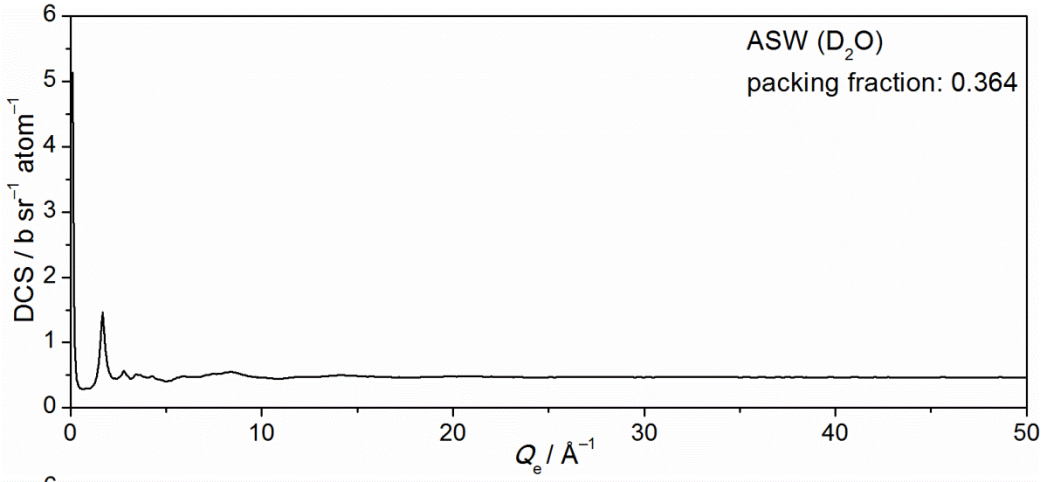
ASW (D_2O)
packing fraction: 0.364
DCS / b sr^{-1} atom^{-1}
Q_e / Å^{-1}

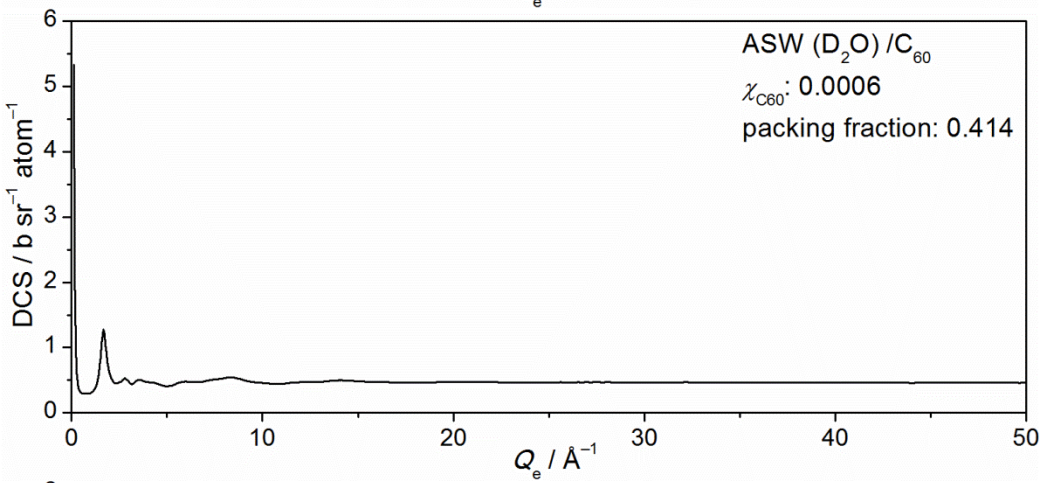
ASW (D_2O) /C_{60}
χ_{C60}: 0.0006
packing fraction: 0.414
DCS / b sr^{-1} atom^{-1}
Q_e / Å^{-1}

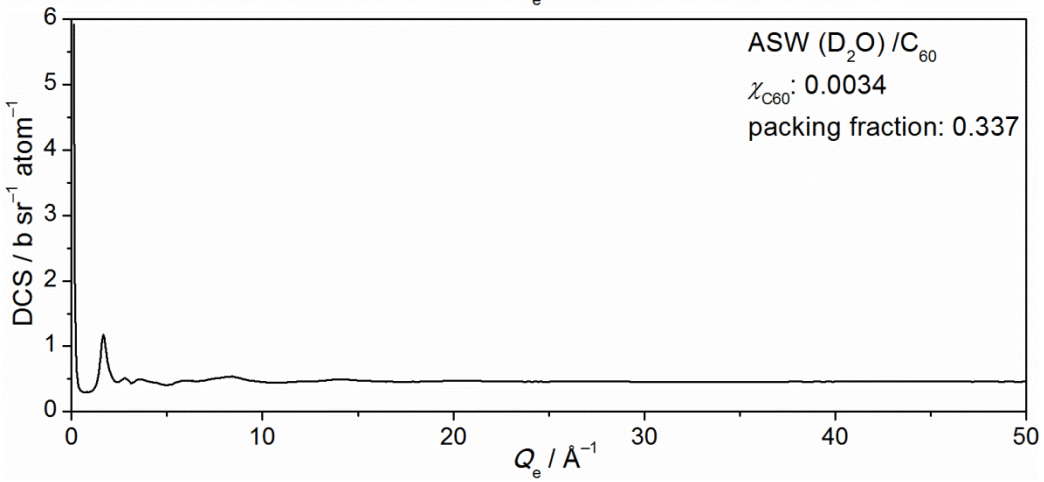
ASW (D_2O) /C_{60}
χ_{C60}: 0.0034
packing fraction: 0.337
DCS / b sr^{-1} atom^{-1}
Q_e / Å^{-1}

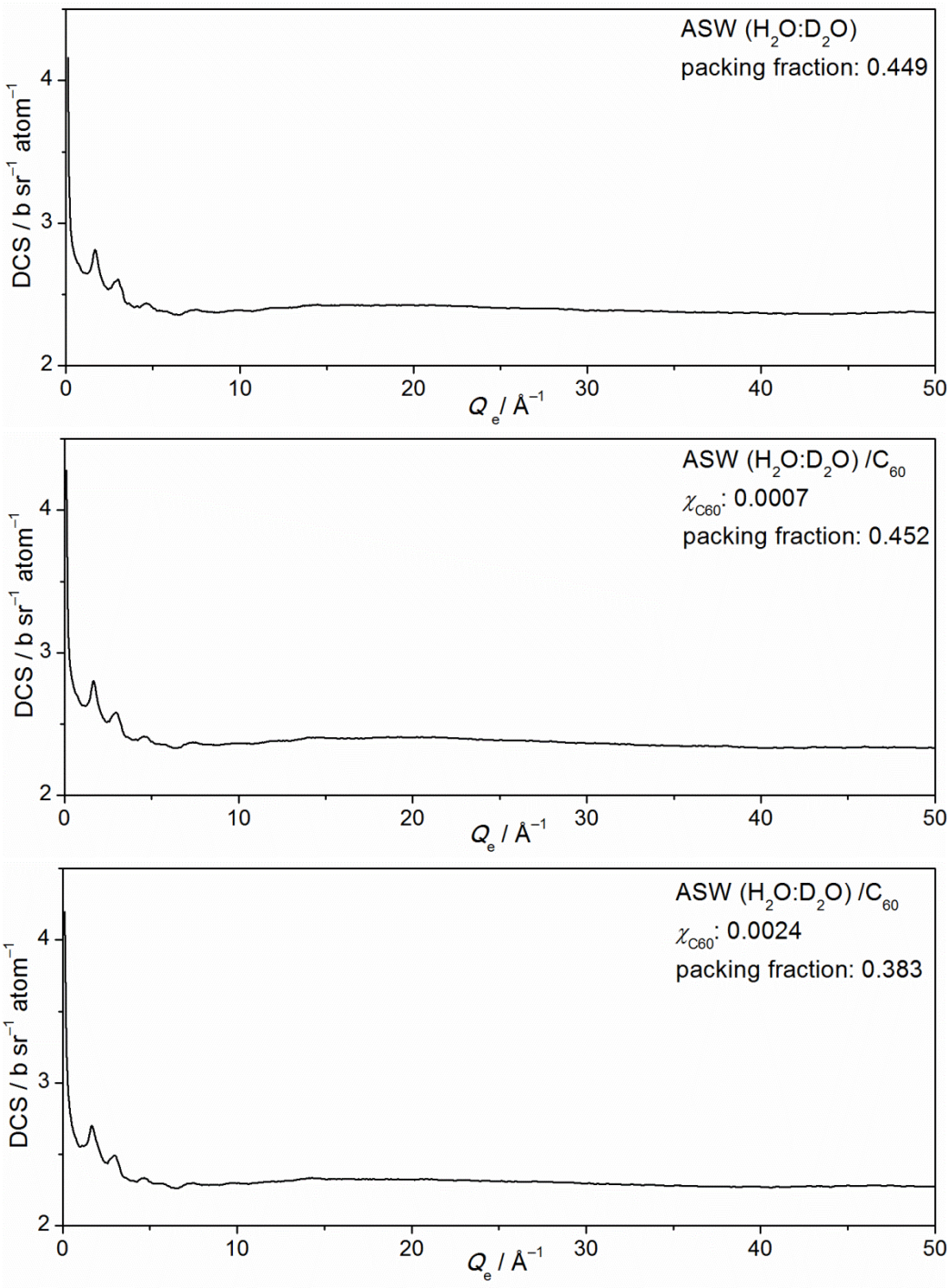

Appendix 8 DCS data for ASW/C_{60} 'trapped solutions' corrected for attenuation and multiple scattering using *GudrunN* software.

APPENDIX 9 INELASTICITY CORRECTED DCS DATA FOR THE ASW/C_{60} 'TRAPPED SOLUTIONS'

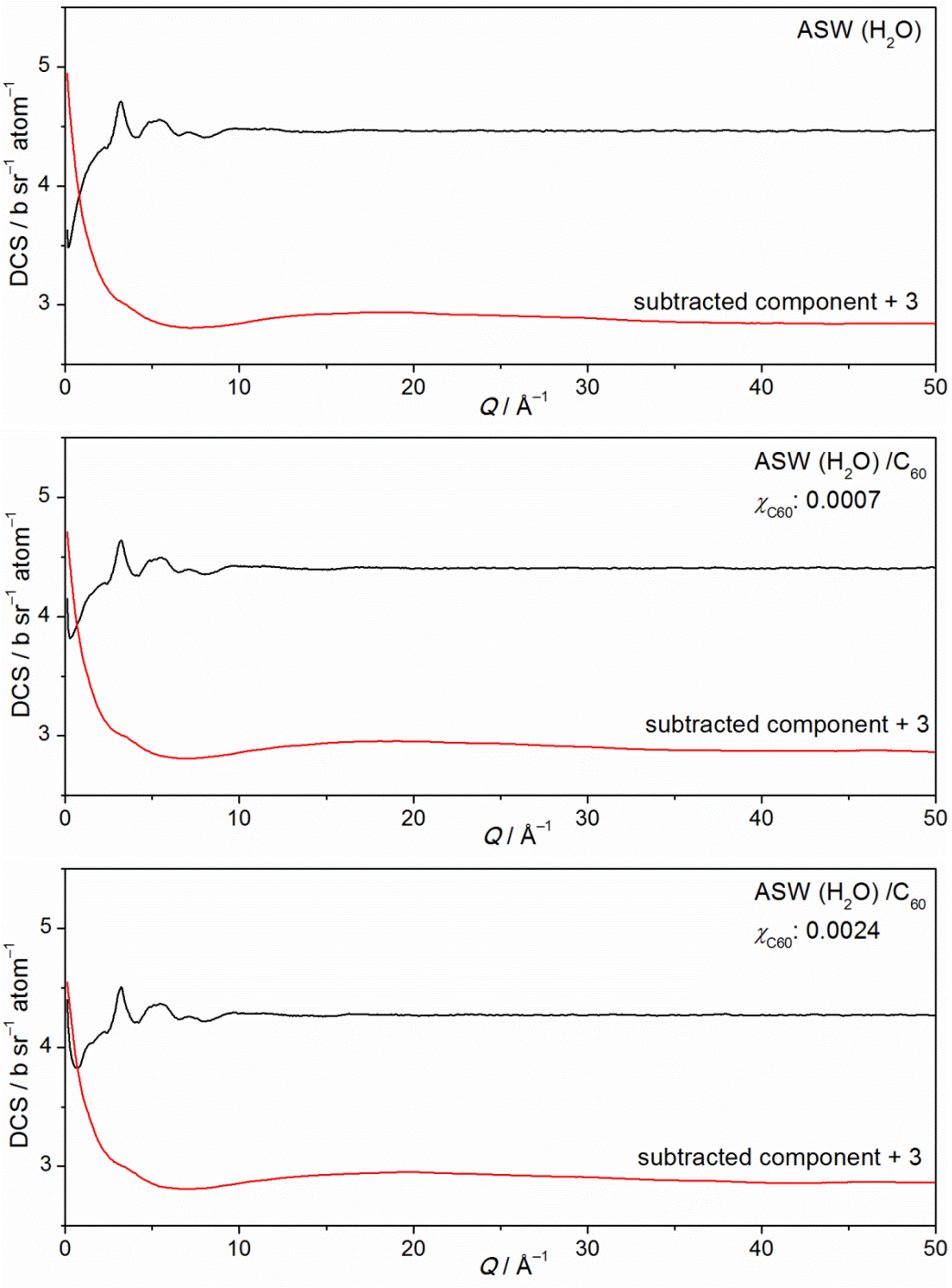

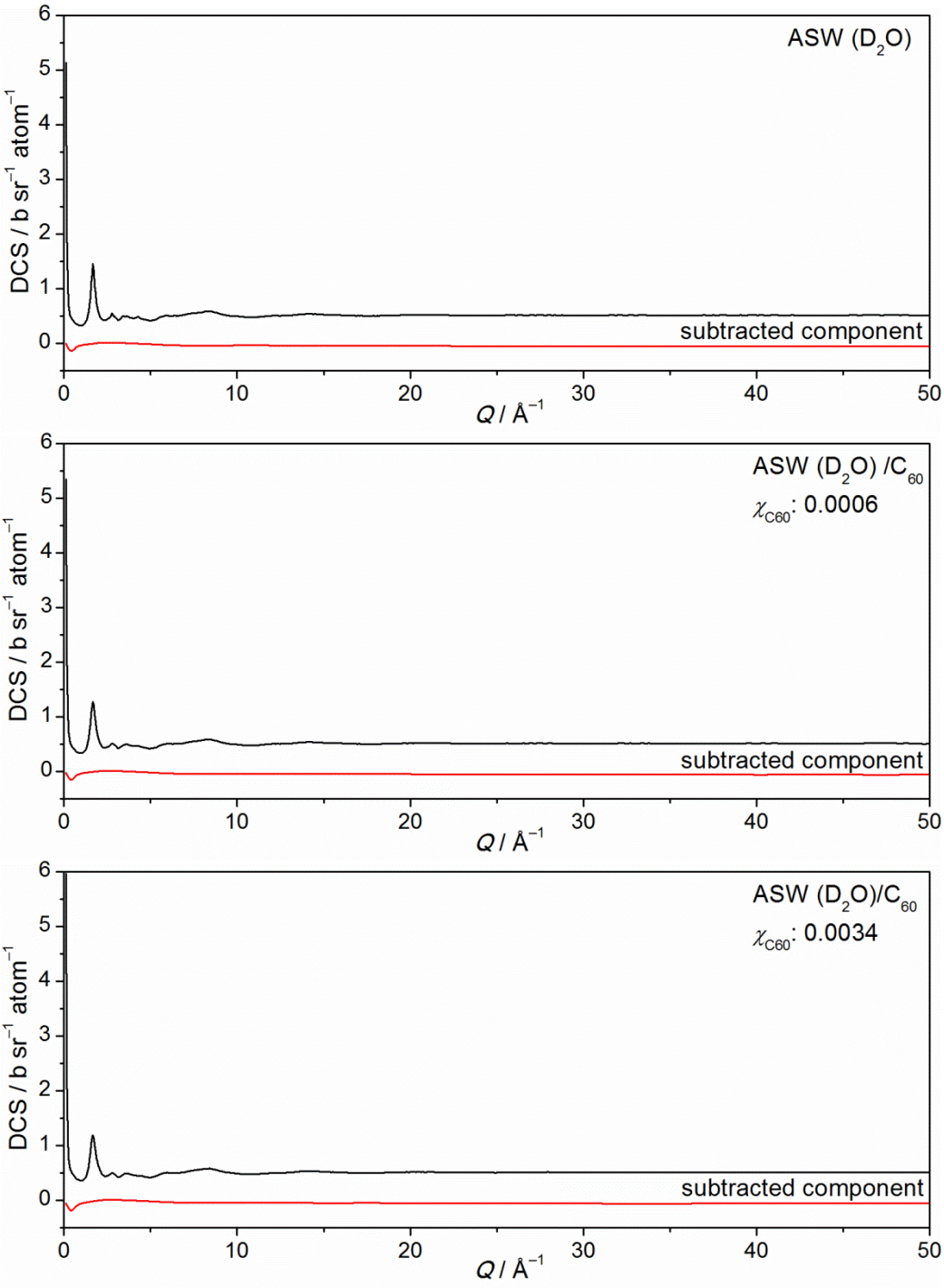
ASW (D_2O)
subtracted component
DCS / b sr^{-1} $atom^{-1}$
Q / $Å^{-1}$
ASW (D_2O) /C_{60}
χ_{C60}: 0.0006
subtracted component
DCS / b sr^{-1} $atom^{-1}$
Q / $Å^{-1}$
ASW (D_2O)/C_{60}
χ_{C60}: 0.0034
subtracted component
DCS / b sr^{-1} $atom^{-1}$
Q / $Å^{-1}$

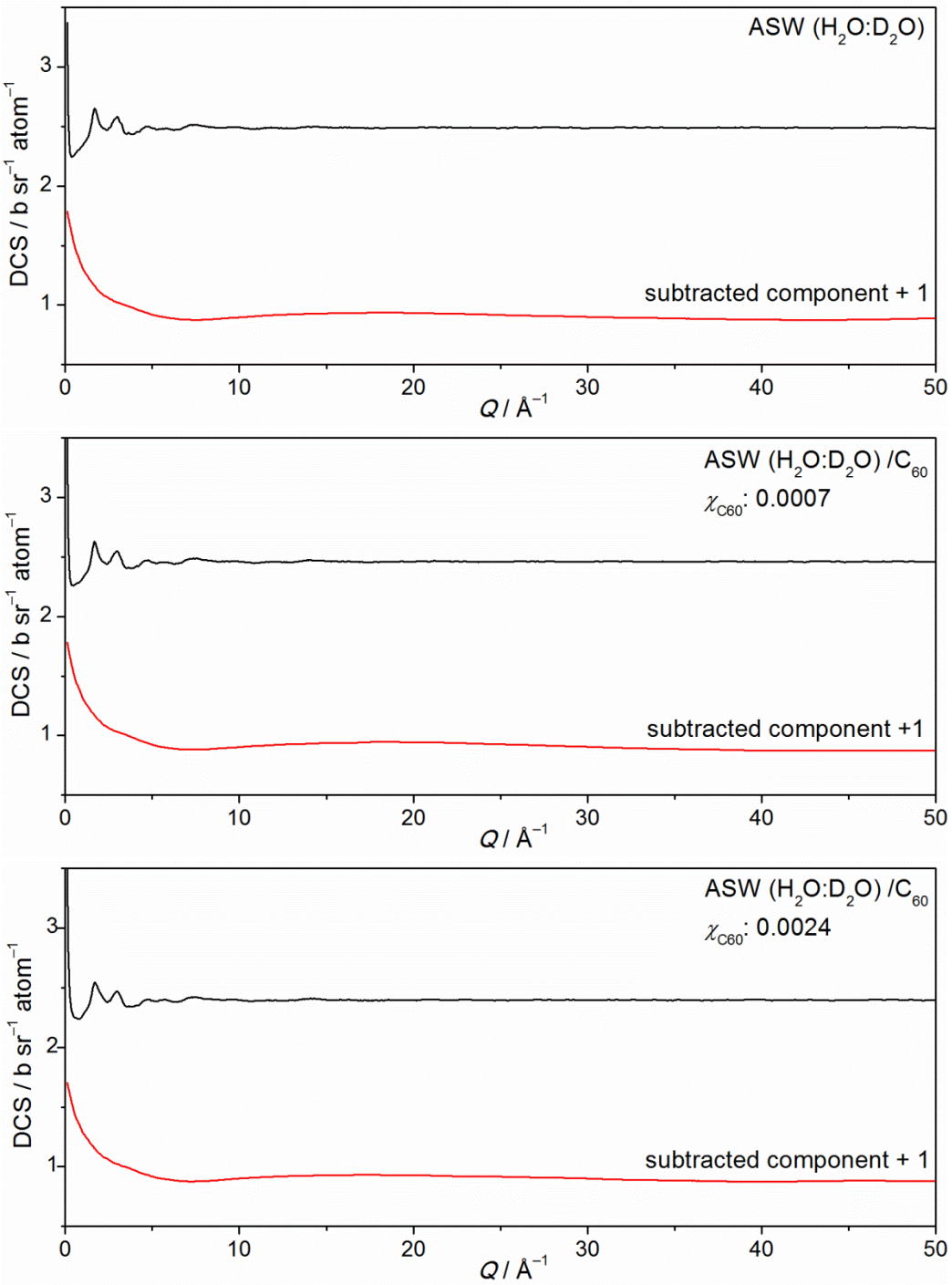

Appendix 9 DCS data for ASW/C_{60} 'trapped solution's corrected for attenuation and multiple scattering and inelasticity using *GudrunN* software. The component subtracted by the inelasticity correction is indicated by the red line.

APPENDIX 10 NEUTRON WEIGHTS FOR H/D SUBSTITUTED CHLOROFORM

	$CDCl_3$		$CHCl_3$		$C(H/D)Cl_3$	
C–C	0.0177	2%	0.0177	4	0.0177	3
C–Cl	0.1528	22%	0.1528	38	0.1528	28
C–H	0.0355	5%	-0.0199	-5	0.0078	1
Cl–Cl	0.3302	47%	0.3302	82	0.3302	61
Cl–H	0.1533	22%	-0.0860	-21	0.0338	6
H–H	0.0178	3%	0.0056	1	0.0009	0
$\langle b \rangle^2$	0.7072		0.4003		0.5431	
$\langle b^2 \rangle$	1.0121		2.1959		1.6035	
Av. DCS	1.126		2.157		1.624	

Appendix 10 Weighting factors in b sr^{-1} $atom^{-1}$ and weighting factors normalised by $\langle b \rangle 2 \times 10^{-2}$ indicating the contributions of each atom pair to the measured diffraction data of the three chloroform liquids. The coherent $\langle b^2 \rangle$ and total $\langle b^2 \rangle$ cross sections (b sr^{-1} $atom^{-1}$) are also indicated.

Appendix 11 Neutron Weights of H/D Substituted Chloroform-Acetone Azeotropes

	CD_3COCD_3 $CDCl_3$		CH_3COH_3 $CDCl_3$		CH_3COCH_3 $CHCl_3$		CD_3COCD_3 $CHCl_3$		$C(H/D)_3COC(H/D)$ $_3CDCl_3$		CD_3COCD_3 $C(H/D)Cl_3$		$C(H/D)_3COC(H/D)$ $_3C(H/D)Cl_3$	
C_o–C_o	0.0015	0 %	0.0015	1	0.0015	2	0.0015	0	0.0015	0	0.0015	0	0.0015	1
C_o–C_m	0.0059	1 %	0.0059	4	0.0059	7	0.0059	1	0.0059	2	0.0059	1	0.0059	2
C_o–H_a	0.0177	3 %	-0.0099	-7	-0.0099	-12	0.0177	4	0.0039	1	0.0177	4	0.0039	1
C_o–O	0.0026	0 %	0.0026	2	0.0026	3	0.0026	1	0.0026	1	0.0026	1	0.0026	1
C_m–C_m	0.0059	1 %	0.0059	4	0.0059	7	0.0059	1	0.0059	2	0.0059	1	0.0059	2
C_m–H_a	0.0353	7 %	-0.0198	-14	-0.0199	-24	0.0354	8	0.0077	3	0.0353	7	0.0077	3
C_m–O	0.0051	1 %	0.0051	4	0.0051	6	0.0051	1	0.0051	2	0.0051	1	0.0051	2
H_a–H_a	0.0532	10 %	0.0167	12	0.0168	20	0.0533	13	0.0026	1	0.0532	11	0.0025	1
H_a–O	0.0154	3 %	-0.0086	-6	-0.0087	-11	0.0155	4	0.0034	1	0.0154	3	0.0034	1
O–O	0.0011	0 %	0.0011	1	0.0011	1	0.0011	0	0.0011	0	0.0011	0	0.0011	0
C_c–C_c	0.0032	1 %	0.0032	2	0.0032	4	0.0032	1	0.0032	1	0.0032	1	0.0032	1
C_c–H_c	0.0064	1 %	0.0064	5	-0.0036	-4	-0.0036	-1	0.0064	2	0.0014	0	0.0014	1
C_c–Cl	0.0274	5 %	0.0274	19	0.0273	33	0.0273	7	0.0274	9	0.0274	6	0.0274	11
H_c–H_c	0.0032	1 %	0.0032	2	0.0010	1	0.0010	0	0.0032	1	0.0002	0	0.0002	0
H_c–Cl	0.0275	5 %	0.0275	20	-0.0154	-19	-0.0154	-4	0.0275	9	0.0060	1	0.0060	2
Cl–Cl	0.0590	11 %	0.0590	42	0.0589	72	0.0588	14	0.0591	19	0.0591	12	0.0592	23
C_o–C_c	0.0043	1 %	0.0043	3	0.0043	5	0.0043	1	0.0043	1	0.0043	1	0.0043	2
C_o–H_c	0.0043	1 %	0.0043	3	-0.0024	-3	-0.0024	-1	0.0043	1	0.0010	0	0.0010	0
C_o–Cl	0.0186	3 %	0.0186	13	0.0186	23	0.0186	4	0.0186	6	0.0186	4	0.0186	7
C_m–C_c	0.0086	2 %	0.0086	6	0.0086	11	0.0086	2	0.0086	3	0.0086	2	0.0086	3
C_m–H_c	0.0087	2 %	0.0087	6	-0.0049	-6	-0.0049	-1	0.0087	3	0.0019	0	0.0019	1
C_m–Cl	0.0372	7 %	0.0372	26	0.0372	45	0.0372	9	0.0372	12	0.0372	8	0.0372	14
H_a–C_c	0.0260	5 %	-0.0146	-10	-0.0146	-18	0.0260	6	0.0057	2	0.0260	5	0.0057	2
H_a–H_c	0.0261	5 %	-0.0146	-10	0.0082	10	-0.0146	-3	0.0057	2	0.0057	1	0.0013	0
H_a–Cl	0.1121	21 %	-0.0629	-45	-0.0628	-77	0.1120	27	0.0245	8	0.1121	23	0.0246	9
O–C_c	0.0038	1 %	0.0038	3	0.0038	5	0.0038	1	0.0038	1	0.0038	1	0.0038	1
O–H_c	0.0038	1 %	0.0038	3	-0.0021	-3	-0.0021	-1	0.0038	1	0.0008	0	0.0008	0
O–Cl	0.0163	3 %	0.0163	12	0.0162	20	0.0162	4	0.0163	5	0.0163	3	0.0163	6
$\langle b \rangle^2$	0.5400		0.1405		0.0820		0.4181		0.3077		0.4771		0.2609	
$\langle b^2 \rangle$	0.7348		2.7814		3.2840		1.2352		1.7588		0.9859		2.0094	
Av. DCS	0.7281		2.6246		3.0244		1.2184		1.7015		1.0037		1.9426	

Appendix 11 Weighting factors in b sr^{-1} $atom^{-1}$ and weighting factors normalised by $\langle b \rangle 2 \times 10^{-2}$ indicating the contributions of each atom pair to the measured diffraction data of the chloroform-acetone liquid mixtures. The coherent $\langle b^2 \rangle$ and total $\langle b^2 \rangle$ cross sections (b sr^{-1} $atom^{-1}$) are also indicated.

Appendix 12 Neutron Weights of H/D Substituted Benzene-Methanol Azeotropes

	C_6D_6: CD_3OD		C_6D_6: CD_3OH		C_6D_6: $CD_3O(H/D)$		C_6H_6: CD_3OD		$C_6(H/D)_6$: CD_3OD		C_6H_6: CD_3OH		$C_6(H/D)_6$: $CD_3O(H/D)$		C_6H_6: CH_3OH		$C_6(H/D)_6$: $C(H/D)_3O(H/D)$	
C_b-C_b	0.0426	10%	0.0425	12	0.0422	11	0.0425	37	0.0424	17	0.0426	57	0.0425	19	0.0422	771	0.0425	31
C_b-C_m	0.0173	4%	0.0173	5	0.0174	4	0.0173	15	0.0173	7	0.0173	23	0.0173	8	0.0174	313	0.0173	13
C_b-O	0.0151	3%	0.0151	4	0.0152	4	0.0151	13	0.0151	6	0.0151	20	0.0151	7	0.0152	274	0.0151	11
C_b-H_b	0.0855	20%	0.0852	24	0.0848	22	-0.0478	-42	0.0188	8	0.0855	-64	0.0852	9	0.0848	-867	-0.0478	14
C_b-H_m	0.0522	12%	0.0522	15	0.0523	13	0.0522	46	0.0522	21	0.0522	71	0.0522	24	0.0523	-529	0.0522	9
C_b-H_o	0.0174	4%	-0.0098	-3	0.0038	1	0.0174	15	0.0174	7	0.0174	-13	-0.0098	2	0.0038	-176	0.0174	3
C_m-C_m	0.0018	0%	0.0018	1	0.0018	0	0.0018	2	0.0018	1	0.0018	2	0.0018	1	0.0018	32	0.0018	1
C_m-O	0.0031	1%	0.0031	1	0.0031	1	0.0031	3	0.0031	1	0.0031	4	0.0031	1	0.0031	56	0.0031	2
C_m-H_b	0.0174	4%	0.0174	5	0.0174	4	-0.0098	-9	0.0038	2	0.0174	-13	0.0174	2	0.0174	-176	-0.0098	3
C_m-H_m	0.0106	2%	0.0107	3	0.0108	3	0.0107	9	0.0107	4	0.0106	14	0.0107	5	0.0108	-108	0.0107	2
C_m-H_o	0.0035	1%	-0.0020	-1	0.0008	0	0.0036	3	0.0036	1	0.0035	-3	-0.0020	0	0.0008	-36	0.0036	1
O-O	0.0013	0%	0.0014	0	0.0014	0	0.0013	1	0.0014	1	0.0013	2	0.0014	1	0.0014	24	0.0013	1
O-H_b	0.0152	3%	0.0152	4	0.0152	4	-0.0085	-7	0.0034	1	0.0152	-12	0.0152	2	0.0152	-154	-0.0085	2
O-H_m	0.0093	2%	0.0093	3	0.0094	2	0.0093	8	0.0093	4	0.0093	13	0.0093	4	0.0094	-94	0.0093	2
O-H_o	0.0031	1%	-0.0017	0	0.0007	0	0.0031	3	0.0031	1	0.0031	-2	-0.0017	0	0.0007	-31	0.0031	1
H_b-H_b	0.0429	10%	0.0428	12	0.0426	11	0.0135	12	0.0021	1	0.0429	18	0.0428	1	0.0426	244	0.0135	2
H_b-H_m	0.0524	12%	0.0524	15	0.0525	13	-0.0294	-26	0.0116	5	0.0524	-40	0.0524	5	0.0525	298	-0.0294	2
H_b-H_o	0.0175	4%	-0.0098	-3	0.0039	1	-0.0098	-9	0.0039	2	0.0175	7	-0.0098	0	0.0039	99	-0.0098	1
H_m-H_m	0.0160	4%	0.0161	5	0.0162	4	0.0161	14	0.0161	6	0.0160	22	0.0161	7	0.0162	91	0.0161	1
H_m-H_o	0.0107	2%	-0.0060	-2	0.0024	1	0.0107	9	0.0107	4	0.0107	-8	-0.0060	1	0.0024	61	0.0107	0
H_o-H_o	0.0018	0%	0.0006	0	0.0001	0	0.0018	2	0.0018	1	0.0018	1	0.0006	0	0.0001	10	0.0018	0
$\langle b \rangle^2$	0.4365		0.3537		0.3939		0.1141		0.2496		0.0741		0.2177		0.0055		0.1350	
$\langle b^2 \rangle$	0.5287		0.9035		0.7168		2.3640		1.4444		2.7366		1.6319		3.8621		2.1955	
Av. DCS	0.572		0.937		0.827		2.298		1.486		2.640		1.643		3.869		2.116	

Appendix 11 Weighting factors in b sr^{-1} $atom^{-1}$ and weighting factors normalised by $\langle b \rangle 2 \times 10^{-2}$ indicating the contributions of each atom pair to the measured diffraction data of the benzene-methanol liquid mixtures. The coherent $\langle b^2 \rangle$ and total $\langle b^2 \rangle$ cross sections (b sr^{-1} $atom^{-1}$) are also indicated.

Appendix 13 DCS Data for the Chloroform Liquids

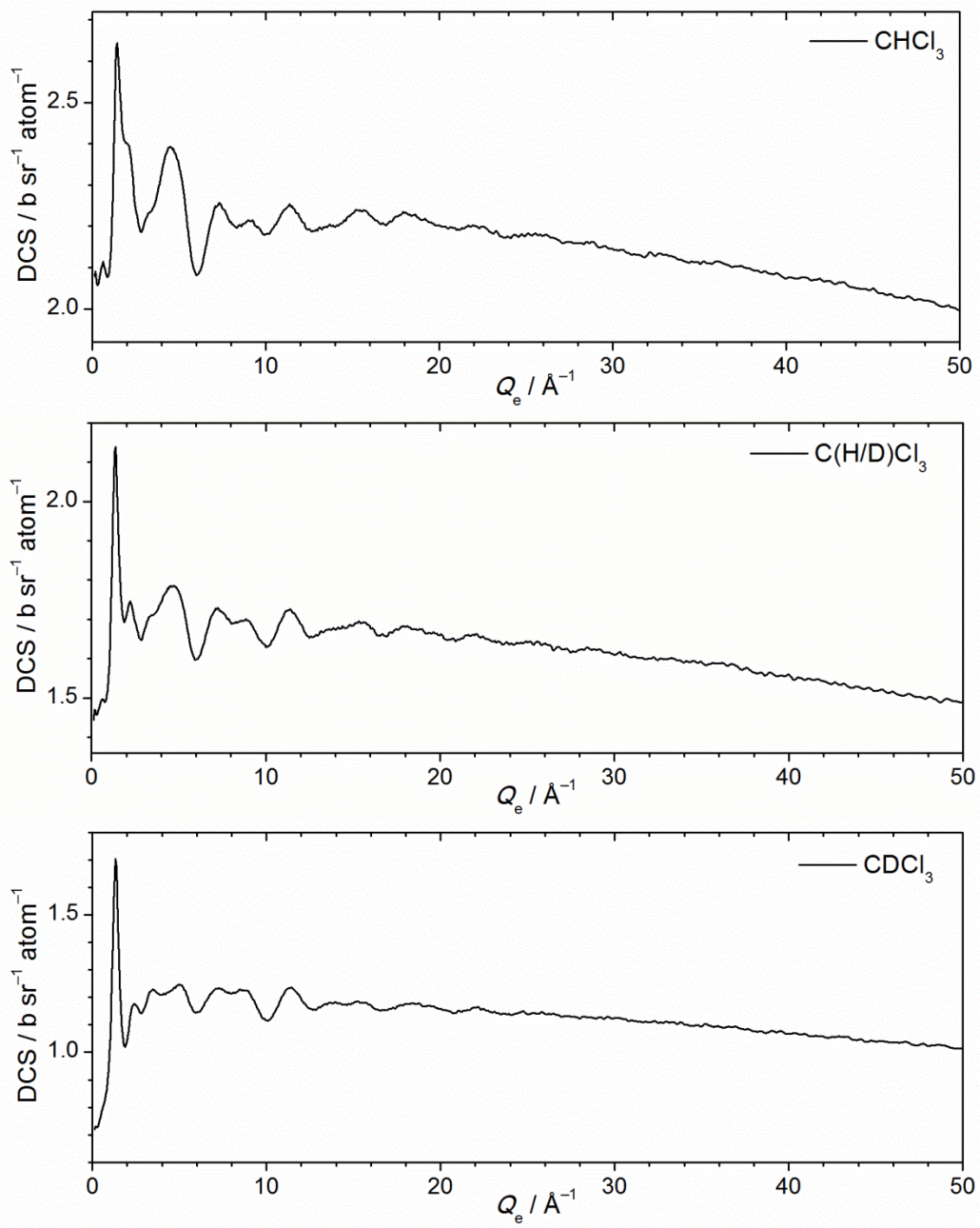

Appendix 13 DCS for $CHCl_3$,$C(H/D)Cl_3$ and $CDCl_3$ corrected for attenuation and multiple scattering.

APPENDIX 14 INELASTICITY CORRECTED DCS DATA FOR CHLOROFORM

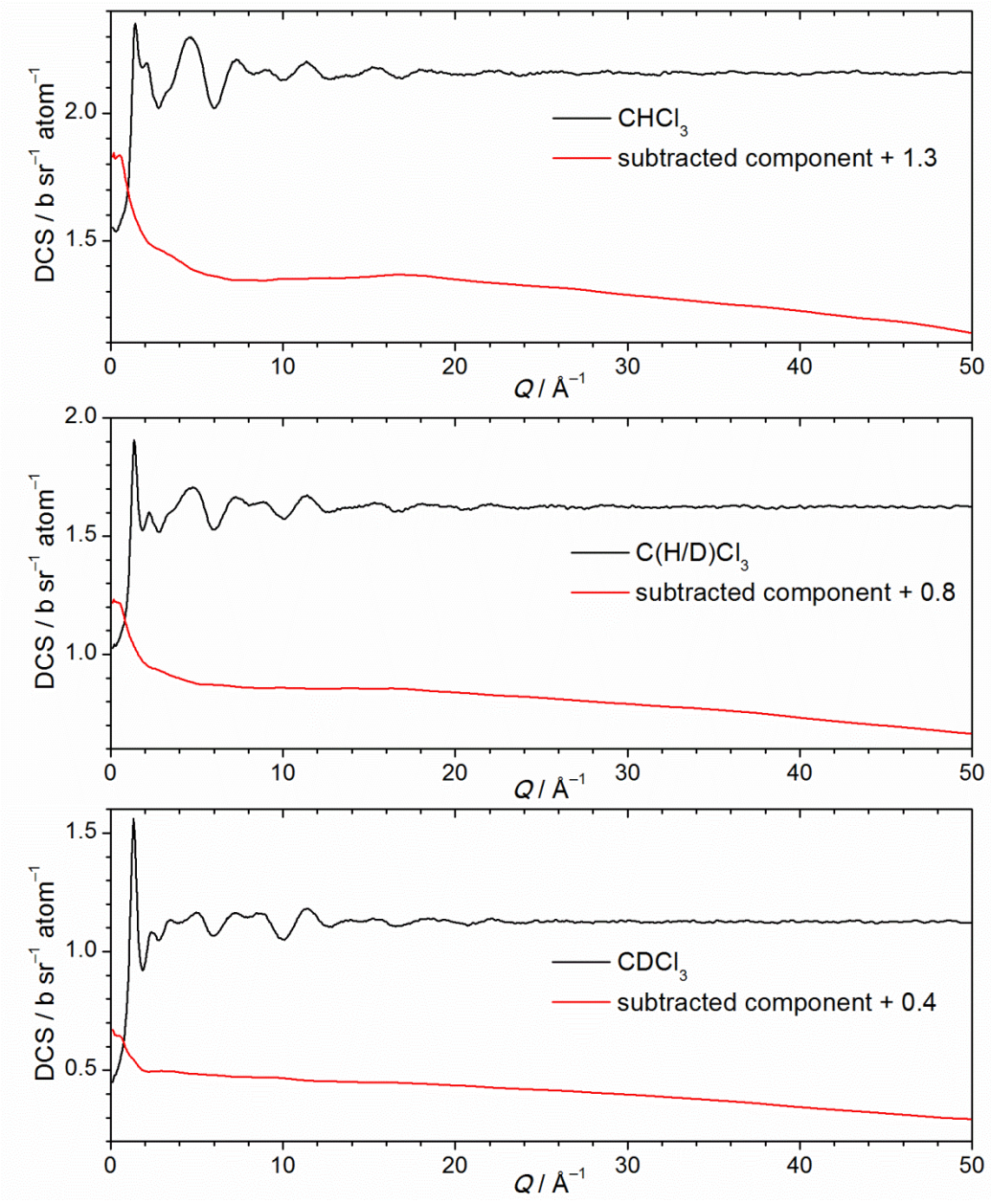

Appendix 14 DCS for $CHCl_3$,$C(H/D)Cl_3$ and $CDCl_3$ corrected for attenuation, multiple scattering and inelasticity. The perturbations removed in the inelasticity correction are indicated by the red line.

Appendix 15 DCS data of the Chloroform-Acetone Azeotrope

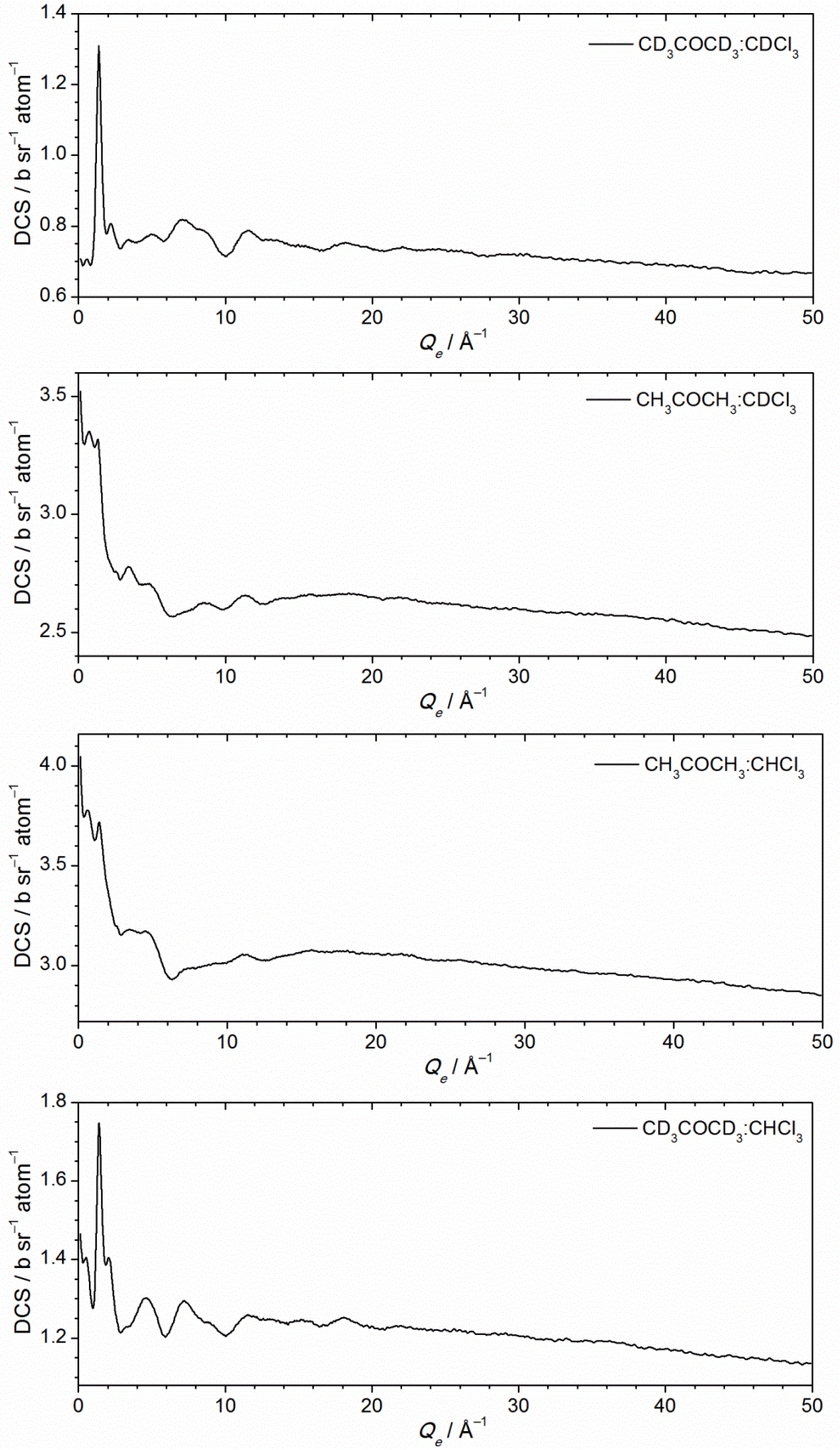

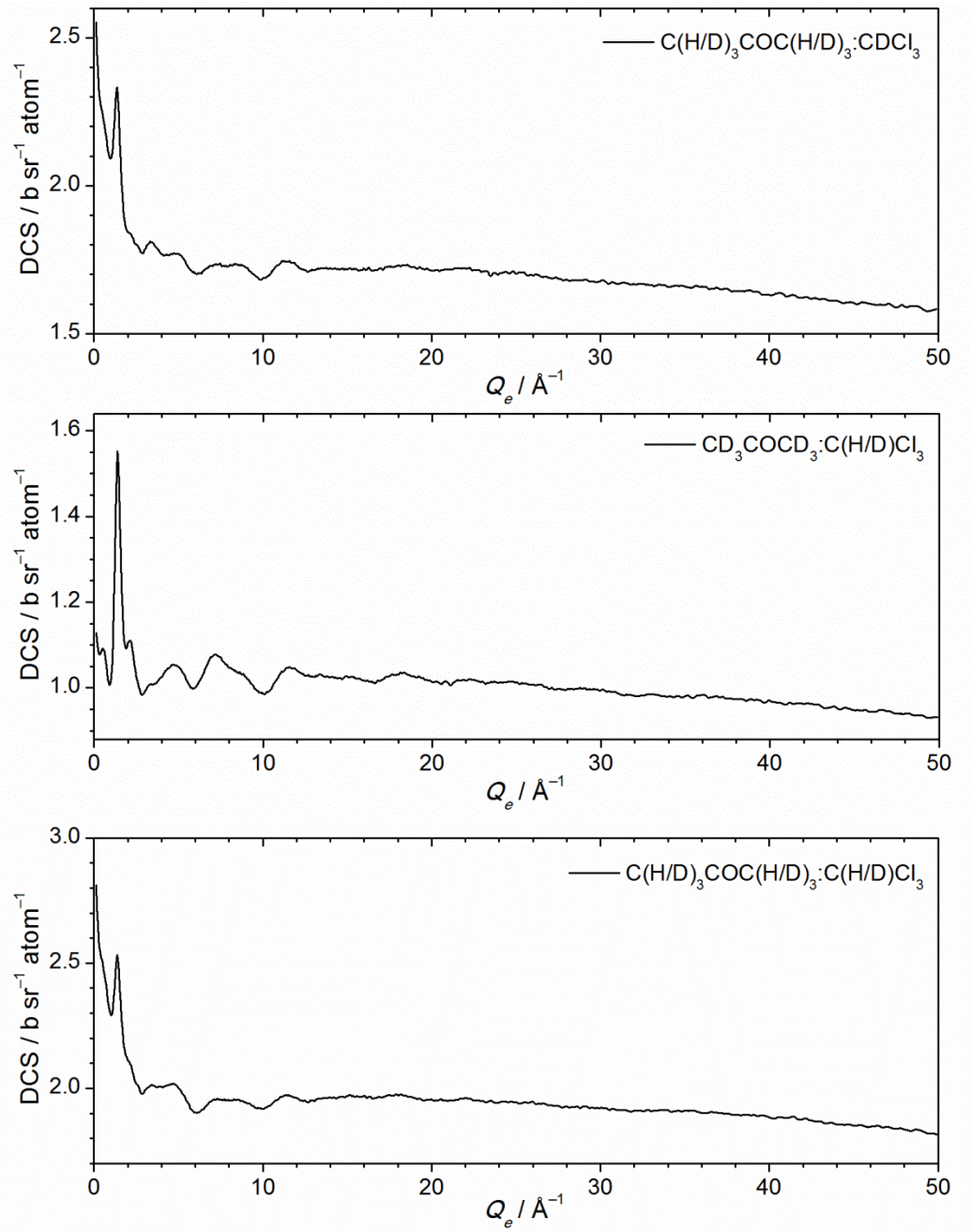

Appendix 15 DCS for chloroform-acetone azeotrope liquid mixtures corrected for attenuation and multiple scattering.

Appendix 16 Inelasticity Corrected DCS Data of the Chloroform-Acetone Azeotropes

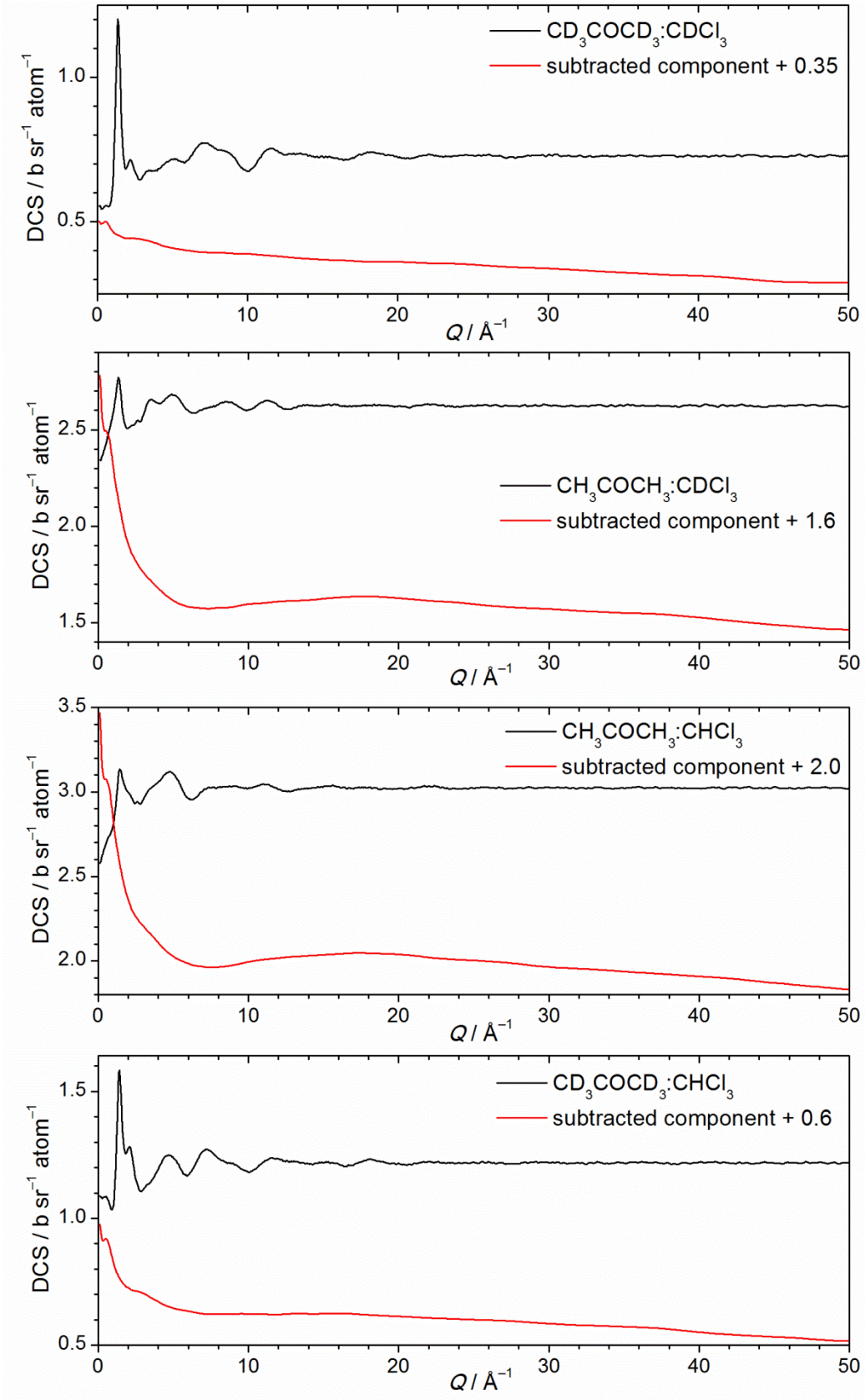

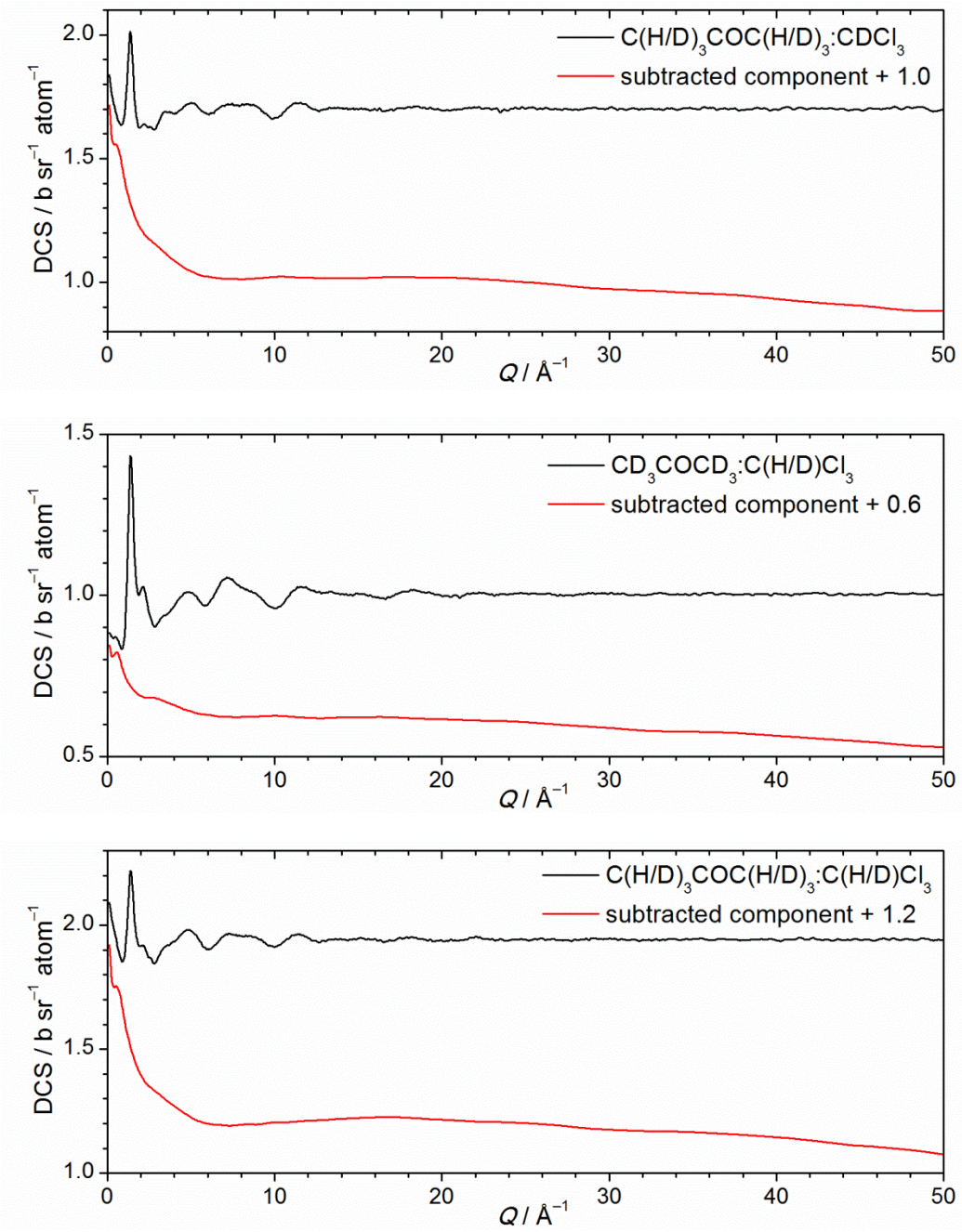

Appendix 16 DCS for chloroform-acetone azeotrope liquid mixtures corrected for attenuation, multiple scattering and inelasticity. The perturbations removed in the inelasticity correction are indicated by the red line.

Appendix 17 DCS Data of the H/D Substituted Benzene-Methanol Azeotropes

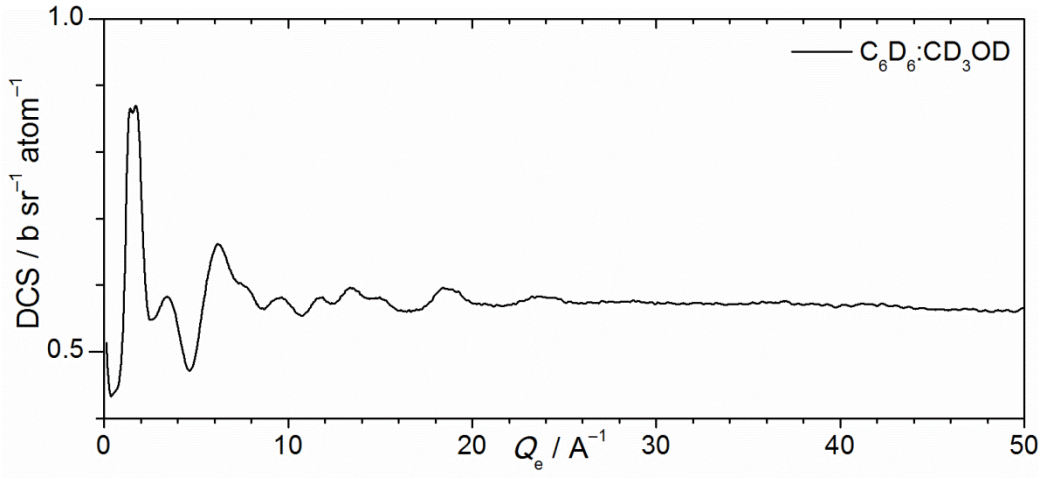

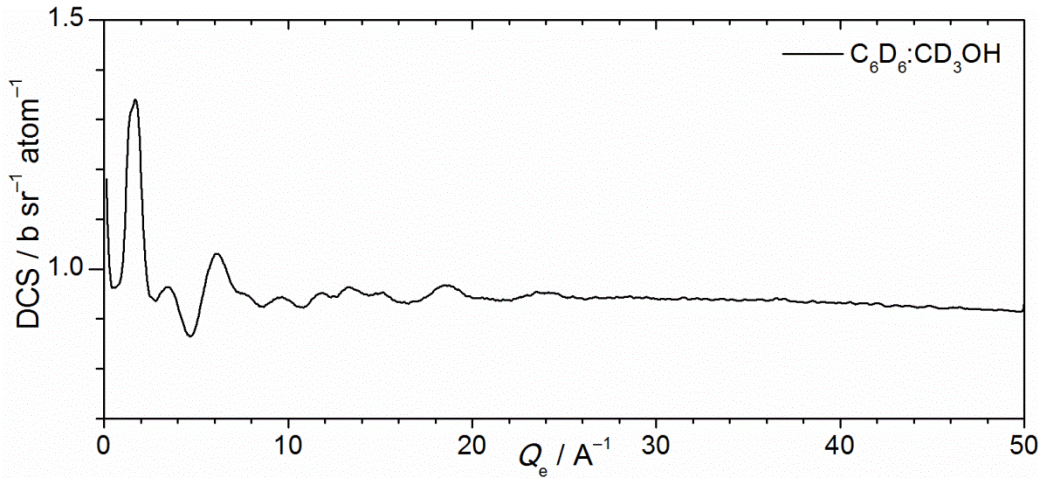

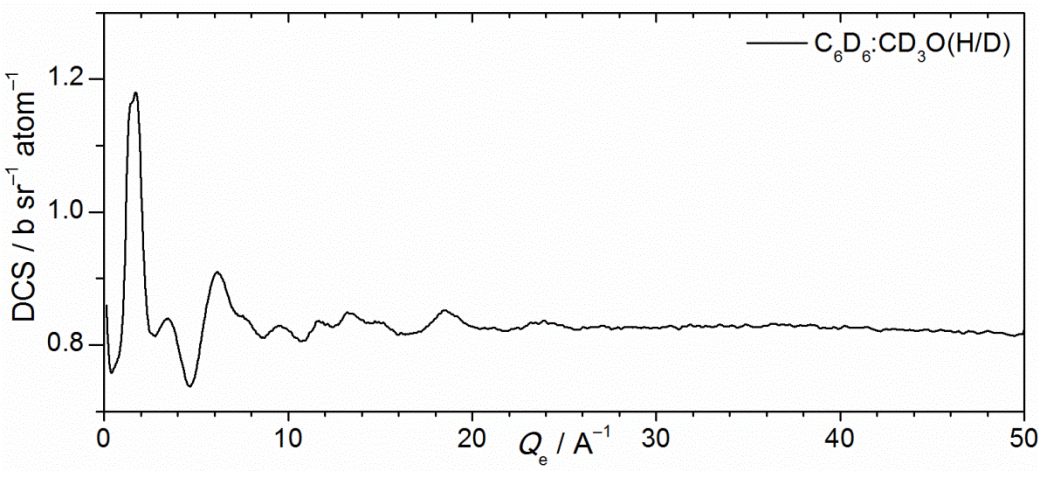

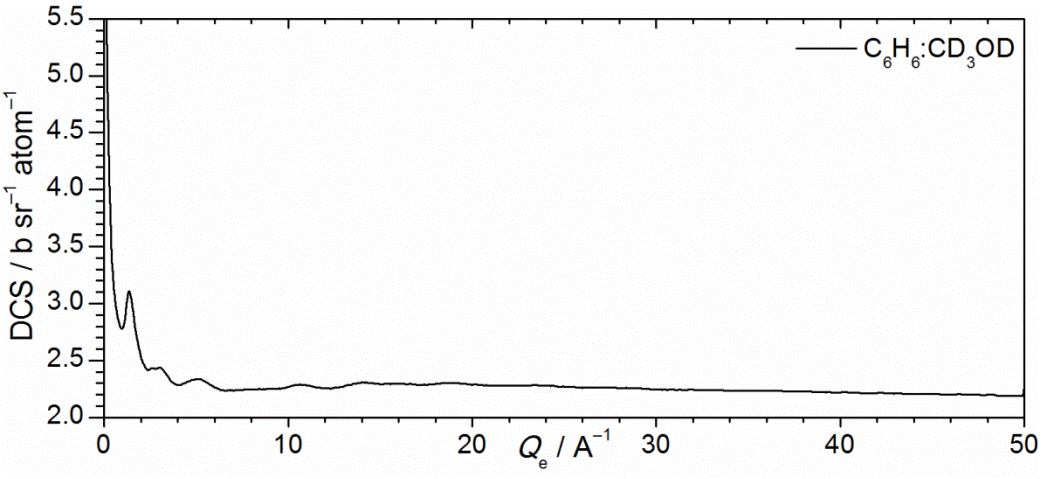
C6H6:CD3OD
DCS / b sr−1 atom−1
Qe / A−1
5.5
5.0
4.5
4.0
3.5
3.0
2.5
2.0
0
10
20
30
40
50

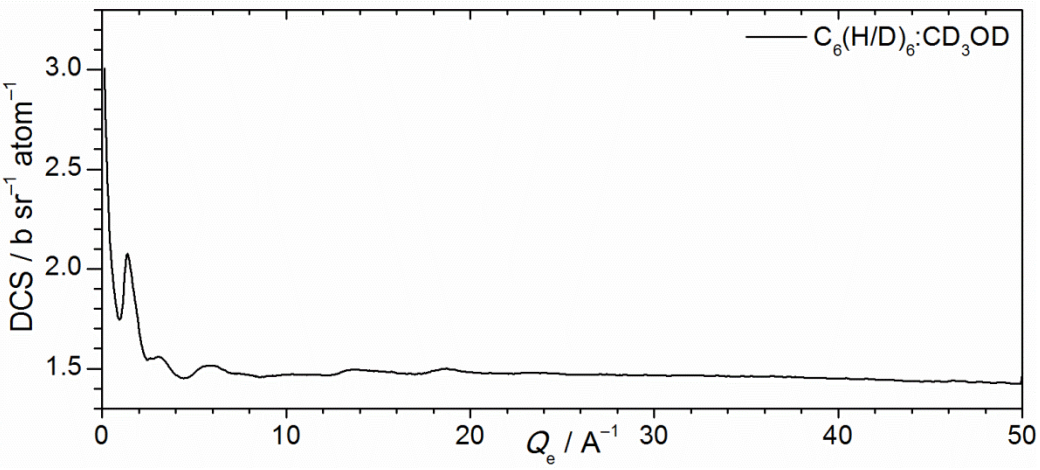
C6(H/D)6:CD3OD
DCS / b sr−1 atom−1
Qe / A−1
3.0
2.5
2.0
1.5
0
10
20
30
40
50

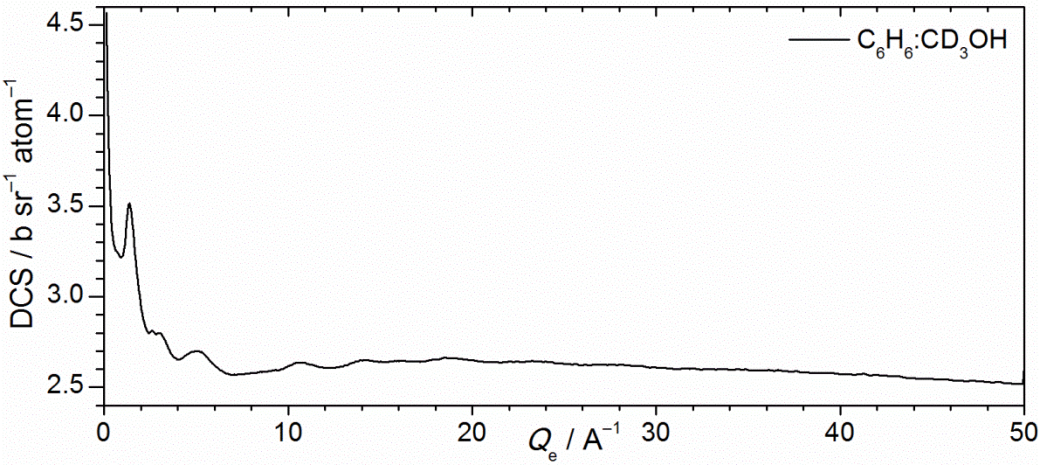
C6H6:CD3OH
DCS / b sr−1 atom−1
Qe / A−1
4.5
4.0
3.5
3.0
2.5
0
10
20
30
40
50

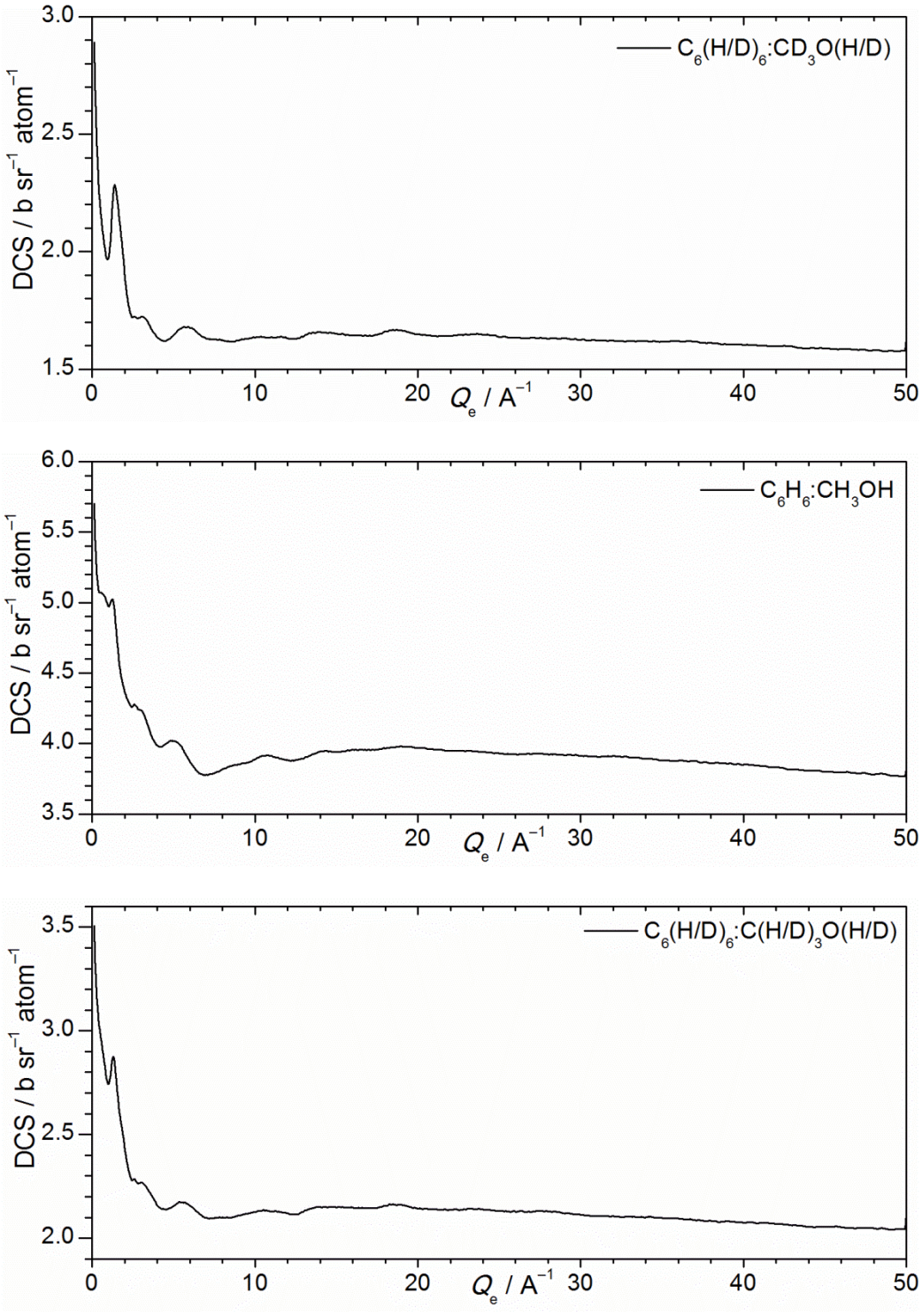

Appendix 17 DCS for benzene-methanol azeotrope liquid mixtures corrected for attenuation and multiple scattering.

Appendix 18 Inelasticity Corrected DCS Data of the Benzene-Methanol Azeotropes

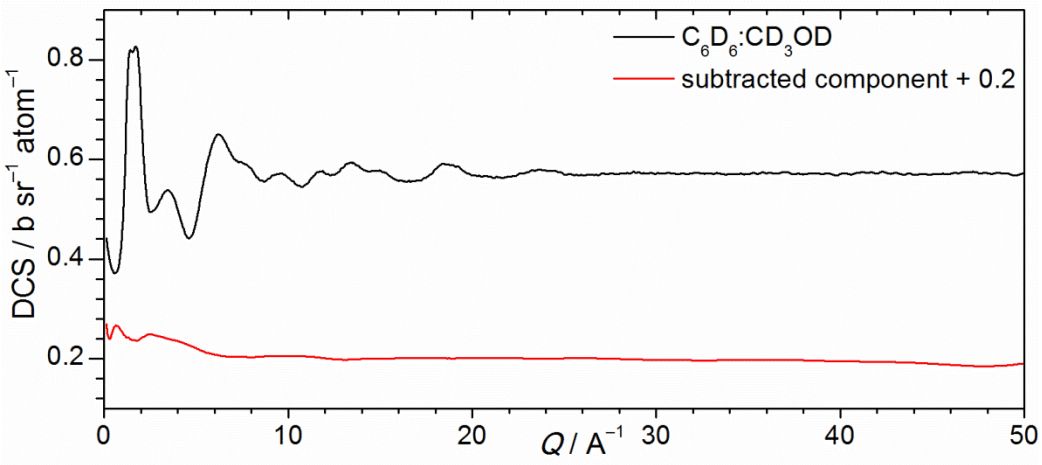

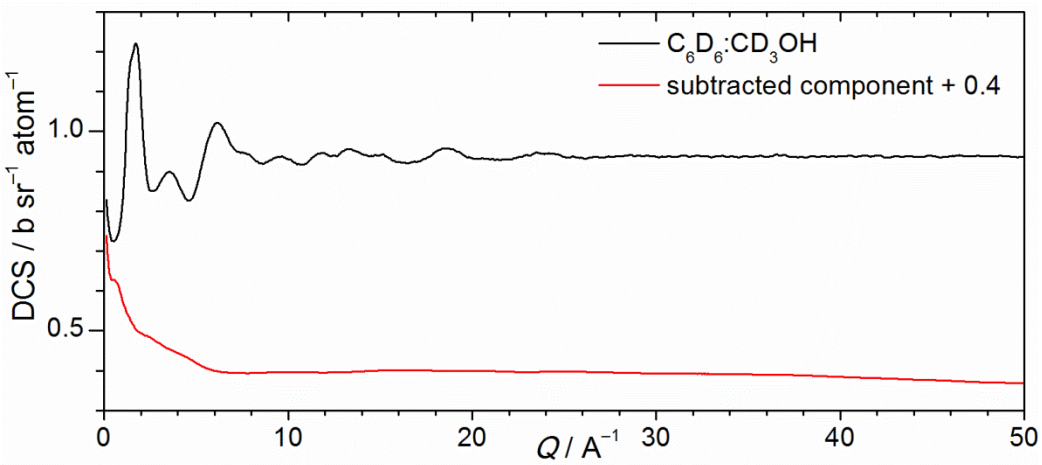

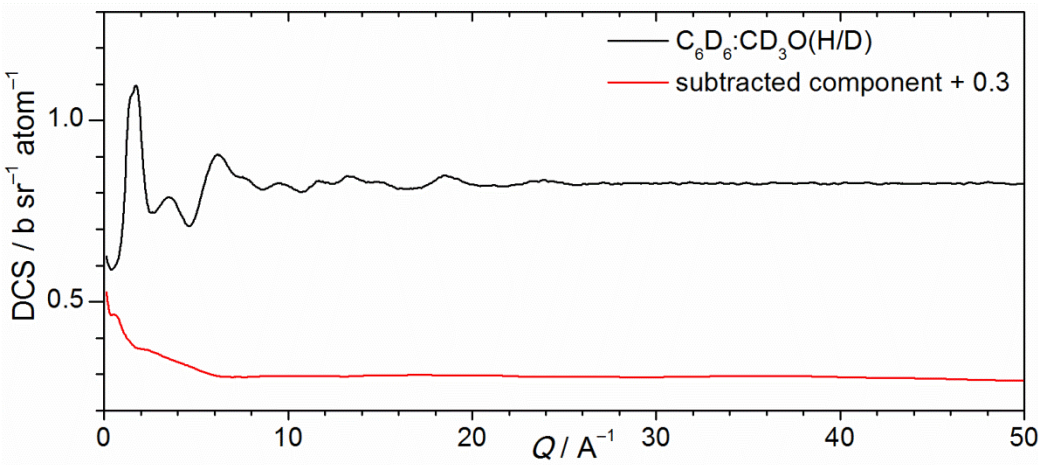

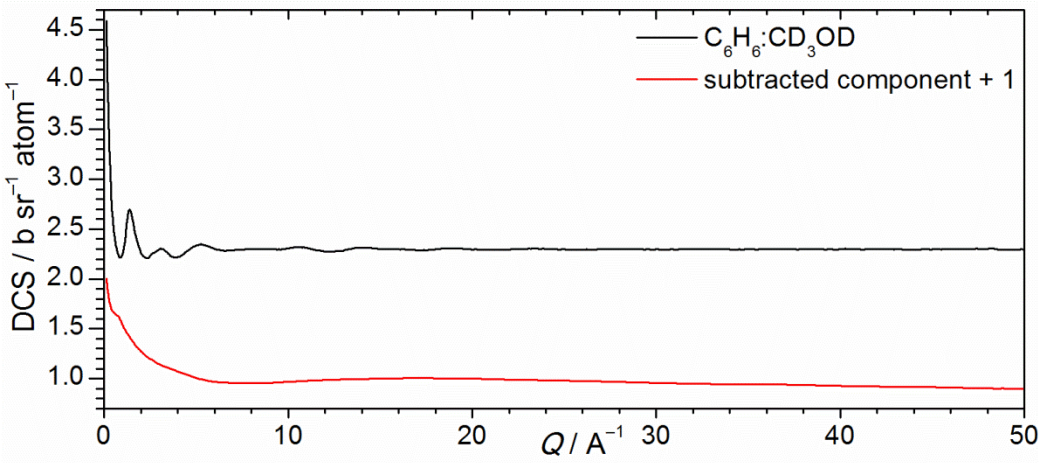
C6H6:CD3OD
subtracted component + 1
DCS / b sr−1 atom−1
Q / A−1

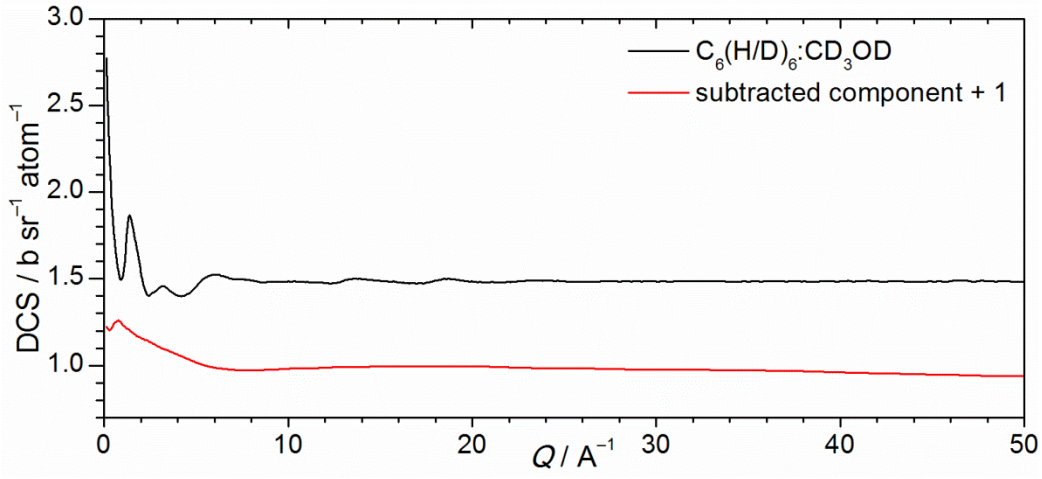
C6(H/D)6:CD3OD
subtracted component + 1
DCS / b sr−1 atom−1
Q / A−1

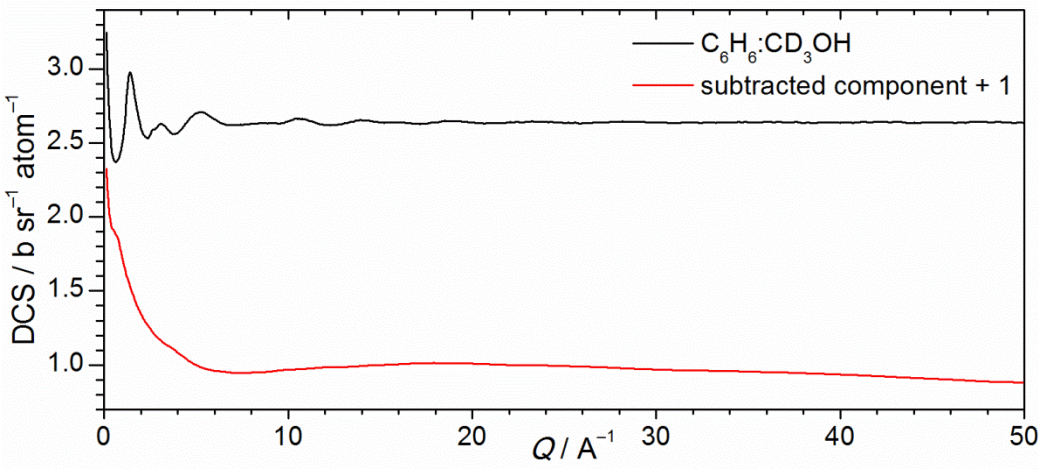
C6H6:CD3OH
subtracted component + 1
DCS / b sr−1 atom−1
Q / A−1

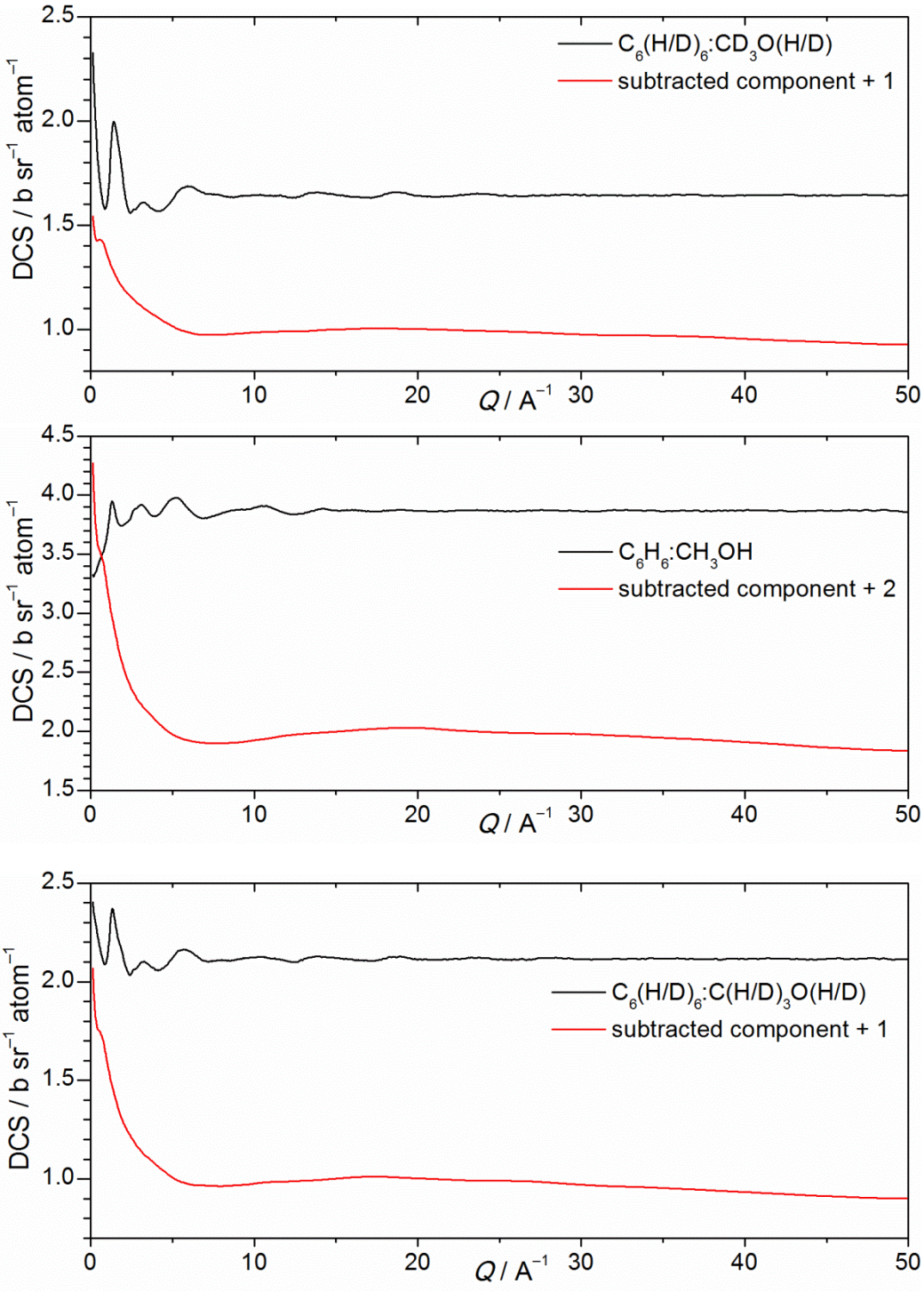

Appendix 18 DCS for benzene-methanol azeotrope liquid mixtures corrected for attenuation, multiple scattering and inelasticity. The perturbations removed in the inelasticity correction are indicated by the red line.

Appendix 19 EPSR Separation of Chloroform Liquid Intra and Intermolecular S(Q) and G(r)

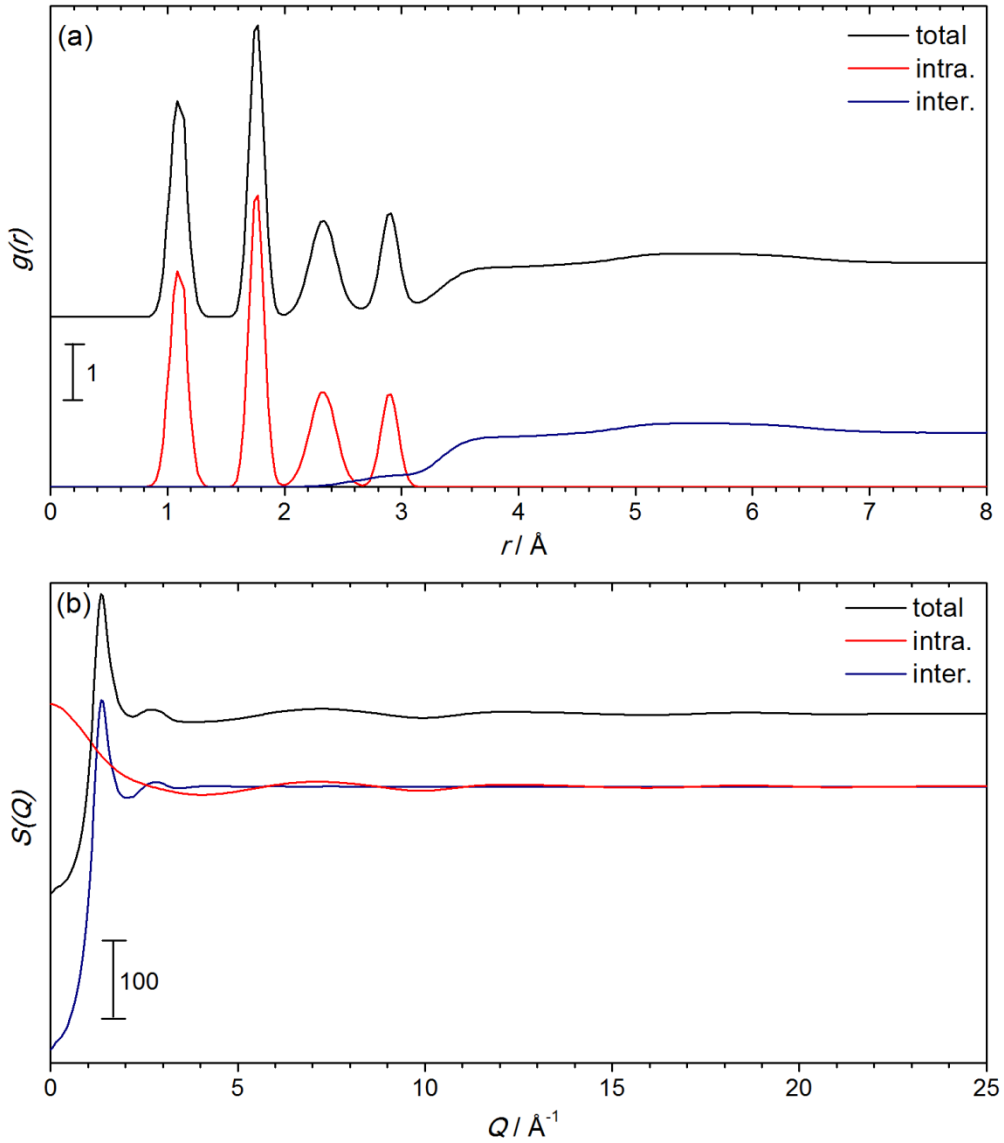

Appendix 19 EPSR separation of pure chloroform liquid intra- and intermolecular components of (a) the *G(r)* and (b) the *S(Q)*.

Appendix 20 EPSR Separation of Chloroform-Acetone Azeotrope Intra/Intermolecular S(Q) and G(R)

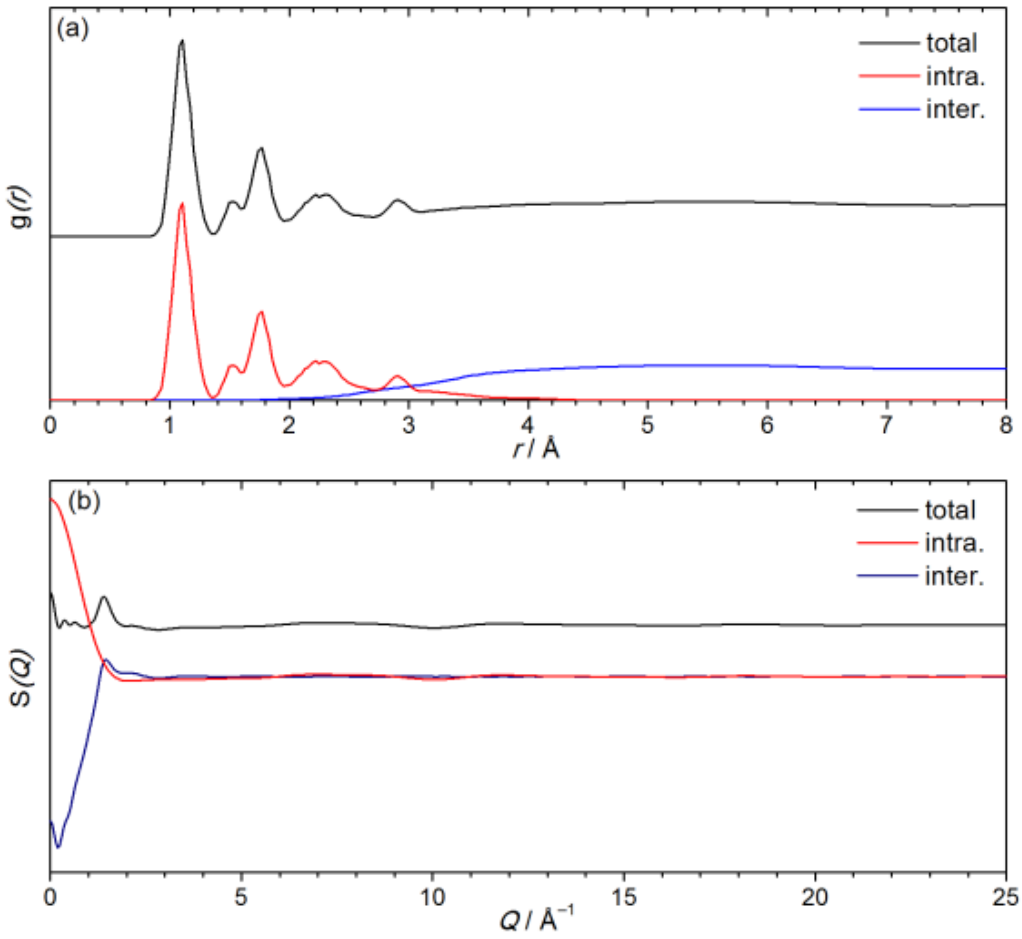

Appendix 20 EPSR separation of chloroform-acetone azeotrope intra- and intermolecular components of (a) the *G(r)* and (b) the *S(Q)*.

APPENDIX 21 'SUPER-DIPOLE' CALCULATIONS

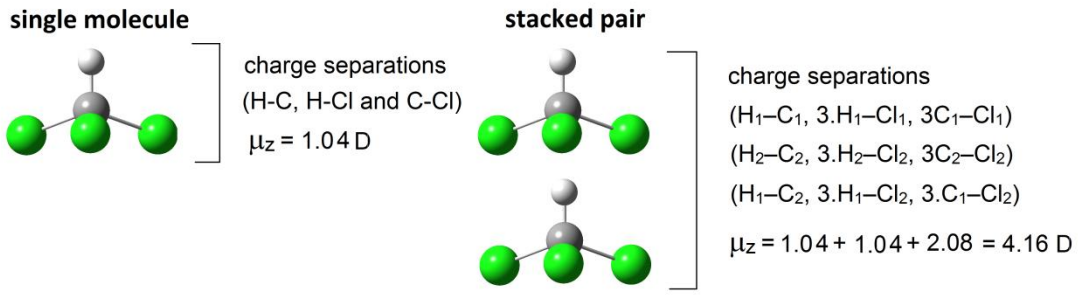

Appendix 21 Calculations indicating the impact of dipole alignment of the chloroform's effective moment. For perfectly aligned molecules the relationship between the effective dipole moment and the chain length is a straightforward summation (*i.e.* effective dipole moment = gas phase dipole moment × stack length).

APPENDIX 22 LOW-TEMPERATURE XRD OF THE CHLOROFORM-ACETONE AZEOTROPE

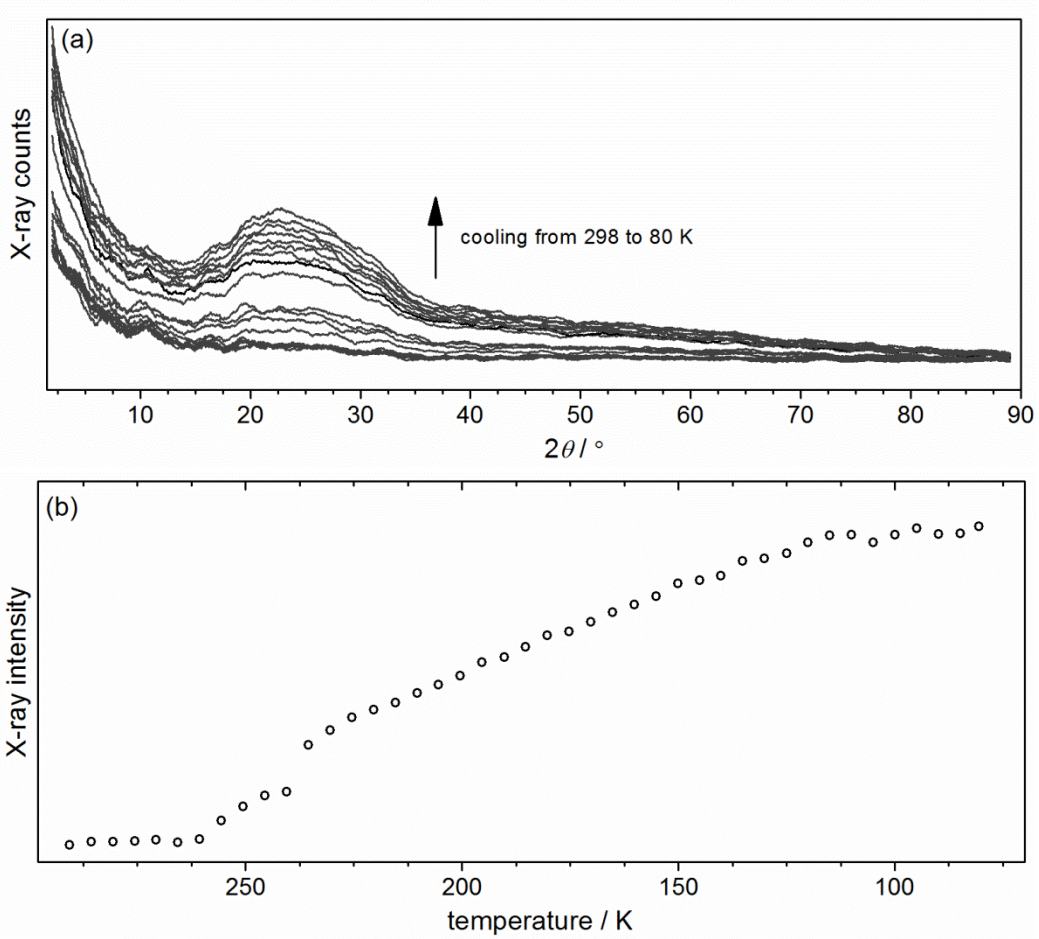

Appendix 22 (a) Smoothed X-ray diffraction patterns of the chloroform-acetone azeotrope recorded as a filled sealed capillary was cooled from room temperature to 80 K at 15 K h^{-1} using a cryostream, and (b) the variation in intensity at 25° with temperature.

Appendix 23 Low-Temperature XRD of the Benzene-Methanol Azeotrope

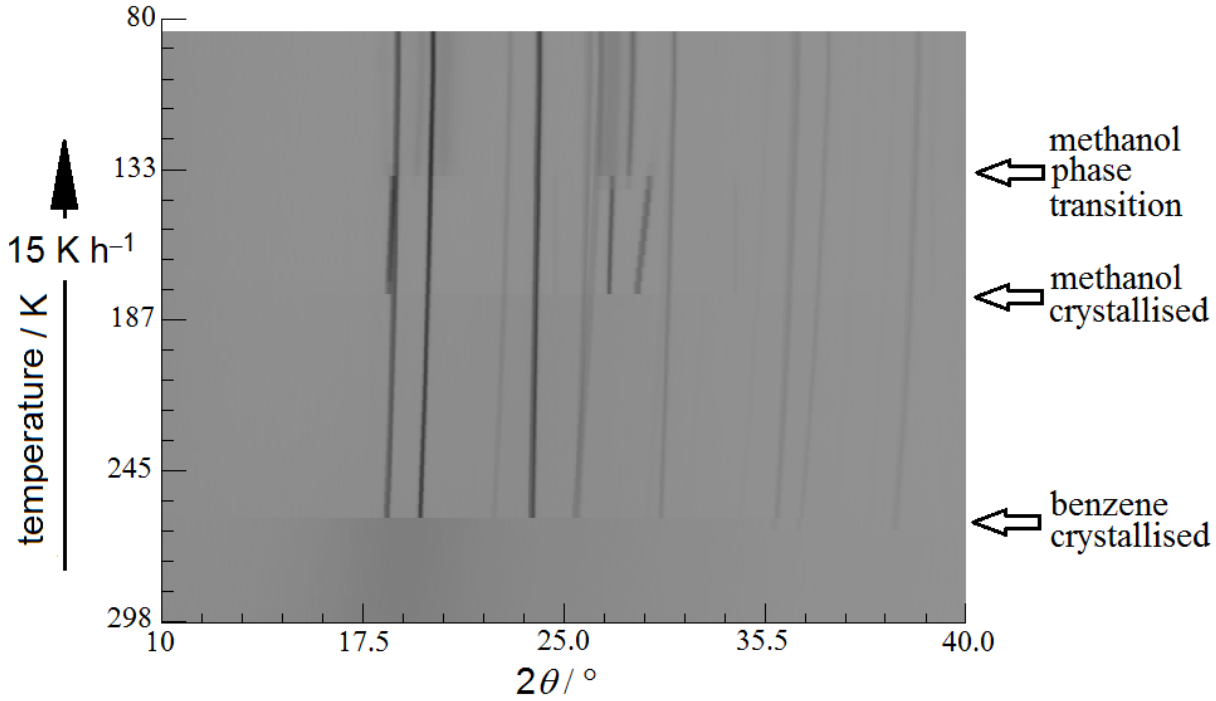

Appendix 22 (a) contour plot showing changes in the X-ray diffraction pattern of the benzene-methanol azeotrope as a filled sealed capillary was cooled from room temperature to 85 K using a cryostream. The temperature at which the benzene[412] and methanol[413] crystallised as well as the temperature of a methanol crystal-crystal phase transition[414] are indicated by the arrows.

APPENDIX 24 SANDALS PROPOSAL SUBMITTED ON 19.4.2011

C_{60} fullerene as a nanoprobe for the detection of the sintering and glass-transition behaviour of amorphous solid water

Amorphous solid water (ASW) is the most abundant form of ice in the universe.[1] It forms as a highly microporous solid from the vapour phase on cold dust particles and grains.[2] Despite its importance in critical cosmological processes,[1] we still have an incomplete understanding of its sintering and glass-transition behaviour upon heating.

1. **Sintering:** ASW, as prepared by vapour deposition onto a substrate at 77 K, has a surface area of several hundred m^2 g^{-1}.[2] Upon heating to 113 K, the surface area decreases to 40 m^2 g^{-1}, which is seen as an exothermic feature in calorimetric measurements.[3] It has been found that the sintering can lead to trapping of gases within the amorphous ice. Due to the inaccessibility of those 'sealed' cavities for gas-adsorption studies, the fate of the internal voids upon further heating is unclear.
2. **Glass-transition:** Just like for the structurally very similar hyper-quenched glassy water (HGW),[4] it was suggested, on the basis of calorimetric data, that ASW exhibits a glass-transition at 136 K with a ΔC_P of 1.9 J K^{-1} mol^{-1}.[3] ASW and HGW are therefore thought to undergo transitions to the highly viscous and deeply supercooled liquid around 136 K. However, other scenarios have also been suggested, and it has been argued that the real glass transition of water should be at much higher temperatures.[5-6] At present, there is still no widely accepted view of the origin of the heat capacity increase at 136 K in the amorphous ices.

New insights into the sintering and glass-transition behaviour of ASW will lead to a better understanding of gas-adsorption processes onto ASW in space and the chemical properties of ASW as a matrix material. The glass-transition behaviour of ASW has been fiercely debated.[5-6] New experimental data will therefore be of significant interest to scientists working in the field of glasses and amorphous solids.

The aim of the proposed measurements is to follow the sintering processes and glass-transition behaviour of ASW by using hydrophobic C_{60} molecules, embedded within the amorphous matrix, as nanoprobes. Wide-Q range data will be measured for the first time for as-made ASW.

By concurrently depositing C_{60} and water from the vapour phase onto a substrate at 77 K in a purpose-built high-vacuum chamber we are able to produce four grams of ASW per day containing C_{60} fullerene molecules finely dispersed within the amorphous matrix. The ASW samples have been characterised by Raman spectroscopy and powder X-ray diffraction in our lab (*cf.* Fig. 1). The broad reflections at ~23° and ~44° in (a), the XRD pattern, and the shape and position of the OH stretching band in (b), the Raman spectrum, are typical for ASW.[7-8]

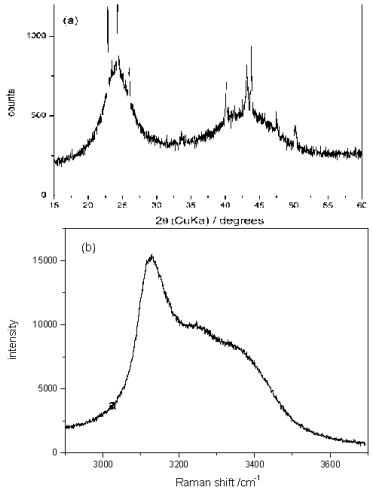

Figure 1 (a) XRD pattern (CuKα) and (b) Raman spectrum in the O-H stretching region of ASW films prepared by deposition of water vapour onto silicon substrates (511) at ~ 90 K. The sharp Bragg peaks in (a) arise from the formation of small amounts of ice I*h* during sample transfer. For neutron diffraction measurements samples will be free of crystalline impurities.

We propose to characterise ASW / C_{60} mixtures on the NIMROD instrument. On the one hand, we will be able to follow changes in the pore-size distribution from the high-Q data. Furthermore, it will be possible to determine the

local structural correlation between C_{60} and the supporting H-bonded glassy network by using the Empirical Potential Structure Refinement (EPSR) technique (*i.e.* from the integration to the next-neighbour distance in the C-O pair distribution function).[9] Above the glass-transition temperature, we expect C_{60} to become more hydrated due to the transition of the matrix to the liquid. The spherical nature and the sixty equivalent carbon atoms make C_{60} an ideal nanoprobe for the detection of the sintering and glass-transition behaviour of ASW. After completing the measurements of the amorphous samples, we would also like to follow the expected phase separation of the highly supersaturated solutions upon crystallisation. The proposed thermal treatments are shown schematically in Fig. 2.

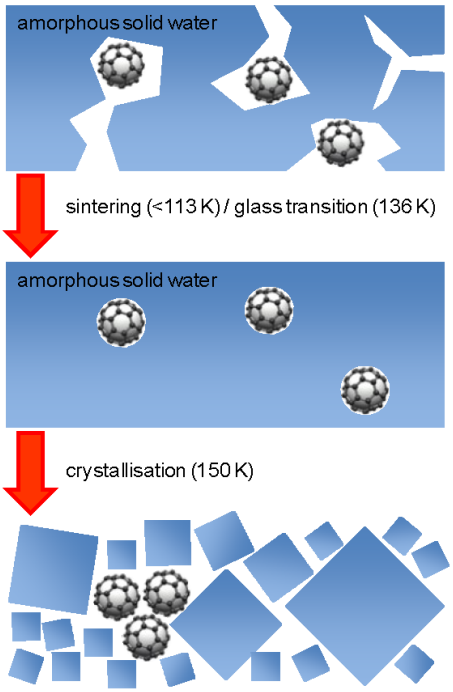

Figure 2 Schematic illustration of the processes expected to occur upon heating of amorphous solid water containing matrix-isolated C_{60} fullerene molecules.

Summary of questions to be addressed in this experiment:

- How does the pore-size distribution of ASW change upon heating?
- How does the local structure around the C_{60} molecules change after annealing above the glass transition temperature of the matrix?
- Does crystallisation of the matrix lead to phase separation (ice / C_{60})?

Experimental

To answer these questions we plan to measure neutron diffraction structure factors (Q-range: 0.02 $Å^{-1}$ – 100$Å^{-1}$) of pure ASW and ASW containing a 0.02 mole fraction of C_{60} (500 water molecules per C_{60}) on the NIMROD instrument in a helium cryostat. The total number of samples measured would be seven (1× pure H_2O ASW, 3× as-made ASW containing C_{60}, and 3× ASW containing C_{60} annealed at 140 K in our vacuum chamber). Hydrogen/deuterium substitution will be used to help estimate the partial structure factors from the measured composite structure factor. To this end, we will prepare samples containing 0, 50 and 100 mole % D_2O for the ASW / C_{60} mixtures. All seven samples will be characterised at 80 K. Two samples (pure H_2O ASW and the as-made H_2O ASW / C_{60} mixture) will be measured additionally at 80 K after successive heating to 120, 140 and 160 K.

A total beam time of 72 hours is requested to carry out the 13 measurements as well as sample transfers and heating/cooling cycles. 12 hours are required for recording standards and backgrounds. The samples will be transferred into standard vanadium sample holders immediately after preparation in Durham and will be transported to ISIS in liquid nitrogen. Our group has extensive experience with sample transfers under liquid nitrogen conditions from previous ISIS experiments.[10-11]

Justification

The wide range of momentum transfers available on the NIMROD instrument is expected to enable the precise determination of structure factors, which are required for an accurate structural refinement using EPSR. The high-Q data is essential to follow changes in the pore-size distribution of ASW.

References

[1] S. Kwok, University Science Books (2007)
[2] E. Mayer *et al.*, *Nature* **319**, 298 (1986).
[3] A. Hallbrucker *et al.*, *J. Phys. Chem.* **93**, 4986 (1989).
[4] D. T. Bowron *et al.*, *J. Chem. Phys.* **125**, 194502 (2006).
[5] Y. Yue *et al.*, *Nature* **427**, 717 (2004).
[6] C. A. Angell, *Science* **319**, 582 (2008).
[7] L. G. Dowell *et al.*, *Nature* **188**, 1144 (1960).
[8] M. G. Sceats *et al.*, in *Water Compr. Treatise*, F. Franks, Ed. (Plenum, New York, 1982).
[9] A. K. Soper, *Chem. Phys.* **202**, 295 (1996).
[10] C. G. Salzmann *et al.*, *Science* **311**, 1758 (2006).
[11] C. G. Salzmann *et al.*, *Phys. Rev. Lett.* **103**, 105701 (2009).

APPENDIX 25 NIMROD PROPOSAL SUBMITTED ON 15.10.2011

Structural investigations of low-temperature "trapped solutions"of C_{60} fullerene in water

Introduction:

This study aims to uncover the structural arrangement of water molecules in unstable solutions containing non-polar hydrophobic molecules. This will improve our understanding of hydrophobic forces, which are responsible for a variety of fundamentally important processes, such as protein folding, enzyme-substrate interactions and surfactant aggregation.[1] Although a robust theoretical framework exists for understanding the relation between water structure and hydrophobic forces,[1] experimentalists have only been able to study water at hydrophobic surfaces,[2] and at the non-polar groups of dissolved amphiphilic molecules.[3] The low water solubility of hydrophobic molecules has been a fundamental obstacle to a better understanding of hydrophobic forces and many questions remain unanswered. These include the length over which water structure is influenced and how the strength of the effect varies with the size of the hydrophobe.[4] We are addressing these questions by investigating the structures and properties of aqueous hydrophobe solutions in their highly metastable glassy states, which can be prepared by vapour co-deposition at 80 K. We call these states "trapped solutions".

The notion that these materials, prepared from the vapour phase, are structurally analogous to liquids may seem unlikely, but is strongly supported for the water system by neutron scattering data,[5] which show that the structure of amorphous solid water (ASW) formed by vapour deposition, is very similar to that of hyperquenched glassy water (HGW) formed by rapidly reducing the temperature of liquid water. This indicates that sintering and annealing effects are sufficiently active at low enough temperatures to reorganise the as-deposited ASW into a structure that rests within an energy minimum shared by HGW and thus thermodynamically related to liquid water. Additionally, a glass transition (T_g) has been reported to exist for both ASW and HGW at 136 K,[6] below the temperature at which these materials crystallise to cubic ice (~150–160 K). We have chosen to study C_{60} fullerene as a model hydrophobe[7] because its 60 carbon atoms are symmetry equivalent which will simplify data analysis. In our lab, we can now prepare up to 4 g of amorphous H_2O/C_{60} deposit per day and with compositions containing C_{60} concentrations of up to 100 g L^{-1}, which allows these experiments to be attempted.

Main questions to be addressed:

- What is the structure of the H_2O/D_2O molecules in the immediate hydration shell of C_{60}? (*i.e.* How well hydrated is C_{60} within the sintered matrix and which hydrogen bonding ring sizes are prevalent?)
- How does the presence of C_{60} affect the structure of the H_2O/D_2O matrix?

Preliminary sample characterisation:

We have performed a number of experiments to characterise the structure and thermal properties of our samples. Figure 1a shows XRD patterns for amorphous H_2O/C_{60} vapour deposits containing 400 or 1800 water molecules per C_{60} (5 or 1 vol% of C_{60}), compositions in which the majority of water molecules are either contained within or beyond a 3-layer hydration shell, respectively. Raman spectra collected in the uncoupled O–D stretching region, shown in Figure 1b, indicate that C_{60} has a substantial influence on the local structure of water molecules within the matrix. The peak maximum is shifted by ~15 cm^{-1} relative to pure ASW and the peak shape is very similar to that observed for crystalline ice. The TPD (temperature programmed desorption) data shown in Figure 1c, specifically the greater temperature required to increase the H_2O desorption rate for deposits containing C_{60}, relative to pure ASW, also suggests that C_{60} influences water structure and increases the strength of hydrogen bonding interactions between water molecules. Sintering (indicated by pressure spikes caused by the collapse of micropores[8] at ~120–140 K) and crystallisation processes (indicated by a decrease in pressure[9] at ~150-165 K) can also be observed in these data, which shows that the temperature at which the H_2O matrix transforms

to cubic ice upon heating is greater for deposits containing C_{60}. In these samples, crystallisation is accompanied by a striking colour change from pink, similar to that observed for C_{60} dissolved in organic solvents, to a yellowish-brown indicative of aggregated C_{60}.[10]

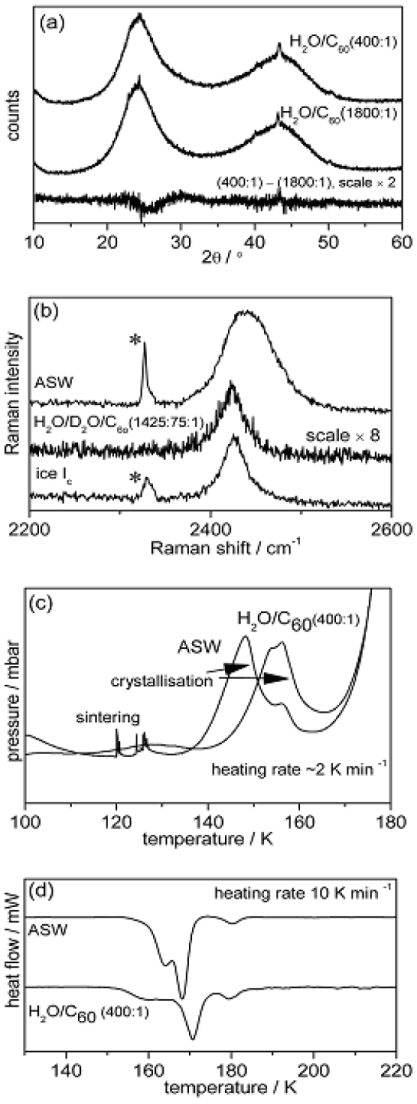

Figure 1 Lab characterisation data for amorphous H_2O (ASW) and H_2O/C_{60} vapour deposits (approximate mole ratios are indicated in parentheses). (a) XRD diffractograms and trace showing difference (sharp peaks at 43° are due to copper sample holder), (b) Raman spectra in the uncoupled O-D spectral region (peaks marked with * are due to pump oil contamination from the Raman cryostat system), (c) TPD data (in these experiments, pressure is proportional to the H_2O desorption rate) and (d) DSC thermograms.

A shift of the main exothermic peak to higher temperatures in the DSC data, shown in Figure 1d, confirms the increased temperature required for transformation of the H_2O matrix to cubic ice in deposits containing C_{60}, relative to ASW. Additionally, a pre-peak feature is present in the thermogram for the deposit containing C_{60}, which indicates some structural relaxation of the sample.

The Experiment:

We now have a unique opportunity to collect neutron diffraction data in order to reveal the structure of H_2O/D_2O molecules in the C_{60} hydration sphere, and to study C_{60}'s impact on the remaining matrix material. In order to study these two distinct regions we propose to collect scattering data for samples containing 0 (ASW), 1 or 5 vol% C_{60} to compare structure factors. We also intend to collect diffraction data for isotopically substituted samples (0, 50 or 100 mol% D_2O), to prepare model structures using the empirical potential structure refinement (EPSR) software. This will allow detailed information about the relative orientation and arrangement of the H_2O/D_2O molecules to be obtained. We request 5 days of beam time on NIMROD to carry out these 9 measurements (9 × 12 hours for sample measurements and transfers, and 12 hours for recording standards and backgrounds). Samples will be prepared and sintered *in situ* in our vacuum chamber to eliminate any micropores,[5] then immediately loaded into suitable vanadium sample holders, which will be transported to ISIS in liquid nitrogen. The wide range of momentum transfers available on NIMROD is expected to enable the precise determination of structure factors, which are required for an accurate structural refinement.

References:

[1] W. Blokzijl, *et al., Angew. Chem. Int. Ed. Engl.* **32**, 1545 (1993)
[2] Y. R. Shen, et al., *Chem. Rev.* **106**, 1140 (2006)
[3] D. T. Bowron, et al., *J. Chem. Phys.* **114**, 6203 (2001)
[4] B. P. Lambeth *et al., J. Chem. Phys.* **133** 221101 (2010)
[5] D. T. Bowron *et al., J. Chem. Phys.* **125** 194502 (2006)
[6] A. Hallbrucker *et al., J. Phys. Chem.* **93**, 4986 (1989)
[7] X. Ma, *et al., Langmuir* **26**, 11886 (2010)
[8] K. P. Stevenson, *et al., Science* **283** 1505 (1999)
[9] R. Smith, *et al., J. Phys. Chem. A.* **115** 5908 (2011)
[10] A. Beeby, *et al., J. Chem. Soc., Chem. Commun.* **2**, 173 (1994)

APPENDIX 26 SANDALS PROPOSAL SUBMITTED ON 7.2.2012

Structural investigations of low-temperature "trapped solutions" of C_{60} fullerene in water

Introduction

The low water solubility of hydrophobic molecules has been a major obstacle to a better understanding of hydrophobic forces which are of importance for fundamental processes such as protein folding, enzyme-substrate interactions and surfactant aggregation.[1] To date, experimentalists have only been able to study water at hydrophobic surfaces and around the non-polar groups of dissolved amphiphilic molecules. [2, 3] Whilst this work provides an understanding of some fundamentally important processes, many questions still remain unanswered, such as the length over which water structure is influenced and how the strength of the effect varies with the size of the hydrophobe.[4]

This study aims to investigate the structural arrangement of water molecules in aqueous C_{60} fullerene solutions in their highly metastable glassy state, which we can now prepare by vapour co-deposition at 77 K. We call these states "trapped solutions". We believe that these materials, prepared from the vapour phase, are structurally analogous to liquids and this view is strongly supported by neutron scattering data,[5] which show that the structure of amorphous solid water (ASW), formed by vapour deposition, is very similar to that of hyperquenched glassy water (HGW) formed by rapidly reducing the temperature of liquid water. This indicates that sintering and annealing effects are sufficiently active at low temperatures to reorganise the as-deposited ASW into a structure that rests within an energy minimum shared by HGW and is thus thermodynamically related to liquid water. Additionally, a glass transition has been reported to exist for both ASW and HGW at 136 K,[6] below the temperature at which these materials crystallise to stacking disordered ice, ice I_{sd} (~150–160 K). (Ice I_{sd} was formerly known as cubic ice.[7])

The low temperature C_{60}/H_2O system is of particular interest to us for the following reasons:

- These trapped solutions are far from equilibrium (aggregated hydrophobes). Therefore, we expect the structural origins of the hydrophobic effect to be very clearly manifested.
- The spherical shape of C_{60} will allow data analyses which would not be possible with structurally more complicated molecules. For example, as demonstrated by Weiss *et al.*[8] in a computational study, we would like to determine the orientations of the H_2O molecules in the hydration shells of C_{60} with respect to the centre of C_{60}.
- C_{60} is a nanoscale object (~1 nm diameter). It has been argued that this lengthscale is at an important cross-over point between the hydrophobic hydration of small molecular hydrophobes and hydrophobic surfaces.[9]
- The carbon/water interface is of strong biological interest.[10]

In our lab, we can now prepare up to 4 g of amorphous H_2O/C_{60} deposit per day and with compositions containing C_{60} concentrations of up to 100 g L^{-1}, which allows these experiments to be attempted.

Main questions to be addressed

- What is the impact of C_{60} on the hydrogen bonding structure of the H_2O molecules, in the hydration shells of C_{60} and in the matrix?
- How well hydrated is C_{60} in these samples?
- Which hydrogen bonding ring sizes are prevalent in the hydration shells?
- Do the water molecules near C_{60} have a net orientation?

Preliminary sample characterisation

We have performed a number of experiments to characterise the structure and thermal properties of our samples. Figure 1a shows XRD patterns for amorphous H_2O/C_{60} vapour deposits containing 400 or 1800 water molecules per C_{60} (5 or 1 vol% of C_{60}), compositions in which the majority of water molecules are either contained within or beyond a 3-layer hydration shell, respectively. Raman spectra collected in the uncoupled O–D stretching region, shown in Figure 1b, indicate that C_{60} has a substantial influence on the local structure of water molecules within the matrix. The peak maximum is shifted by ~15 cm^{-1} relative to pure ASW and the peak shape is very similar to that observed for crystalline ice. The TPD (temperature programmed desorption) data shown in Figure 1c, specifically the greater temperature required to

increase the H_2O desorption rate for deposits containing C_{60}, relative to pure ASW, also suggests that C_{60} influences water structure and increases the strength of hydrogen bonding interactions between water molecules. Sintering (indicated by pressure spikes caused by the collapse of micropores,[11] at ~120–140 K) and crystallisation processes (indicated by a decrease in pressure,[12] at ~150–165 K) can also be observed in these data, which shows that the temperature at which the H_2O matrix transforms to ice I_{sd} upon heating is greater for deposits containing C_{60}. In these samples, crystallisation is accompanied by a striking colour change from pink (similar to that observed for C_{60} dissolved in organic solvents), to a yellowish-brown indicative of aggregated C_{60}.[13]

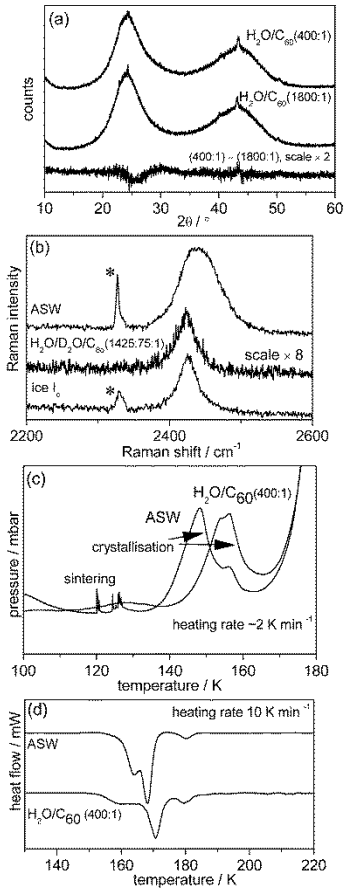

Figure 1 Lab characterisation data for amorphous H_2O (ASW) and H_2O / C_{60} vapour deposits (approximate mole ratios are indicated in parentheses). (a) XRD diffractograms and trace showing difference (sharp peaks at 43° are due to copper sample holder), (b) Raman spectra in the uncoupled O-D spectral region (peaks marked with * are due to pump oil contamination from the Raman cryostat system), (c) TPD data and (d) DSC thermograms.

A shift of the main exothermic peak to higher temperatures in the DSC data, shown in Figure 1d, confirms the increased temperature required for transformation of the H_2O matrix to ice I_{sd} in deposits containing C_{60}, relative to ASW.

The experiment at ISIS

We now have a unique opportunity to collect neutron diffraction data in order to reveal the structure of H_2O molecules in the C_{60} hydration shells, and to study C_{60}'s impact on the remaining matrix material. In order to study these two distinct regions we propose to collect scattering data for samples containing 0 (ASW), 1 or 5 vol% C_{60} to compare structure factors. We also intend to collect diffraction data for isotopically substituted samples (0, 50 or 100 mol% D_2O), to prepare model structures using the empirical potential structure refinement (EPSR) software. This will allow detailed information about the relative orientation and arrangement of H_2O molecules to be obtained. We request 5 days of beam time on SANDALS to carry out these 9 measurements (9 × 12 hours for sample measurements and transfers, and 12 hours for recording standards and backgrounds). Samples will be prepared and sintered *in situ* in our vacuum chamber to eliminate any micropores,[5] then immediately loaded into suitable vanadium sample holders, which will be transported to ISIS in liquid nitrogen. The range of momentum transfers available on SANDALS is expected to enable the precise determination of structure factors, which are required to create representative model structures using EPSR.

We are applying for rapid access as the research described forms a critical part of an EPSRC-sponsored studentship. The student is currently in the second year of his studies. Access to neutron data at this stage is vital to allow his project to proceed. The research is also supported by the Royal Society.

References

1. W. Blokzijl, et al., *Angew. Chem. Int. Ed. Engl.*, 1993, **32**, 1545-1579.
2. Y. R. Shen, et al., *Chem. Rev.*, 2006, **106**, 1140-1154.
3. D. T. Bowron, et al., *J. Chem. Phys.*, 2001, **114**, 6203-6219.
4. B. P. Lambeth, et al., *J. Chem. Phys.*, 2010, **133**, 221101.
5. D. T. Bowron, et al., *J. Chem. Phys.*, 2006, **125**, 194502.
6. A. Hallbrucker, et al., *J. Phys. Chem.*, 1989, **93**, 4986-4990.
7. T. L. Malkin, et al., *Proc. Natl. Acad. Sci. USA*, 2011, doi: 10.1073/pnas.1113059109.
8. D. R. Weiss, et al., *J. Phys. Chem. B.*, 2008, **112**, 2981-2990.
9. K. Lum, et al., *J. Phys. Chem. B*, 1999, **103**, 4570-4577.
10. P. Ball, *Chem. Rev.*, 2008, **108**, 74-108.
11. K. P. Stevenson, et al., *Science*, 1999, **283**, 1505-1507.
12. R. S. Smith, et al., *J. Phys. Chem. A*, 2011, **115**, 5908-5917.
13. A. Beeby, et al., *Chem. Comm.*, 1994, 173-175.

APPENDIX 27 EXPERIMENTAL REPORT FOR RB1200000

ISIS Experimental Report **Rutherford Appleton Laboratory**		**RB Number:**	1200000
		Date of Report:	8/4/2013
Title of Experiment:	Structural investigations of low-temperature "trapped solutions" of C_{60} fullerene in water	**Local Contact:**	Sam Callear
Principal Proposer:	C. G. Salzmann*1	**Instrument:**	SANDALS
Affiliation:	UCL*1 and University of Durham*2		
Experimental Team:	C. G. Salzmann*1, J. J. Shephard*2, and J. S. O. Evans*2.	**Date of Experiment:**	4.8.2012

Nine amorphous solid water (ASW) - C_{60} mixtures were measured at 80 K on SANDALS in order to investigate the impact of C_{60} on the water structure. Empty TiZr sample containers, empty cryostat and empty instrument measurements were also carried out. The packing fraction and composition of the samples were calculated from the change in mass of the containers during a two stage cleaning process using an estimated density for the hydrogenated sample of 0.938 g cm^{-1}. The merged data, run numbers and composition of the samples measured are given in Figure 1. The measured packing fraction, which varied between 0.23 and 0.47 for different samples was used to adjust the scattering level of these traces. There was a large amount of small angle scattering in all samples. This indicates that the ASW was porous and that the annealing procedure carried out to 115 K in the depositon vacuum chamber was insuffient to create a homogenius material. Initial data processing suggests that the introduction of C_{60} into the ASW matrix had little effect on the water structure. The main difference between traces with different C_{60} concentrations can be attributed to additional intramolecular C_{60} distances and the impact of the different scattering length density of C_{60} relative to ASW on the average scattering levels.

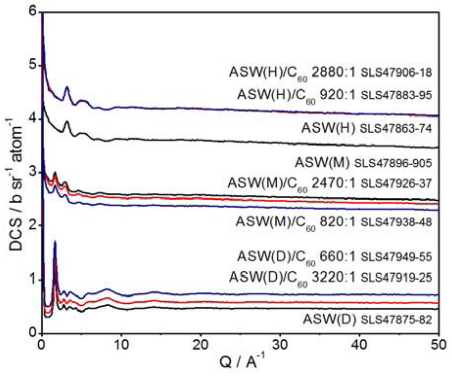

Figure 1 Merged DCS data for ASW/C_{60} trapped solutions at 80 K. The measured sample composition and SANDALS run numbers are also given.

In addition to the proposed measurements, the deuterated ASW sample with the greatest C_{60} concentration (~2.5 vol %) was heated from 80 to 220 K at 0.4 deg min and diffraction data were collected at 10 minute intervals (SLS47956-997). A selection of this data is shown in Figure 2. This data indicates that three structural changes occurred upon heating. At temperatures between 80 and 140 K, the decreases in small angle scattering indicates sintereing and pore collapse. At temperatures between 130 and 150 K, before the onset of crystalisation, the width of the fisrt sharp diffraction peak decreases indicating changes in medium range order. Between 150 and 170 K Bragg peaks appear, due to the crystalisation of ASW. A further series of measurements on NIMROD are currently proposed in order to repeat this experiment for pure ASW. We would now like to use the low Q data and higher count rates available on NIMROD to find out how complete the sintering proccesse are before crystallisation and the cause of the change in medium range. In particular we are interested to find out if the sharpening of the FSDP indicates the final stages of sintereing, the initial stages of crystalisation or a glass to liquid transition.

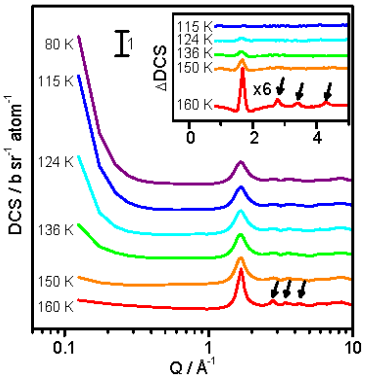

Figure 2 Diffraction data of a D_2O ASW sample containing 2.5 vol% C_{60} recorded upon heating. The curves are shifted vertically for clarity. The inset shows the differences between the data recorded at the successively higher temperatures and at 80 K. Arrows indicate the appearance of Bragg peaks.

APPENDIX 28 SANDALS PROPOSAL SUBMITTED ON 16.4.2012

The microstructure of the acetone – chloroform azeotrope

Background

While separation procedures based on distillation are often adversely affected by the occurrence of azeotropes, a wide range of applications benefit from the fact that the vapour composition of an azeotrope is the same as the composition of the liquid phase. Prominent examples include cleaning solvents in the electronics industry[1] as well as safe and low-cost anaesthetics.[2] However, the design of liquid mixtures with desirable physico-chemical properties can be a daunting task.[3] From the experimental perspective, a major challenge now lies in the structural characterisation of the aggregates in the liquid which can consist of like and unlike species.

The acetone – chloroform system is the classic textbook example of a negative-pressure azeotrope, *i.e.* the vapour pressures of the binary mixtures are lower than expected for ideal mixtures (*cf.* Fig. 1), the mixing is exothermic and the excess volumes of mixing are negative.[4-6] These deviations from ideal behaviour are thought to originate from attractive hydrogen-bonding interactions which are present in the mixtures but not in the pure liquids.[4, 5] Although the acetone – chloroform system has been studied extensively since 1900,[6] the composition and structure of the acetone – chloroform azeotropic cluster has not yet been determined experimentally.

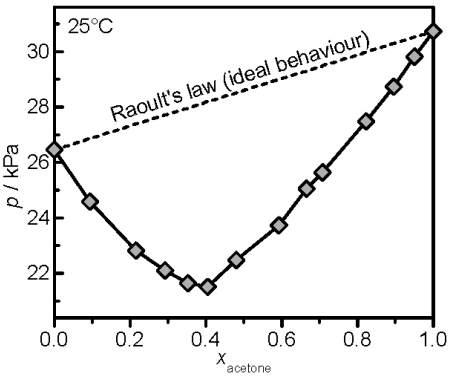

Figure 1. *Vapour pressure – composition diagram for mixtures of acetone and chloroform at 25°C. (data taken from ref. 5.)*

Previous studies have predicted the structure of the azeotropic clusters based on thermodynamic data,[5] infrared spectroscopy[7] and Monte-Carlo simulations.[8] The suggested structures are conflicting and contain, apart from one acetone molecule, either one or two chloroform molecules. Figure 2 shows the structures of the proposed clusters together with "cartoon-style" radial distributions functions of the interatomic distances between the hydrogen atoms of acetone (Ha) and chloroform (Hc). In structure (a) there is a single hydrogen bond between the oxygen lone-pair electrons and the hydrogen atom of the chloroform. In (b) there are two hydrogen bonds between the oxygen lone pairs and the hydrogen atoms on the two chloroform molecules. In (c) there are two hydrogen bonds as in (b) but with additional hydrogen-bonding interactions between the chlorine atoms and the methyl hydrogen atoms. In structure (d), a small trimeric chain is formed by a hydrogen-bond between the oxygen of acetone and the hydrogen of chloroform and also between a chlorine atom on this molecule and the hydrogen on a second chloroform molecule.

The SANDALS instrument at ISIS provides a unique opportunity to determine the composition, structure and concentration of the azeotropic clusters in the acetone – chloroform mixtures. This could finally prove that interspecies association is causing the negative-azeotrope behaviour of acetone – chloroform mixtures. Furthermore, the structural insights gained from this study will help to further optimise the potentials of the force fields used in the computer models of chloroform and acetone (*cf.* ref. 8).

In order to obtain a reliable set of partial structure factors and radial distribution functions from empirical potential structure refinement (EPSR),[9] we will carry out a range of isotopic-substitution measurements (H/D and $^{35}Cl/^{37}Cl$). The $^{35}Cl/^{37}Cl$ substitution seems particularly important with respect to differentiating between structures (b) and (c). In order to investigate the occurrence of structure (d), it will be important to confirm that there are no chloroform clusters present in the pure liquid as it is generally assumed.[5]

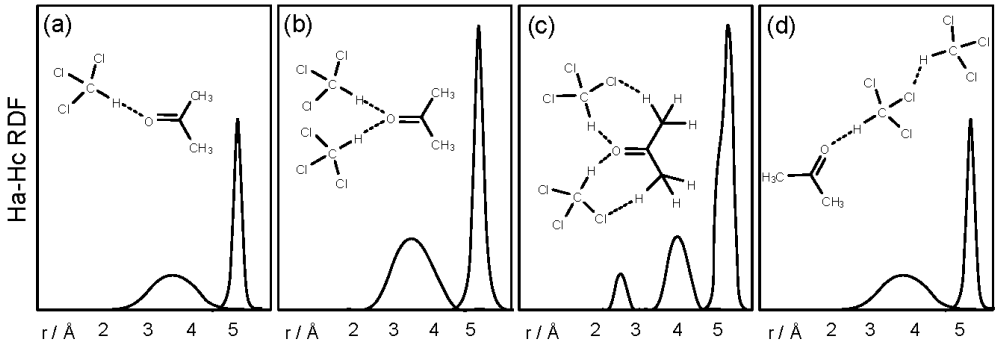

Figure 2. *Structures proposed to date for the acetone – chloroform azeotropic cluster and "cartoon-style" first-neighbour radial distribution functions for the hydrogen (acetone – chloroform) atom pairs. The RDFs were approximated by considering the geometries and conformations of the various clusters types.*

Experiment

All experiments will be carried out at 25°C and an acetone mole fraction of 0.405 will be used for all azeotropic mixtures (*cf.* Fig. 1).[5] In order to obtain a sufficient level of confidence in the partial structure factors from EPSR, seven acetone – chloroform mixtures will be prepared with either 0%(H), 50%(M) or 100%(D) deuterium substitution of the acetone hydrogens (Ha) and/or the chloroform hydrogens (Hc) to give samples with the following isotopic compositions: Ha(D)/Hc(D), Ha(H)/Hc(D), Ha(H)/Hc(H), Ha(D)/Hc(H), Ha(M)/Hc(D), Ha(D)/Hc(M) and Ha(M)/Hc(M). Due to the large incoherent scattering from ^{35}Cl atoms,[10] isotopically pure ^{37}Cl chloroform, prepared by the haloform reaction with $^{37}Cl_2$ made from $Na^{37}Cl$,[10] will be used for these mixtures. In addition, we will measure two mixtures of deuterated acetone and $CDCl_3$, one containing $CDCl_3$ with the naturally occurring isotope composition of chlorine (75.78% ^{35}Cl and 24.22% ^{37}Cl) and another with a 50% mixture of the standard $CDCl_3$ and our $CD^{37}Cl_3$. For the measurements on pure chloroform, we will measure $CD^{37}Cl_3$, $CH^{37}Cl_3$ and $CDCl_3$ with the natural chlorine isotope composition. All chloroform samples will be dried and kept under inert gas which will make the addition of a stabiliser unnecessary.

We request a total of 4 days on SANDALS in order to carry out these 12 measurements. (12×7 = 84 hours for measurements and 12 hours for sample transfers and standards.) This work is supported by an EPSRC-sponsored PhD studentship and a URF grant by the Royal Society.

References

1. http://www2.dupont.com/Vertrel/en_US/.
2. G. A. Busato, et al., *Update Anaesth.*, 2004, **18**, 1
3. W. Malesinki, *Azeotropy and other theoretical problems of vapour-liquid equilibrium*, Interscience Publishers, 1965.
4. F. Dolezalek, *Z. Phys. Chem.*, 1908, **64**, 727
5. A. Apelblat, et al., *Fluid Phase Eq.*, 1980, **4**, 229-255
6. J. v. Zawidzki, *Z. Phys. Chem.*, 1900, **35**, 129
7. M. R. Jalilian, et al., *Spectrochim. Acta A*, 2005, **62**, 322-325
8. G. Kamath, et al., *Phys. Chem. B*, 2005, **109**, 19463-19473
9. A. K. Soper, *Chem. Phys.*, 1996, **202**, 295-306
10. H. Bertagnolli, et al., *Mol. Phys.*, 1978, **36**, 1769-1777

Appendix 29 Experimental Report for RB1220357

ISIS Experimental Report **Rutherford Appleton Laboratory**		**RB Number:**	1220357
		Date of Report:	1/10/2013
Title of Experiment:	The microscopic structure of the acetone - chloroform azeotrope	**Local Contact:**	Silvia Imberti
Principal Proposer:	C. G. Salzmann[1]	**Instrument:**	SANDALS
Affiliation:	UCL[1] and University of Durham[2]		
Experimental Team:	C. G. Salzmann[1], J. J. Shephard[1,2], and J. S. O. Evans[2].	**Date of Experiment:**	8/10/2012

To better understand the structural origin of negative pressure azeotropy, seven chloroform-acetone mixtures with acetone mole fractions of 0.405 and with different levels of H/D isotopic substitution were measured on SANDALS. The liquids were weighed into 1 mm wide TiZr containers, the temperature was maintained at 25°C using an external water bath and sample changing was automated. In addition, we measured three pure chloroform samples and nine benzene-methanol mixtures with methanol mole fraction of 0.55. Chloroform was considered to be a useful control experiment and the benzene-methanol mixtures, which display positive pressure azeotropy at this composition, were included with the aim of providing a more complete understanding into the nature of azeotropy in general. The absorption and multiple scattering corrected merged DCS data for chloroform (Fig.1(a)) were found to have a prominent underlying slope in the DCS, which we presume to be ascociated with the large absorption cross section of ^{37}Cl. The slopes were less pronoundced in the chloroform-acetone data (Fig 1(b)) and absent in the benzene-methanol data (Fig 1(c)). The average DCS levels were mostly found to correspond closely to the expected values. However, there were some exceptions with lower than expected DCS levels, later found to be caused by leaky TiZr sample containers. These measurements were repeated and the final data set, shown in Fig. 1, was checked for decreases in average DCS with time.

In addition to ongoing structural modelling using EPSR, initial data proccessing has indicated very clear differences in the structural origin of positive and negative pressure azeotropy in these systems. Whilst there were large changes in local ordering relative to the pure liquids in the chloroform-acetone mixtures, the benzene-methanol mixtures displayed very few changes in local order and a low-Q intensity consistent with clustering or large concentration fluctuations. The structural modelling of the pure chloroform liquid data is close to being completed and has revealed the details of several favourable molecular arrangements in the liquid. In particular, we have found evidence for halogen-halogen bonding interactions and have been able to show the importance of dipole alignments, which results in oscilations in the orientation correlation functions to the third molecular shell.

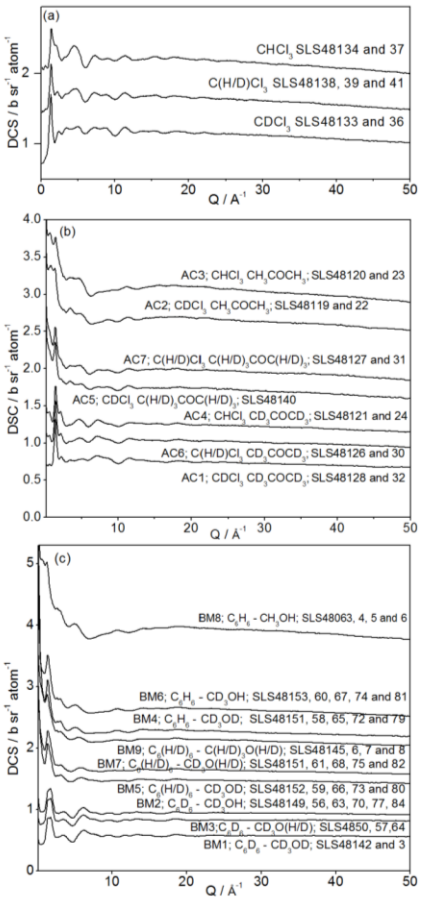

Figure 1 Merged DCS data of (a) chloroform, (b) azeotropic mixtures of chloroform and acetone, and (c) benzene and methanol. The H\D composition of the samples and run numbers for the DCS level checked data are indicated.

APPENDIX 30 SANDALS PROPOSAL SUBMITTED ON 16.4.2013

Medium-range order changes in amorphous solid water upon thermal annealing

Background

Amorphous solid water (ASW) is the most abundant form of ice in the universe.[1] It forms as a highly microporous solid from the vapour phase on cold dust particles and grains.[2] Despite its importance in critical cosmological processes[1] and its prominence as one of the polyamorphs of water, we still have an incomplete understanding of its glass-transition behaviour. It has been suggested on the basis of calorimetric data that ASW, and the structurally similar hyper-quenched glassy water,[3] exhibit glass transitions at 136 K.[4] However, the calorimetric feature is weak for a transition from a glass to a highly viscous and deeply supercooled liquid, and occurs at a temperature close to the onset of crystallisation at ~150 K. There have also been other scenarios proposed for this feature, such as a change in reorientation dynamics,[5] and it has been argued that the real glass transition of water should be at higher temperatures.[6-7]

The situation is complicated further by sintering processes which also take place upon heating ASW towards the onset of crystallisation. ASW, as prepared by vapour deposition onto substrates at 77 K, has a surface area of several hundred m^2 g^{-1} which has been shown by gas adsorption studies to decrease to 40 m^2 g^{-1} upon heating to ~113 K.[2] This process gives rise to additional exothermic features in calorimetric measurements of unannealed ASW.[4] The exact details of the sintering processes above ~113 K are still unclear.

New insights into the glass-transition behaviour of ASW will lead to a better understanding of the chemical properties of ASW as a matrix material and the impact of temperature on the transport and reactions of gas species trapped within the ice layers surrounding astral bodies. Furthermore, new experimental data will be of significant interest to scientists working in the field of glasses and amorphous solids, and will help resolve the fierce debate on the glass-transition behaviour of ASW – one of the fundamental unsolved issues in the water phase diagram.[5-7]

Our research aims to resolve these questions about the structural relaxation and dynamics of ASW. As part of these efforts, we have recently conducted a short proof-of-concept experiment on SANDALS, in addition to our primary experiment, which was carried out successfully. Figure 1 shows selected diffraction data collected upon heating a D_2O ASW sample which contained 2.5 vol% C_{60} fullerene. (C_{60} was incorporated to investigate its hydrophobic hydration in ASW.)

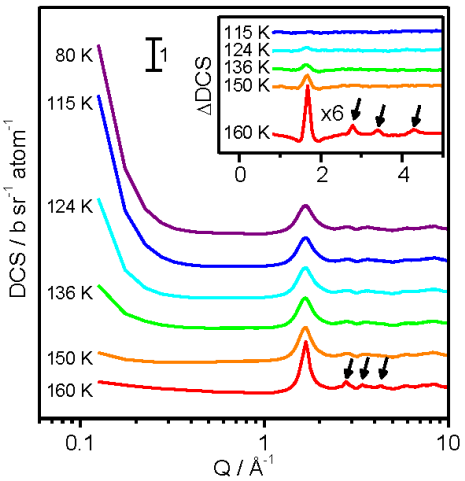

Fig. 1. Diffraction data of a D_2O ASW sample containing 2.5 vol% C_{60} recorded upon heating on the SANDALS instrument. The curves are shifted vertically for clarity. The inset shows the differences between the data recorded at the successively higher temperatures and at 80 K. Arrows indicate the appearance of Bragg peaks.

These data show two striking changes upon heating: (1) Changes in the shape and intensity of the first sharp diffraction peak (FSDP) before the onset of crystallisation and (2) a significant decrease in the low-Q intensities. Bragg peaks, which indicate crystallisation, only occur at 160 K as indicated by the arrows.

Figure 2 shows the results of a principle component analysis applied to the entire variable temperature data set in order to track the temperature range over which the different processes occurred. From this analysis, the decreases in the low-Q intensities appear to proceed until 145 K and changes in shape of the FSDP appear to begin at around 130 K. We note that this sample was annealed at 115 K in our vacuum chamber before the measurement at ISIS. The low-Q intensities may therefore be even higher for as deposited samples as indicated by the question mark in Fig. 2.

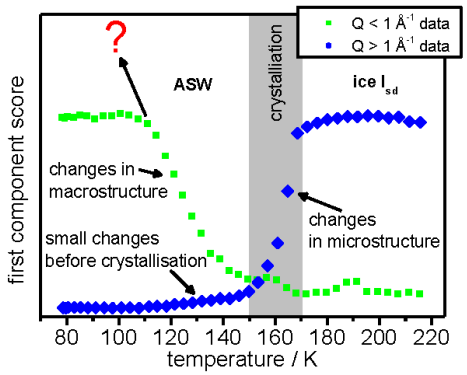

Fig. 2. Variation with temperature of the score for the first component from principle component analysis of the low Q (squares) and higher Q (diamonds) data.

The most likely explanations for these findings are that the decreases in the low-Q intensities are caused by progressive sintering processes in ASW (*i.e.* closing of pores) and that the changes in the FSDP are due to changes in medium-range order.[8] The latter could be associated with the initial stages of the crystallisation process, indicate a glass transition or even be connected to the final stages of the sintering process.

In order to fully clarify these findings and to address the open questions related to ASW mentioned above we would now like to find out the extent to which these changes in the diffraction data with temperature were caused by the presence of C_{60}. We therefore propose to repeat this experiment by heating pure D_2O ASW from 80 to 200 K at 0.1 K min $^{-1}$. This sample should be measured without the annealing step in the vacuum chamber in order to capture the entire extent of the sintering process, a factor which complicates the choice of control experiments required to pin down the cause of the sharpening of the FSDP.

In addition to the pure ASW, unannealed ASW containing 2.5 vol% C_{60} should be measured under the same conditions in order to allow a meaningful comparison of the C_{60}-containing and pure ASW data. Furthermore, in a third experiment we would like to record diffraction data upon heating the structurally similar low-density amorphous ice (LDA).[3] Pore-free LDA will be made by heating high-density amorphous ice at ambient pressure.[9] This experiment will provide key control-information required to interpret the ASW and ASW/C_{60} data because features related to sintering are expected to be absent.

Summary of questions to be addressed:

- To what extent are changes in the shape of the FSDP and decreases in low-Q intensities associated with processes occurring in ASW or related to the presence of C_{60}?
- Can the changes in the FSDP also be observed for non-porous LDA?
- How complete are the sintering processes in ASW before crystallisation occurs?
- Are the changes in medium-range order associated with the final stages of the sintering process, the initial stages of the crystallisation process or are they an indication of a glass to liquid transition?

Experimental

To answer these questions we plan to measure neutron diffraction structure factors on the SANDALS instrument (Q-range: 0.1 Å^{-1} – 50 Å^{-1}) in a cryostat while heating the following samples from 80 to 200 K at 0.1 K min^{-1}:

(1) pure unannealed D_2O ASW
(2) pure D_2O low-density amorphous ice
(3) unannealed D_2O ASW containing 2.5 vol% C_{60}

As for our previous SANDALS experiment, gram quantities of the ASW samples will be prepared in our vacuum chamber at UCL. The LDA sample will be obtained by heating high-density amorphous ice (HDA) at ambient pressure in our lab. The HDA sample will be prepared by pressure-induced amorphisation of ice I*h* at 77 K[9] using our high-pressure / low-temperature piston cylinder setup. The samples will then be transferred into standard TiZr sample cans at ISIS under liquid nitrogen and transferred into the cryostat precooled to 80 K. The group has extensive experience with sample preparation / transfer under liquid nitrogen conditions.[10-11]

A total beam time of 3 days is requested to carry out the 3 heating experiments as well as sample transfers. 12 hours are required for recording empty beam, empty cryostat, empty can and vanadium data.

References

[1] S. Kwok, University Science Books (2007)
[2] E. Mayer *et al.*, *Nature* **319**, 298 (1986).
[3] D. T. Bowron *et al.*, *J. Chem. Phys.* **125**, 194502 (2006).
[4] A. Hallbrucker *et al.*, *J. Phys. Chem.* **93**, 4986 (1989).
[5] C. G. Salzmann *et al.*, *Phys. Chem. Chem. Phys.* **13**, 18468 (2011).
[6] Y. Yue *et al.*, *Nature* **427**, 717 (2004).
[7] C. A. Angell, *Science* **319**, 582 (2008).
[8] J. M. Zaug *et al.*, *Nature Mat.* 7, 890 (2008).
[9] O. Mishima *et al.*, *Nature* **310**, 393 (1984).
[10] C. G. Salzmann *et al.*, *Science* **311**, 1758 (2006).
[11] C. G. Salzmann *et al.*, *Phys. Rev. Lett.* **103**, 105701 (2009).

APPENDIX 31 SANDALS PROPOSAL SUBMITTED ON THE 16.10.2013

Halogen Bonding in Liquid Halomethanes

Halogenated molecules can form favourable halogen-bonding interactions R–X•••B where X is either chlorine, bromine or iodine, and B a Lewis-base acceptor.[1] Due to their non-covalent, mostly electrostatic nature halogen bonds share many similarities with hydrogen bonds (R–H•••B),[2] and are of fundamental importance in, for example, the folding and activity of proteins,[3] and the polymorphism of pharmaceuticals.[4] The number of scientific publications per year devoted to the topic of "halogen bonding" has risen by more than a factor of 10 in the past decade illustrating the emerging prominence and importance of this type of non-covalent interaction.[1]

Halogen bonding is a consequence of attractions between a region of positive charge at the distal end of the halogen atom and nucleophilic electron-rich species. The positively charged region, called a σ-hole,[1] is understood to be associated with the electron deficiency of the outer lobe of a half filled p-bonding orbital along the extension of the covalent bond.[2, 5] The blue-shaded regions on the halogen atoms of the various tri- and dihalomethanes in Fig. 1 indicate σ-holes.

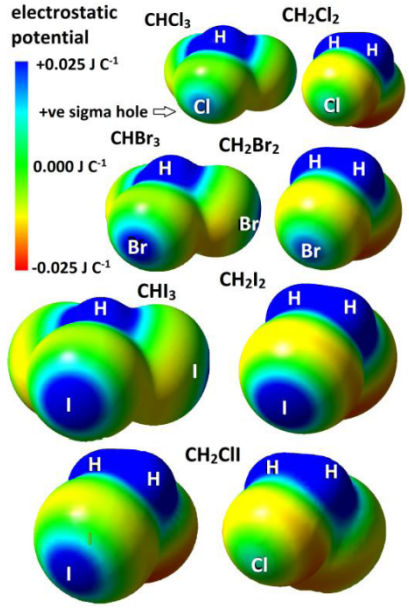

Figure 1 *Preliminary DFT study of various di- and trihalomethanes showing the 0.001 electrons bohr^{-3} isodensity surface colour mapped for electrostatic potential.*

The most common halogen-bond acceptors in biological systems are nitrogen, oxygen or sulphur lone-pair orbitals. However, in fields of study such as crystal engineering it is increasingly common to find examples of halogen bonding where the negatively charged region of a second halogen atom acts as the halogen-bond acceptor.[6,7,8]

In a recent SANDALS experiment we have identified the importance of halogen bonding in liquid chloroform ($CHCl_3$).[9] We show in this study that the empirical potentials introduced by EPSR correct for the inadequate partial charge description, changing the structure of the computational model to give molecular arrangements consistent with σ-hole charge separations.[10] Figure 2 shows the Cl–Cl RDF for liquid chloroform from our EPSR-optimised structural model marked with a grey-shaded area to indicate contacts at distances smaller than 3.5 Å, the sum of the van der Waals radii. Coordination number analysis indicates that 92 % of molecules form at least one halogen bond and analyses of bond angles are consistent with interactions of chlorine σ-holes with the negative circumferences of other chlorine atoms.

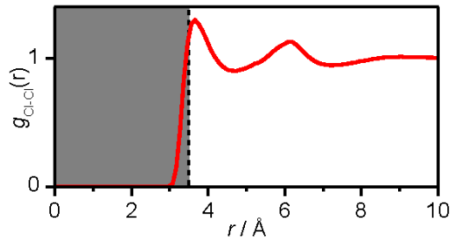

Figure 2 *Isotropic Cl-Cl radial distribution function of liquid chloroform showing a large proportion of Cl-Cl distances smaller than the sum of the van der Waals radii.*

On the basis of our recent findings we now propose a general and systematic study into the phenomenon of halogen bonding in the liquid state which we believe will make important contributions to this emerging field. The overall aims of this study are:

- to demonstrate the existence of halogen bonding in a range of liquid halomethanes.
- to investigate the influence of increasing strength of halogen bonding in the sequence X = Cl, Br and I on the structures of the liquids.

- to clarify the importance of halogen bonding for the excellent properties of halomethanes as solvents in chemistry.
- to understand the relative balance of halogen bonding and local packing effects on the overall structures of the liquids.
- to use the new knowledge to better understand how halogen bonding impacts upon systems relevant to biology and crystal engineering.

(1) Dihalomethanes (CH_2X_2 with X = Cl, Br and I)

The dihalomethanes are the optimal model compounds for studying the relative strength of halogen bonding for X = Cl, Br and I as they are the one family in which all three compounds are liquids at ambient pressure and room temperature. Fig. 1 shows that the expected σ-hole is much more dominant in case of diiodomethane than it is for dichloromethane. Consistent with this, DFT calculations have shown that C–Cl is a weaker halogen-bond donor to formaldehyde in the gas phase than C–I.[11] We therefore expect diiodomethane to be structurally more ordered than dichloromethane as a consequence of stronger halogen bonding. However, it is unclear what the situation will be if more attractive halogen-bonding interactions are sterically disfavoured, especially in the case of the large iodine atoms. It is also not clear how differences in the electrostatic and dispersive nature of halogen bonds, which are also predicted to vary with halogen size,[11] manifest structurally. It was postulated that the predicted increase in electrostatic contribution to the bond with increasing halogen size leads to a more directional bond. However, as yet there is no structural evidence for this.

(2) Chloroiodomethane (CH_2ClI)

A further level of insight will be gained by investigating the structure of liquid chloroiodomethane which displays the greatest possible mismatch in halogen size and difference in potential at the sigma holes (*cf.* Fig. 1) as well as a lower symmetry than the dihalomethanes mentioned above. This part of the project will give additional insights into the relative strengths of Cl–Cl and I–I but also Cl–I interactions, and will therefore provide a critical test of the results obtained in part (1).

(3) Bromoform ($CHBr_3$) & comparisons with previous work on chloroform ($CHCl_3$)

The comparison of our existing structural data for chloroform with those obtained from new measurements on bromoform will give further insights into the relative strength and character of Cl–Cl and Br–Br interactions. As shown in Fig. 1, the σ-holes of the trihalomethanes are slightly more pronounced than in the corresponding dihalomethanes. Furthermore, the comparison of structural data for the trihalomethanes and the dihalomethanes will enable us to draw important conclusions on how local packing effects, which depend on the geometries of the molecules, can interfere with halogen bonding. In essence, the trihalomethanes can be regarded as flat trigonal pyramids which are expected to pack very differently compared to the 'banana-shaped' dihalomethanes.

Experimental

In total we request 5 days of beam time to carry out 15 SANDALS measurements (15 × 6 hours + 30 hours for vanadium, backgrounds and empty container measurements). The 15 SANDALS measurements correspond to 3 measurements of each liquid at room temperature (CH_2Cl_2, CH_2Br_2, CH_2I_2, CH_2ClI and $CHBr_3$) with different levels of H/D isotopic substitution (x_H = 0, 0.5 and 1). All compounds are commercially available (protiated and deuterated) and safe to handle (*i.e.* non-flammable). The neutron measurements will be complemented by total scattering X-ray measurements which will enable a more accurate separation of the data into partial structure factors due to the dominating X-ray scattering lengths of the halogens. For effective data analysis, Dr A. Soper has recently kindly agreed to update his plot2D programme so that it will be possible to illustrate the structures of the various liquid halomethanes in a more effective way than the traditionally used orientational correlation functions.[12]

1. P. Politzer, J. S. Murray and T. Clark, *Phys. Chem. Chem. Phys.*, 2013, **15**, 11178.
2. P. Politzer, J. S. Murray and P. Lane, *Int. J. Quant. Chem.*, 2007, **107**, 3046-3052.
3. M. R. Scholfield, C. M. V. Zanden, M. Carter and P. S. Ho, *Protein Sci.*, 2013, **22**, 139-152.
4. R. Wilcken *et al.*, *J. Med. Chem.*, 2013, **56**, 1363-1388.
5. H. Torii and M. Yoshida, *J. Comput. Chem.*, 2010, **31**, 107-116.
6. F. F. Awwadi, R. D. Willett, K. A. Peterson and B. Twamley, *Chem. Eur. J.*, 2006, **12**, 8952-8960.
7. A. Anthony *et al.*, *Cryst. Eng.*, 1998, **1**, 1-18.
8. B. K. Saha *et al.*, *Cryst. Growth Des.*, 2005, **5**, 887-899.
9. J. J. Shephard, J. S. O. Evans, A. K. Soper, S. Imberti and C. G. Salzmann, *Phys.Chem. Chem. Phys.*, 2013, submitted.
10. H. Torii, *J. Mol. Liq.*, 2005, **119**, 31 - 39.
11. K. E. Riley and P. Hobza, *J. Chem. Theory Comput.*, 2008, **4**, 232-242.
12. A. K. Soper, *J. Chem. Phys.*, 1994, **101**, 6888-6901.